UCLouvain
Louvain Drug Research Institute
Biomedical Magnetic Resonance

Monitoring the effect of anti-cancer drugs on extracellular pH and pO_2 using magnetic resonance

Chloé Buyse

Thesis submitted in fulfillment of the requirements for a Ph.D. degree in Biomedical and Pharmaceutical Sciences

2024

Thesis director:
Professor Bernard Gallez

Acknowledgements

Après quatre des années les plus importantes de ma vie, je tenais à exprimer ma gratitude pour toutes les personnes ayant contribué à l'aboutissement de cette thèse et qui m'ont fait grandir en tant que chercheuse, mais aussi en tant que personne.

Je voudrais d'abord commencer par remercier mon promoteur, le Professeur Bernard Gallez, de m'avoir permis de réaliser non seulement mon mémoire il y a déjà 5 ans, mais également ma thèse au sein du laboratoire REMA. Je suis très reconnaissante de tout le suivi, de l'encadrement, des conseils et corrections diverses que vous m'avez accordés et qui m'ont permis de me guider tout au long de mon parcours. Merci pour votre confiance, et may the spin be with you always.

Je remercie également la Professeure Bénédicte Jordan, qui m'a accompagnée pendant ces quatre ans. Merci pour votre investissement dans mon travail, vos corrections, de m'avoir fait évoluer grâce à vos remarques constructives sur mes présentations lors de labmeetings ainsi que par la relecture de ce travail.

Merci à mon président de jury, le Professeur Pierre Sonveaux ainsi qu'aux autres membres de mon comité d'encadrement, le Professeur Cyril Corbet et le Docteur Frank Peeters, pour leur investissement dans mon travail durant ces quatre années, pour leur suivi et suggestions lors de mes comités, me partageant leurs savoirs et expériences, afin de faire avancer mon projet et mes recherches. Je les remercie pour leurs relectures de ce manuscrit et leurs suggestions de modifications afin de l'améliorer. Merci également au Docteur Julien Valette et au Professeur Mark Pagel, d'avoir accepté de rejoindre mon jury en tant que

membres externes, de réviser mon manuscrit et d'avoir amené des discussions enrichissantes lors de ma défense privée.

Je souhaite exprimer ma sincère reconnaissance envers mes collègues du laboratoire REMA, dont le soutien a été indispensable à la réalisation de ce travail.

Je voudrais tout d'abord remercier du fond du cœur Nicolas, d'avoir pris sous son aile l'étudiante un peu perdue que j'étais il y a 5 ans. Tu as pris le temps de m'enseigner, avec une grande patience, l'art subtil qu'est la résonance magnétique. Merci d'avoir été toujours disponible et d'avoir pris des heures de ton temps pour m'expliquer, m'apprendre et m'accompagner pendant ces cinq ans. Tu as toujours su trouver les mots d'encouragement que j'avais besoin d'entendre pour me faire avancer et me remotiver. Je n'y serais certainement pas arrivé sans toi. Merci à Lionel, l'autre personne sans qui je ne serais pas arrivée au bout de cette thèse, le « couteau Suisse » de REMA. Tu m'as tellement appris et aidé pendant ces quatre ans. Merci d'avoir passé des soirées, des jours fériés et des weekends à l'IRM avec moi, toujours avec ta bonne humeur et tes jeux de mots de grande qualité.

Merci à Natacha : que dire à part dire que tu es le rayon de soleil du labo ? Je réalise la chance que j'ai eu de partager avec toi, et au même moment, nos mémoires puis nos thèses, ce qui veut dire aussi partager nos galères et nos bonheurs. Merci pour ton soutien inconditionnel, ton écoute et tes encouragements sans faille. Ton rire qui résonne à travers les pièces du labo me manquera beaucoup. Merci Barbara, de m'avoir prêté pour un petit moment ta RPE et d'avoir formé avec moi un duo féminin face à ce milieu masculin. Merci pour le meilleur fou-rire de ma vie, pour les discussions de résultats devant la RPE ou dans votre ancien bureau avec Lionel, tes encouragements et ton

soutien. J'ai beaucoup de chance d'avoir partagé un bout de ton parcours avec toi. Vous êtes des femmes et des chercheuses brillantes et j'ai beaucoup appris grâce à vous. J'ai hâte de voir ce que l'avenir vous réserve.

Merci à mes anciens collègues, avec qui j'ai eu l'honneur de partager le bureau sans-fenêtre-mais-avec-un-poster-d'une-fenêtre : Donatienne, Chantale et Jérôme. Merci d'avoir été si encourageants à mes débuts, toujours avec une oreille pour mes problèmes de manips et d'avoir partagé des gossips de qualité. Un merci tout particulier à Jérôme qui a, lui aussi, sacrifié de nombreuses soirées, parfois des nuits, pour m'aider à l'IRM. Merci à Natalie, pour nos conversations, nos rires et nos motivations mutuelles dès ton arrivée dans la cave. Merci à Caner de m'avoir montré comment manipuler des souris et passer des cellules en six minutes top chrono. J'ai une pensée pour Stefania, les deux Céline et Florian, qui ont partagé une petite partie de mon parcours en REMA. Merci d'avoir accompagné mes débuts au labo. Un grand merci également à Elise, Mohammad, Giulia, Mélina, Madeline et Yasmine. Je tiens aussi à remercier mes deux excellentes mémorantes, Aude et Samia. Ce fut un plaisir d'avoir pu travailler à vos côtés et de vous avoir vu évoluer au sein du laboratoire. Une grande partie de ce travail est le vôtre également.

Merci à tous pour les laser games, escape games, les gâteaux d'anniversaire, les pauses de midis à rallonge et surtout d'avoir essuyé mes larmes, de m'avoir reboosté lors de moments où je ne croyais plus en moi et d'avoir été les meilleurs collègues, et amis, dont j'aurais pu rêver pour m'accompagner pendant ces 5 ans au laboratoire REMA.

Je remercie mes amis et ma famille pour leur soutien tout au long de ce parcours. Merci à Estelle, mon acolyte SBIM depuis nos débuts à l'université et tous les jours depuis. Merci à mes plus grands supporters : mes parents, ma sœur, Louise

et Tom. Vous avez été ma plus grande source de motivation lorsque les difficultés, le stress et la peur me paralysaient. J'espère vous avoir rendu fiers.

Je finirais par remercier la personne la plus importante, mon mari Clément. Tu as été mon plus grand soutien, la force tranquille qui m'a permis d'avancer et d'arriver jusqu'ici. Je ne te remercierais jamais assez pour tes épaules sur lesquelles j'ai pu me reposer, et ton amour inconditionnel, depuis toujours.

Foreword

The monitoring of acidosis and hypoxia is crucial as both factors are involved in cancer progression and impact the efficacy of anti-cancer treatments. The aim of the thesis is to monitor, with noninvasive magnetic resonance techniques, pharmacological modulations of extracellular pH (pH_e) and partial pressure of oxygen (pO_2).

The **Introduction** of this thesis firstly generally describes the bioenergetics of cancer cells. In the second part, tumor extracellular acidosis, how it develops and its implications in tumor progression and treatment resistance are depicted. Methods to modify tumor pH_e and how to measure the changes are also described in this part. The third part of the introduction explains how tumor hypoxia arises and how cancer cells adapt to it. Again in this part, pharmacological modulations and different ways to measure hypoxia are described.

In the **Aims of the thesis**, the objectives and methodologies of this thesis project are described.

The **Results** chapter contains the three research papers written during this thesis. The first article describes how the effect of a pharmacological inhibition of the mitochondrial pyruvate carrier with UK-5099 can be measured with ^{31}P-nuclear magnetic resonance spectroscopy and how it compares to Chemical Exchange Saturation Transfer. The second article depicts the impact of a treatment with another inhibitor, syrosingopine, inhibiting the monocarboxylate transporters 1 and 4, measured with Chemical Exchange Saturation Transfer. The last article explains how Electron Paramagnetic Resonance spectroscopy can measure the effects of UK-5099 on both pH_e and pO_2 simultaneously.

The last part of this thesis, **Limitations and Perspectives**, summarizes and discusses the major findings of this thesis work. The advantages and limitations of our three methods are discussed and compared.

List of abbreviations

3-APP	3-Aminopropyl Phosphonate
ACC	Acetyl-CoA Carboxylase
ACLY	ATP-Citrate Lyase
ACSS2	Acetyl-CoA Synthetase 2
ADP	Adenosine Diphosphate
AE2	Anion Exchanger 2
APT	Amide Proton Transfer
ASCT2	ASL-like Na^+-dependent neutral amino acid transporter 2
ATP	Adenosine Triphosphate
BOLD	Blood Oxygen Level-Dependent
CA	Carbonic Anhydrase
CAF	Cancer-Associated Fibroblast
CaM	Calmodulin
CAR	Chimeric Antigen Receptor
CEST	Chemical Exchange Saturation Transfer
CHP	Calcineurin Homologous Protein
CPT-1	Carnitine Palmitoyltransferase-1
CW	Continuous Wave
DCE	Dynamic Contrast Enhanced
dHB	Deoxyhemoglobin
DSC	Dynamic Susceptibility Contrast
ECAR	Extracellular Acidification Rate
ECM	Extracellular Matrix
EMT	Epithelial-Mesenchymal Transition
eNOS	Endothelial Nitric Oxide Synthase
EPR	Electron Paramagnetic Resonance
ERK	Extracellular-signal-regulated Kinase

ETC	Electron Transport Chain
FA	Fatty Acid
FAO	Fatty Acid Oxidation
FASN	Fatty Acid Synthase
FDG	Fluorodeoxyglucose
FID	Free Induction Decay
FT	Fourier Transformation
GLS	Glutaminase
GLUD	Glutamate Dehydrogenase
GLUT1	Glucose Transporter 1
GSH	Glutathione
GSK-3	Glycogen Synthase Kinase-3
HAP	Hypoxia-Activated Prodrug
HIF-1	Hypoxia Inducible Factor-1
HK	Hexokinase
HRE	Hypoxia Response Element
IEPA	(±)2-imidazole-1-yl-3-ethoxycarbonylpropionic acid
iNOS	Inducible Nitric Oxide Synthase
LDH	Lactate Dehydrogenase
MAPK	Mitogen-Activated Protein Kinase
MCT	Monocarboxylate Transporter
MPC	Mitochondrial Pyruvate Carrier
MRI	Magnetic Resonance Imaging
MRS	Magnetic Resonance Spectroscopy
mTOR	Mechanistic Target of Rapamycin
NADPH	Nicotinamide Adenine Dinucleotide Phosphate
NBC	Na^+/HCO_3^- co-transporter
NHE	Na^+/H^+ Exchanger 1
NMR	Nuclear Magnetic Resonance

NO	Nitric Oxide
NOE	Nuclear Overhauser Enhancement
NSCLC	Non-small Cell Lung Cancer
OAA	Oxaloacetate
OCR	Oxygen Consumption Rate
OE	Oxygen-Enhanced
PD-L1	Programmed Death-Ligand 1
PDK	Pyruvate Dehydrogenase Kinase
PDK1	Phosphoinositide-Dependent Protein Kinase 1
PET	Positron Emission Tomography
PFK	Phosphofructokinase
PHD	Prolyl Hydroxylase
pH_e	Extracellular pH
pH_i	Intracellular pH
pHLIP	pH (low) Insertion Peptide
P_i	Inorganic Phosphate
PI3K	Phosphoinositide 3-kinase
PIP_2	Phosphatidylinositol 4,5-bisphosphate
PKB	Protein Kinase B
PKM2	Pyruvate Kinase M2
pO_2	Partial Pressure of Oxygen
ppm	Parts-per Million
PPP	Pentose Phosphate Pathway
pTAM	Monophosphonated Triarylmethyl radical
PTEN	Phosphatase and Tensin Homolog
pVHL	Von Hippel-Lindau
RF	Radiofrequency
ROI	Region of Interest
ROS	Reactive Oxygen Species

RTK	Receptor Tyrosine Kinase
S6K	p70 S6 Kinase
SIRT	Histone Deacetylase Sirtuin
SREBP	Sterol Regulatory Element-Binding Protein
SSP	Serine Synthesis Pathway
TAG	Triacylglycerides
TAM	Tumor-Associated Macrophage
TCA	Tricarboxylic Acid
TE	Echo Time
TEC	Tumor-derived vascular endothelial cell
TR	Repetition Time
Tregs	Regulatory T cells
TSP-1	Thrombospondin-1
UPR	Unfolded Protein Response
VEGF	Vascular Endothelial Growth Factor

Table of Contents

Introduction **18**

1. Bioenergetics of cancer cells 19

1.1. Metabolic flexibility of tumor cells 19

1.1.1. Glucose metabolism 20

1.1.1.1. Warburg effect 20

1.1.1.2. The PI3K/AKT network influences glucose metabolism 22

1.1.1.3. Mammalian target of rapamycin, mTOR 25

1.1.1.4. Hypoxia-inducible factor 25

1.1.1.5. MYC, Ras and TP53 27

1.1.2. Glutamine metabolism 27

1.1.3. Fatty acid metabolism 29

1.2. External stimulation 32

2. Acidosis 34

2.1. Acidosis regulation in cancer cells 34

2.1.1. Origin of acidosis 34

2.1.2. pH gradient reversal 35

2.1.3. Transporters 35

2.1.3.1. Na^+/H^+ Transporter 36

2.1.3.2. Carbonic Anhydrases 37

2.1.3.3. Monocarboxylate Transporters 38

2.1.4. Extracellular H^+ accumulation and venting 39

2.2. Consequences of tumor microenvironment acidosis 40

2.2.1. Metabolic reprogramming 40

2.2.2. Tumor progression 42

2.2.2.1. Proliferation and survival 42

2.2.2.2. Invasiveness, angiogenesis and metastasis 43

2.2.3. Treatment resistance 44

2.3. Pharmacological modulation of extracellular pH 47
2.3.1. Treatments targeting tumor acidosis 47
2.3.1.1. Sodium bicarbonate treatment 47
2.3.1.2. Proton-pump inhibitors 48
2.3.1.3. NHE1 inhibitors 48
2.3.1.4. CAIX inhibitors 49
2.3.1.5. MCT inhibitors 50
2.4. Assessment of tumor acidosis 54
2.4.1. SNARF-1 54
2.4.2. Seahorse XF 54
2.4.3. Electrodes 55
2.4.4. pHLIP 56
2.4.5. Nuclear Magnetic Resonance 57
2.4.5.1. Magnetic Resonance Spectroscopy 62
2.4.5.1.1. ^{1}H-MRS 63
2.4.5.1.2. ^{31}P-MRS 64
2.4.5.1.3. ^{19}F-MRS 65
2.4.5.2. Magnetic Resonance Imaging 66
2.4.5.2.1. CEST MRI 67
2.4.6. Electron Paramagnetic Resonance 74
3. Hypoxia 80
3.1. Contributing factors leading to hypoxia 80
3.1.1. Chronic hypoxia 81
3.1.2. Cycling hypoxia 82
3.2. Cancer cell responses to hypoxia 83
3.2.1. Gene activation 83
3.2.2. Effect on metabolism 85
3.2.3. Resistance to therapies 86
3.3. Pharmacological modulation of hypoxia 89
3.3.1. Treatments targeting hypoxia 90

3.3.1.1. Improving oxygen delivery 90
3.3.1.2. Decreasing oxygen consumption 91
3.3.2. Hypoxia-activated prodrugs 92
3.3.3. Inhibitors of molecular targets involved in hypoxic cell survival 93
3.4. Assessment of tumor hypoxia 94
3.4.1. Direct measurements 95
3.4.1.1. Electrodes 95
3.4.1.2. Fiber-optic devices 95
3.4.1.3. Magnetic Resonance Imaging 96
3.4.1.3.1. ^{19}F-imaging 96
3.4.1.4. Electron Paramagnetic Resonance oximetry 96
3.4.1.4.1. Soluble probes 97
3.4.1.4.2. Insoluble particulate probes 99
3.4.2. Indirect measurements 101
3.4.2.1. Seahorse XF 101
3.4.2.2. Magnetic Resonance Imaging 101
3.4.2.2.1. Endogenous contrast 101
Oxygen Enhanced MRI 102
Blood oxygen level-dependent contrast MRI 102
3.4.2.2.2. Exogenous contrast 103
3.4.2.3. PET radiotracers 103
3.4.2.4. Cellular response to hypoxia 104
Aims of the thesis 106
Results 110
1. Impact of Inhibition of the Mitochondrial Pyruvate Carrier on the Tumor Extracellular pH as Measured by CEST-MRI 111
2. Evaluation of Syrosingopine, an MCT Inhibitor, as Potential Modulator of Tumor Metabolism and Extracellular Acidification 127
3. Sensitive simultaneous measurements of oxygenation and extracellular pH by EPR using a stable monophosphonated trityl radical and lithium phthalocyanine 141
Discussion and perspectives 152

1. Main achievements of the thesis 153
1.1. pH_e measurements using ^{31}P-NMR and CEST-MRI 153
1.2. pO_2 measurements 154
2. Limitations, unsolved questions and perspectives 155
2.1. Methodological/technical issues 155
2.1.1. Discrepancies between ^{31}P-NMR and CEST-MRI 155
2.1.2. Discrepancies with other studies 156
2.1.3. Measurement of pH_e and pO_2 using EPR 157
2.1.4. Accuracy of calibrations 159
2.1.5. Probe distribution 160
2.1.6. Clinical translation 161
2.1.6.1. ^{31}P-NMR 161
2.1.6.2. CEST-MRI 162
2.1.6.3. EPR spectroscopy 162
2.2. (Patho)physiological issues 163
2.2.1. Cell models 163
2.2.1.1. Selected cell models 163
2.2.1.2. Other models 164
2.2.1.3. Different cell culture conditions 167
2.2.1.4. Different induction sites 167
2.2.2. Metabolism issues 168
2.2.3. Open questions about metabolic plasticity 170
2.2.4. Interest in measuring pH_i 173
3. Integrating biomarkers imaging in the development of treatment targeting cancer metabolism 174
Conclusions **177**
Bibliography **178**

Introduction

1. Bioenergetics of cancer cells

1.1. Metabolic flexibility of tumor cells

Cancer metabolism has been a growing area of research in cancer biology since Otto Warburg first observed, in the 1920s, an increase in glucose consumption in tumors in comparison with non-proliferating normal tissues [1, 2]. Dysregulated metabolism is a key hallmark of cancer cells. Proliferative cells present a heightened metabolic activity that supports their survival, growth and proliferation, as well as metabolic plasticity, to adapt to nutrient availability [3].

This characteristic is often the result of the induction of certain pathways, leading to the acquisition of genetic mutations in genes called proto-oncogenes and tumor suppressor genes, implicated in the regulation of cell cycle and proliferation. A mutation, translocation or amplification of proto-oncogenes can result in their activation, referred to as "gain-of-function" mutation, and lead to excessive proliferation. On the contrary, "loss-of-function" mutations in tumor suppressor genes induce a reduction in their capacity to inhibit cell growth and to induce apoptosis [2, 4-6].

In normal cells, production and release of growth-promoting signals instructing cells to enter and progress through the cell cycle are carefully controlled, guaranteeing the maintenance of a normal and functional tissue. Amongst the most commonly found dysregulations are: mutations in oncogenes such as Myc, Kras or found in the phosphatidylinositol 3-kinase (PI3K)-AKT-mammalian target of rapamycin (mTOR) signaling network, in the mitogen-activated protein kinases (MAPK) signaling pathway or a loss of function of the p53 tumor-suppressor [7-10]. Directly linked to those mutations is one of the best

characterized phenotype observed in tumor cells: the Warburg effect, or aerobic glycolysis [1, 2].

1.1.1. Glucose metabolism

1.1.1.1. Warburg effect

In most healthy mammalian cells, glucose is metabolized into pyruvate through glycolysis, then oxidized to CO_2 in the mitochondria through oxidative phosphorylation. The yield of this oxidation is 36 mol ATP/mol glucose. Oxygen is necessary for this process, as it is the final electron acceptor to completely oxidize glucose. When oxygen is limited, pyruvate will be converted into lactate which regenerates the NAD^+ pool, allowing glycolysis to continue but the ATP production will be minimal (Figure 1) [6, 11].

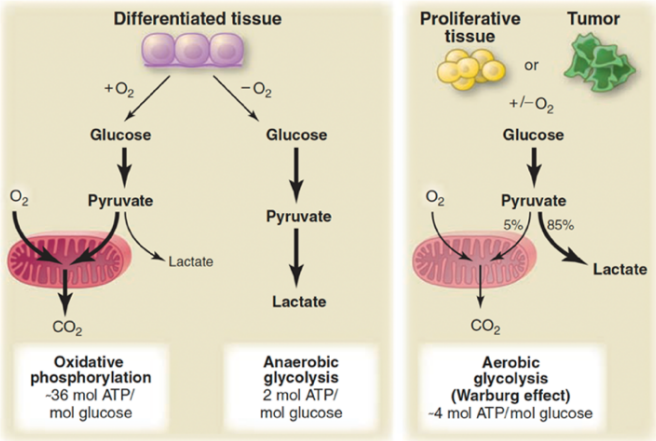


Figure 1 – Differences between oxidative phosphorylation, anaerobic glycolysis and aerobic glycolysis or Warburg effect. When oxygen is present, non-proliferating cells oxidize most of the pyruvate in the mitochondria during oxidative phosphorylation. In limited oxygen conditions, glucose-derived pyruvate can be redirected from oxidative phosphorylation towards lactate production. Proliferative tissues or tumor cells, whether or not oxygen is present, can convert most of the glucose to lactate, while their mitochondrial metabolism still remains functional. Original figure from Vander Heiden et al [11].

Warburg described in 1956 that proliferating cells can, whether oxygen is present or not, convert glucose into lactate. This phenomenon is now known as aerobic glycolysis, or Warburg effect [1, 12]. His hypothesis was that cancer cells showed dysfunctional mitochondria respiration. It was later demonstrated that many cancers maintain mitochondrial respiration while also exhibiting aerobic glycolysis [5, 13]. Aerobic glycolysis only yields 4 mol ATP/mol glucose. Many different explanations are put forward to try and understand why cells would still favor this pathway despite it resulting in less energy. One explanation that was advanced is that less ATP production is only a problem when resources are limited for cells, which is not the case for proliferating mammalian cells [14]. It was shown that cells using aerobic glycolysis still present a high ratio of ATP/ADP and NADH/NAD^+.

An increase in glycolytic flux creates intermediates taking part in alternative pathways, such as the pentose phosphate pathway (PPP) and the serine synthesis pathway (SSP), to support the metabolic demand of proliferating cells. The oxidative branch of the PPP generates pentose phosphate for nucleotide synthesis and nicotinamide adenine dinucleotide phosphate (NADPH) to support lipid synthesis, NADPH oxidase (NOX) signaling and the regeneration of reduced glutathione (GSH) to help cells against oxidative stress [15, 16] (Figure 2).

Serine and glycine can be synthesized from 3-phosphoglycerate (3PG), a glycolytic intermediate, through the SSP. Both serine and glycine can be incorporated into purine nucleotide bases. Serine can contribute to the production of mitochondrial NADPH while glycine, along with cysteine and glutamate, is a direct precursor of glutathione (GSH) [16, 17] (Figure 2).

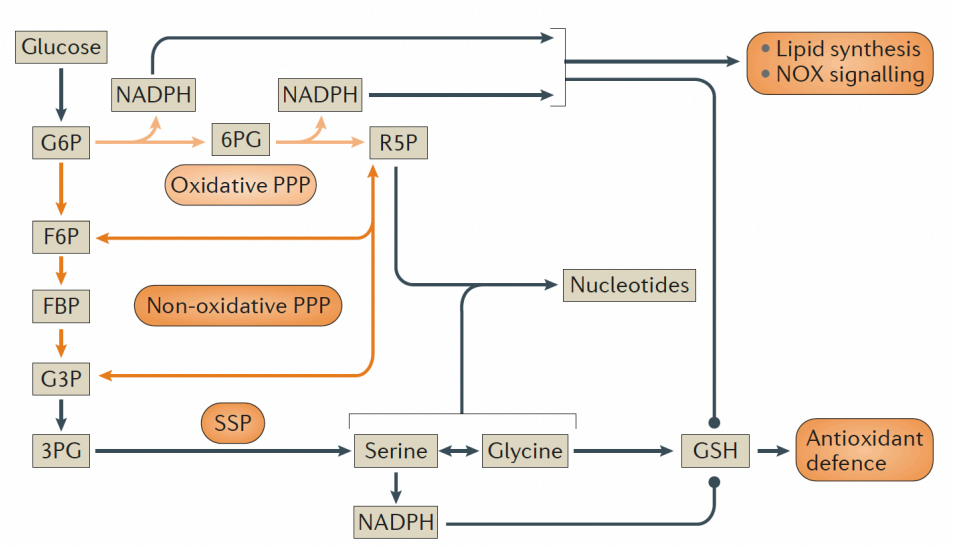


Figure 2 – Intersection of the pentose phosphate and serine pathways. Both pathways participate to the production of nucleotides and antioxidants to support proliferation and fight oxidative stress. G6P: glucose-6-phosphate; F6P; fructose-6-phosphate; FBP: fructose-1,6-bisphophate; G3P: glyceraldehyde-3-phosphate; 6PG: 6-phosphogluconate. Original figure from Yang and Vousden [16].

1.1.1.2. The PI3K/AKT network influences glucose metabolism

In physiological conditions, the PI3K-AKT-mTOR (Figure 3) is stimulated and further activated in response to insulin, growth factors and cytokines in healthy cells. In tumor cells however, this pathway is activated by mutations in the PI3K complex, loss-of-function mutation and deletion of tumor suppressor genes such as phosphatase and tensin homolog (PTEN) or by the amplification and activation of receptor tyrosine kinases (RTKs) [2, 4, 5, 10].

The activation of PI3K by both RTKs and Ras enables it to phosphorylate phosphatidylinositol 4,5-bisphosphate (PIP_2) to produce phosphatidylinositol 3,4,5-trisphosphate (PIP_3). In normal conditions, this phosphorylation is regulated by PTEN, which dephosphorylates PIP_3 to regenerate PIP_2, whereas

in cancer cells, PTEN is often the subject of loss-of-function mutations. This loss-of-function of PTEN leads to an accumulation of PIP_3 at the cell membrane, creating binding sites for downstream effector proteins. Among them is the serine-threonine kinase AKT, also known as protein kinase B (PKB). Its binding to PIP_3 induces its phosphorylation by phosphoinositide-dependent protein kinase 1 (PDK1), activating it [3, 10]. Active AKT is now able to phosphorylate downstream substrates, many of them playing a role in biological functions such as cell growth, proliferation, survival and metabolism.

AKT activation has been shown to be sufficient to promote aerobic glycolysis [18, 19]. Indeed, AKT was found to promote the translocation to the plasma membrane of the glucose transporter 1 (GLUT1), ubiquitously expressed in cancer, allowing glucose uptake [20]. It also promotes the translocation of GLUT4, generally found in insulin-sensitive tissue such as cardiac, muscular and adipose tissues [20, 21]. AKT promotes the activation, through phosphorylation, of several glycolytic enzymes. It increases the association of hexokinase 2 (HK2) with the mitochondria, which provides a source of ATP, necessary for glucose phosphorylation mediated by HK2 [22]. AKT phosphorylates and activates 6-phosphofructo-2-kinase/fructose-2,6-biphosphatase (PFKFB2), the enzyme catalyzing the conversion of fructose-6-phosphate into fructose-2,6-bisphosphate, which in turns, acts as an allosteric activator of phosphofructokinase 1 (PFK1). PFK1 synthesizes fructose-1,6-biphosphate from fructose-6-phosphate, increasing the glycolytic flux [10, 23, 24].

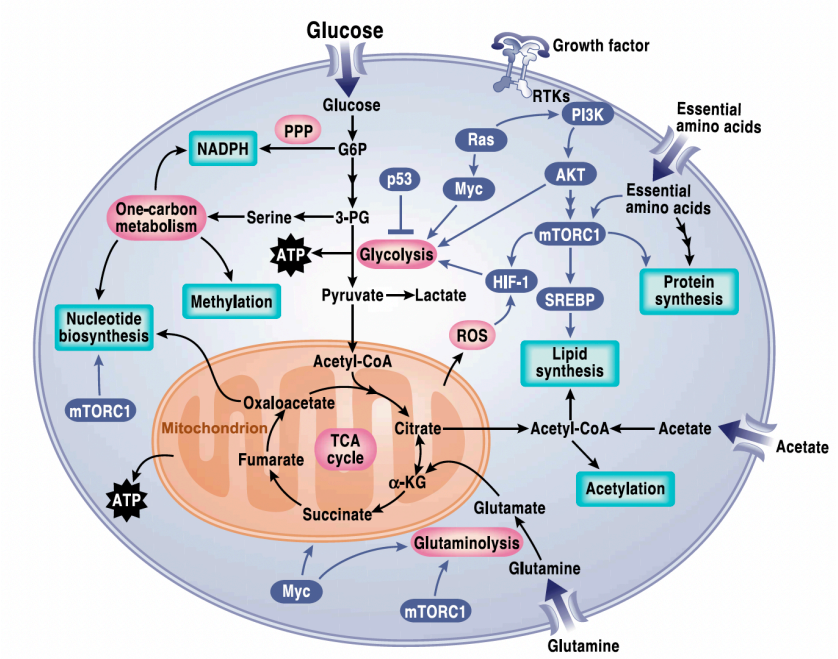


Figure 3 – Signaling pathways regulating cancer metabolism. Glucose enters the cells and is transformed into pyruvate after several steps producing ATP. This glucose-derived pyruvate can either be transformed into lactate or oxidized in the TCA cycle. Intermediates from glycolysis, such as G6P or 3-PG, can engage into alternative branches: to produce NADPH in the PPP or transformed into serine to fuel one-carbon metabolism and provide resources for nucleotide biosynthesis. Glutamine can fuel the TCA cycle. Citrate can provide acetyl-CoA, engaging in lipid synthesis. These metabolic pathways are positively regulated by PI3K/AKT, HIF-1, Myc and negatively by p53. TCA: tricarboxylic acid; G6P: glucose-6-phosphate; 3-PG: 3-phosphoglycerate; α-KG: alpha-ketoglutarate; ATP: adenosine triphosphate; HIF-1: hypoxia-inducible factor 1; mTORC1: mechanistic target of rapamycin complex 1; PPP: pentose phosphate pathway; RTK: receptor tyrosine kinase; ROS: reactive oxygen species; SREBP: sterol response element binding protein. Original figure from De Berardinis et al. [4].

It has also been suggested that AKT can phosphorylate and increase the activity of the pyruvate dehydrogenase kinase 1 (PDK1) under hypoxic conditions. PDK1 is an inhibitor of the pyruvate dehydrogenase (PDH), which is responsible for the conversion of pyruvate into acetyl-CoA, in fine facilitating a glycolytic switch to support cancer cell proliferation under hypoxia [25].

1.1.1.3. Mammalian target of rapamycin, mTOR

AKT then activates mTOR by phosphorylating and inhibiting its negative regulator tuberous sclerosis 2 (TSC2). mTOR is a protein kinase composed of two protein complexes: mTORC1, sensitive to rapamycin, and mTORC2, indirectly targeted by rapamycin. mTORC1 has been linked to the regulation of several pathways, such as glucose and mitochondrial metabolisms, as well as protein, nucleotide and lipid synthesis. The functions of mTORC2, on the other hand, still need to be further investigated, most of the studies focusing on mTORC1. It was suggested that mTORC2's functions may overlap with those of mTORC1 [5, 7, 26, 27].

Most importantly, mTORC1 stimulates the hypoxia-inducible factor-1 (HIF-1), a key regulator of the glycolytic response [5, 28].

1.1.1.4. Hypoxia-inducible factor

HIF-1 is a transcription factor that can be stabilized by hypoxia and mediates gene expression. HIF-1 is a heterodimer, composed of two subunits: HIF-1α and HIF-1β. Its regulation can be oxygen-dependent or -independent.

Growth factors and cytokines can increase HIF-1 levels in an oxygen-independent manner, by stimulating its synthesis, via activation of the PI3K or mitogen-activated protein kinase (MAPK) pathways. mTOR in the PI3K pathway, as well as the extracellular-signal-regulated kinase (ERK) in the MAPK pathway, phosphorylates p70 S6 kinase (S6K), which eventually leads to an increase in the rate at which HIF-1α mRNA is translated into protein [28].

The oxygen-dependent regulation of HIF-1 is based on the hydroxylation of the HIF-1α subunit by prolyl hydroxylase (PHD) enzymes, leading to their degradation in the proteasome after ubiquitination by the Von Hippel-Lindau (pVHL) ubiquitin ligase [5, 6]. When oxygen is restricted, this degradation will not take place. HIF-1α can then form a complex with the constitutively active subunit HIF-1β, and bind to the promoter region of hypoxia response elements [30] to amplify the transcription of genes involved in glycolysis: glucose transporters (GLUT1 and GLUT3), hexokinase 2 (HK2), phosphofructokinase 2 (PFK2) and pyruvate kinase M2 (PKM2) (Figure 4).

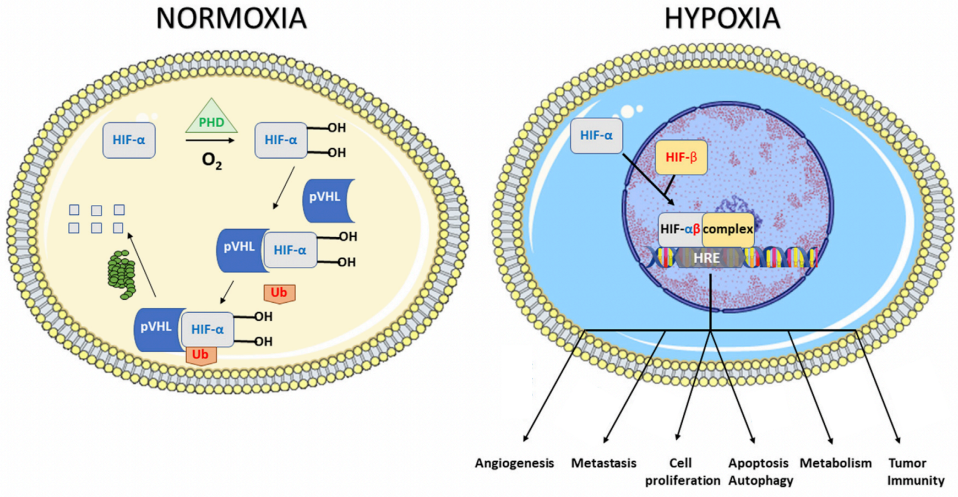


Figure 4 – Regulation of HIF-1α. Under normoxia, proline residues on HIF-1α are hydroxylated by prolyl hydroxylases (PHD). This leads to their ubiquitination by the Von Hippel-Lindau ubiquitin ligase (pVHL) and their proteasomal degradation. Under hypoxia, the PHDs lose their activity, the hydroxylation and subsequent degradation of HIF-1α is inhibited. Both subunits of HIF-1 can form a complex, enter the nucleus and bind to the hypoxia responsive element [30] of target genes. Adapted figure from Gallez [31].

HIF is responsible of reducing the amount of glucose-derived pyruvate going into the TCA cycle by stimulating pyruvate dehydrogenase kinases (PDKs),

inactivating the mitochondrial pyruvate dehydrogenase complex. This reinforces a glycolytic phenotype. It increases the expression of the vascular endothelial growth factor (VEGF), involved in the angiogenic switch. HIF also suppresses reactive oxygen species (ROS) production by the mitochondrial electron transport chain [5, 32-34]. The "Hypoxia" section of this work goes into more details about the different genes regulated by HIF-1.

1.1.1.5. MYC, Ras and TP53

MYC is described as one of the most frequently deregulated oncogenes in cancer. In healthy tissues, MYC is activated by growth factors [8]. It exerts its effect on glycolytic enzymes and lactate dehydrogenase A (LDHA), responsible for the interconversion of pyruvate into lactate. It also induces the expression of enzymes involved in nucleotide biosynthesis [3]. Other mutations in the TP53, MYC or Ras-related oncogenes signaling pathways will consistently affect glucose and glutamine metabolisms (Figure 3) [35, 36].

1.1.2. Glutamine metabolism

Glutamine metabolism has been studied for a long time and has been reported to be one of the most important sources of reduced nitrogen for maintenance of nucleotide biosynthesis and nonessential amino acids for tumor cells [37, 38]. Indeed, Fluorodeoxyglucose (FDG)-Positron Emission Tomography (PET) clinical studies have shown negative results for up to 30% of tumors, depending on the tumor type, are found when studying glucose intake by the tumor, meaning that tumor cells are capable of using alternative fuel sources [5, 14, 39].

Glutamine metabolism (Figure 5) is similar to glucose metabolism in the way that they are both metabolized by proliferating cells in different pathways, supporting biosynthesis and energetics. It was found that in glioblastoma cells, 60% of the metabolized glutamine was degraded into lactate and alanine, producing NADPH, coenzyme necessary for fatty acid (FA) synthesis [40].

Glutamine itself can be used for nucleotides biosynthesis or be converted to glutamate by the glutaminase (GLS or GLS2). Glutamate can then contribute to the synthesis of glutathione or be converted to α-ketoglutarate through either the glutamate dehydrogenase (GLUD) or aminotransferases [41]. Oxidative glutaminolysis provides oxaloacetate (OAA) for nucleotide and amino acid synthesis [35, 40]. The reductive carboxylation of glutamine leads to citrate and NADPH production for FA synthesis [42].

Ras regulates glutamine metabolism by directing it into pathways that support biosynthesis, redox homeostasis, cell survival and growth [35]. Myc induces the expression of the ASL-like Na^+-dependent neutral amino acid transporter 2 (ASCT2/SLC1A5), glutaminase (GLS), catalyzing the conversion of glutamine to glutamate, and LDHA [43].

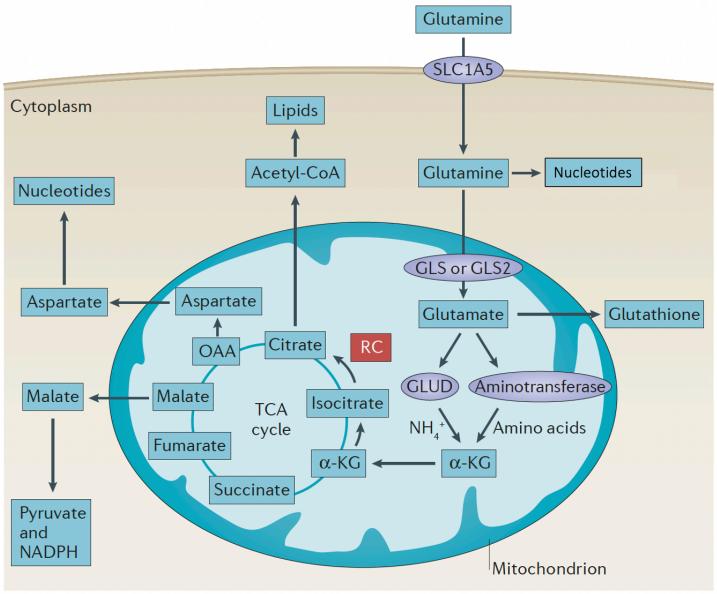


Figure 5 – Oxidative and reductive glutamine metabolic pathways. Glutamine can be converted to glutamate by the glutaminase (GLS or GLS2). Glutamate can contribute to the formation of glutathione or be converted to α-ketoglutarate (α-KG) by the glutamate dehydrogenase (GLUD) or aminotransferases. α-KG can either follow the oxidative glutaminolysis pathway to provide OAA or be reduced to citrate for acetyl-CoA and lipid synthesis. RC: reductive carboxylation. Adapted figure from Altman et al. [41].

1.1.3. Fatty acid metabolism

De novo FA synthesis is usually restricted to the liver, adipose tissue and lactating breast [44]. However, a commonly found characteristic in cancer cells, along with increased glycolysis, is their increased FA synthesis. Tumor cells can redirect excess pyruvate towards de novo FA synthesis, representing an important source of anabolic substrates as well as signaling molecules of a lipid nature [39, 45].

Acetyl-CoA is a requisite substrate for FA synthesis [46]. It mostly derives from pyruvate fueling the TCA cycle, generating citrate. The ATP-citrate lyase

(ACLY) then cleaves citrate into oxaloacetate and acetyl-CoA in the cytoplasm. The latter is used for the production of malonyl-CoA by the acetyl-CoA carboxylase (ACC). Fatty acid synthase (FASN) finally condenses malonyl-CoA and acetyl-CoA to form saturated FA palmitate [44]. Energy-rich FAs can be stored as triacylglycerides (TAGs) in large vacuoles in adipocytes or in smaller lipid droplets [45].

Fatty acids are catabolized by the fatty acid oxidation (FAO), or β-oxidation, which generates $FADH_2$ and NADH, used by the Electron Transport Chain [21]. Fatty acid synthesis and oxidation are mutually exclusive and regulated by negative feedback: high levels of malonyl-CoA will block the activity of the carnitine palmitoyltransferase 1 (CPT1). The CPT1 is associated to the outer mitochondrial membrane and is responsible for the formation of acylcarnitine groups, which enter the mitochondrial matrix. The acyl chain is then transferred back to CoA by CPT2 [45, 47]. ACLY has been shown to be required for cancer cell growth and survival [48]. Acetate also contributes to supply acetyl-CoA, thanks to the acetyl-CoA synthetase 2 (ACSS2), which ligates acetate and CoA (Figure 6) [49].

The SREBPs are a family of three transcriptional factors that can bind to sterol regulatory elements (SREs) in the promoters of genes encoding for enzymes involved in FA synthesis [45, 50]. The previously described PI3K/AKT/mTOR pathway is an important regulator in the expression of these enzymes. Indeed, AKT phosphorylates the glycogen synthase kinase-3 (GSK-3), inactivating it. The physiological role of GSK-3 is to inactivate, through phosphorylation, cell-cycle regulators as well as factors governing cell fate and differentiation, one of them being SREBP. So, by inactivating GSK-3, AKT enhances the function of SREBP, leading to FA synthesis. Moreover, AKT phosphorylates and activates

ACLY, consequently increasing acetyl-CoA concentrations [4, 7, 45]. SREBP also controls ACSS2 expression.

The MYC and Ras networks also play a role in FA synthesis, as it activates the expression of many enzymes involved in lipogenesis form citrate [8, 44].

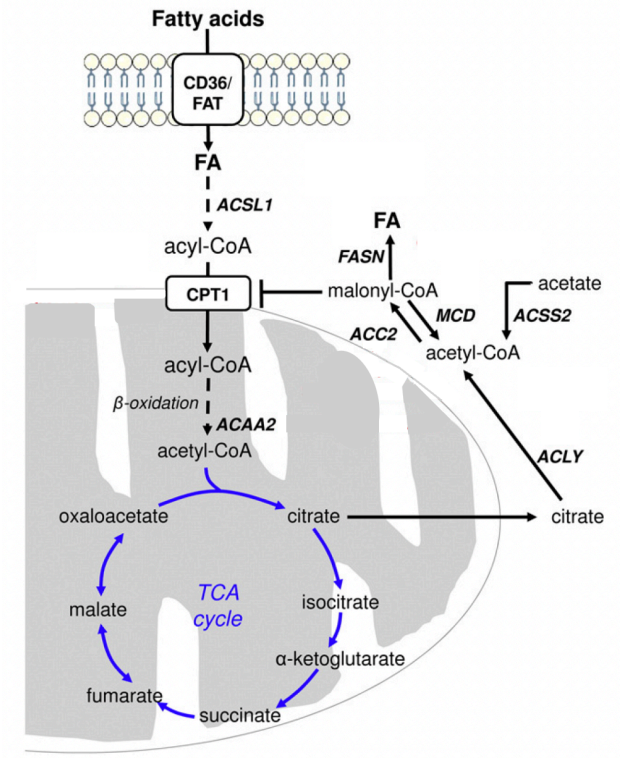


Figure 6 – Fatty acid metabolism. Fatty acids enter cells through the CD36/FAT transporters and the mitochondria through CPT1 after transformation into acyl-CoA by the long-chain-fatty-acid-CoA ligase-1 (ACSL1). Acyl-Coa is oxidized into acetyl-CoA which fuels the TCA cycle. FA synthesis starts with citrate converted into acetyl-CoA by the ATP citrate lyase (ACLY) and is polymerized by the acetyl-CoA carboxylase (ACC2) and fatty acid (FASN) enzymes to form fatty acids. MCD: malonyl-CoA decarboxylase. Adapted figure from Corbet and Feron [51].

1.2. External stimulation

External stimulation by several actors of the tumor microenvironment (TME) such as cancer-associated fibroblasts (CAFs), tumor-associated macrophages (TAMs), endothelial cells, immune cells and adipocytes also contribute to cancer progression and metastasis.

Usually quiescent fibroblasts become activated in response to tissue injury and the associated stimuli. Those CAFs can be classified into different functional subtypes, each of them playing a role in the enhancement of tumorigenesis by secreting cytokines, chemokines and pro-angiogenetic factors (Figure 7) [52, 53]. CAFs are involved in proliferation and metastasis, angiogenesis, extracellular matrix (ECM) remodeling and immunosuppression [53].

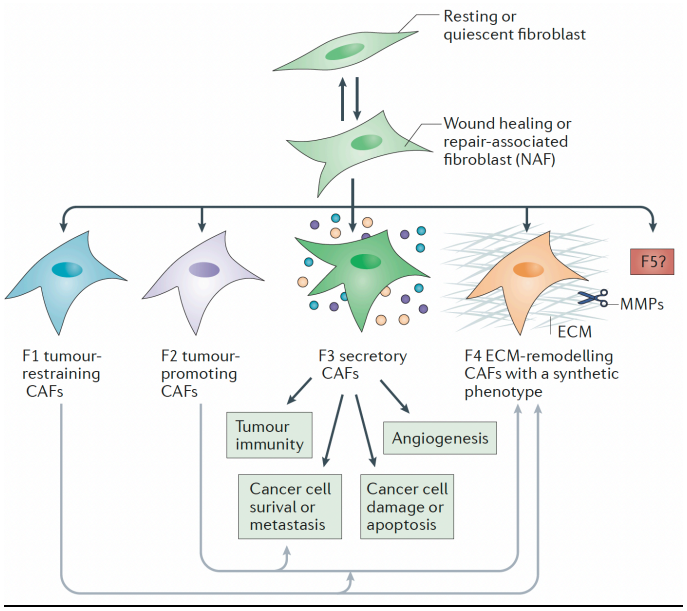


Figure 7 – Proposed classification for fibroblasts. Quiescent fibroblasts are activated and become wound healing or repair-associated fibroblasts that can be categorized in 5 subtypes, depending on their functions. NAF: normal activated fibroblast. Original figure from Kalluri et al. [52].

Immune cells can either suppress tumor growth or promote it. Several different populations of T-cells can be found within the TME and can influence tumorigenesis: cytotoxic T-cells ($CD8^+$) will target tumor cells for destruction, whereas regulatory T cells (Tregs) can promote tumor development and progression by secreting interleukin IL-2 or growth factors [53].

The M2 phenotype of macrophages are known to secrete cytokines and vascular endothelial growth factor (VEGF) to support tumor growth, progression and induction of new blood vessels.

Adipocytes, too, play an important role in cancer progression as they secrete metabolites, enzymes, hormones, growth factors and cytokines, in addition to metalloproteases, which modify the ECM [53].

2. Acidosis

As stated before, cancer cells will also respond to their microenvironment. There is a complex dynamic between cell growth and tumor environment. The metabolic requirements of cells as well as their products, proteins and metabolites, will affect the microenvironment [54].

At the early stages of tumors, the microenvironment is disparate. Epithelial cells, forming a basement membrane on which tumor cells evolve, are avascular. As cells hyper-proliferate away from the blood vessels, they inevitably become more distant from the basement membrane and the underlying vessels. This gives rise to adaptation which can take different forms as the TME becomes hypoxic: cells become apoptotic or adapt and turn to a glycolytic phenotype, generating fluctuations in concentrations of protons (H^+), glucose and partial pressure of oxygen (pO_2) [6, 34]. This participates to the selection of cells that constitutively upregulate glycolysis [55].

2.1. Acidosis regulation in cancer cells

2.1.1. Origin of acidosis

The conversion of glucose into pyruvate leads to the production of H^+ ions, which will be consumed to regenerate NAD^+ when pyruvate is reduced into lactate. The production of H^+ ions comes from the consumption of glycolysis-derived ATP by ATPases and kinases: hydrolysis to support the generation of biomass and phosphorylation cascades to support oncogenic signaling, respectively [39].

Another source of H^+ ions is the mitochondrial oxidative metabolism, in oxygenated tumor regions. Indeed, the conversion of pyruvate to acetyl-CoA by the pyruvate dehydrogenase (PDH) produces CO_2, which can diffuse out of the cells and be hydrated to H_2CO_3 and further dissociated to HCO_3^- and H^+ [56].

Lastly, as it will be discussed in the "Hypoxia" part of this work, tumor often present a chaotic vasculature which prevents the efficient wash-out of H^+ ions [39].

2.1.2. pH gradient reversal

An accumulation of H^+ ions inside the cytosol can alter pH homeostasis between the intracellular pH (pH_i) and extracellular pH (pH_e) of the tumor cells. Important processes such as cell proliferation, invasion, migration and metastasis but also ATP synthesis or enzyme function, are affected by changes in the pH_i/pH_e ratio as small as 0.1 [39, 58]. In healthy tissues, pH_i is about 7.2 and the $pH_e \sim 7.4$. Cancer cells develop molecular mechanisms to maintain their preferred equilibrium between the intra- and extracellular pH, which will be responsible for their "reversed pH gradient": a higher $pH_i \sim 7.4$, though their pHe is ~ 6.5-7.1 [39, 58]. An alkaline pH_i actually grants advantages to tumor cells, promoting glycolysis and conferring a resistance to apoptosis [58].

In order to maintain their "high" pH_i, cells will increase the expression and activity of different plasma membrane transporters and ion pumps [39, 58].

2.1.3. Transporters

The major players helping to regulate H^+ ions, and most commonly described, are represented in Figure 8 below. They include: carbonic anhydrases II, IX and XII (CAII, CAIX and CAXII), Na^+/HCO_3^- cotransporters (NBC), Na^+/H^+

exchanger 1 (NHE1), Na^+/K^+-ATPase, the monocarboxylate transporters (MCTs), vacuolar ATPase (V-ATPase) and the H^+/K^+-ATPase [54].

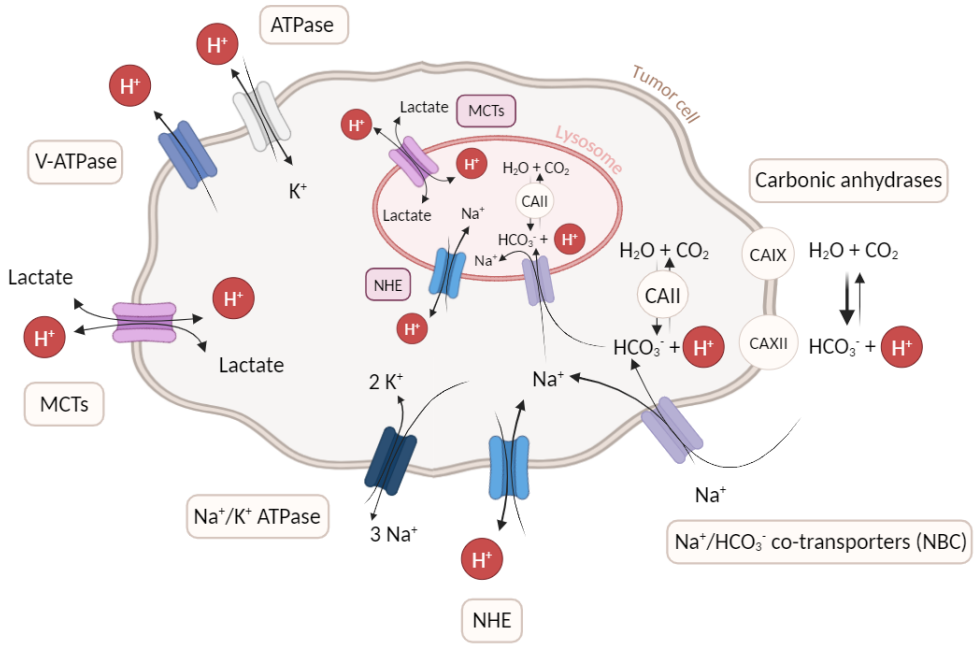


Figure 8 – Transporters involved in the regulation of pH_i and pH_e. The major transporters include carbonic anhydrases (CAII, CAIX and CAXII), Na^+/HCO_3^- cotransporters (NBC), the Na^+/H^+ exchanger 1 (NHE1), the Na^+/K^+-ATPase, lactate/ proton monocarboxylate transporters (MCTs), the vacuolar ATPase (V-ATPase) and the H^+/K^+-ATPase.

In this part, the most relevant transporters involved in this work will be presented.

2.1.3.1. Na^+/H^+ Transporter

There are nine different isoforms of the Na^+/H^+ transporters, or SLC9A family, NHE1 being the most studied in anti-cancer therapies. NHE1 is a membrane glycoprotein, 815-amino acid long and ubiquitous to all mammalian cells [59, 60]. It exchanges one intracellular proton with one extracellular sodium ion.

NHE1 is activated by an accumulation of H^+ ion intracellularly, decreasing the pH_i. Its activation is regulated by the phosphorylation of amino acids in its C-terminal cytosolic domain by kinases such as Erk1/2, ErbB2 or p38 mitogen-activated protein kinase (p38MAPK). Interactions of this C-terminal domain with intracellular calcium-binding proteins or lipids such as calmodulin (CaM), the calcineurin homologous proteins (CHP) or PIP_2 can also regulate its activation. Interestingly, the carbonic anhydrase II, catalyzing the production of HCO_3^- and H^+ from the hydration of CO_2, also associates with NHE1 to increase its activity. This results in a rapid activation in NHE1, increasing pH_i. Moreover, it has been demonstrated that a deregulation of NHE1 activity plays a major role in leading to metastasis in human breast cancer [60, 61].

2.1.3.2. Carbonic Anhydrases

Carbonic anhydrases (CA) are a family of 16 ubiquitous zinc-binding enzymes, present in prokaryotes and eukaryotes, responsible for the reversible conversion of CO_2 molecules. Five of them are cytosolic enzymes (CAI, CAII, CAIII, CAVII and CAXIII), five are membrane-bound enzymes (CAIV, CAIX, CAXII, CAXIV and CAXV), two are mitochondrial (CAVA and CAVB), one is secreted in saliva and milk (CAVI) and the three last ones have no catalytic activities (CAVIII, CAX and CAXI). Not all of these isoforms are associated with tumors; two are especially interesting for cancer therapies: CAIX and CAXII.

CAIX is a dimeric transmembrane isoform catalyzing the reversible hydration of CO_2, generating H^+ ions. Under physiological conditions, the expression of CAIX is limited and mainly found in the stomach and peritoneal lining. It is the most active CA isoform and the most strongly overexpressed gene in response to hypoxia, through HIF-1, in human cancer cells, leading to CAIX being a

marker of poor prognosis for breast cancer. CAIX expression is not only induced by hypoxia, it can also be induced under normoxia, by cell-density-mediated pseudohypoxia and by lactate or redox-mediated stabilization of HIF-1. CAXII is also a transmembrane isoform but with less catalytic activity than CAIX but is expressed in many tumor types as well [54, 62-65].

2.1.3.3. Monocarboxylate Transporters

The monocarboxylate transporters (MCT) family is composed of 14 isoforms, four of them being located at the cell membrane [66]. Those four isoforms are bi-directional proton-dependent transporters of monocarboxylates (such as lactate, pyruvate and ketone bodies). The ten others are less studied. MCTs 1-4 are proton-dependent transporters of lactate, pyruvate as well as ketone bodies, such as acetate and β-hydroxybutyrate, making them important for tumor and stromal cells. MCT2 and MCT3 are not the objects of a lot of studies [62, 67, 68].

MCT1 is encoded by the *SLC16A1* gene which is ubiquitously expressed. It has a high affinity for lactate (3-6 mM): when intracellular lactate levels are low, it acts as the main importer but can also act as an exporter of lactate. This is particularly important for the liver, where lactate is used for neoglucogenesis but also in some cancer cells that consume lactate as a metabolic fuel [67, 69, 70].

The symporter of lactate/H^+ MCT4 is encoded by the gene *SLC16A3* and is strongly expressed in glycolytic tissues, such as in skeletal muscles [71]. Its upregulation in many tumors is mediated by HIF-1 and represents a marker of poor prognosis in head and neck squamous cell carcinoma. It has a low affinity

for lactate (25-30 mM): therefore, it does not import serum lactate (usually < 2 mM), making it, almost exclusively, a lactate exporter [72].

Moreover, MCTs are important players in a variety of conditions, other than cancers. Mutations in the promoter region of MCT1 leads to its expression in insulin-secreting β cells. This causes exercise-induced hyperinsulinemia, a hypoglycemic disorder where lactate is oxidized during exercise and induces hypoglycemia by signaling insulin secretion [68]. MCT4 has been observed to be overexpressed in obesity, in muscle, which decreases after weight loss.

2.1.4. Extracellular H^+ accumulation and venting

H^+ ions, lactate and CO_2 will find themselves in the extracellular compartment, their venting rate depending on trans-membrane concentration gradients and leading to a decrease in pH_e. In the case of well-perfused tissues, there is an easy diffusion between the cells and capillary blood. In some regions of the tumors, moderate hypoxia can induce the expression of CAIX, responsible for the hydration of CO_2 into H^+ and HCO_3^-. HCO_3^- can re-enter cells through to NBC transporters and be used to regenerate CO_2 thanks to CAII [39]. The accumulation of CO_2, H^+ and lactate will decrease their venting [73].

As a chaotic perfusion is often observed in tumors, venting of CO_2, lactate and H^+ is hindered by long diffusion distances, leading to an extracellular buildup of these elements [73, 74]. However, although a low pH_e is conductive for tumor progression, cells have a tolerance limit. For example, an excessively low pH_e makes it costly for cells to maintain favorable pH_i, thermodynamically [75]. Stromal cells were shown to play a role in facilitating the venting of excess H^+ from the microenvironment. In particular, stromal myofibroblasts have been

found to absorb excess extracellular acidity through the anion exchanger 2 (AE2) and to transmit this acid excess across a syncytium formed by cells coupled by the gap junction-forming protein connexin-43 [76].

2.2. Consequences of tumor microenvironment acidosis

In order to survive extracellular acidosis, cells need to develop mechanisms to adapt to this environment. Indeed, exposure to acidosis will provoke either necrosis or apoptosis, through p53- and caspase-3-dependent mechanisms [6].

2.2.1. Metabolic reprogramming

Acidosis has been shown to affect the transcriptomic profile of tumor cells [77-79]. HIF-2α has been proposed to regulate genes participating in metabolic adaptations to acidosis [39]. Indeed, HIF-2α is upregulated when cells are exposed to an acidic condition in vitro, while HIF-1α is downregulated. The increase in HIF-2α has many consequences: increase in the expression of the glutamine transporter ASCT2 and glutaminase 1, resulting in an increase of the reductive and oxidative glutamine metabolism (Figure 9).

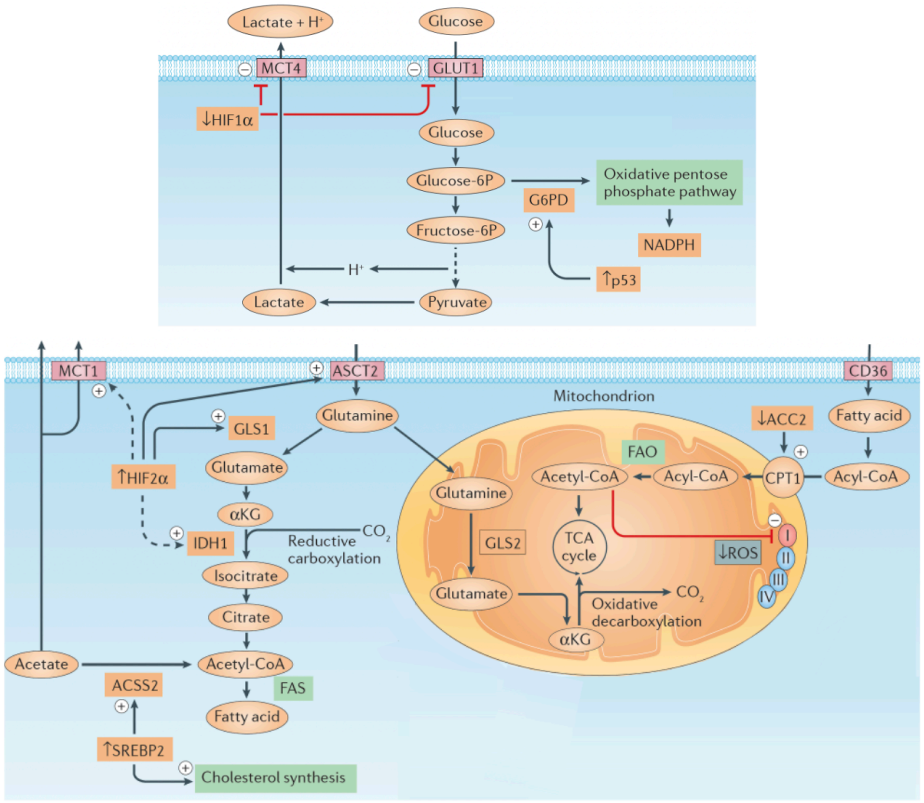


Figure 9 – Metabolic reprogramming. Acidosis decreases the expression of HIF-1α in tumors cells, while the expression of HIF-2α increases. This leads to alteration in glucose, glutamine and fatty acid metabolisms. Adapted figure from Corbet and Feron [39].

A direct consequence of increased glutamine metabolism is the increased levels of NAD^+, resulting in the increased activity of histone deacetylases sirtuin 1 and 6 (SIRT1 and SIRT6). A deacetylation of both HIF-2α and HIF-1α leads to their activation and deactivation, respectively [39, 77, 78, 80]. HIF-1α being downregulated under acidosis, genes involved in glucose metabolism, such as GLUT1 and MCT4, will find themselves downregulated as well, leading to a reduction of glucose consumption [39, 78].

Moreover, the group of Corbet et al. [80] has shown that cells actually use fatty acids and sometimes glutamine to generate acetyl-CoA instead of glucose. Indeed, they showed that under acidosis, α-ketoglutarate (α-KG) deriving from glutamine was shown to contribute to FA synthesis, as acetyl-CoA is produced from citrate [78]. Interestingly, they also found that cytosolic FA synthesis and mitochondrial FA oxidation could co-exist in acidosis-adapted cancer cells. This is due to the downregulation of acetyl-CoA carboxylase 2 (ACC2), a mitochondria-bound enzyme catalyzing the irreversible carboxylation of acetyl-CoA to malonyl-CoA. In normal conditions, malonyl-CoA inhibits FA oxidation by blocking carnitine palmitoyltransferase-1 (CPT-1). Under acidic conditions, SIRT1/6-mediated histone deacetylation of ACC2 leads to its downregulation and thus a decrease in malonyl-CoA, resulting in FA oxidation [29, 80].

In addition, extracellular acidosis was shown to stimulate the nuclear translocation and promotor binding of sterol regulatory element-binding protein 2 (SREBP2), inducing its activation. The consecutive activation of ACSS2, induced the conversion of acetate into acetyl-CoA [81].

2.2.2. Tumor progression

2.2.2.1. Proliferation and survival

A direct effect of the reverse pH gradient found in tumor cells is the fact that a pH_i of 7.2 or higher is required and increases the rate at which cells enter the G_O/G_1 phase of the cell replication cycle. A higher pH_i also suppresses the mitotic arrest that is induced by an activated DNA damage checkpoint and confers to cancer cells a resistance to apoptosis. An acidic pH_i induces conformational changes in BAX, a pro-apoptotic protein. This facilitates its

insertion into the outer mitochondrial membrane to form pores, increasing the membrane permeability and the release of cytochrome c and other pro-apoptotic proteins into the cytosol [58, 82].

A high pH_i is also known to promote glycolysis. Indeed, the activity of several enzymes regulating glycolysis is dependent on pH, such as lactate dehydrogenase (LDH) and phosphofructokinase 1 (PFK1). The activity of LDH, converting pyruvate to lactate and regenerating NAD^+, is maximal at $pH_i = 7.5$. PFK1 has a > 100-fold increase in activity between $pH_i = 7$ and 7.5 [58, 83].

On a side note, it is known that the Warburg effect provides advantages for cells in terms of biosynthetic demands. Lactate production from pyruvate by the lactate dehydrogenase allows cells to regenerate NAD^+ and to maintain NAD^+/NADH redox balance. This leads to a faster glucose flux through glycolysis, allowing glucose to enter biosynthetic pathways faster, sustaining the need for an increased proliferation [15].

2.2.2.2. Invasiveness, angiogenesis and metastasis

Both alkaline pH_i and acidic pH_e play a role in invasiveness. An alkaline pH_i leads to a pH-dependent activity of actin-binding proteins, such as cofilin or profilin. These proteins help actin form polymerized filaments, driving membrane protrusion in migrating cells [58].

Low pH_e increases the proteolytic activity of tumor-associated macrophages (TAMs), cancer-associated fibroblasts (CAFs) but also of tumor cells, by inducing the release of cathepsins D, L and/or B, which are secreted lysosomal cysteine proteases in the extracellular matrix (ECM) [39, 58, 84]. Those cathepsins degrade the ECM by remodeling cell-matrix adhesion and cell-cell interactions. This degradation induces the liberation of VEGF, a pro-

angiogenetic molecule. A low pH_e induces the transcriptional activation and increased mRNA stability of VEGF in pancreatic adenocarcinoma [84].

Moreover, it was found that acidosis could promote autocrine TGF-β2 signaling, favoring the formation of lipid droplets. An upregulation of thrombospondin-1 (TSP-1), glycoprotein responsible for the activation of TGF-β2, was found in acidosis-adapted cells. This, in turns, leads to a phosphorylation of Smad2/3 transcription factors, subsequently activating a partial epithelial-mesenchymal transition (EMT) gene program. The TGF-β2 autocrine signaling also favors the uptake of long-chain FA which are then oxidized in mitochondria for energy production. They were also observed to be stored as triacylglycerols in lipid droplets. Partial EMT induced by TGF-β2 autocrine signaling as well as lipid storage was found to play a role in survival to a programmed cell death induced upon cell detachment from the extracellular matrix, called anoikis and to support in vivo metastatic spreading [85].

2.2.3. Treatment resistance

There are many categories of chemotherapeutic agents that can be classified by their modes of action: alkylating agents, DNA intercalators, antimitotic agents, … Some of these agents have two ionization states which is affected by pH_e [86].

While neutral drugs will freely cross the cell membrane, the charged status of basic or acid drugs will be influenced by the pH_e (Figure 10).

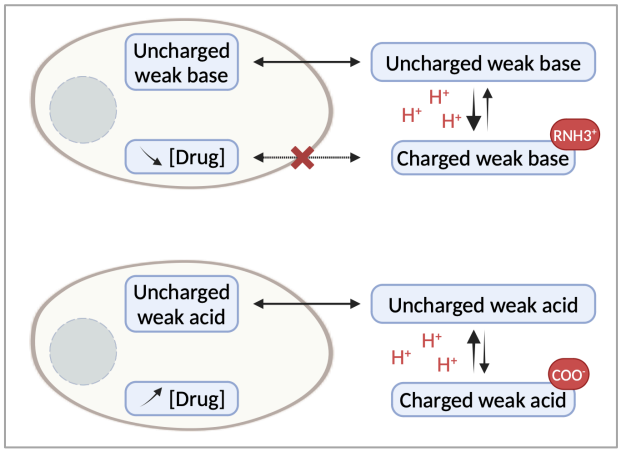


Figure 10 – Ion trapping: environmental pH influences chemotherapeutic compounds distribution. An acidic extracellular compartment is unfavorable for weak base chemotherapeutic agents as they become positively charged with decreasing pH. On the contrary, an alkaline intracellular pH is more favorable to weak acid chemotherapeutic agents. Adapted from Corbet and Feron [39].

Weak acid drugs (chlorambucil for instance) are negatively charged and are in equilibrium with the uncharged form, which have a tendency to concentrate in regions where the pH is more alkaline, typically intracellularly [39]. The opposite happens for weak basic drugs, such as doxorubicin, whose uncharged form will be in equilibrium with its positively charged at acidic pH form. As cell membranes are less permeable to charged forms, this will lead to an accumulation of the weak bases in the extracellular compartment.

Thus, the distribution of these drugs across the plasma membrane of tumor cells and but above all, their efficacity, can be dependent on the pK_a of the drugs, the pH_i and pH_e values as well as their lipophilic or hydrophilic nature [86].

A theoretical model states that the intracellular to extracellular distribution (C_i/C_e) of weak electrolytes that are membrane permeable in their non-ionized states and impermeable in their ionized states, is dependent on their pK_a and on the pH gradient across the membrane barrier [87].

To illustrate this, weak acid chlorambucil has a pK_a = 5.8. When using the following equation:

$C_i/C_e = (1 + 10^{pHi-pKa}) / (1 + 10^{pHe-pKa})$; for a theoretical pH_i = 7.2 and pH_e = 7.4 ;

C_i/C_e of chlorambucil is equal to 0.64.

Whereas when in acidic conditions, for example: pH_i = 7 and pH_e = 6.5 ;

C_i/C_e = 2.8 ;

Illustrating that there is indeed an intracellular accumulation of weak acids at low pH.

On the other hand, weak base doxorubicin has a pK_a = 8.2. Using the equation: $C_i/C_e = (1 + 10^{pKa-pHi}) / (1 + 10^{pKa-pHe})$; with the same pH_i and pH_e values as in the first example:

At pH_i = 7.2/pH_e = 7.4 ; C_i/C_e of doxorubicin equals 1.5.

At pH_i = 7/pH_e = 6.5 ; C_i/C_e = 0.32 ;

Meaning that doxorubicin tends to accumulate intracellularly when pH values are closer to the physiological values.

Extracellular acidosis is also involved in cell resistance to radiotherapy [84]. Radiotherapy's target is the genetic material of cells, inhibiting their division and proliferation. Studies have shown that an extracellular environment induces a prolonged G_2-cycle arrest. During this prolonged step of the cell cycle replication, cancer cells that present a lower pH_e show an increased DNA damage repair system [88-91].

2.3. Pharmacological modulation of extracellular pH

2.3.1. Treatments targeting tumor acidosis

As acidosis plays an important role in tumor aggressiveness, targeting one or several participating actors represents a promising anti-tumor approach and has been studied for a long time.

2.3.1.1. Sodium bicarbonate treatment

It is possible to modify pH_e by administrating sodium bicarbonate ($NaHCO_3$) ad libitum. A treatment with $NaHCO_3$ has been observed to induce pH_e alkalization, sensitizing MCF-7 cells to doxorubicin and improving its therapeutic effectiveness in vivo [92]. Another study showed that an oral $NaHCO_3$ treatment can significantly decrease the incidence of metastases in breast and prostate cancer models [93]. In both studies, pH_i was not significantly affected by the $NaHCO_3$ treatment.

Clinical feasibility has been discussed, as only moderate concentrations of $NaHCO_3$ are necessary to induce a change in pH_e in preclinical models, and an achievable daily dose of 37 g for a 70 kg human has been calculated by a mathematical model. However, it remains applicable only to small tumors. The same model predicted that a buffer with a $pK_a \sim 7$ could potentially show better effects than $NaHCO_3$ whose $pK_a = 6.1$, with the difficulty to use an unnatural buffer that could be associated with side effects and toxicity [94].

2.3.1.2. Proton-pump inhibitors

Proton-pump inhibitors (PPI) are the most common molecules targeting acidosis. These molecules, targeting H^+/K^+-ATPase or the V-ATPase are used not only for cancer therapy, but were first used as antiacids. Omeprazole, pantoprazole, esomeprazole are prodrugs activated by acidity to generate a sulfenamide which in turns reacts with cysteine residues of the proton pump, inactivating it [54, 96]. These molecules have been shown to negatively impact tumor growth in B-cell lymphoma [96], melanoma, adenocarcinomas [97] and murine triple negative breast cancer [98]. Recently, a phase II clinical trial combining rabeprazole with the chemotherapeutic agent capecitabine in gastrointestinal cancer has found no significant improvement in the capecitabine activity. However, the combination of PPI with chemotherapy still deserves to be further investigated [99].

2.3.1.3. NHE1 inhibitors

NHE1 is the most important and better studied transporter in cancer research. The first discovered NHE1 inhibitor is actually a diuretic that has been clinically used for 30 years, called amiloride. This molecule blocks epithelial sodium channels in cells of the distal nephron. One study from 1983 reported an inhibition of tumor growth of H6 hepatoma and DMA/J mammary adenocarcinoma in male A/J mice when treated with amiloride [100]. It was later shown that amiloride not only blocks sodium channels but also NHEs. Amiloride and its derivatives represent one class of NHE1 inhibitors. The inhibitory potency of amiloride is related to the ionization of their guanidine functions. Indeed, guanidium which equilibrates with guanidine, competes with

Na^+ at the external Na^+ transport site of the Na^+/H^+ exchanger [101]. At physiological pH, the guanidine function of amiloride has a pK_a = 8.78, is completed protonated and can interact with NHE under their cationic form [102, 103]. At a lower pH, drugs with a lower pK_a will be more efficient. Amiloride showed antimetastatic effects in tumors in rats. Recently, amiloride was used to induce an acidification of pH_i in multiple myeloma cells, leading to hypoxia-mediated apoptosis [61, 100, 104, 105].

Another class of NHE inhibitors are the guanidine derivatives, such as cariporide. They are derived from amiloride, after several substitutions, leading to benzoylguanidines [103]. Cariporide is a more selective and powerful NHE1 inhibitor than amiloride. It was shown that cariporide plays a role as a cardioprotectant, having a positive effect on myocardial reperfusion [106]. It was also reported that a treatment with cariporide decreases NHE1 expression as well as tumor cell invasion and proliferation [59]. Cariporide has a pK_a of 6.28, making it positively charged at a low pH and more efficient at low pH [103].

2.3.1.4. CAIX inhibitors

There are two strategies for targeting CAIX: by monoclonal antibodies or by small molecules targeting CAIX catalytic function [107]. CAIX is mostly located on the extracellular membrane, making it an easy target. Among the small molecules targeting CAIX, there are two big classes: the sulfamides and the coumarins.

Sulfamides bind to the zinc ion in the catalytic site of CAIX, blocking its entrance and preventing the hydration of CO_2 into HCO_3^- [108]. Acetazolamide has been shown to reduce proliferation and increase apoptosis in vitro and also

to sensitize colorectal carcinoma HT-29 cells to radiotherapy in vivo [57]. Another sulfamide, CAI17, was shown to reverse the hypoxia-induced decrease of pH_e in the 4T1 breast cancer cell model [65].

Coumarins are reported to be hydrolyzed into hydroxycinnamic acids that bind irreversibly to the entrance of the catalytic site. Coumarins are very selective of CAIX. Inhibiting CAIX with coumarins was shown to decrease metastases in a pre-clinical breast tumor model and to decrease pH_i, making it interesting for further combinations of treatments with chemotherapeutic agents [65, 108].

However, it has been shown that an inhibition of CAIX induces an increase in CAII expression [95]. This highlights the fact that, when inhibiting a participating actor in pH_e and pH_i regulation, we could expect a compensation in the expression of other transporters, taking over the regulation of pH.

2.3.1.5. MCT inhibitors

While MCTs are interesting targets for anti-cancer therapies, they are ubiquitous and implicated in the use of lactate in important active tissues, such as muscles or the brain. It is important to have selective inhibitors or a combination that can reduce the concentration needed to avoid effects on other tissues [109]. Many experiments are using a combination of molecules to try and achieve drug-induced metabolic rewiring in cancer cells, to make them vulnerable to a secondary treatment.

Cinnamates were the first group of small molecule inhibitors that were tested and shown to induce a decrease in cell viability as well as in pH_i [110]. The group of Sonveaux et al. [70] has shown that inhibiting MCT1 with α-cyano-4-hydroxycinnamate (CHC) and with silencing RNAs delays tumor growth,

induces tumor core necrosis and decreases tumor hypoxia, in cells that preferably consume lactate for oxidative metabolism. This comes from the fact that inhibiting MCT1 not only affects oxidative cells, but also hypoxic cells. Indeed, an inhibition of MCT1 in oxidative cells induces a metabolic switch towards glycolysis in these cells, leading to hypoxic cells starvation and tumor radiosensitization. They didn't observe any notable side effects. However, cinnamates were not specific enough for further clinical development [110].

Interestingly, cinnamates can be hydroxylated, forming a group of cinnamic acid lactone derivatives, the coumarins, used for CAIX inhibition [111].

Another example is the inhibitor of MCT1 and MCT2, AR-C155858. When tested, this molecule decreased cell viability and pH_i but also induced a reduction in lactate export and glycolysis (after incubation with oligomycin, an antibacterial agent that blocks mitochondrial ATP synthesis, proton translocation and O_2 uptake) [112-114]. AR-C155858 binds to a site on MCT1 and MCT2, accessible from the cytosol, and inhibits both of these transporters with the same potency. It does not inhibit MCT4 [112]. A more specific and potent inhibitor of MCT1 was derived from AR-C155858, called AZD3965. Once again, a decrease in the pH_i was found when cells from various cancers (lymphoma, lung and colon cancers) were treated with AZD3965. A dependence on mitochondrial metabolism was found, sensitizing the cells to mitochondrial complex 1 inhibitors, such as metformin [110].

AZD3965 was used in combination with metformin [115]. Metformin is the most widely prescribed antidiabetic for type 2 diabetes. It inhibits the mitochondrial complex I, resulting in defective cAMP and protein kinase A signaling in response to glucagon. This all leads to reduced blood glucose levels. It was shown that metformin could have antitumoral effects, through the

systemic reduction of insulin levels and the induction of energetic stress [116]. Exposing lymphoma and colon carcinoma cells to AZD3965 was found to induce an intracellular accumulation of lactate and thus an increase in mitochondrial metabolism to survive. A co-administration of metformin and mitochondrial pyruvate carrier (MPC) inhibitor UK-5099 resulted in increased cell death, highlighting the shift to an oxidative mitochondrial metabolism after an inhibition of MCT1 [115].

Recently, the results of the Phase I part (dose-escalation) of the first-in-human clinical trial targeting MCT1 were published. Dose-escalation of AZD3965 was assessed in 40 patients with solid tumors or lymphoma with high expression of MCT1 and low expression of MCT4. Their first results showed that AZD3965 is tolerated at doses that produce target engagement, with the most common adverse effect reported being eye disorders. They evaluated pH_e with Phosphorus-31 Nuclear Magnetic Resonance (^{31}P-NMR) but found no consistent change between before and after treatment. They went on to Phase II of the study, the dose-expansion phase, testing an oral administration dose of 10 mg of AZD3965 twice daily. Those results are not yet published [117].

Benjamin et al. [118] used a combination of metformin and syrosingopine to target cancer cells. Syrosingopine is a derivative of reserpine, both of them being clinically approved antihypertensive molecules. The same group proposed that syrosingopine inhibits MCT1 and MCT4 by directly interacting with the transporters. They also proposed that syrosingopine can inhibit MCT2 but not MCT3 [67]. Syrosingopine sensitized cancer cells to metformin and induced apoptosis in 35 cancer cell lines (including promyelocytic leukemia, colon, pancreatic, prostate and breast cancers) but had no effect on normal cells [118].

Another example of drug-induced metabolic rewiring was published by the group of Pr. Corbet [119]. They showed that a treatment with the small alkylating anticancer molecule 3-bromopyruvate (3-BrPA) induced the hypermethylation of the *SLC16A1* (MCT1) gene promoter, leading to its silencing. This could render 3-BrPA-resistant cancer cells vulnerable to an inhibition of MCT4 with diclofenac. This lead to a downregulation of MCT1 in various cancer cells, inducing a dependence of cells to rely on lactate release by MCT4. They combined 3-BrPA with diclofenac, a nonsteroidal anti-inflammatory drug that was reported to inhibit MCT4 and found that this co-treatment could inhibit the growth of spheroids and human colon cancer HCT-116 tumors in mice [119].

Here below is a table summarizing the different compounds and their targets:

Transporter family	**Isoform**	**Compound**	**Compound category**
ATPase	H+/K+-ATPase (V-ATPase)	Omeprazole Esomeprazole Pantoprazole	Proton-pump inhibitors
NHE	NHE1	Amiloride Cariporide	Na^+ channel blocker Guanidine derivative NHE1 inhibitor
CA	CAIX	Acetazolamide	Sulfamide CA inhibitor
MCT	MCT1/2 MCT1/4	AR-C155858 AZD3965 Syrosingopine	MCT inhibitor MCT inhibitor MCT inhibitor
NBC	NBC1-4	S0859, S3705	NBC inhibitor
MPC	MPC1/MPC2	7ACC2 UK-5099	MPC inhibitor

Figure 11 – Illustrative examples of modulators of tumor pH_e and their targets.

2.4. Assessment of tumor acidosis

In order to evaluate and potentially image the efficacy of those proton extruder inhibitors, several techniques are available. Measuring and imaging pH is of essential biomedical and clinical relevance, not only in tumors but also in other afflictions, such as kidney dysfunction for instance [120, 121].

2.4.1. SNARF-1

pH_i can be measured using the fluorescent pH sensor 5-(and-6)-carboxyseminaphthorhodafluor-acetoxymethylester (C.SNARF1-AM). This sensor has a pK_a of 7.5 and enters cells thanks to its lipophilic side. Once in the cells, this molecule is cleaved by esterases and trapped inside the cell. C.SNARF1-AM has a pH-dependent emission shift from yellow-orange to deep red fluorescence under acidic and basic conditions, respectively. The ratio of the fluorescence intensities at two emission wavelengths (~580 nm and ~640 nm) is used for quantitative determinations of pH. pH_e values can be evaluated by the same method, with SNARF-4F 5-(and-6)-carboxylic acid, which remains in the extracellular compartment.

2.4.2. Seahorse XF

The Seahorse XF analyzer can be used to measure the Extracellular Acidification Rate (ECAR). Sensor probes create a transient microchamber 200 microns above plated cells. Every 2 to 5 minutes, changes in concentrations of free protons caused by proton excretion (glycolysis) are measured. After one measurement is completed, the probes lift, restoring cell values to baseline, enabling repeated measurements. ECAR (mpH/min) is measured in real time

with the Glycolysis Stress Test Kit (Agilent), on living adherent cells in a non-invasive manner, by injecting modulators of glycolysis (Figure 12). Different cell types can be analyzed at the same time, on a 96-well plate. After the experiment, ECAR measurements are normalized by the protein content (μg) in each well.

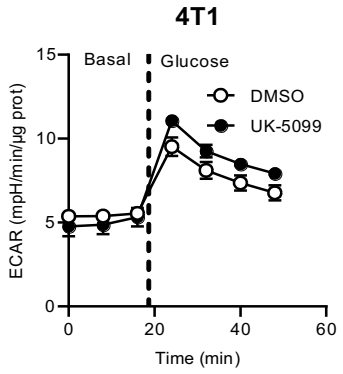


Figure 12 – Example of Extracellular Acidification Rate (ECAR) parameters measured by Seahorse XF analyzer. ECAR values are expressed in mpH/min/μg protein as a function of time (minutes). ECAR was measured on plated cells using the Glycolysis Stress Test Kit (Agilent), after addition of glucose, oligomycin and 2-DG (only glucose is represented here).

2.4.3. Electrodes

For years, glass pH electrodes, ranging from micro (~ 1 μm diameter) to mini (up 5 mm diameter) have been the standard of measure to study tumor pH. This method, although fast and accurate (if calibrated with an external buffer) requires several different incisions to consider different parts of the tumor. The measurement is thus dependent on the interstitial fluid pH and could be affected by damaged cells and blood released from ruptured capillaries. Furthermore, it is limited to surface-accessible tumors [122, 123].

2.4.4. pHLIP

pH (low) insertion peptide (pHLIP) is a 36-amino acid fluorescently labeled peptide that is either found soluble in water, bound to the surface of a membrane, or inserted across a membrane as an α-helix. This peptide has been successfully used to target and map acidity in vivo, its affinity for membranes being 20-times higher at pH 5 than pH 8. An acidic pH induces the protonation of an aspartic acid residues of pHLIP, making it possible to translocate and enter into the lipid bilayer by forming a helix (Figure 13) [124].

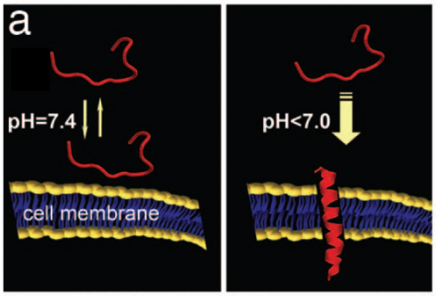


Figure 13 – pH (low) insertion peptide. pHLIP has three different states: soluble in water, bound the membrane surface at pH = 7.4 and inserted across the lipid bilayers as an α-helix at low pH. Adapted from Andreev et al. [124].

pHLIP can either be used as is, and analyzed by fluorescence or can be associated to a radioisotope, such as ^{18}F or ^{64}Cu, to image tumor tissue or metastases, together with Positron Emission Tomography (PET). PET is one of the most commonly used methods in both research and clinical imaging and relies on the delivery of radioactive imaging agents to targeted tissue. It has several good advantages: high sensitivity, no penetration depth limit and possible quantification of the concentration of the injected tracer [125, 126].

However, studying pH or its heterogeneity in small tumors with PET can be difficult because of its low spatial resolution (~ 2 mm^3) [125, 126]. pHLIP conjugated to a radioisotope gives a semi-qualitative measure of pH, as the result is dependent on the equilibrium between the conformation of pHLIP that can

insert into a cell membrane, and the one that cannot. It could guide tumor resection, by helping the visualization of the tumor margins [124, 126, 127].

2.4.5. Nuclear Magnetic Resonance

In this work, we compared different Magnetic Resonance techniques: ^{31}P-MRS, CEST MRI and EPR spectroscopy. These methods will be described in the following pages.

Nuclear Magnetic Resonance (NMR) is based on the intrinsic magnetic property of some atomic nuclei, called nuclear spin: nuclei can be considered as charged rotating particles, generating a magnetic dipole. The proton and its magnetic dipole can be compared to a small magnet, characterized by a magnetic moment $\vec{\mu}$. Nuclear spin values, noted I, are proper to each atom and are quantified according to their nuclear structure, their number of protons and neutrons [128]. Spins can take either half-integer or integer values:

Mass number A
X
Z Atomic number

A odd	I = ½	I = ½; ^{1}H, ^{31}P, ^{19}F
A even and Z odd	I = n	I = 1; ^{2}H, ^{14}N
A and Z even	I = 0	I = 0; ^{12}C, ^{16}O

Figure 14 – Nuclear spins. The nuclear spin of an atom depends on its atomic structure. Atoms with an odd mass number (A) have a nuclear spin I value that is half-integer such as ½. Atoms with an even A number and an odd atomic number (Z) present an integer I value n. Atoms with even A and Z numbers have a zero I value. **A:** mass number**. Z:** atomic number

In order to be observable in NMR, nuclei must present a magnetic moment $\vec{\mu}$ and a nuclear spin value I different from zero. The magnetic moment $\vec{\mu}$ is

associated to the nuclear spin angular momentum $\vec{S}$ and the gyromagnetic ratio γ: $\vec{\mu} = \gamma \vec{S}$ with $\vec{S} = \hbar\vec{I}$ where $\vec{I}$ is the spin operator in quantum mechanics and $\hbar = h/2\pi$ with h Planck's constant.

Nuclear Magnetic Resonance measures the transition of one energy state to another, in a magnetic field $\vec{B}_0$. The number of energy states that a nucleus can take is calculated by the following equation: 2 x I + 1. This means that for a nucleus whose spin = 0, such as ^{12}C, there is only one energy state possible, meaning that ^{12}C will not have a NMR signal. Nuclei with a spin value of ½ have two possible energy states corresponding to two possible orientations (of the magnetic moment $\vec{\mu}$) within an external magnetic field, $\vec{B}_0$.

These two states are: low energy, corresponding to $\vec{\mu}$ parallel (spin up) to the magnetic field $\vec{B}_0$ and high energy, corresponding to $\vec{\mu}$ antiparallel (spin down) to the magnetic field $\vec{B}_0$. The statistical distribution of the number of spins between the two energy states is determined by the Boltzmann law:

$$\frac{N_{up}}{N_{down}} = \frac{N_{low}}{N_{high}} = exp\left(\frac{\Delta E}{kT}\right)$$

where N_{up} = number of spins in the low energy state (spin up); N_{low} = number of spins in the high energy state (spin down); ΔE = difference in energy between the two states; k = Boltzmann constant: 1.3806452 x 10^{-23} joules/kelvins; T = absolute temperature in kelvin.

The intensity of the NMR signal is dependent on the difference of occupation by the spins of the two energy states (high and low). In NMR, as the difference between the two states is small, the signal is small, meaning that NMR is not a very sensitive technique. However, the signal intensity is also affected by the

applied magnetic field, as well as the natural abundance of the isotope of interest. Typical clinical MR systems have a magnetic field strength of 1.5T and can go up to 3T. All the experiments presented in this manuscript were done on a 11.7T MR preclinical system. The most abundant isotope for hydrogen is ^{1}H, with a natural abundance of 99.985%. The most abundant carbogen isotope is ^{12}C but as it was previously stated, its spin is equal to 0, meaning it's undetectable in NMR, whereas ^{13}C has a spin = ½, giving signal in NMR but with only a 1.11% natural abundance.

In reality, when placed in a magnetic field $\vec{B}_0$, magnetic moments $\vec{\mu}$ will precess about the magnetic field, at a certain frequency. This precession frequency, known as the Larmor Frequency, is dependent on the intrinsic nuclear property (gyromagnetic ratio, γ) and the magnetic field strength: $\omega_0 = \gamma.B_0$. When taking into account an entire spin population, there is a higher number of them that will be oriented parallel to the magnetic field $\vec{B}_0$, in a low energy position. The vector sum of the magnetic moments $\vec{\mu}$ over a volume (a voxel for example) yields the macroscopic magnetization $\vec{M}$. At thermal equilibrium, $\vec{M}$ is parallel to $\vec{B}_0$ which is by convention the z-direction ($M_z = M_0 \ \ and \ M_{xy} = 0$).

As the net magnetization $\vec{M}_0$ is small compared to the applied magnetic field $\vec{B}_0$, a second magnetic field, perpendicular to $\vec{B}_0$, is applied. This second magnetic pulse is an oscillating excitation radiofrequency (RF) pulse, called $\vec{B}_1$ and rotating at the same precession frequency as ω_0. The energy will be absorbed by the nuclei, resulting in spins switching from the lower energy state to the higher energy state. The consequence is that the net magnetization rotates away from the Z axis, towards the transverse xy-plane at an angle (flip angle), resulting in the reduction of the net magnetization along the Z axis. Depending on the

duration and intensity of the RF pulse, the flip angle varies. The RF pulse also causes the protons to now precess in phase. The result is the formation of a transversal magnetization M_{xy}, which happens at the same time as the reduction in the longitudinal magnetization M_z (magnetization parallel along the z-direction ($\vec{B}_0$) is called longitudinal and magnetization in the transverse xy-plane is called transversal). When the RF pulse is stopped, the longitudinal component M_z gradually relaxes back to the equilibrium value M_0. This relaxation happens according to a time constant, T_1 (spin lattice relaxation time) which corresponds to the time the net magnetization $\vec{M}_Z$ needs to get back to 63% of its original value, at equilibrium. At the same time, the transversal magnetization M_{xy} decreases, also according to a time constant, called T_2 or spin-spin relaxation time. This is the time needed for the signal to decay of 37% of its original value (Figure 15).

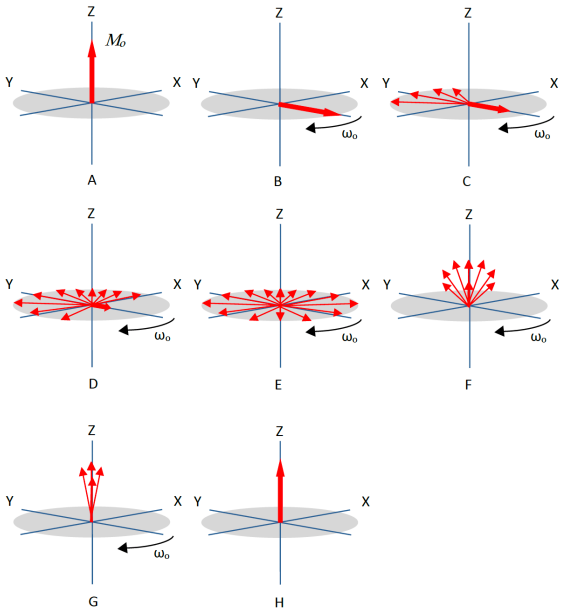


Figure 15 – Excitation and relaxation of spins. a) When no pulse is applied, the net magnetization is parallel to the magnetic field $\vec{B}_0$ and the z-axis. **b)** When a RF pulse is applied at the Larmor frequency, energy is absorbed by the protons. The net magnetization then flips and rotates away from the z-axis. **c), d), e)** The transversal magnetization decreases, it is the T_2 relaxation. **f)** and **g)** The longitudinal relaxation increases, back to the equilibrium position, representing the T_1 relaxation time. h) The net magnetization is back to equilibrium, parallel to the magnetic field. Original figure from [129].

A detector coil is placed with axis in the transverse plane to detect this temporal evolution of the rotating decaying transverse magnetization back to equilibrium $M_{xy} = 0$. The resulting signal, a sinusoid of decreasing amplitude, is called the free induction decay (FID) [130]. The Fourier transformation (FT) is then necessary to get an NMR spectrum, representing the signal over frequency instead of the signal over time (Figure 16) [130, 132-134].

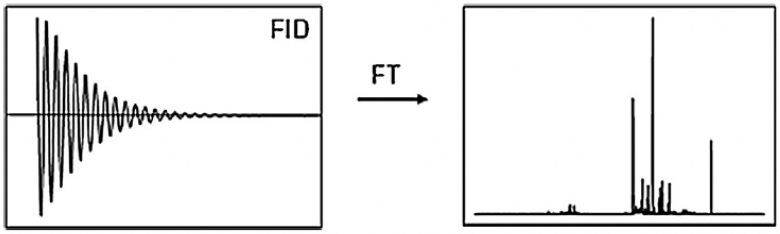


Figure 16 – Free induction decay. The sinusoid of decreasing amplitude signal, FID, gives a spectrum after the Fourier Transformation. Original figure from Tognarelli et al. [130].

2.4.5.1. Magnetic Resonance Spectroscopy

The most common application of NMR is Magnetic Resonance Spectroscopy (MRS) and is most frequently used to study endogenous nuclei such as ^{1}H, ^{31}P but also ^{13}C, ^{23}Na and ^{19}F [126].

In MRS, the final spectrum is resulting from the different chemical environment perceived by each atom of a molecule of interest, resulting in each of them having a specific absorption frequency. Nuclei can have, in their direct environment, electrons that present a negative charge. This leads to a "shielding effect", meaning that the presence of electropositive compounds increases the electronic shield of the nucleus, decreasing its absorption frequency. On the contrary, electronegative compounds decrease the electronic shield, increasing the absorption frequency.

This all leads to a spectrum with different "peaks" which is the reflection of the differences in perceived magnetic fields, resulting in different resonance frequencies. Those differences are greater as the applied magnetic field increases. Thus, it makes it difficult to compare spectra acquired from different spectrometers, the magnetic fields being a little different on each of them. To

get a spectrum comparison independent from the applied field value, chemical shifts δ are used.

The chemical shift of a nucleus, expressed in parts-per million (ppm), can be calculated by: $\delta = ((\nu - \nu_{ref}) \times 10^6)/\nu_{ref}$, being the difference in resonance frequency of the nucleus (ν) and a standard (ν_{ref}), compared to the frequency of the standard. The use of ppm as a unit makes it magnetic field intensity independent.

MRS can be used for a lot of different applications: ^{13}C-NMR spectroscopy is particularly interesting to measure the metabolic fate of different substrates, such as ^{13}C-glucose or ^{13}C-glutamine [135, 136]. MRS can also be used to study ligand-receptor interactions, their interaction modifying the spectrum. It can be used for in vitro, whole tissue samples or in vivo studies.

2.4.5.1.1. ^{1}H-MRS

The most abundant atoms in the human body are hydrogen atoms, representing 67% of all atoms in the body. ^{1}H-MRS can be used to study tumor pH without the need for an external probe. Indeed, two histamine protons are pH-sensitive, meaning that the difference of chemical shift between the two protons can be correlated to pH.

^{1}H-MRS can also be used with exogenous molecules, such as (±)2-imidazole-1-yl-3-ethoxycarbonylpropionic acid (IEPA). It presents a proton whose chemical shift is pH-dependent and one who is not. pH can be calculated by measuring the difference between the two chemical shifts. However, measuring pH_e using IEPA can induce a bias in the measurement as IEPA is a pH buffer and can alter pH_e at the concentrations needed for detection by MRS [120, 126].

The ^{1}H probe Yb-DOTP^{5-} ([H_8dotp = 1,4,7,l0-tetraazacyclododecane-N, N', N", N"'-tetrakis-(methylenephosphonic acid)]) can successfully measure pH_e in the range 5.0-7.5 at 39°C and does not need a comparison to an internal reference to do so [137].

2.4.5.1.2. ^{31}P-MRS

Phosphorus-31 (^{31}P) has a natural abundance of 100% and ^{31}P-MRS has been used for a long time to get information on tissue pH non-invasively, using pH-dependent chemical shift changes in molecules of interest. For example, the chemical shift of endogenous inorganic phosphate (P_i) compared to the one of phosphocreatine (PCr) reports pH, mostly pH_i as ~2-3 mM of P_i is intracellular against only ~1 mM is extracellular [126, 138]. P_i's chemical shift is the reflection of the proportion of each form, HPO_4^{2-} and $H_2PO_4^-$. There is a rapid exchange between the two forms, resulting in a single chemical shift, which is thus affected by the higher concentration of one form versus the other in the tissue at the moment of acquisition [134].

On the other hand, extracellular pH can be assessed using exogenous probes, such 3-aminopropylphosphate (3-APP). 3-APP is an extracellular probe, chemically inert and non-toxic (Figure 17) and can measure pH_e within a physiological range of pH 6 to 8, its pK_a ~7.1 [139, 140].

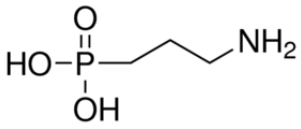


Figure 17 – Chemical structure of 3-aminopropylphosphonate

Extracellular pH is measured by the difference calculated between 3-APP's chemical shift compared to one of ATP's or NTP's chemical shift as an internal reference, as shown in Figure 18.

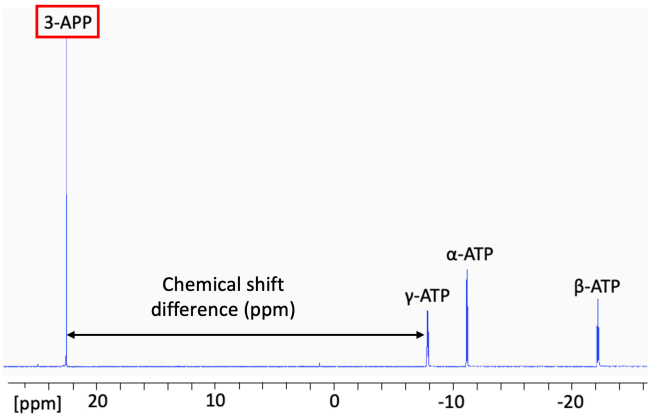


Figure 18 – ^{31}P spectrum of 3-APP. Acquired with a Bruker Ascend 600 MHz NMR system equipped with a broadband cryoprobe. pH_e is calculated based on the chemical shift difference between 3APP chemical shift and γ-ATP.

^{31}P-MRS can thus provide information about both pH_i and pH_e at the same time, using P_i chemical shift and 3-APP, respectively. One of its disadvantages is that even though its natural abundance is 100%, it only has a signal sensitivity of 6.6% compared to the one of ^{1}H [126].

2.4.5.1.3. ^{19}F-MRS

In comparison with ^{31}P, ^{19}F has a 83% signal sensitivity and a 100% natural abundance. The use of the ^{19}F probe, 3-[N-(4-fluoro-2-trifluoromethylphenyl)-sulphamoyl]-propionic acid (ZK-150471) has been reported to detect pH_e changes in tumors [141]. The ^{19}F spectrum of ZK-150471 presents two different peaks, the chemical shift difference between those two peaks giving information about pH_e.

2.4.5.2. Magnetic Resonance Imaging

Magnetic Resonance Imaging (MRI) is a non-invasive technique that provides detailed and multiparametric information on the anatomy, function and metabolism of an organ of interest.

The spatial coding of the MR image is acquired by applying several magnetic field gradients, encoding voxels positions in frequency form. Those frequencies are stored in a space called k-space. In order to first select the anatomical volume of interest, a slice selection gradient (SSG) is applied. Secondly, each point within this volume needs to be vertically and horizontally encoded, this is done by applying a phase encoding gradient (PEG), and a frequency-encoding gradient (FEG), respectively. In order to obtain an image from the raw data written in the k-space, a 2D inverse Fourier Transform is necessary (Figure 19).

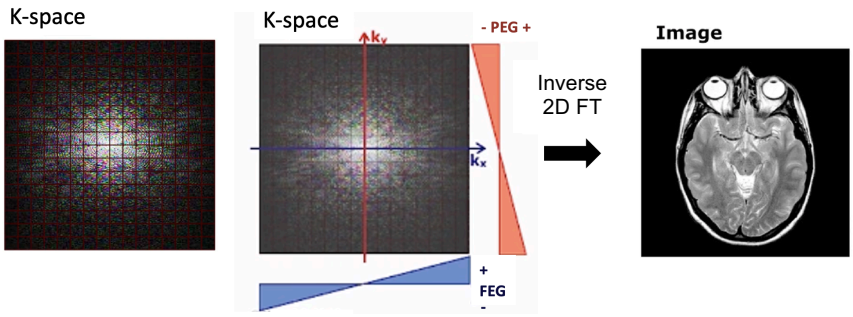


Figure 19 – From the k-space to an image. Representation of the k-space with different gradients: phase- and frequency-encoding gradients. An inverse 2D Fourier Transform is necessary to obtain an image (https://www.imaios.com/en/e-mri/mri-image-formation/k-space-exploration).

There are many different pulse sequences that can be used to acquire MR images. The most common one is a spin echo (SE) sequence. This sequence is characterized by a series of events: an initial RF pulse is given, inducing a 90° flip of the net magnetization into the transverse plane.

Due to inhomogeneities in the magnetic field, magnetization vectors of spin isochromats fan out (in the so-called rotating frame; rotating at the Larmor frequency) because some spins are precessing slower/faster than the Larmor frequency, leading to phase incoherence. After a brief delay a second pulse is applied (flip angle 180°), resulting in a 180° flip of the magnetization vectors. The faster precessing spins are now catching up to the slower ones and vice versa, re-establishing phase coherence. The signal is now recorded as an echo and the sequence starts again with a 90° pulse.

SE sequences are very dependent on two different parameters: the echo time (TE) and the time for which the pulse sequence is repeated, called repetition time (TR) [130]. Both parameters will affect image contrast.

Each tissue is characterized by its own T_1 and T_2, for a given magnetic field, and are used to acquire images with different contrasts. In images that are predominately determined by the T_1 properties of the tissue, tissues with short T_1 (fat) will appear hyperintense while tissues with long T_1 (water) will appear darker. In T_2-weighed images, the opposite happens: tissues with long T_2 (water) give a very bright signal, hyperintense, whereas tissues with a short T_2 (fat) appear very dark, hypointense [134, 142-144].

2.4.5.2.1. CEST MRI

Chemical Exchange Saturation Transfer (CEST) MRI is based on the characteristics that some chemical molecules possess protons exchangeable with water protons. Hydrogen is usually the most commonly studied nucleus in standard MRI, due to it being the most abundant nucleus in the body [145].

When applying a radiofrequency pulse at the specific resonance frequency of the exchangeable protons from the molecule of interest, a saturation will be reached. Saturation is a temporary state in which tissue shows a reduced net magnetization. This can be exploited to achieve image contrast, by exciting only the certain types of tissues, such as fat, to reduce its signal or even entirely remove it.

In CEST, an exchange is made: a spin from the exchangeable proton of the agent of interest, aligned against the magnetic field, is transferred to spin population of water, and inversely, a spin aligned with the magnetic field from the water population will join the population of spins of the agent of interest. This process leads to a decrease in the water signal intensity (Figure 20) [126, 145].

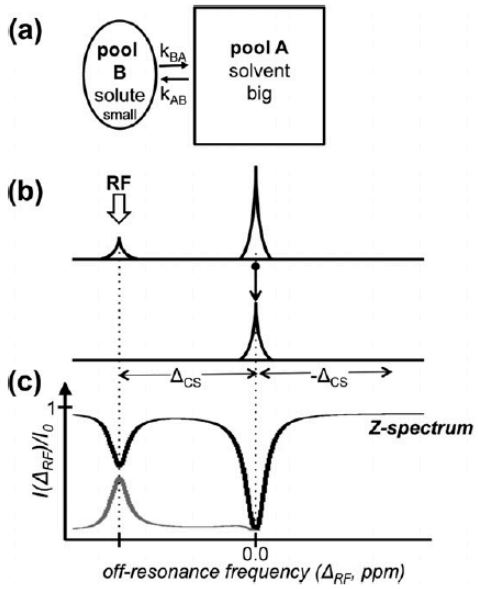


Figure 20 – Schematic representation of a CEST experiment. a) The experiment starts with two pools of protons which are in exchange with each other. **b)** The two pools have different chemical shifts. A RF pulse is applied at the resonance frequency of pool B, resulting in the saturation transfer to pool A, decreasing its signal. c) z-spectrum representing the decrease of the water signal intensity. Adapted from Vinogradov et al. [146].

In practice, the most commonly used sequence for CEST saturation is a type of SE sequence, called Rapid Acquisition with Relaxation Enhancement (RARE), with a continuous wave irradiation.

Any molecules presenting exchangeable protons can be analyzed with CEST MRI. These molecules can be endo- or exogenous and are classified by their chemical shifts: dia- or paramagnetic. Many diamagnetic CEST (diaCEST) agents are endogenous and nonmetallic ions. Paramagnetic CEST (paraCEST) agents are usually exogenous and always involve metallic ions.

- *Endogenous diaCEST agents*

One advantage of CEST is that there is not always the need to inject probes, as you can indirectly study diaCEST agents by measuring the reduction of the water signal. The diaCEST agents can be classified according to their exchangeable groups: amide CEST, amine CEST and hydroxyl CEST.

Amide CEST, also called amide proton transfer (APT), is the most used application of CEST. Amide groups are mostly found in proteins and peptides and are used to detect cancer and ischemic stroke. An accumulation of protein in tumor due to increased metabolism leads to an increase in APT level. As for ischemic strokes, APT CEST imaging is based on the variation of pH. It has been demonstrated that the exchange rate between amide protons of intracellular proteins or peptides and the protons of water molecules are proportional to the hydroxide ion concentration and proportional to pH [147, 148]. As pH decreases in ischemic regions, leading to a lowered APT exchange rate and thus, a decrease in APT CEST signal [149, 150].

Amine CEST is used to measure amino acids and peptides. The two most common applications are glutamate (gluCEST) and creatine studies. GluCEST

is particularly interesting for neurological and neurodegenerative diseases, such as in Alzheimer's disease where decreased levels of gluCEST have been observed. Creatine [130] CEST can be used to study muscle energy metabolism in both normal and pathological conditions.

Finally, hydroxyl CEST targets molecules such as glycosaminoglycan, myo-inositol or glucose (glucoCEST). Glycosaminoglycan is an indicator for cartilage damage and degeneration in arthritis. Glucose is ubiquitously found in the human body and can represent a biomarker for a lot of pathologies, including stroke, cancer and psychiatric or neurodegenerative diseases [145, 149, 151-155].

- *Exogenous paraCEST agents*

CEST MRI can be used to image lactate but the small difference between the chemical shift of the lactate and water protons makes it difficult. It has been shown that lactate can be studied using an exogenous paramagnetic reagent, EuDO3A, which can shift the lactate CEST peak away from its original position near bulk water. The formation of a complex between lactate and EuDO3A leads to the apparition of a new peak in the Z-spectrum, its amplitude increasing in proportion to the amount of added lactate [156].

Exogenous paramagnetic CEST agents can also be used for pH measurements [157]. Paramagnetic Gd(III) is the most used contrast agent, it shortens the T_1 relaxation time, causing brighter contrast in T_1-weighted images. However, Gd(III)-based agents have a fast water relaxation, making it difficult to generate a CEST contrast between an agent and water.

- *Exogenous diaCEST agents*

Iopamidol (Figure 21) is an FDA approved contrast agent that has been used as a diagnostic agent for clinical computed tomography (CT) scans protocols since 1981. It has three amide protons, two of them are equivalent, with the same MR frequency and one with a different one. The exchange rate of its protons is pH-dependent. A ratiometric method has been developed to measure pH without having to worry about the contrast agent concentration [145, 149, 151-155].

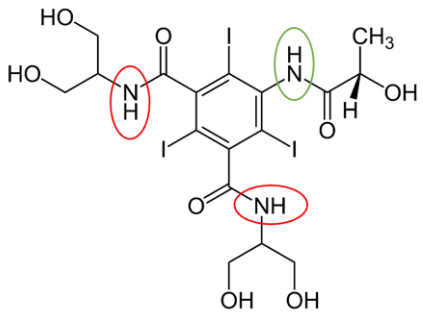


Figure 21 – Chemical structure of iopamidol. The amide protons relevant for CEST MRI are represented: two equivalent amide protons are circled in red and the third one is circled in green.

The spectrum resulting from the decrease of the water signal intensity is called z-spectrum, plotting the water saturation (S_{Sat}) normalized by the signal without saturation (S_0) as a function of saturation frequency (Figure 22) [159].

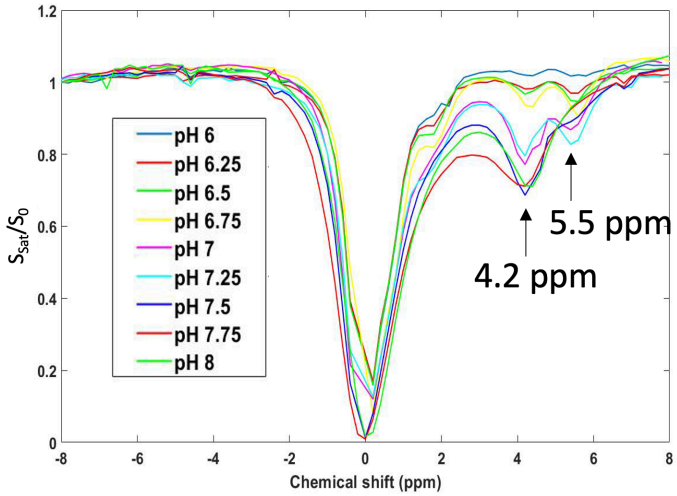


Figure 22 – Z-spectrum of iopamidol in buffered solutions, at nine pH values. Centered normalized water intensity (S_{Sat}/S_0) vs. the saturation frequency: 4.2 and 5.5 ppm. Exchange rates between iopamidol protons and water protons are dependent on pH, resulting in different z-spectra.

As seen in Figure 21, there are two exchange sites, corresponding to the different amide protons of iopamidol, whose chemical shifts are 4.2 and 5.5 ppm. Their chemical exchange rate is pH-dependent. A z-spectrum is recorded for each voxel composing the selected region of interest [160]. To get information about pH, the saturation transfer is measured:

$$ST = (S_{-\Delta\omega} - S_{+\Delta\omega})/S_0$$

With ST = saturation transfer, S = signal intensity at 4.2 or 5.5 ppm ($\Delta\omega$) and S_0 = signal without saturation. In order to have a measure that is not dependent on the contrast agent concentration, the next step is to measure a ratio of the saturation values calculated at 4.2 and 5.5 ppm: [121]

$$R_{ST} = \frac{ST_{5.5ppm}}{ST_{4.2ppm}}$$

As pH can be measured in each voxel composing the studied ROI, parametric images can be built, giving an information about the distribution of pH values inside the ROI.

CEST MRI with iopamidol has been applied to measure and image pH values in kidney in preclinical and clinal settings [152, 161, 162]. One of the most common application of CEST MRI is called "acidoCEST MRI", as iopamidol or a similar molecule [163] has been successfully used to measure tumor acidosis, in several different tumor types and to report sensitive measurements of pH_e: murine and human breast cancers, murine pancreatic tumor, multiple myeloma or lung adenocarcinoma [123, 164-168].

- *Clinical applications of CEST-MRI*

APT CEST is the most developed branch within clinical CEST imaging. One study compared APT MRI and ^{31}P-MRS imaging (^{31}P-MRSI) to study tumor metabolism in breast cancer patients on a 7T clinical MRI. Their analysis showed a significant correlation between APT CEST and pH but not what was expected: an increase of pH showed a decrease in APT signal. They found a linear correlation between phosphoethanolamine (PE)/Pi ratio, used a cell proliferation marker, and pHi with ^{31}P-MRSI: PE/Pi increases as pH_i decreases. Their explanation is that, at low pH_i, there is an increased intracellular concentration of proteins and peptides, resulting in higher CEST effects. This shows that it is still difficult to discriminate between the effects of pH changes and protein content changes, in addition to not being able to distinguish between the intra- or extracellular factor of these changing parameters, when using APT-MRI, especially in a complex tumoral environment [169].

The study of Nuclear Overhauser Enhancement (NOE) mediated chemical exchange saturation transfer imaging has gained a lot of interest, especially in the context of brain imaging [170]. NOE mediated CEST imaging is based on the magnetization transfer between the water protons and aliphatic and olefinic components of mobile proteins, peptides, metabolites and lipids [159]. It was found that NOE mediated CEST imaging could provide additional information on the structure of peritumoral hyperintensities in glioblastoma, compared to standard MR sequences, acquired at 7T. NOE mediated CEST imaging displayed isolated high intensity regions that were not displayed on T_1-weighed gadolinium contrast images or T_2-weighed images [171]. NOE imaging has also been proven to be able to differentiate between various gliomas grades [172].

Acido-CEST has been successfully used in humans to measure pH in knee cartilage and meniscus after injection of iopamidol or iohexol (another FDA-approved diamagnetic contrast agent), on a 3T clinical MRI scanner [173].

One study also investigated the ability of CEST to measure glutamate and creatine in the human brain, using Glu-weighted CEST and Cr-weighed CEST. They found that glutamate could be a contributor to a measured contrast at 2 ppm in brains, while creatine didn't show any measurable contribution [174].

2.4.6. Electron Paramagnetic Resonance

Electron Paramagnetic Resonance (EPR) is a magnetic resonance method, whose principle is similar to NMR but is focusing on electrons. Indeed, EPR is used to characterize paramagnetic species, meaning species with unpaired electrons. In continuous wave (CW)-EPR, the energy is given to the system by a fixed frequency microwave irradiation (GHz). The external magnetic field is

swept until the position where the energy given to the system is equal to difference of energy between the two spin energy levels. This is the resonance condition (Figure 23).

$\Delta E = h\nu = g\beta B_0$

where h = Planck constant, ν = applied resonance frequency, g = characteristics of the unpaired electron (depends on the electronic structure), β = Bohr magneton, B_0 = magnetic field [175].

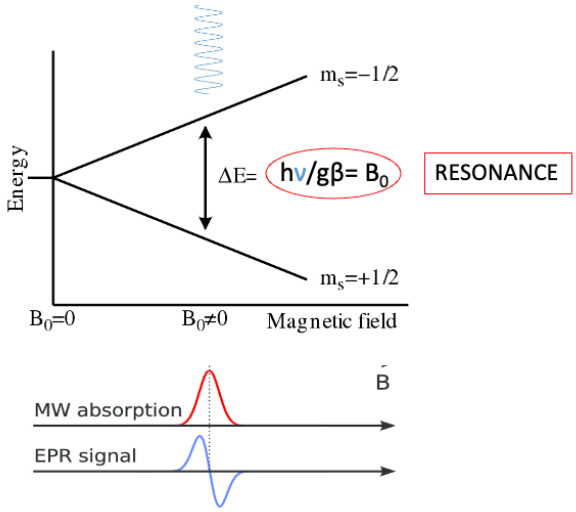


Figure 23 – Principle of EPR. In CW-EPR, the resonance condition is acquired when the energy given to the system is equal to the energy difference between the two spin populations at different energy levels, high and low. The first derivative of the absorption spectrum gives the EPR signal.

Compared to NMR, EPR spectrometers operate at higher frequencies and lower magnetic fields. The difference between the two spin energy levels is higher in EPR, making it a more sensitive technique than NMR, for the same probe concentration.

Depending on whether the experiments are done in vitro or in vivo, the frequency, as well as the applied magnetic field will not be the same. X-band EPR spectrometers work at a frequency of 9.5 GHz, permitting a 1 mm penetration depth in water, which is enough for in vitro studies. For in vivo studies, to avoid sample overheating, there is a need to decrease the frequency, for example using L-band EPR spectrometers, at the frequency of 1 GHz (1 cm penetration in aqueous samples) (Figure 24).

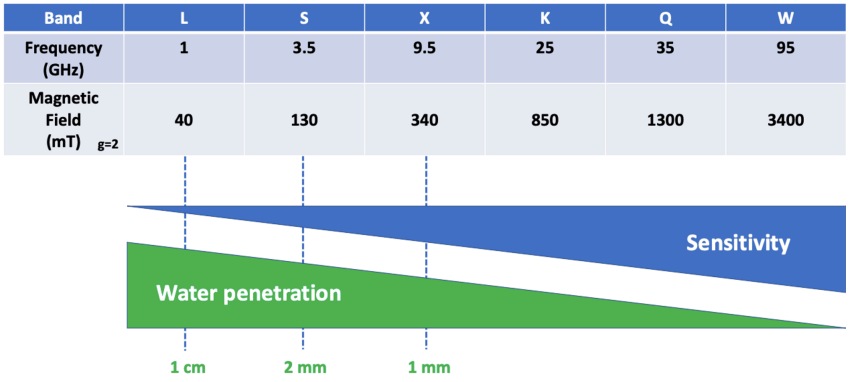


Figure 24 – Frequency and magnetic field values affect the sensitivity and water penetration. For in vitro studies, the X-band EPR spectrometer, working at 9.5 GHz with a water penetration of 1 mm is preferred. When working in vivo, a decrease in frequency to 1 GHz is usually observed, working with an L-band EPR spectrometer. A decrease in magnetic field is involved with a decrease in sensitivity. The difference in energy between the two spin populations being directly proportional to the magnetic field, less energy is needed to reach this energy difference, translating to a lower sensitivity.

Some endogenous radicals are stable enough to be studied without the need for administering an exogenous probe, such as melanin [176, 177]. Other free radicals can be studied by adding to the biological system a stable radical, for example a nitroxide or a trityl. Depending on its interaction with its environment, the nitroxide's spectrum could be modified. Some important free radical species have a short half-life and are often found in insufficient amount

within a tissue of interest because of their high reactivity. To detect these, diamagnetic probes need to be added to the system, to react with the reactive species and form a paramagnetic spin-adduct with a longer half-line, this is called "spin-trapping" [178].

There are two main classes of probes that can be used for EPR spectroscopy and imaging: soluble or particulate probes. Nitroxides are the first example of soluble probes commonly used. Indeed, imidazoline nitroxides are sensitive to pH changes because a change of pH induces a change in the spin density of the unpaired electron on the N-oxyl group of these nitroxides. This affects the spectrum of the nitroxide, decreasing the distance between the peaks and increasing the g factor. Imidazoline nitroxides were shown to be nontoxic, and to efficiently measure pH in mice stomach [179]. Bobko et al. [180] have synthetized and tested two nitroxides which were shown to successfully evaluate pH_e in mice with mammary tumors, as well as tissue oxygenation, redox status and glutathione (GSH) concentration [180].

The second class of soluble probes are the triarylmethyl radicals (TAMs). As nitroxide radicals have a fast bioreduction, it makes it difficult to follow pH and oxygen changes in vivo. TAMs radicals are more suitable for in vivo use as they are very stable in vivo, with a longer half-life. The same group proposed the use of a TAM radical for the dual measurement of pH and oxygen. They showed that the deuterated monophosphonated p_1TAM-D, derived from a Finland trityl, was successful at measuring pH and pO_2 in mice with breast cancer [181, 182]. Its structure is represented in Figure 25. Later, they confirmed the capacity of pTAM to measure P_i concentration in tumors in vivo, in addition to pH_e and pO_2 [183].

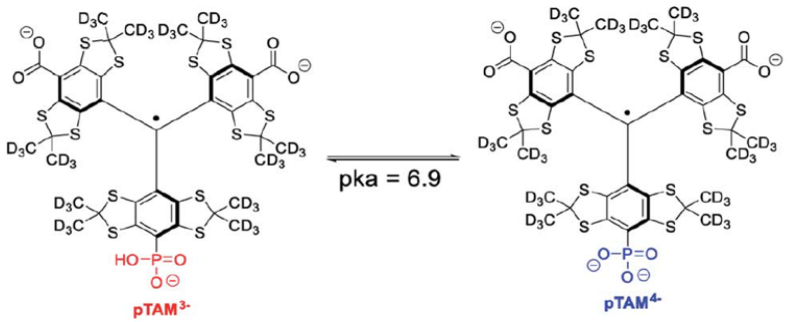


Figure 25 – Chemical structure of pTAM spin probe and its ionic forms at physiological pH. Original figure from Gluth et al. [184].

pTAM's spectrum is composed of two doublets of doublets: one doublet resulting from the basic and acidic form of pTAM that are both present and measured at the same time. The presence of two doublets is due to the phosphorus hyperfine splitting: the interaction between the free electron and the phosphorus in pTAM's structure. As phosphorus-31 has a nuclear spin of ½ and the number of spectrum splitting is characterized, in this case, by the equation: 2I +1 (I = nuclear spin) ; pTAM's EPR signal is split into two lines [185]. pTAM is extracellular, the fraction of the acidic form versus the basic form giving information about pH_e [184].

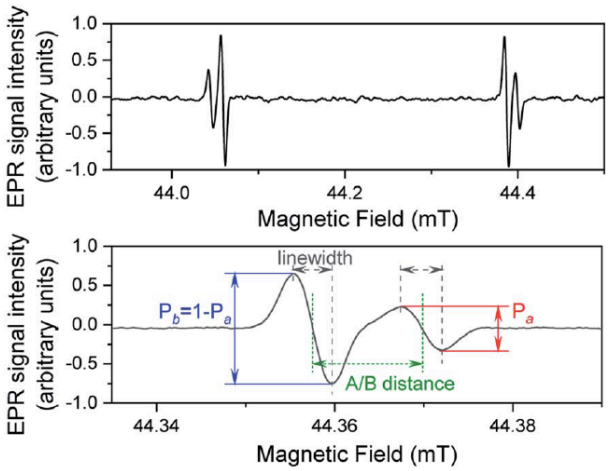


Figure 26 – Spectrum of pTAM. Top: full pTAM spectrum. Bottom: focus on one of the doublets with both ionic forms: the molar fraction P_a versus the basic fraction P_b (= 1-Pa) is a function of the pH of the solution. The linewidths are function of the oxygen concentration. pTAM also gives information about inorganic phosphate which modulates the exchange rate between the two ionic forms and the A/B distance. Original figure from Gluth et al. [184].

pTAM was also used to simultaneously map pH_e, pO_2 and P_i in vitro, with a 750 MHz continuous-wave EPR and in vivo with a low-frequency microwave L-band EPR operating at 1.1 GHz [186, 187]. However, the in vivo studies are limited to intratissue injection as it is complicated to get to a sufficient local concentration with an intravenous injection, pTAM reportedly binding to albumin through hydrophobic interactions, causing a loss in the signal intensity.

Gluth et al. then developed a new and improved pTAM, synthesized starting from Ox071 which does not bind to albumin and is very hydrophilic, called HOPE71. Its X-band and L-band sensitivities are comparable to pTAM, with the addition that it can now be administered intravenously to study and image pH_e, pO_2 and P_i concentration using EPR [188].

3. Hypoxia

Hypoxia is defined as reduced O_2 levels or decreased O_2 partial pressures that can occur in a variety of pathological conditions such as stroke, tissue ischemia, inflammation and tumor growth, resulting in limitations of cellular or organ functions [189, 190]. Tumor cells that are further than 80 to 150 μm of a capillary supplying O_2 are considered hypoxic. Hypoxic regions inside a tumor can present a pO_2 as low as 10 mmHg or less, resulting from several factors [39]. Hypoxic regions are present in 50 to 60% of human tumors and are known to be involved in increased tumor aggressiveness and resistance to therapies, making hypoxia a hallmark of cancer [191].

3.1. Contributing factors leading to hypoxia

The cause of tumor hypoxia could be simplistically explained as an inadequate oxygen supply that is not able to meet the requirement of demanding cells. Indeed, tumors are composed of a large number of cells, that continues to proliferate. Some tumor cells, along with other cells present in the tumor microenvironment, such as tumor-associated macrophages, can present high oxidative phosphorylation and a high oxygen consumption rate.

Impaired oxygen delivery plays a major role in the prevalence of hypoxia. There are in fact multiple factors contributing to hypoxia (Figure 27) and multiple spatial and temporal differences leading to different kinds of hypoxic states. They can be classified into two types of hypoxia: acute or chronic hypoxia.

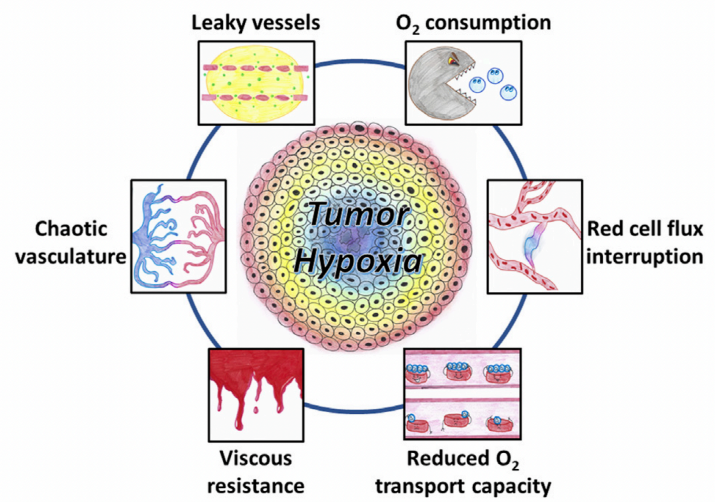


Figure 27 – Factors contributing to hypoxia. Increasing oxygen consumption as well as impaired oxygen delivery contribute to hypoxia. Chaotic vasculature, regions with abnormal vascular density, contour irregularities and abnormal branching angles are often found in tumors. Immature vessels show an increase leakiness, which combined with poor lymphatic drainage causes an increase in interstitial fluid pressure. Viscous resistance can contribute to vascular stasis. Tumor-associated anemia reduces the oxygen transport capacity. Original figure from Gallez [31].

3.1.1. Chronic hypoxia

Chronic hypoxia is also known as "diffusion-limited" hypoxia and is characterized by variations happening with a time frame of hours, days, up to weeks. In chronic hypoxia, cells quickly proliferating away from the nutritive blood vessels receive less oxygen than necessary, those blood vessels not following their growth rhythm [190, 192]. This results in two types of oxygen gradients: radial and longitudinal. The radial gradient is due to bigger diffusion distances from the perivascular space to cells. A reduction in vascular pO_2 along the incoming path of blood flow leads to a longitudinal gradient [31]. It is known that the vascular system in tumors is chaotic compared to normal tissues. Irregular geometry of vascular networks is commonly found in tumors: tumor

regions with abnormal vascular density, contour irregularities, enlarged or blind ending vessels and abnormal branching angles.

As cells proliferate further and further away from blood vessels, they will release angiogenic factors, such as VEGF. Endothelial cells divide at a slower rate than tumor cells, leading to immature and highly permeable vessels. A combination of increased leakiness from the vessels and a poor lymphatic drainage causes an increase in interstitial fluid pressure, decreasing the difference in pressure between arterial and venous ends, ending in blood flow stasis. This vascular stasis can be worsened by increased viscous resistance, coming from an increased in the rigidity of red blood cells occurring with after a decrease in pH_e.

Another factor contributing to chronic hypoxia are the tumor-associated or therapy-associated anemias, where a reduced oxygen transport capacity happens [31, 192-194].

3.1.2. Cycling hypoxia

Cycling hypoxia, also called acute or transient hypoxia, is the second type of hypoxia. It results from temporary flow stops, due to transient perturbations of the microcirculation or to fluctuations in red blood cell fluxes [191, 193]. This causes a subtype of cycling hypoxia, called transient hypoxemia. Physical obstructions can lead to cyclic hypoxia, as it is not uncommon for aggregates of tumor cells, blood cells or fibrin (protein involved in blood clotting) clots to be found in the vessel lumen. This leads to another subtype of cycling hypoxia, ischemic hypoxia, along with the rapid vascular remodulation occurring with tumor growth [191].

In conclusion, both high oxygen consumption and impaired oxygen delivery contribute to the apparition of hypoxia in solid tumors.

3.2. Cancer cell responses to hypoxia

There are a lot of different cellular consequences to hypoxia. While chronic hypoxia is more associated to the loss of vital functions, activation of signaling pathways to maintain proliferation and resistance to therapy, cycling hypoxia is associated to increased genomic instability and promoting tumor cell survival by selecting cell clones that are more aggressive and resistant to apoptosis [191].

3.2.1. Gene activation

When oxygen levels in tumors are < 1% O_2, many changes in gene expression occur, mediated by the HIF-1α pathway. Most of them are involved in tumor progression. A non-exhaustive list is presented in Figure 28: genes involved in angiogenesis, cell proliferation, metastasis, increased metabolism and tumor immunity are impacted [193].

As seen in Figure 28, hypoxia leads to the transcriptional activation of several genes of actors involved in glycolysis, stimulating cells to consume glucose and produce lactate, being partly responsible for acidosis [3].

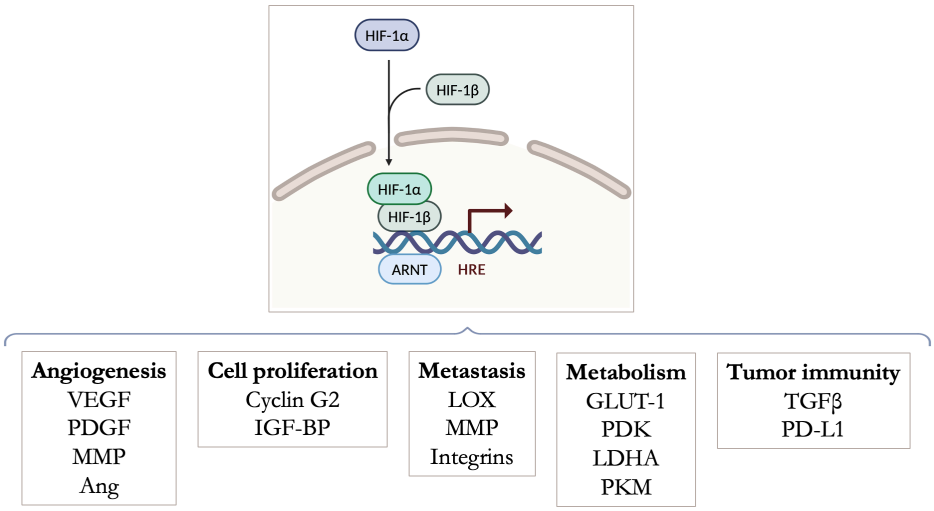


Figure 28 – Hypoxia inducible growth factor and illustrative target genes. Genes involved in angiogenesis, cell proliferation, metastasis, metabolism and tumor immunity are transcriptionally activated by HIF-1. VEGF: vascular endothelial growth factor; PDGF: platelet-derived growth factor; MMP: matric metalloproteinases; Ang: angiotensine; IGF-BP: insulin-like growth factor-binding protein; LOX: lysyl oxidase; GLUT-1: glucose transporter-1; PDK: pyruvate dehydrogenase kinase; LDHA; lactate dehydrogenase A; PKM: pyruvate kinase M1/2; TGFβ: transforming growth factor β; PD-L1: programmed death-ligand 1. Adapted figure from Gallez [31].

Depending on the cell type, degree and length of hypoxia, differences can be observed. Both chronic and acute hypoxia lead to a more aggressive phenotype and poor prognosis. During acute hypoxia, the activity of HIF-1α is stabilized by the production of Reactive Oxygen Species (ROS) [193].

Independently from HIF-1α activation, severe chronic hypoxia (< 0.02% O_2) causes the endoplasmic reticulum to go into stress. This leads to an unfolded protein response and subsequent activation of survival signals. If the stress persists, it can lead to apoptosis activation [5, 31].

It is important to note that hypoxia is not the only factor that can induce the expression of HIF-1α. ROS and growth factors through receptor tyrosine

kinases can regulate the expression of HIF-1α, in an oxygen-independent manner. Pathways such as NFκB, PI3K/AKT/mTOR, and MAPK/ERK mediate its expression. However, those are pathways that are also regulated by hypoxia, giving HIF-1α multiple and additional ways to be stimulated [31].

3.2.2. Effect on metabolism

Depending on the availability of nutrients reaching tumor cells, they can adapt to find alternative carbon sources to support their biosynthesis needs. Indeed, in cancer cells under hypoxia, a shift from glucose metabolism to acetate has been observed to support fatty acid and lipid biosynthesis. It was found that ACSS2 was upregulated in cells exposed to prolonged low oxygen and lipid conditions, HIF and SREBP2 synergistically controlling its transcription [49], leading to the synthesis of acetyl-CoA from acetate. Furthermore, it was found that cells under hypoxia also rely on the reductive carboxylation of α-KG derived from glutamine [195].

The formation of lipid droplets was found to also be promoted in breast cancer, under hypoxia. It was observed that an accumulation of these droplets was induced by the upregulation of fatty acid binding protein (FABP) 3 and 7 and of perilipin 2 (PLIN2), responsible for an increase in FA uptake and the formation of lipid droplets, respectively. This happened in a HIF-1α-, time- and oxygen concentration-dependent manner [196].

Just as hypoxia is a fluctuating factor and not homogenous across a given tumor, nutrient availability is variable and fluctuates. Figure 29 depicts how changing tumor cell metabolism can affect lipid synthesis and how cells can adapt back and forth depending on the oxygen and nutrient situation.

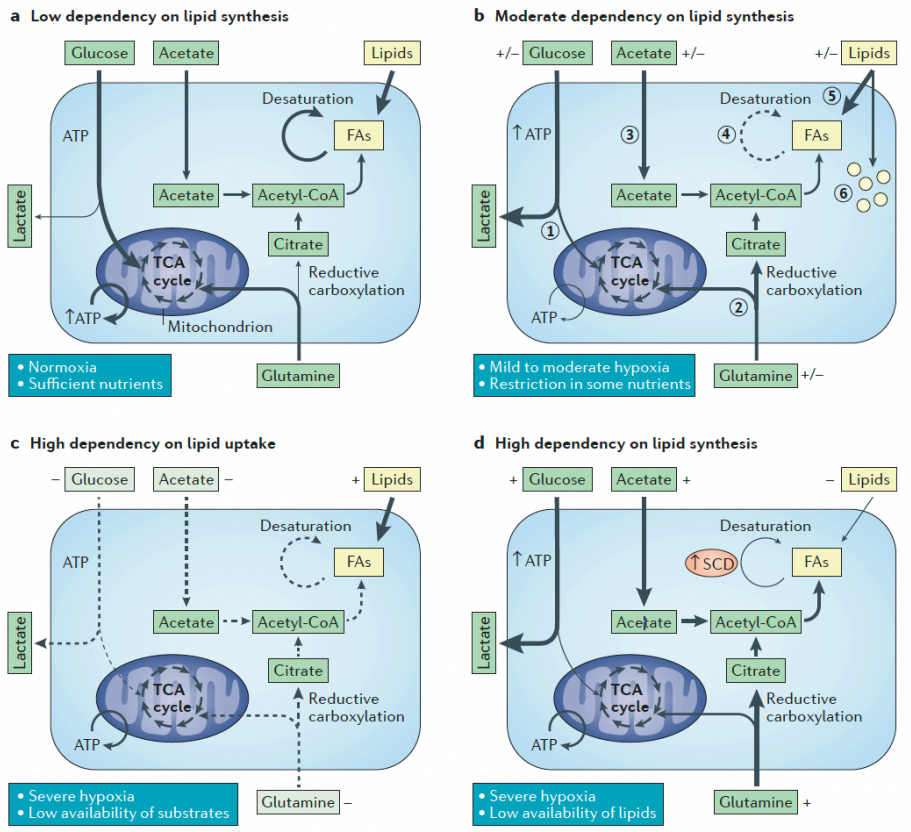


Figure 29 - Impact of nutrient and oxygen deprivation on metabolic adaptations. a) In normoxic conditions, tumor cells have access to different nutrient sources. They can present de novo lipid synthesis and also lipid uptake to support their rapid growth and proliferation. **b)** In cancer cells under mild to moderate hypoxic conditions, glucose is diverted to lactate, away from the TCA cycle, reducing the amount of citrate available for FA synthesis. Acetate and glutamine now represent important carbon sources for FA synthesis. Cells can also uptake exogenous unsaturated fatty acids and partly store them in lipid droplets for energy provision. **c)** Under severe hypoxia and when nutrient availability is scarce, cells highly depend on unsaturated fatty acids uptake from the extracellular matrix. **d)** When lipid availability is low, the dependency on acetate and glutamine metabolism for their de novo FA synthesis increases. Original figure from Röhrig et al [45].

3.2.3. Resistance to therapies

Chronic hypoxia, below 2% O_2, is involved in resistance to multiple therapies: radiotherapy, some forms of chemotherapy and immunotherapy.

Resistance to radiotherapy associated to tumor hypoxia has been studied for more than 100 years. When radiation is absorbed by a biological tissue of interest, it creates highly reactive free radicals. Those free radicals can then act directly or indirectly (through water radiolysis) on their target, DNA. They are able to break chemical bonds, producing chemical changes leading to a clonogenic death, cells losing their reproductive capability.

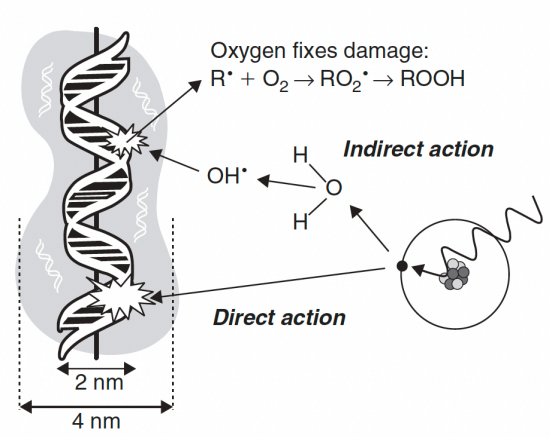


Figure 30 – Oxygen-fixation hypothesis. Free radicals induced on DNA can act directly, leading to clonogenic death. They also have an indirect mode of action: they can be repaired under hypoxia or be set in the presence of oxygen. Original figure from Horsman and Van Der Kogel [197].

The free radicals induced on DNA can react with O_2 if it is present, to quickly form $RO_2^{\bullet}$ and react furthermore to form ROOH. A change in the chemical structure of DNA now occurs, the damages become stable, set by the presence of O_2, preventing DNA repair. This is called the oxygen-fixation hypothesis, represented in Figure 30. In the absence of oxygen, unstable $R^{\bullet}$ radicals can react with H^+ and restore their original form, with no need for biological or enzymatic intervention [31, 193, 197].

The oxygen enhancement ratio (OER), ratio of doses that are necessary to obtain the same cell death under hypoxic and aerobic conditions, clearly demonstrates that hypoxic tumor cells require a dose 2.5 to 3 times higher to be killed than normoxic cells (Figure 31).

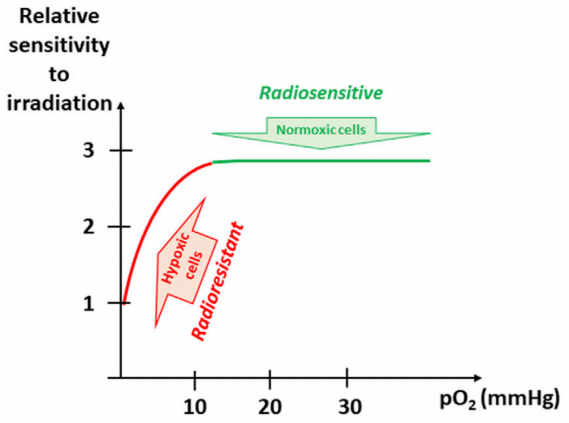


Figure 31 – Evolution of sensitivity to irradiation as a function of pO_2. The more hypoxic the cells, the more radioresistant they are. The oxygen enhancement ratio (OER) increases dramatically when pO_2 is increased from 1 to 10 mmHg, then stays stable whether or not pO_2 increases. Original figure from Gallez [31].

It is rather complicated to evaluate the implication of tumor hypoxia on the effect of chemotherapy alone in the clinical setting, as it is always part of a combined therapy strategy, either with surgery or with radiotherapy. Chemotherapeutic agents target rapidly dividing cells. However, in hypoxic regions, tumor cells theoretically divide at a slower rate because of the lack of nutrients and oxygen availability, therefore decreasing the effect of chemotherapeutic drugs. Moreover, hypoxia was shown to increase the expression and activity of the p-glycoprotein (P-gp), inducing a lower intracellular drug concentration. The abnormal vasculature of solid tumors also plays a role in chemotherapy resistance, as the delivery of drugs will be impaired [31].

Several factors are involved on tumor resistance to immunotherapy. The different examples cited here are simplified and non-exhaustive.

As mentioned above, HIF-1α is involved in immune evasion by modifying the expression of genes impacting the survival, cytolytic and migratory activity of immunostimulatory effector cells such as $CD4^+$ cells, $CD8^+$ cytotoxic cells, natural killer-T (NKT) cells and natural killer cells (NK) [31]. The tumor growth factor TGFβ was shown to promote the inhibition of lymphocyte proliferation (NK, T and B cells) and the apoptosis of NK or T cells [31, 198]. HIF-1α also upregulates the expression of Programmed death-ligand 1 (PD-L1) in hypoxic cells. This, in turns, results in the inhibition of T cell proliferation and mediated lysis. The immunosuppressive HLA-G (histocompatibility antigen class I, G) is upregulated on the surface of hypoxic tumor cells. Immune cells such as B cells, T cells, NK cells, dendritic cells, monocytes and macrophages express immunosuppressive molecules that bind to the overexpressed HLA-G on the surface of tumor cells in a hypoxic environment. This participates to the tumor escape from immune surveillance [31, 198].

3.3. Pharmacological modulation of hypoxia

There are several courses of action to target hypoxia: try to reduce tumor hypoxia to potentially increase the response to radiation therapy, use prodrugs that can become selectively active in hypoxic cells or inhibit molecular targets involved in the survival of hypoxic cells [31].

3.3.1. Treatments targeting hypoxia

There are two ways to view treatments that alleviate tumor hypoxia: either improve oxygen delivery or decrease the amount of oxygen consumed by tumor cells.

3.3.1.1. Improving oxygen delivery

Improving the delivery of oxygen to tumor cells can be done using different strategies. While their vasculature is often chaotic with immature blood vessels, tumor vascular patterns can be heterogeneous. Some mature vessels are able to regulate blood flow but sometimes show a dysregulation of their vasodynamic balance (vasoconstriction:vasodilation), due to alterations in the production of vasoactive agents and/or their regulation. This is the provascular approach, whose success is thus dependent on the proportion of vasoreactive vessels compared to immature vessels. Gallez et al. [199] tested 34 different vasodilators, including angiotensin-converting enzyme inhibitors, beta-blockers, potassium channel openers, calcium antagonists, nitric oxide (NO) donors and peripheral vasoactive agents. They found that 24 of them were able to increase tumor oxygenation, measured with EPR oximetry [31, 200, 201].

The next approach consists of trying to normalize tumor vasculature using antiangiogenic treatments. It may sound counterintuitive as an antiangiogenic treatment should lead to a decrease in oxygen and nutrient supplies, but if the time window is chosen correctly, this can lead to a transient normalization of the chaotic vasculature. Indeed, it was shown that this could lead to a reoxygenation of the tumor, increasing the perfusion and could potentiate the response to radiotherapy, chemotherapy and immunotherapy [202-204].

Other techniques, such as promoting the release of oxygen by hemoglobin using allosteric effectors [205, 206], adding oxygen to the circulation [131, 207] or using compounds acting on tumor blood flow have also been investigated [208, 209].

3.3.1.2. Decreasing oxygen consumption

The other strategy is to reprogram the cellular metabolism of tumor cells, to try and make them diminish the oxygen consumption rate (OCR) of cells. This has been studied for a long time, as Secomb et al. [210] have presented in 1995 a mathematical model suggesting that decreasing oxygen consumption could be more efficient to reduce tumor hypoxia than to increase oxygen delivery, a relatively large increase in blood flow being necessary to see an improvement.

Oxygen is mostly consumed by oxidative cells, by their mitochondria through oxidative phosphorylation and the electron transport chain. In 1977, Durand et al. [211] showed that a treatment with rotenone, antimycin A or oligomycin, three inhibitors of cell respiration, was able to increase oxygen availability and radiation sensitization in spheroids. Since then, several molecules targeting mitochondrial respiration have been tested: non-steroidal anti-inflammatory drugs, glucocorticoids, anti-diabetic metformin or anti-malarial atovaquone [211-215].

Mitochondrial pyruvate carrier (MPC) inhibitors have been shown to affect oxygen consumption. Corbet et al. [216] have identified 7ACC2 as an inhibitor of mitochondrial pyruvate carrier transport. They found that a treatment with 7ACC2 was able to reduce hypoxia and sensitize SiHa tumor xerographs to radiotherapy. They compared this inhibitor with another one, UK-5099, and confirmed that the inhibition of MPC radiosensitizes tumors. Moreover, it was

found that when conditioning chimeric antigen receptor (CAR) T cell with UK-5099, chromatin accessibility at pro-memory genes is induced, resulting in improved antitumor effects in an immunocompetent mouse solid tumor model and in a human leukemia model xenograft [217].

Other approaches have been proposed: cytotoxic drugs could accomplish a decrease in OCR, as a reduction in the cell number naturally leads to less oxygen consumed. This has been demonstrated with the chemotherapeutic agent paclitaxel [218]. It was found that paclitaxel-loaded micelles could decrease the number of cells, inducing a decrease in the compression of venous vessels along with a decrease in interstitial fluid pressure, in turns increasing blood flow and oxygen delivery in tumors [215, 218].

Another course of action to target OCR that has been studied are molecules involved in the formation of the free radical nitric oxide (NO), which also target mitochondrial respiration. Using NO donors (such as isosorbide dinitrate), insulin, stimulating the endothelial nitric oxide synthase (eNOS) or the inducible nitric oxide synthase (iNOS) can favor the response to radiation therapy [219-222].

3.3.2. Hypoxia-activated prodrugs

Some drugs can be reduced by reductases in a hypoxic environment to form cytotoxic molecules targeting tumor cells, and are called hypoxia-activated prodrugs (HAPs). These bioreductive drugs have little toxicity for normal tissues, as they are inhibited by oxygen which prevent the complete reduction of the compound into its active form, by competing for the single electron of the first reduced form. Superoxide dismutase (SOD) then detoxifies the superoxide

form, resulting in low toxicity in normoxic regions. This gives them an advantage for cancer therapy: as radiation therapy is effective in non-hypoxic cells and HAPs only target hypoxic cells, their combination could present maximal response. There are several classes of HAPs that have been developed such as nitromidazoles or quinones [31, 223, 224].

Nitroaromatic compounds, such as pimonidazole, now used in immunohistochemical staining for assessing tumor hypoxia, were tested as radiosensitisers. Indeed, they have high electron affinities, allowing them to stabilize radiation-induced DNA damage, inducing cell death. However, when tested in clinical trials, this compound did not show any benefice when combined with radiation in cervical carcinoma patients [31, 223-225].

Tirapazamine (3-amino-1,2,4-benzotriazine1,4-dioxide, TPZ) is a type of HAP that can generate an oxidative radical, through a one-electron reduction. It can diffuse into hypoxic regions and cause oxidative damage. It was found to effectively increase the effect of radiation in vitro as well as in pre-clinical models. Promising results were obtained in a Phase II clinical trials when TPZ was combined with the chemotherapeutic agent cisplatin, yet the Phase III did not confirm the benefit of this combined therapy [31, 223, 224, 226, 227].

3.3.3. Inhibitors of molecular targets involved in hypoxic cell survival

One of the major ways to interfere with hypoxia is to target the transcription factor HIF. As previously mentioned, HIF-1 regulates the expression of many genes, involved in angiogenesis, cell proliferation, survival, metastasis, metabolism and tumor immunity. Inhibition of HIF-1 can be done in several ways: by modulating its expression, interfering with the protein synthesis,

promoting its degradation and/or dimerization or by inducing a change in DNA binding and transcriptional activity [31, 228, 229].

Modulating the expression of HIF-1α by playing on mRNA levels with the oligodeoxynucleotide EZN-2968 has shown to downregulate its expression in human biopsies of treated patients [230]. Other modulators of mRNA levels include topoisomerase 1 inhibitors [31].

In order to interfere with the HIF-1α protein synthesis, several agents have been studied. A natural flavonoid, chrysin, has been described to inhibit HIF-1α protein synthesis through AKT signaling. Glyceollins, on the other hand, reduce its synthesis by blocking the PI3K/AKT/mTOR pathway [228].

Degradation of HIF-1α can be achieved by using the cellular chaperone, Hsp90, targeted by inhibitors to promote HIF-1α degradation in a VHL-independent manner [228]. Inhibitors of histone deacetylase (HDAC) work in the same way [31, 228].

Lastly, interfering with HIF-1α binding to DNA was shown to effectively impact its transcriptional activity. Anticancer agent anthracyclines, such as daunorubicin and doxorubicin, were shown to inhibit the binding of HIF-1α to the HRE sequences of target genes. These molecules, however, act as DNA intercalant, making it difficult to dissociate this from the inhibition of HIF-1α binding to DNA [31, 228].

3.4. Assessment of tumor hypoxia

The measurements of tumor hypoxia can be difficult, with the need to be non-invasive, sensitive (as pO_2 values in tumors is usually very low), probes needing to reach regions of poor perfusion. There are many different proposed methods

to measure hypoxia, direct or indirect, measuring more of the perfusion and potential hypoxic regions in tumors.

3.4.1. Direct measurements

3.4.1.1. Electrodes

The pO_2 can be measured by mini-electrodes: a current is generated by the reduction of oxygen at the cathode extremity, proportional to the pO_2. However, they have to be directly inserted into the tissues, making them very invasive. Because it measures a reduction in oxygen, it can also lead to an underestimation of the pO_2.

The "gold standard" method in the clinical setting for assessing tumor oxygenation used to be the computerized Eppendorf pO_2 histography system [31, 190]. This method involved an electrode that's mechanically moved through the tissue of interest. In that way, there is minimum tissue compression and consumption of the oxygen by the electrode but it is limited to accessible tumors and is unable to distinguish between necrosis and hypoxia [231].

3.4.1.2. Fiber-optic devices

The fiber-optic oxygen-sensing device called OxyLite (Oxford Optronix, Oxford, UK) has been compared to electrodes. In this system, a fluorophore at the end of the tip is stimulated by photodiodes, the lifetime of the fluorescence being inversely proportional to the oxygen tension at the probe tip [232]. The main difference with the electrodes is that the devices are inserted one time and once the OxyLite is at an equilibrium, a continuous readout of the tissue pO_2 is done. OxyLite has been used to measure pO_2 in several studies and compared to

different other methods, as there is a need to find methods that are less invasive than electrodes in general [219, 233-236].

3.4.1.3. Magnetic Resonance Imaging

3.4.1.3.1. ^{19}F-imaging

Fluorine (^{19}F)-imaging can provide quantitative maps of tumor oxygenation because of the spin lattice relaxation rate ($R_1 = 1/T_1$) of ^{19}F is directly proportional to the oxygen concentration in the tissue. It requires the injection of a perfluorocarbon emulsion intratumorally or intravenously (which can then lead to an extensive uptake by the liver). Also, pO_2 measurements could potentially be biased by the fact that the perfluorocarbon emulsion could only reach well-oxygenated regions of the tumors, ignoring regions of hypoxia/necrosis, overestimating pO_2 values [31, 192, 237]. This method has been used to predict the tumor response to irradiation and to map fluctuations in tumor hypoxia [238-240].

3.4.1.4. Electron Paramagnetic Resonance oximetry

The principle of EPR is described in the "2.4.6. Electron Paramagnetic Resonance" section and won't be described again here. EPR can be used to measure oxygen concentration in biological samples or tissue. In reality, when dissolved in fluids near room temperature (such as in a cell sample), oxygen has a fast spin relaxation which causes a broadening of the spectrum until it is undetectable, meaning that it cannot be directly detected by EPR. Thus, in order to measure O_2 with EPR, sensors are used because oxygen changes their relaxation rates, making it possible to obtain information about oxygen concentration. Measurements depending on T_1 and T_2 of EPR spin probes

provide a direct indication of oxygen status in a biological system. The most common method is to use the T_2, as an increase in the oxygen concentration induces a decrease in the T_2, broadening of the hyperfine line [241].

There are two kind of oxygen sensors that can be used to track oxygen changes in a solution or a tissue: soluble probes or insoluble, particulate probes.

3.4.1.4.1. Soluble probes

For soluble probes, the Smoluchowski equation governs the Heisenberg exchange rate (ω) between molecule O_2 in solution and the radical:

$$\omega = 4 \pi R (D(O_2) + DSP) [O_2]$$

Where R = interaction distance; $D(O_2)$ = oxygen diffusion coefficient ; DSP = spin probe diffusion coefficient. And the variation of the linewidth (ΔLW):

$$\Delta LW = 4 \pi R k p (D(O_2) + DSP) \Delta[O_2]$$

Where k = proportionality constant; p = probability that exchange will occur upon each collision. This shows that the variation of the linewidth (ΔLW) is directly proportional to the variation of the oxygen concentration ($\Delta [O_2]$) [243].

As explained in the "2.4.6. Electron Paramagnetic Resonance" section, nitroxides can be used to study oxygen changes. One of the most commonly used probe for oximetry is the perdeuterated nitroxide 4-oxo-2,2,6,6-tetramethylpiperidine-d16-^{15}N-1-oxyl (^{15}N-PDT). The broadening of its spectrum linewidth is directly proportional to the increasing oxygen concentration and can be calibrated as a function of oxygen level as seen in Figure 32.

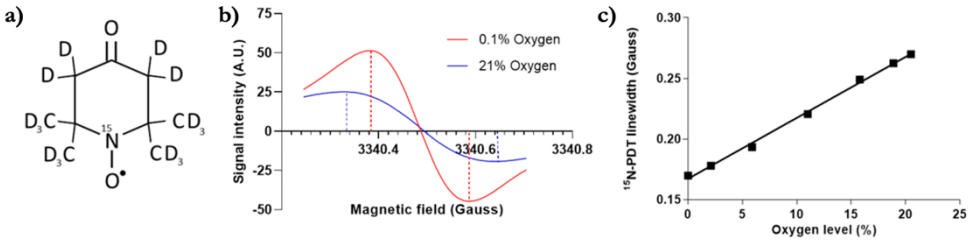


Figure 32 – Perdeuterated nitroxide 4-oxo-2,2,6,6-tetramethylpiperidine-d16-^{15}N-1-oxyl. **a)** Structure of ^{15}N-PDT. **b)** The broadening of its spectrum linewidth directly proportional to the increasing oxygen concentration. **c)** Its linewidth variation can be reported as a function of oxygen, leading to a calibration curve. Original figures from d'Hose [244].

For in vitro studies using X-band EPR oximetry, nitroxides are commonly used to measure oxygen consumption rate (OCR) (Figure 33). It is possible to follow, in real time, the narrowing of the nitroxide's spectrum linewidth and to plot it as a function of the decreasing oxygen concentration [245].

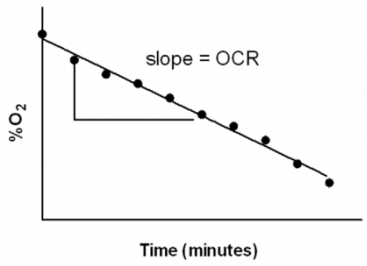


Figure 33 – Oxygen consumption rate. Percentages in O_2 consumed are represented as a function of time. The slope representes the oxygen consumption rate. Adapted figure from Danhier et al. [245].

A second class of soluble probes for oxygen measurement are the triarylmethyl (trityl) radicals. They have a very narrow EPR linewidth, in the range of 30 to 100 mG. TAMs are very sensitive to oxygen changes, their spectrum broadening of about 500 mG/mM of oxygen [182].

As previously described in the "2.4.6. Electron Paramagnetic Resonance" section, the monophosphonated trityl pTAM's spectrum (Figure 26) gives

information about pO_2, thanks to the pO_2-dependent changes in the linewidth of its spectrum [184].

EPR using nitroxides and trityl radicals have been used for a long time to study and map, image pO_2 [182, 220, 246]. Soluble probes can easily distribute within the tissue of interest but often rapidly cleared from the systems, which doesn't allow a longitudinal follow-up of the pO_2 values, unless multiple injections are done.

However, it is also possible to exploit changes in electron spin relaxation rate, such as $R_1 = 1/T_1$, using pulsed-EPR with triarylmethyl radicals [247]. In pulsed EPR, pulses of microwave radiation are used instead of a continuous wave. Pulsed EPR oximetry presents the advantage to have minimal motion artefacts and short imaging times [248]. pO_2 images acquired with pulsed EPR using trityl OX063 were found to be less dependent on trityl concentration and more accurate than R_2-based images [249]. It has a spatial resolution of ~1 mm and was able to measure pO_2 to ~1 mmHg. It can be used a low frequency, 250 MHz, allowing a penetration depth accessible to human imaging [250].

The use of particulate insoluble probes can also solve this problem.

3.4.1.4.2. Insoluble particulate probes

Particulate probes' oxygen sensitivity relies on the broadening of their EPR linewidth, which can be calibrated as a function of pO_2. Compared to soluble probes, particulate materials have a much higher sensitivity to oxygen changes. They are able to detect variations as low as about 1 mmHg. Particulate probes measure pO_2 at the region of injection and are very stable overtime and for long periods of time [31, 182]. This makes them ideal for longitudinal studies.

Particulate oxygen sensors include charcoals, carbon blacks, lithium phthalocyanine (LiPc) and derivatives, such as octa-n-butoxy-naphthalocyanine (LiNc-BuO). Carbon-based materials are often preferred for studying pO_2 in tumors as they have a high sensitivity at low pO_2 (Figure 34) [219, 251].

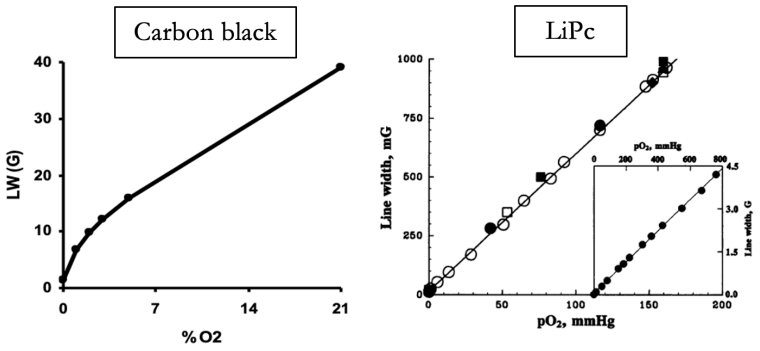


Figure 34 – Comparison of linewidth evolution as a function of oxygen. Carbon blacks have a higher sensitivity at small O_2 concentrations (expressed in percentages) compared to LiPc (pO_2 expressed in mmHg). Adapted figure from Gallez [175].

LiPc has a very narrow linewidth under 0% of O_2, 25-30 mG, and a linear linewidth calibration as a function of pO_2 (Figure 35). A few crystals inserted inside the tissue of interest are enough to have precise pO_2 estimations [192].

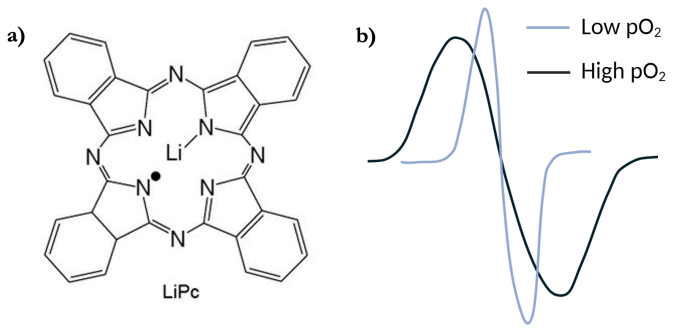


Figure 35 – Structure of lithium phthalocyanine. b) The variation in its linewidth can be calibrated as a function of pO_2. Adapted figure from Dhimitruka et al. [182].

Particulate probes are inserted once into the tissue and can be used to evaluate pO_2 over time, but they only give a mean value of pO_2, not taking into account the tumor heterogeneity. In order to do that, there need to be several injections made at several sites in the tumor, making this method invasive.

3.4.2. Indirect measurements

To have an idea of the hypoxic environment that can be found inside a tumor, it is possible to measure tumor perfusion or vascularization.

3.4.2.1. Seahorse XF

The principle and functioning of the Seahorse XF have previously been described in the "2.4.2. Seahorse XF" point of the acidosis section of this document for the measurement of ECAR. The Seahorse XF can also be used to measure Oxygen Consumption Rate (OCR). The sensor probes now measure changes in dissolved oxygen, caused by cellular oxygen consumption (respiration) (*Agilent* - https://www.agilent.com/en/products/cell-analysis/how-seahorse-xf-analyzers-work).

3.4.2.2. Magnetic Resonance Imaging

3.4.2.2.1. Endogenous contrast

Relaxation times T_1, T_2 or T_2^* can be used as endogenous MRI contrast. T_2^* is the combination of T_2 relaxation and magnetic field inhomogeneity, also called dephasing time. The inverse of the relaxation times is referred to as relaxation rates R_1 ($1/R_1$), R_2 ($1/R_2$) and R_2^* ($1/R_2^*$). R_1 and R_2^* are oxygen-sensitive

endogenous MRI contrasts that can be used as potential biomarkers of tumor hypoxia [31].

- *Oxygen Enhanced MRI*

The spin lattice R_1 relaxation rate is increased by the dissolved paramagnetic molecular oxygen in tissue fluid and in blood plasma. Oxygen-enhanced MRI is based on changes in R_1: a switch of the inhaled gas from air to 100% oxygen or carbogen induces a change in dissolved arterial oxygen which may lead to a change in tumor oxygenation and thus a change in R_1 [252-254].

Of note, molecular oxygen is not the only factor influencing the basal R_1 of a tissue, which therefore cannot be used as a marker of tissue oxygenation.

- *Blood oxygen level-dependent contrast MRI*

Blood oxygen level-dependent (BOLD) contrast is an MRI contrast mechanism based on the study of changes in the hemodynamic of tissues of interest. BOLD MRI does not measure direct changes in pO_2 but relies on the ratio between paramagnetic deoxyhemoglobin (dHB) and diamagnetic oxyhemoglobin. dHB works as an endogenous contrast agent for blood oxygenation as it enhances the effective transverse relaxation rates R_2^* of water in blood and in the tissue surrounding the blood vessels. An increase in blood oxygen saturation, leading to a decrease in dHB concentration induces a decrease in R_2^*. BOLD MRI can map, in real time, changes in oxygenation and/or perfusion of tumors [192, 237, 255, 256]. However, this method can present limitations in terms of quantitative relationships between signal intensity and true changes in pO_2.

Interestingly, changes in R_1 are resulting from changes in the vascular and tissue oxygen content while changes in R_2^* are due to changes in the vascular compartment.

3.4.2.2.2. Exogenous contrast

Dynamic Contrast-Enhanced (DCE) MRI requires the exogenous administration of a gadolinium-based contrast agent. As gadolinium shortens the T_1 relaxation time, a monitoring of the distribution and washout in tissues of the contrast agent is possible. DCE-MRI can provide functional parameters using pharmacokinetic models, reflecting blood perfusion and vascular permeability [257].

3.4.2.3. PET radiotracers

PET can be used to characterize hypoxia by administrating intravenously a radiotracer, a nitroimidazole. Under normoxia, this molecule can stay in the extracellular compartment or diffuse into cells, where it is reduced. In hypoxia, nitroimidazoles can undergo an oxygen-reversible single-electron reduction by reductases only present in viable hypoxic cells. This leads to the formation of reactive oxygen radicals that can covalently bind to macromolecular cellular components, accumulating only in viable hypoxic and not necrosis regions [258].

Nitroimidazoles have mostly been marked with the fluor ^{18}F positron emitter, the most common one being ^{18}F-Fluoromisonidazole (^{18}F-FMISO). It is highly lipophilic and can be easily trapped in hypoxic cells and is rapidly cleared from the urinary system [259]. It is the first one to have been used in the clinic.

The ^{18}F-fluoroazomycin-arabinofuranoside (^{18}F-FAZA) is another common radiotracer, more hydrophilic than the first one. Its clearance is even faster than the one of ^{18}F-FMISO but ^{18}F-FAZA provides a higher signal-to-noise ratio, resulting in better contrast images than when using ^{18}F-FMISO. While a rapid clearance can interfere with the ability to distinguish between hypoxia and low blood flow, it also improves the PET contrast between hypoxic and normoxic tissues [237].

^{18}F-FAZA has been proven to accumulate in hypoxic regions in vitro [260, 261] and in vivo [262, 263]. ^{18}F-FAZA-PET imaging could be very useful in targeting areas of hypoxia in tumors, even though this method predominantly measures chronic hypoxia and not the changing states of transient hypoxia [264].

One last example is ^{18}F-flortanidazole (^{18}F-HX4), which is also quickly cleared from normoxic tissues and accumulates in highly hypoxic regions. Once again, this method does not give quantitative information about pO_2 but these molecules could help guide and follow the response to radiotherapy treatments [31, 237].

3.4.2.4. Cellular response to hypoxia

Another indirect approach to evaluate hypoxic regions in tumors is to study the consequences of being exposed to hypoxia. Indeed, as explained before, cells under hypoxia will up- or downregulate genes.

Amongst the most classically overexpressed genes found in hypoxic cells are HIF-1α and CAIX. Their expressions and their mRNA levels can be assessed in biopsies, using immunohistochemistry or gene expression arrays, respectively

[265]. CAIX expression has been found to be concordant with the hypoxia marker, pimonidazole [160] but sometimes not completely overlapping [266].

Antibodies against HIF-1α and CAIX are easily accessible but in addition to being invasive, this method relies on the expression of two factors that is not only affected by hypoxia, but also by pH, cell density and oncogene activation. Nevertheless, studying the cellular response to hypoxia can be useful for tumor characterization or prognostic purposes.

It is also possible to couple those antibodies with labelled positron emitter to study their accumulation directly in tumors, without the biopsy. Several radiotracers targeting CAIX have been developed, tested in pre-clinical models and correlated with CAIX expression [31, 237, 267].

Aims of the thesis

Aims of the thesis

The acidosis and hypoxia of the tumor microenvironment may have profound impact on cancer progression and on the efficacy of treatments. New treatments in cancer research are targeting these fundamental characteristics of the tumor microenvironment. Innovative therapies may significantly benefit from the possibility to use pharmacodynamic biomarkers that may guide the treatments.

In this work, we assessed the capability of noninvasive magnetic resonance biomarkers to tackle drug-induced changes in pH and/or pO_2.

Our first goal was to efficiently measure pH_e values and evaluate if a significant change in those values could be detected when using treatments supposedly able to modify pH_e. For this purpose, we compared ^{31}P-NMR spectroscopy and CEST-MRI. In order to modify pH_e values, we studied the effect of an MPC inhibitor, UK-5099. We evaluated pH_e values before and after treatment in mice bearing the triple-negative mouse breast cancer 4T1 cell model. Our hypothesis was that a significant acidification could be measured with both methods after MPC inhibition.

In the second study, we focused on measuring pH_e values with CEST-MRI, to monitor the effect of another pharmacological treatment: syrosingopine, an inhibitor of MCT1 and MCT4. We evaluated the effect of a treatment with syrosingopine on pH_e values first in vitro, comparing the human breast cancer model MDA-MB-231 and the head and neck squamous cell carcinoma model FaDu, both presenting different expression of MCTs: MDA-MB-231 only expressing MCT4, FaDu expressing both MCT1 and MCT4. We then studied the effect of syrosingopine on pH_e in mice bearing the MDA-MB-231 tumor model.

Our last goal was to achieve simultaneous measurements of pH_e and pO_2, using a duel probe. We combined a soluble probe, pTAM, which was reported to be sensitive to both pH_e and pO_2 with lithium phthalocyanine crystals that is highly sensitive to changes in pO_2. We measured both parameters before and after treatments with UK-5099 in 4T1 tumor-bearing mice.

Aims of the thesis

Results

1. Impact of Inhibition of the Mitochondrial Pyruvate Carrier on the Tumor Extracellular pH as Measured by CEST-MRI

Published in *Cancers*, 2021, *13*, 4278

Buyse, C.; Joudiou, N.; Corbet, C.; Feron, O.; Mignion, L.; Flament, J.; Gallez, B.

doi : 10.3390/cancers13174278

cancers

MDPI

Article

Impact of Inhibition of the Mitochondrial Pyruvate Carrier on the Tumor Extracellular pH as Measured by CEST-MRI

Chloé Buyse [1,†], Nicolas Joudiou [2,†], Cyril Corbet [3], Olivier Feron [3], Lionel Mignion [1], Julien Flament [4] and Bernard Gallez [1,*]

[1] Louvain Drug Research Institute, Biomedical Magnetic Resonance, Université catholique de Louvain (UCLouvain), 1200 Brussels, Belgium; chloe.buyse@uclouvain.be (C.B.); lionel.mignion@uclouvain.be (L.M.)
[2] Louvain Drug Research Institute, Nuclear and Electron Spin Technologies (NEST) Platform, Université catholique de Louvain, 1200 Brussels, Belgium; nicolas.joudiou@uclouvain.be
[3] Pole of Pharmacology and Therapeutics (FATH), Institut de Recherche Expérimentale et Clinique (IREC), Université catholique de Louvain (UCLouvain), 1200 Brussels, Belgium; cyril.corbet@uclouvain.be (C.C.); olivier.feron@uclouvain.be (O.F.)
[4] Commissariat à l'Energie Atomique et aux Energies Alternatives (CEA), Centre National de la Recherche Scientifique (CNRS), Molecular Imaging Research Center (MIRCen), Laboratoire des Maladies Neurodégénératives, Université Paris-Saclay, 92265 Fontenay-aux-Roses, France; julien.flament@cea.fr
* Correspondence: bernard.gallez@uclouvain.be
† Contributed equally to this work.

Simple Summary: Dysregulated metabolism is a key hallmark of cancer cells and many solid tumors are acidic. Acidosis is responsible for cancer aggressiveness and for resistance to several treatments. In the present study, we evaluated to which extent tumor acidosis was influenced upon inhibition of the import of pyruvate into the mitochondria, the powerhouse of the cell. Using advanced molecular imaging to measure non-invasively the acidity in a model of breast cancer, we found that while some tumor regions became much more acidic, others did not show any change. This study highlights the capacity of this advanced technology to reveal the heterogeneity of response to the treatment.

Abstract: (1) Background: The acidosis of the tumor micro-environment may have profound impact on cancer progression and on the efficacy of treatments. In the present study, we evaluated the impact of a treatment with UK-5099, a mitochondrial pyruvate carrier (MPC) inhibitor on tumor extracellular pH (pHe); (2) Methods: glucose consumption, lactate secretion and extracellular acidification rate (ECAR) were measured in vitro after exposure of cervix cancer SiHa cells and breast cancer 4T1 cells to UK-5099 (10 μM). Mice bearing the 4T1 tumor model were treated daily during four days with UK-5099 (3 mg/kg). The pHe was evaluated in vivo using either chemical exchange saturation transfer (CEST)-MRI with iopamidol as pHe reporter probe or ^{31}P-NMR spectroscopy with 3-aminopropylphosphonate (3-APP). MR protocols were applied before and after 4 days of treatment; (3) Results: glucose consumption, lactate release and ECAR were increased in both cell lines after UK-5099 exposure. CEST-MRI showed a significant decrease in tumor pHe of 0.22 units in UK-5099-treated mice while there was no change over time for mice treated with the vehicle. Parametric images showed a large heterogeneity in response with 16% of voxels shifting to pHe values under 7.0. In contrast, ^{31}P-NMR spectroscopy was unable to detect any significant variation in pHe; (4) Conclusions: MPC inhibition led to a moderate acidification of the extracellular medium in vivo. CEST-MRI provided high resolution parametric images (0.44 μL/voxel) of pHe highlighting the heterogeneity of response within the tumor when exposed to UK-5099.

Keywords: pH; acidosis; glycolysis; tumor; mitochondrial pyruvate carrier (MPC); MRI; CEST; ^{31}P-NMR; imaging; biomarker

check for updates

Citation: Buyse, C.; Joudiou, N.; Corbet, C.; Feron, O.; Mignion, L.; Flament, J.; Gallez, B. Impact of Inhibition of the Mitochondrial Pyruvate Carrier on the Tumor Extracellular pH as Measured by CEST-MRI. *Cancers* **2021**, *13*, 4278. https://doi.org/10.3390/cancers13174278

Academic Editors: David Wong and Dario Livio Longo

Received: 29 May 2021
Accepted: 30 July 2021
Published: 25 August 2021

Publisher's Note: MDPI stays neutral with regard to jurisdictional claims in published maps and institutional affiliations.

Copyright: © 2021 by the authors. Licensee MDPI, Basel, Switzerland. This article is an open access article distributed under the terms and conditions of the Creative Commons Attribution (CC BY) license (https://creativecommons.org/licenses/by/4.0/).

1. Introduction

Dysregulated metabolism is a key hallmark of cancer cells. Glucose fermentation through glycolysis even in the presence of oxygen (aerobic glycolysis) is a common feature of malignant tumors [1–4]. This exacerbated glycolytic flux in tumors is leading to extracellular acidosis that is known to stimulate tumor migration and invasiveness [1–4]. In addition, acidosis in the tumor microenvironment is associated with the modulation of activity of anti-cancer agents [4–6]. Clinical studies have shown that an acidic microenvironment results in less favorable prognosis associated with metastatic potential and drug resistance [7].

Among the modulators of tumor metabolism, mitochondrial pyruvate carrier (MPC) has recently received particular attention. MPC is located in the mitochondrial inner membrane and is responsible for importing pyruvate, the end-product of glycolysis, from the cytosol to the mitochondrial matrix. MPC is Janus-faced regarding cancer progression [8–10]. Some cancers exhibit partial to complete loss of MPC expression that is associated with increased cell proliferation and stem cell marker expression [9,11]. It has actually been shown that MPC disruption could promote cancer progression in colon cancer [11,12], prostate cancer [13,14], and kidney cancer [15,16]. Conversely, cancers that rely on mitochondrial pyruvate utilization to maintain growth are negatively impacted by MPC disruption [9]. For example, in breast cancer, studies showed that chemical or estrogen-related receptor alpha (ERRα)-mediated disruption of the MPC inhibited proliferation in cell lines [9,17,18]. The chemical inhibition of the MPC also decreased the growth of the SiHa cervix cancer cell line [19]. It was also found that the inhibition of mitochondrial respiration induced by bona fide MPC inhibitors 7ACC2 and UK-5099 led to the alleviation of tumor hypoxia and the radiosensitization of the FaDu tumor model [19]. In the same study, it was also found that the extracellular acidification rate (ECAR) measured in vitro was increased after exposure of SiHa cells to 7ACC2. As pyruvate cannot undergo oxidative phosphorylation (OXPHOS) in the mitochondria, there is an accumulation of pyruvate that is transformed into lactate, inhibiting the import of lactate from the extracellular medium and favoring the export of lactate through MCT4 (Figure 1).

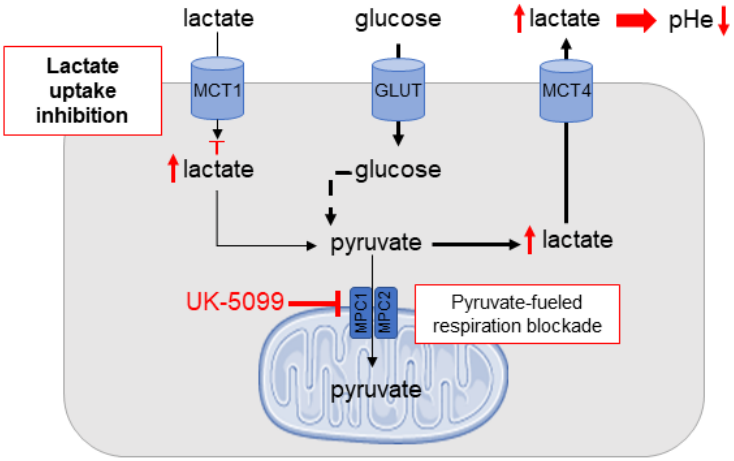


Figure 1. Model depicting the mechanism of extracellular acidification upon MPC inhibition.

Because acidosis within the tumor micro-environment may have profound impact on cancer progression and treatment efficacy, this last observation prompted us to further explore the effect of MPC inhibition on the extracellular pH (pHe) in vivo. To reach this goal, we have used two non-invasive nuclear magnetic resonance methods [20]. Among magnetic resonance imaging (MRI) modalities, the chemical exchange saturation transfer (CEST) approach has emerged as a technology that provides high spatial resolution and

sensitivity for in vivo imaging of tumor acidosis [20–22]. For this purpose, hydrophilic X-ray iodinated contrast media that are confined in the extracellular medium can be used for CEST-MRI [20–22]. Due to the natural process of chemical exchange of labile protons between molecules, these protons on the CEST agent are transferred to a nearby water molecule. This transfer of saturation from the exchangeable proton to the water proton reduces the MRI signal amplitude of water. Iopamidol possesses two amide proton pools that can be saturated at 4.2 and 5.5 ppm (Figure 2A). A ratiometric procedure allows to measure pHe independently on the concentration of iopamidol in the pH range of 6.0 to 8.0. This technique has been used in a variety of tumor models [23–27] and in cancer patients [28,29]. The technique has also been used to monitor the changes in pHe in tumors induced by treatments such as administration of bicarbonate [30,31] or after the pyruvate dehydrogenase kinase inhibitor dichloroacetate [32]. In parallel, we also exploited ^{31}P-NMR spectroscopy using 3-aminopropylphoshonate (3-APP) that has long been used to assess pHe in different tissues and especially in tumors [33–36] (Figure 2B).

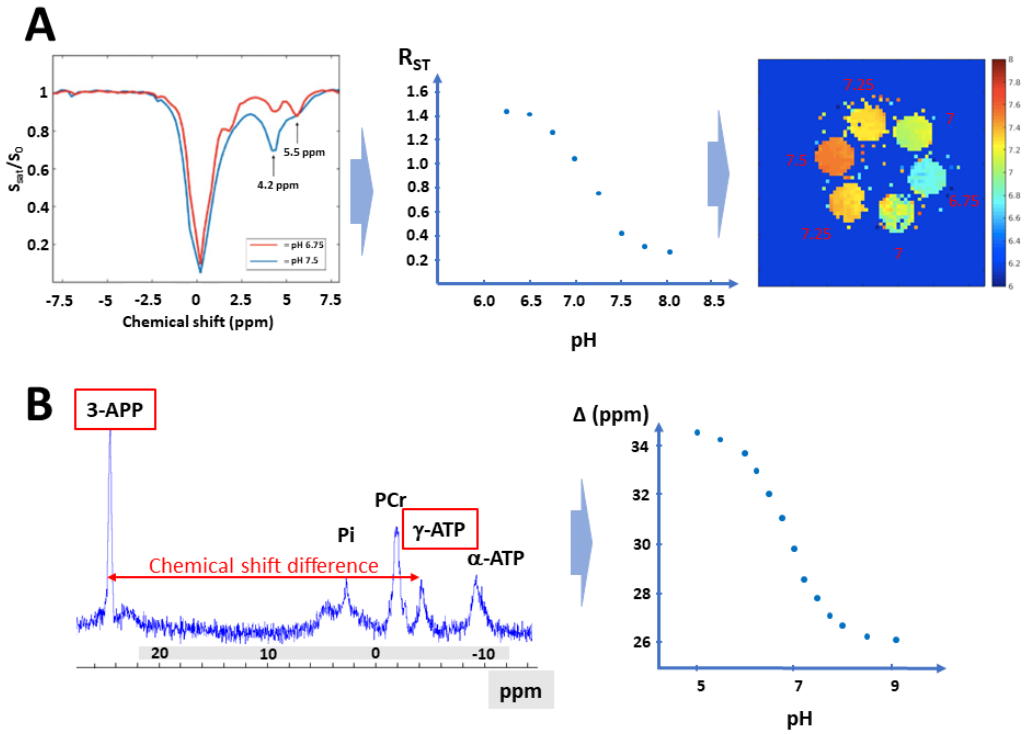


Figure 2. Principle of two popular MR methods to assess pHe. (**A**): CEST-MRI is based on the transfer of saturation from the exchangeable proton to the water proton reducing the MRI signal amplitude of water. Left: Z-spectrum: normalized water intensity (S/S_0) vs. off-resonance frequency of the saturating RF for iopamidol in buffered solutions at pH 6.75 and 7.5. Center: calibration of the saturation transfer as a function of pH. Right: the calibration of the saturation transfer as a function of pH provides parametric map of pH as illustrated in tubes equilibrated at different pH. (**B**): Left: typical ^{31}P-NMR spectrum recorded in a tumor. The pHe is estimated by measuring the difference in chemical shift between the signal coming from 3-APP used as extracellular pH reporter probe and the signal coming from on phosphorous present on ATP. Right: calibration of the difference in chemical shift between 3-APP and γ-ATP as a function of pH.

In the present study, we evaluated the effect of the MPC inhibitor UK-5099 on extracellular acidification. First, we observed in vitro that the exposure of SiHa (cervix cancer) and 4T1 (breast cancer) cell lines to UK-5099 led to an increase in extracellular acidification rate. Using CEST-MRI, we found that daily treatment with UK-5099 led to a significant decrease of 0.22 pHe units in mouse 4T1 tumors. The response was rather heterogenous within tumors with a shift towards acidification for about 16% of the voxels. This change in pHe was not detectable using ^{31}P-NMR spectroscopy using 3-APP as pHe reporter.

2. Materials and Methods

2.1. Cell Culture

The 4T1 breast cancer cells were cultured at 37 °C in a humidified atmosphere with 5% CO_2 and maintained in RPMI-1640 medium (Thermo Fisher Scientific, Merelbeke, Belgium) supplemented with 10% heat-inactivated FBS (Thermo Fisher Scientific). SiHa cervix cancer cells were maintained in DMEM supplemented with 10% heat-inactivated FBS. Both cell lines were acquired from ATCC where they are regularly authenticated by short tandem repeat profiling. All cell lines were tested for mycoplasma contamination with the PCR-based MycoplasmaCheck assay (Eurofins, Ebersberg, Germany) before being used.

2.2. Lactate Production and Extracellular Acidification Rate (ECAR)

For glucose and lactate dosage, cells (2×10^5 cells/well; 3 wells/condition) were seeded in 12-well plates with 2 mL of their routine culture medium. After 24 h, medium was replaced by 500 µL of DMEM pH 7.4 containing 10 mmol/L D-glucose and supplemented with 2 mmol/L L-glutamine and 10% dialyzed FBS (Sigma-Aldrich, Overijse, Belgium), in presence of 10 µmol/L UK-5099 (Sigma-Aldrich) or vehicle (DMSO; Sigma-Aldrich). Initial concentrations of glucose and lactate in the experimental medium were also assessed by including control wells containing only cell culture medium (no cells) on each plate. After incubation for 24 h, extracellular media were collected and deproteinized by centrifugation (15 min, 10,000 rpm, 4 °C) in 10 kDa cut-off filter tubes (VWR). Glucose and lactate concentrations were measured in the samples (50 µL) by using enzymatic assays (CMA Microdialysis AB, Kista, Sweden) and a CMA 600 analyzer (Aurora Borealis, Solna, Sweden). Data analysis was done by calculating the difference in metabolite concentrations between the control wells and the experimental wells. Data were then normalized by the protein content in each well and expressed in µmol/h/mg protein.

Oxygen consumption rate (OCR) and extracellular acidification rate (ECAR) were measured by using the Seahorse XF96 analyzer (Agilent, Santa Clara, CA, USA). Briefly, cells (1.5×10^4 cells/well; 6 wells/condition) were seeded in Seahorse 96-well cell culture plates in their routine culture medium, in presence of 10 µmol/L UK-5099 or vehicle (DMSO, Sigma-Aldrich). After 24 h, medium was replaced by 175 µL unbuffered serum-free DMEM pH 7.4 supplemented with 2 mmol/L L-glutamine, still in presence of the treatment. OCR and ECAR values were assessed before (3 cycles of 3 min mixing/4 min measuring) and after (4 cycles of 3 min mixing/4 min measuring) the injection of 10 mmol/L D-glucose. Glucose-dependent ECAR was calculated by comparing the values before and after addition of the substrate. Data were normalized by the protein content in each well and expressed in pmol/min/µg protein or mpH/min/µg protein for OCR and ECAR, respectively.

2.3. Tumor Model

All experiments involving animals were performed in accordance with the Belgian law concerning the protection and welfare of the animals and were approved by the UCLouvain ethics committee (Agreement reference: 2018/UCL/MD/021).

The 2×10^5 4T1 cells in 100 µL of PBS were injected intramuscularly in the right hind paw of 15-week-old female BALB/c JNRj mice. On Day 7 or 8, when tumors reached a volume of about 200 mm^3 (real values measured by MRI were 203 ± 14 mm^3), the pHe of tumors was measured and found comparable in both groups (control or treated). Mice

were treated with daily intraperitoneal injection of UK-5099 (3 mg/kg) or vehicle for 4 days. Tumors were last analyzed on Day 10 or 11 after induction (Figure 3).



Figure 3. Experimental protocol to assess the effect of UK-5099 on extracellular pH in vivo.

2.4. CEST-MRI Experiments

- CEST calibration in vitro

All experiments were performed on a 11.7T Biospec MRI (Bruker, Ettlingen, Germany). Solutions containing 30 mmol/L of Iopamidol (Iopamiron 300, Bracco, Milan, Italy) and HEPES were set at 9 different pH (from 6.25 to 8). Calibrations were done at 37 °C. CEST acquisitions were acquired with a 40-mm ^{1}H volume coil. The CEST sequence was a RARE sequence (TR = 4.0 s, TE = 23.0 milliseconds, rare factor = 10, slice thickness = 2 mm, FOV = 30 mm, matrix size = 64 × 64, in-plane special resolution = 468 µm) with an additional continuous 4 µT irradiation for 4 s. The Z spectrum was acquired between −8 to 8 ppm (81 frequencies) for a total acquisition time of 27 min 20 s.

- In vivo analysis

Mice were anesthetized with Isoflurane (Isoflo, Zoetis, Zaventem, Belgium) and placed in a device allowing their analysis and maintenance of the anesthesia at 1–2% Isoflurane. Their breathing was monitored by a pressure sensor placed in the abdomen for the entire duration of the experiment and their temperature was monitored and maintained at 37 °C by a blanket heater connected to a water bath. Iopamidol was injected intravenously through the tail vein (3 g Iodine/kg). Mice were placed in a 40-mm ^{1}H volume coil. CEST images were acquired using the same parameters as in vitro experiment. Acquisition were started 20 min after the injection. All voxels were analyzed using a custom-written script in Matlab (The MathWorks Inc., Natick, MA, USA). The Z-spectra were centered on the bulk water signal to correspond to the zero frequency. Values were measured at the frequency offsets of 4.2 and 5.5 ppm and used in the Equation (1):

$$ST = (S_{-\Delta\omega} - S_{+\Delta\omega})/S_0 \quad (1)$$

where S = signal intensity at 4.2 or 5.5 ppm and S_0 = bulk water signal intensity without saturation. Saturation transfer values at 4.2 and 5.5 ppm can be used to calculate their ratio (2):

$$RST = (ST\ 5.5)/(ST\ 4.2) \quad (2)$$

In order to eliminate outliers, different filters were applied to the data. A threshold of 2% was used to discriminate between enhanced and not enhanced voxels. Negative ST values were excluded as well as RST values above 0.2 and below 1.55. pH values were calculated based on the RST and the corresponding pH values of the calibration curve. pH maps were obtained by overlaying anatomical images and pH values in each voxel. Only tumors giving a pH map including more than 10 voxels (volume = 0.44 µL) were kept for the statistical analysis.

2.5. P-NMR Spectroscopy

- pH Calibration in vitro

Solutions were prepared with 10 mM 3-APP, 10 mM ATP and HEPES (Sigma-Aldrich) and adapted to 15 different pH values (from 5 to 9). pH values were measured using a pH-meter (InoLab pH 730 WTW, Weilheim, Germany). Solutions were placed in the setting later used for the in vivo studies. The values used for the calibration were studied at 37 °C. A RARE sequence was followed by a ^{31}P single pulse sequence (TR = 500 ms, number of repetitions = 1024, total acquisition time = 8 min, resolution = 2.44 Hz) acquired with a ^{1}H/^{31}P surface coil.

- In vivo spectroscopy

Anesthetized mice were injected intraperitoneally with 300 µL of 3-APP (75 mg/mL) 30 min before analysis. Prior to spectral acquisitions, two RARE sequences were used: axial (FOV = 30 × 20 mm, matrix size = 128 × 128 mm, in-plane special resolution = 234 × 156 µm) and sagittal (FOV = 25 × 20 mm, matrix size = 128 × 128 mm, in-plane special resolution = 195 × 156 µm). Spectroscopy was done using the same sequence as for in vitro acquisition with the addition of 9 saturations slices placed according to the two anatomical RARE sequence. For in vivo acquisition, the number of repetitions was 4096 for a total acquisition time of 34 min.

- Spectra analysis

Spectrum were analyzed using TopSpin (Bruker, Ettlingen, Germany). For pH values determination, the chemical shift of γ-ATP was used as an internal reference. The pH for each spectrum was calculated according to the equation:

$$\mathrm{pH} = \mathrm{Ao} + \log\left[(\delta - \delta_{\mathrm{min}})/(\delta_{\mathrm{max}} - \delta)\right] \quad (3)$$

where Ao = 6.8672; δ_{max} = 26.0916 and δ_{min} = 34.6452

2.6. Statistical Analysis

Statistical analysis was performed using GraphPad Prism software (San Diego, CA, USA). pH values before and after treatments were compared by a paired *t*-Student test with $p \leq 0.05$ considered significant. Results are represented as mean ± SE. The number of experiments is provided in each Figure.

3. Results

In vitro, we observed that the exposure of cancer cells (SiHa and 4T1) to UK-5099 (10 µM) for 24 h led to a significant increase in glucose consumption and lactate release in the media as well as a significant increase ECAR as shown in Figure 4. However, there was no significant difference in OCR between control cells and cells exposed to UK-5099 (Figure 4).

Cancers **2021**, *13*, 4278

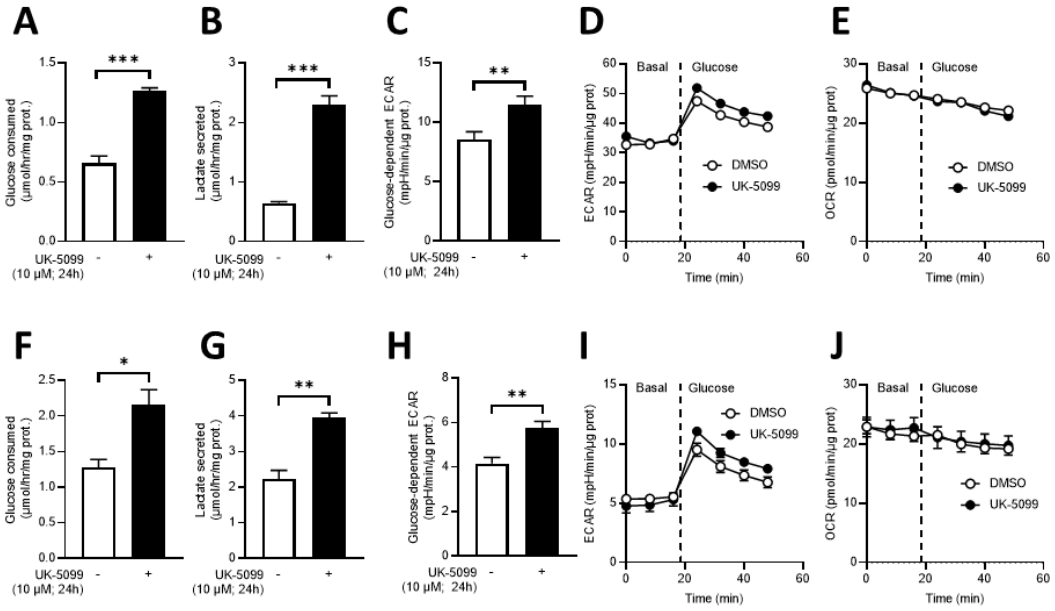


Figure 4. Impact of UK-5099 on metabolic parameters. SiHa (top, (**A**–**E**)) and 4T1 (bottom, (**F**–**J**)) cells were treated for 24 h with 10 µM UK-5099 in glucose-containing medium. Effect of treatment on glucose consumption (**A**,**F**), lactate release (**B**,**G**), extracellular acidification rate (ECAR) (**C**,**H**), time course of extracellular acidification (**D**,**I**) and oxygen consumption rate (OCR) (**E**,**J**). * $p < 0.05$; ** $p < 0.01$; *** $p < 0.001$.

For the in vivo studies, we applied an administration scheme of UK-5099 inspired from a previous work where this compound was shown to radiosensitize tumors [19]. MR protocols were applied on separate cohorts of mice for CEST-MRI and ^{31}P-NMR spectroscopy to avoid any possible interference between the pH reporter probes administered before the MR analysis. The MR protocols were applied before and after 4 days of treatment. Representative distribution of pHe within tumors before and after 4 days of treatment are presented in Figure 5.

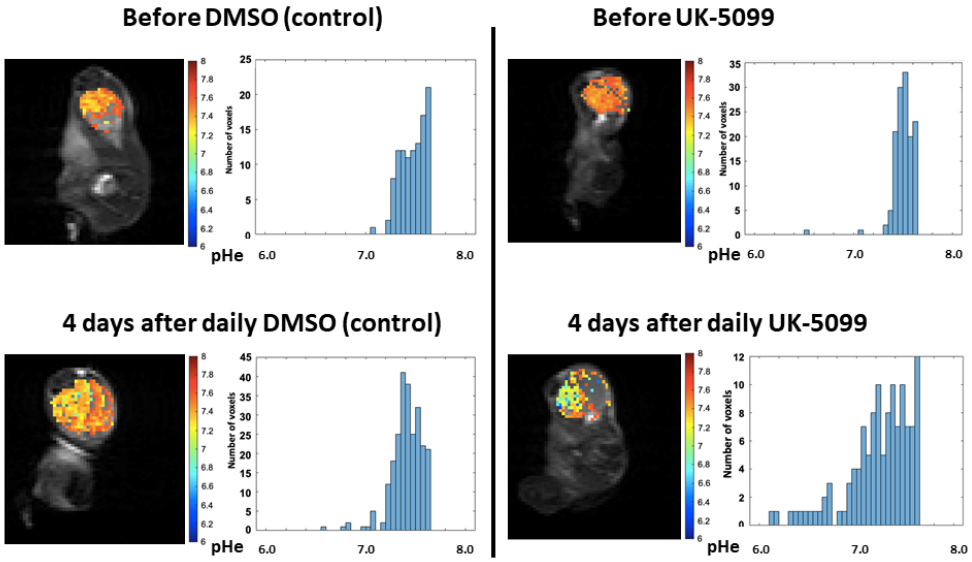


Figure 5. Evolution of pHe evaluated by CEST-MRI. Typical images and histograms of distribution of pHe values recorded before and after vehicle administration (**left**), before and after UK-5099 administration (**right**) (daily IP injection during 4 days, 3 mg/kg). Images are recorded on the same mice. Note that the pHe values remained rather identical in the control group while there is a clear shift in pHe towards more acidic values. Note also the large heterogeneity of pHe values recorded after the UK-5099 treatment.

The analysis of the pooled data recorded on 8 tumors in each group shows that there was no significant change ($p > 0.05$), neither in the mean or in in the median pHe values in the mice injected daily with the vehicle. In contrast, pHe was significantly decreased ($p < 0.05$) in mice daily treated with UK-5099 (Figure 6), with a difference of 0.22 pHe units for the mean values, and 0.20 pHe units for the median values.

The pooled histograms of distribution of pHe values recorded before and after treatment ($n = 8$ mice in each group) are shown in Figure 7. Values are almost superimposable in the control group while there is a clear shift of values towards acidic pHe. This is confirmed by the analysis of the skewness of the distribution which is the measure of the asymmetry of a histogram. The skewness was negative in all cases, the tail being longer on the left side (meaning lower pHe values). The tail towards more acidic values after UK-5099 is clearly seen in Figure 7 (right panel). The number of voxels with a pHe value inferior to 7.0 increased from 1.5% to 16.2% after 4 days of UK-5099 treatment. This means also that a large majority of voxels remained with a pHe superior or equal to 7.0.

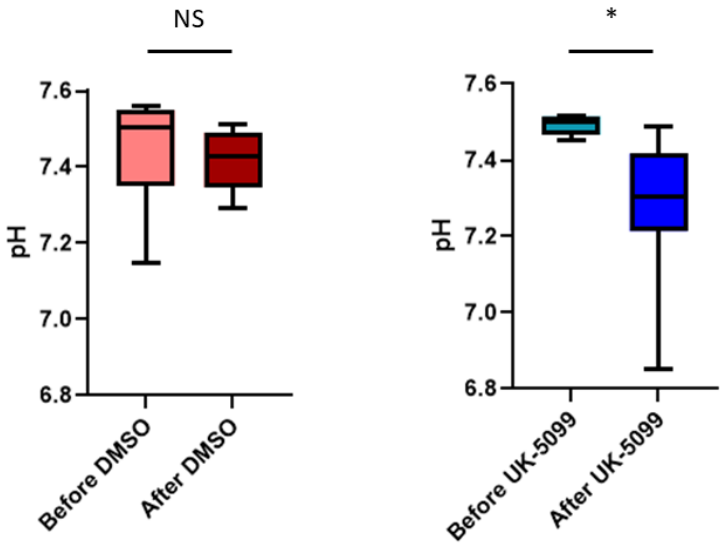


Figure 6. Evolution of pHe (estimated by CEST-MRI) in 4T1 tumors in mice before and after treatment 4 days with DMSO (control) or UK-5099. NS: not significant; *: $p < 0.05$ (paired t-test, $n = 8$ in the DMSO group and $n = 8$ in the UK-5099 group).

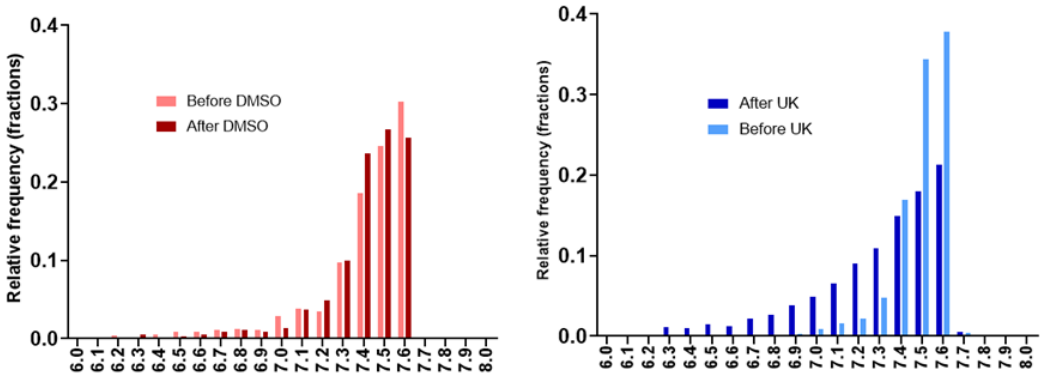


Figure 7. Histograms of distribution all pHe values recorded in individual voxels using CEST-MRI. **Left**: pHe values before (light red) and after (dark red) treatment during 4 days with vehicle. **Right**: pHe values before (light blue) and after (dark blue) treatment during 4 days with UK-5099.

We also tested the evolution of pHe using ^{31}P-NMR spectroscopy using 3-APP as pHe reporter. With this method, we did not find any significant change in pHe values in control and UK-5099 treated mice (Figure 8).

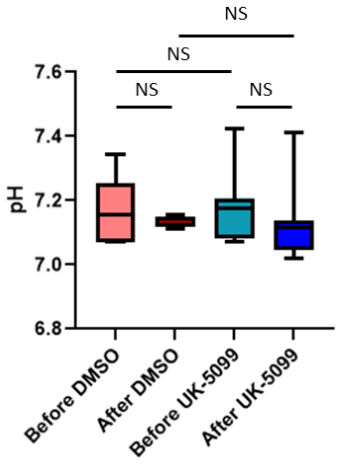


Figure 8. Evolution of pHe (estimated by ^{31}P-NMR spectroscopy) in 4T1 tumors in mice before and after treatment 4 days with DMSO (control) or UK-5099 (NS: not significant, paired *t*-test, $n = 8$ for each group).

4. Discussion

The objective of this study was to evaluate the impact of the MPC inhibitor UK-5099 on the pHe in tumors. Previous observations have shown that 7ACC2, another MPC inhibitor, increased ECAR in several cancer cell lines and that UK-5099 increased lactate release by cancer cells in the presence of glucose [19]. It was also found that the inhibition of cellular lactate influx was an indirect consequence of intracellular pyruvate accumulation [19]. We have first evaluated in vitro the glucose consumption, the lactate secretion and the ECAR in the cervix cancer cell line SiHa and the triple negative breast cancer cell line 4T1. The extents of glucose consumption and lactate release were higher at the basal level for 4T1 cells than for SiHa cells. We observed that the glucose consumption, lactate secretion and acidification rate were significantly increased upon exposure of the cells to UK-5099 10 µM (Figure 4). We did not observe any change in OCR due to UK-5099 exposure (Figure 4). The presence of glutamine in the medium may account for this observation as the absence of change in oxygen consumption may be due to an increase in glutamine utilization. We next aimed to explore the effect of UK-5099 on mouse 4T1 breast tumors in vivo. CEST-MRI revealed that the pHe was significantly decreased after the administration of UK-5099 during 4 days (Figure 6). This effect was rather modest with a shift of 0.22 pHe unit towards acidification. ^{31}P-NMR spectroscopy using 3-APP that is measuring pHe over the whole tumor did not show any significant effect of the treatment (Figure 8). Of note, the presence of residual muscle tissue in the volume sampled by ^{31}P-NMR spectroscopy (as observed by the presence of phosphocreatine in the spectrum, Figure 2) may also account for the inability to detect a pHe change when using this technique. Most importantly, the effect that we did observe using CEST-MRI was highly heterogenous within the tumors, as shown by visualizing the images (Figure 5) or by analyzing the histograms of distribution (Figure 7). Only a small proportion of voxels (16%) shifted towards acidic values (pHe < 7.0), an effect that was sufficient to shift the pHe mean and median values (Figure 6).

Considering the large in vitro effect of MPC inhibition on ECAR (Figure 4), the modest effect observed in vivo using CEST-MRI or even absence of effect using ^{31}P-NMR is somehow surprising. It should be noted that a discrepancy between in vitro and in vivo responses as well as heterogeneity in responses within tumors have already been reported in several studies on tumor metabolism [37–40], highlighting the limitation of in vitro studies to truly reflect the complex tumor behavior. As far as pHe is concerned, difference in pH buffering capacity between in vitro and in vivo conditions may account for our

observations. Indeed, it is likely that tumors exhibit a higher buffering capacity since circulating blood can remove the excess H^+ whereas H^+ released from cultured cancer cells accumulate in the dish. Temporal and regional fluctuations in tumor perfusion may actually also account for the observed heterogeneity in "acidic voxels" upon mouse treatments with UK-5099.

It should also be emphasized that cancer cells do not represent the majority of cells present in the tumor microenvironment (TME). In addition to non-cellular components of extracellular matrix, the TME consists of tumor cells, stromal fibroblasts, endothelial cells and immune cells like microglia, macrophages and lymphocytes [41,42]. Presently, the effect of MPC blockade has not been investigated on all types of cells composing the TME, and we may expect a different impact of treatment on these non-cancerous cells. Another possible contributor to this lower acidification of the TME could be a compensatory mechanism occurring when tumors are treated chronically with an MPC inhibitor. Tumor cells indeed exhibit extraordinary metabolic plasticity to adapt to constraints or changes in their environment [6,43–46]. It has been previously demonstrated that cells may tolerate loss of MPC activity by metabolic rewiring to compensate for the loss of pyruvate oxidation [8]. Among compensatory mechanisms, increase in glutamine utilization [47,48] and pyruvate-alanine cycling [49] have been described when mitochondrial pyruvate transport is impaired. If present, those mechanisms may lead to a lower glycolysis utilization or less transformation of pyruvate into lactate with a consequent lower effect on extracellular acidification.

Finally, our study highlights the high value of using a high-resolution imaging (0.44 µL/voxel) of pHe for monitoring the effect of anti-cancer drugs. While ^{31}P-NMR spectroscopy did not detect any significant change in pHe after UK-5099 treatment (Figure 8), CEST-MRI did reveal a large heterogeneity in response to the exposure to the MPC inhibitor. More importantly, image analysis and histograms distributions of pHe values showed that a small part of the tumors were affected by extracellular acidification (Figures 5 and 7). As discussed earlier, this heterogeneity of response may be the consequence of differences in regional perfusion, distinct responses coming from different cells present in the TME but also from compensatory mechanisms. Further investigation is warranted to identify the most relevant factors influencing pHe.

Of note, the pHe values evaluated before treatment were slightly lower when estimated by ^{31}P-NMR than with CEST-MRI. While ^{31}P-NMR measures the pHe over the whole tumor, our CEST-MRI protocol was done on a single slice through the center of the tumor. Differences in position may possibly account the difference observed between both techniques. It is also worth to mention that the basal pHe values (before treatment) measured in our study for the 4T1 tumor model were higher than 7.0 (for CEST-MRI and ^{31}P-NMR) while a recent study that compared several breast cancer cell lines suggested lower pHe values for the same model (6.96 ± 0.03) [27]. Different experimental conditions may potentially explain these differences: different conditions of cell culture before inoculation and time-window for the MRI study during the tumor growth. We also noticed that the anesthesia used was different: ketamine/xylazine in the reference study [27] and isoflurane in the present study. As ketamine/xylazine is known to induce a rapid drop in tumor perfusion and oxygenation [50–52], we hypothesize that this experimental factor may potentially contribute to subtle difference in glycolytic activity and pHe values recorded for the same tumor model. A possible factor that may also account for differences between the pHe measured and data from the literature relies on our CEST measurements that were done only on post-contrast images as described in [23,30]. More recent papers have used the difference between the CEST contrast after iopamidol injection and the CEST contrast before iopamidol injection, allowing the measurement of the sole CEST contribution due to iopamidol and removing the endogenous one [27,28,31]. We cannot exclude that that the protocol based on the sole post-iopamidol CEST imaging has led to an overestimation of pHe values. In the future, it would be interesting to further evaluate the effect of MPC inhibitors with other pHe imaging modalities such as biosensor

imaging of redundant deviation in shifts (BIRDS). BIRDS is a rapid chemical shift imaging technique in which paramagnetically shifted non-exchangeable protons on DOTA-based macrocyclic complexes are directly detected. While BIRDS is limited so far to pre-clinical studies because the sensors are not yet approved by health agencies, it could be interesting to analyze the impact of MPC inhibitors as the technique has demonstrated its value in cancer animal models [53–56].

5. Conclusions

MPC inhibition led to a moderate acidification of the extracellular medium in vivo. CEST-MRI provided high resolution parametric images of pHe highlighting the heterogeneity of response within the tumor when exposed to UK-5099. Our study adds to the previous demonstration on the utility of longitudinal monitoring of tumor acidosis during anti-cancer treatments [30–32]. As the feasibility of using CEST-MRI has already been demonstrated in patients for pH measurement [28,29,57,58], it is likely that this technology could be useful as imaging biomarker for guidance of treatments targeting tumor metabolism.

Author Contributions: Conceptualization, B.G., N.J., C.B., C.C., O.F.; methodology, C.B., N.J., C.C., O.F., L.M., J.F. and B.G.; software, N.J. and J.F.; validation, C.B., N.J., C.C., O.F. and B.G.; formal analysis, C.B. and N.J.; investigation, C.B. and N.J.; resources, N.J., C.C., O.F., L.M., J.F. and B.G.; writing—original draft preparation, C.B. and B.G.; writing—review and editing, C.B., N.J., C.C., O.F., L.M., J.F. and B.G.; supervision, N.J. and B.G.; project administration, B.G.; funding acquisition, C.C., O.F. and B.G. All authors have read and agreed to the published version of the manuscript.

Funding: This research was funded by Fonds National de la Recherche Scientifique (FNRS J008220F and 7463520) (B.G.), the Foundation against Cancer 2020/074 (O.F.) and the Fonds Joseph Maisin (C.C.). C. Buyse is a Televie Ph.D. student. The study used the facilities of the Nuclear and Electronic Spin Technologies (NEST) platform of UCLouvain.

Institutional Review Board Statement: All experiments involving animals were performed in accordance with the Belgian law concerning the protection and welfare of the animals and were approved by the UCLouvain ethics committee (Agreement reference: 2018/UCL/MD/021).

Informed Consent Statement: Not applicable.

Data Availability Statement: Rough data available on request.

Conflicts of Interest: The authors declare no conflict of interest.

References

1. DeBerardinis, R.J.; Chandel, N.S. Fundamentals of cancer metabolism. *Sci. Adv.* **2016**, *2*, e1600200. [CrossRef]
2. Elia, I.; Doglioni, G.; Fendt, S.M. Metabolic hallmarks of metastasis formation. *Trends Cell Biol.* **2018**, *28*, 673–684. [CrossRef] [PubMed]
3. Gatenby, R.A.; Gillies, R.J. Why do cancers have high aerobic glycolysis? *Nat. Rev. Cancer* **2004**, *4*, 891–899. [CrossRef] [PubMed]
4. Corbet, C.; Feron, O. Tumor acidosis: From the passenger to the driver's seat. *Nat. Rev. Cancer* **2017**, *17*, 577–593. [CrossRef]
5. Wojtkowiak, J.W.; Verduzco, D.; Schramm, K.J.; Gillies, R.J. Drug resistance and cellular adaptation to tumor acidic pH microenvironment. *Mol. Pharm.* **2011**, *8*, 2032–2038. [CrossRef]
6. Schoonjans, C.A.; Joudiou, N.; Brusa, D.; Corbet, C.; Feron, O.; Gallez, B. Acidosis-induced metabolic reprogramming in tumor cells enhances the anti-proliferative activity of the PDK inhibitor dichloroacetate. *Cancer Lett.* **2020**, *470*, 18–28. [CrossRef]
7. Kato, Y.; Ozawa, S.; Miyamoto, C.; Maehata, Y.; Suzuki, A.; Maeda, T.; Baba, Y. Acidic extracellular microenvironment and cancer. *Cancer Cell Int.* **2013**, *13*, 89. [CrossRef] [PubMed]
8. Bender, T.; Martinou, J.C. The mitochondrial pyruvate carrier in health and disease: To carry or not to carry? *Biochim. Biophys. Acta* **2016**, *1863*, 2436–2442. [CrossRef] [PubMed]
9. Buchanan, J.L.; Taylor, E.B. Mitochondrial pyruvate carrier function in health and disease across the lifespan. *Biomolecules* **2020**, *10*, 1162. [CrossRef]
10. Ruiz-Iglesias, A.; Manes, S. The importance of mitochondrial pyruvate carrier in cancer cell metabolism and tumorigenesis. *Cancers* **2020**, *13*, 1488. [CrossRef]
11. Schell, J.C.; Olson, K.A.; Jiang, L.; Hawkins, A.J.; Van Vranken, J.G.; Xie, J.; Egnatchik, R.A.; Earl, E.G.; DeBerardinis, R.J.; Rutter, J. A role for the mitochondrial pyruvate carrier as a repressor of the Warburg effect and colon cancer cell growth. *Mol. Cell* **2014**, *56*, 400–413. [CrossRef]

12. Tai, Y.; Cao, F.; Li, M.; Li, P.; Xu, T.; Wang, X.; Yu, Y.; Gu, B.; Yu, X.; Cai, X.; et al. Enhanced mitochondrial pyruvate transport elicits a robust ROS production to sensitize the antitumor efficacy of interferon-gamma in colon cancer. *Redox. Biol.* **2019**, *20*, 451–457. [CrossRef]
13. Zhong, Y.; Li, X.; Yu, D.; Li, X.; Li, Y.; Long, Y.; Yuan, Y.; Ji, Z.; Zhang, M.; Wen, J.G.; et al. Application of mitochondrial pyruvate carrier blocker UK5099 creates metabolic reprogram and greater stem-like properties in LnCap prostate cancer cells in vitro. *Oncotarget* **2015**, *6*, 37758–37769. [CrossRef] [PubMed]
14. Li, X.; Ji, Y.; Han, G.; Li, X.; Fan, Z.; Li, Y.; Zhong, Y.; Cao, J.; Zhao, J.; Zhang, M.; et al. MPC1 and MPC2 expressions are associated with favorable clinical outcomes in prostate cancer. *BMC Cancer* **2016**, *16*, 894. [CrossRef]
15. Tang, X.P.; Chen, Q.; Li, Y.; Wang, Y.; Zou, H.B.; Fu, W.J.; Niu, Q.; Pan, Q.G.; Jiang, P.; Xu, X.S.; et al. Mitochondrial pyruvate carrier 1 functions as a tumor suppressor and predicts the prognosis of human renal cell carcinoma. *Lab. Investig.* **2019**, *99*, 191–199. [CrossRef]
16. Koh, E.; Kim, Y.K.; Shin, D.; Kim, K.S. MPC1 is essential for PGC-1alpha-induced mitochondrial respiration and biogenesis. *Biochem. J.* **2018**, *475*, 1687–1699. [CrossRef]
17. Park, S.; Safi, R.; Liu, X.; Baldi, R.; Liu, W.; Liu, J.; Locasale, J.W.; Chang, C.Y.; McDonnell, D.P. Inhibition of ERRalpha Prevents Mitochondrial Pyruvate Uptake Exposing NADPH-Generating Pathways as Targetable Vulnerabilities in Breast Cancer. *Cell Rep.* **2019**, *27*, 3587–3601. [CrossRef] [PubMed]
18. Jung, K.H.; Lee, J.H.; Park, J.W.; Moon, S.H.; Cho, Y.S.; Lee, K.H. Troglitazone exerts metabolic and antitumor effects on T47D breast cancer cells by suppressing mitochondrial pyruvate availability. *Oncol. Rep.* **2020**, *43*, 711–717. [CrossRef] [PubMed]
19. Corbet, C.; Bastien, E.; Draoui, N.; Doix, B.; Mignion, L.; Jordan, B.F.; Marchand, A.; Vanherck, J.C.; Chaltin, P.; Schakman, O.; et al. Interruption of lactate uptake by inhibiting mitochondrial pyruvate transport unravels direct antitumor and radiosensitizing effects. *Nat. Commun.* **2018**, *9*, 1208. [CrossRef] [PubMed]
20. Anemone, A.; Consolino, L.; Arena, F.; Capozza, M.; Longo, D.L. Imaging tumor acidosis: A survey of the available techniques for mapping in vivo tumor pH. *Cancer Metastasis Rev.* **2019**, *38*, 25–49. [CrossRef] [PubMed]
21. Consolino, L.; Anemone, A.; Capozza, M.; Carella, A.; Irrera, P.; Corrado, A.; Dhakan, C.; Bracesco, M.; Longo, D.L. Non-invasive investigation of tumor metabolism and acidosis by MRI-CEST imaging. *Front. Oncol.* **2020**, *10*, 161. [CrossRef]
22. Chen, L.Q.; Pagel, M.D. Evaluating pH in the extracellular tumor microenvironment using CEST MRI and other imaging methods. *Adv. Radiol.* **2015**, 206405. [CrossRef] [PubMed]
23. Chen, L.Q.; Randtke, E.A.; Jones, K.M.; Moon, B.F.; Howison, C.M.; Pagel, M.D. Evaluations of tumor acidosis within in vivo tumor models using parametric maps generated with Acido CEST MRI. *Mol. Imaging Biol.* **2015**, *17*, 488–496. [CrossRef] [PubMed]
24. Jones, K.M.; Randtke, E.A.; Howison, C.M.; Pagel, M.D. Respiration gating and Bloch fitting improve pH measurements with acidoCEST MRI in an ovarian orthotopic tumor model. *Proc. SPIE Int. Soc. Opt. Eng.* **2016**, *9788*, 978815. [PubMed]
25. Randtke, E.A.; Granados, J.C.; Howison, C.M.; Pagel, M.D.; Cardenas-Rodriguez, J. Multislice CEST MRI improves the spatial assessment of tumor pH. *Magn. Reason. Med.* **2017**, *78*, 97–106. [CrossRef]
26. Lindeman, L.R.; Randtke, E.A.; High, R.A.; Jones, K.M.; Howison, C.M.; Pagel, M.D. A comparison of exogenous and endogenous CEST MRI methods for evaluating in vivo pH. *Magn. Reason. Med.* **2018**, *79*, 2766–2772. [CrossRef] [PubMed]
27. Anemone, A.; Consolino, L.; Conti, L.; Irrera, P.; Hsu, M.Y.; Villano, D.; Dastru, W.; Porporato, P.E.; Cavallo, F.; Longo, D.L. Tumour acidosis evaluated in vivo by MRI-CEST pH imaging reveals breast cancer metastatic potential. *Br. J. Cancer* **2021**, *124*, 207–216. [CrossRef] [PubMed]
28. Jones, K.M.; Randtke, E.A.; Yoshimaru, E.S.; Howison, C.M.; Chalasani, P.; Klein, R.R.; Chambers, S.K.; Kuo, P.H.; Pagel, M.D. Clinical translation of tumor acidosis measurements with AcidoCEST MRI. *Mol. Imaging Biol.* **2017**, *19*, 617–625. [CrossRef]
29. Krikken, E.; van der Kemp, W.J.M.; Khlebnikov, V.; van Dalen, T.; Los, M.; van Laarhoven, H.W.M.; Luijten, P.R.; van den Bosch, M.A.A.J.; Klomp, D.W.J.; Wijnen, J.P. Contradiction between amide-CEST signal and pH in breast cancer explained with metabolic MRI. *NMR Biomed.* **2019**, *32*, e4110. [CrossRef]
30. Chen, L.Q.; Howison, C.M.; Jeffery, J.J.; Robey, I.F.; Kuo, P.H.; Pagel, M.D. Evaluations of extracellular pH within in vivo tumors using acidoCEST MRI. *Magn. Reason. Med.* **2014**, *72*, 1408–1417. [CrossRef]
31. Longo, D.L.; Bartoli, A.; Consolino, L.; Bardini, P.; Arena, F.; Schwaiger, M.; Aime, S. In vivo imaging of tumor metabolism and acidosis by combining PET and MRI-CEST pH imaging. *Cancer Res.* **2016**, *76*, 6463–6470. [CrossRef]
32. Anemone, A.; Consolino, L.; Conti, L.; Reineri, F.; Cavallo, F.; Aime, S.; Longo, D.L. In vivo evaluation of tumour acidosis for assessing the early metabolic response and onset of resistance to dichloroacetate by using magnetic resonance pH imaging. *Int. J. Oncol.* **2017**, *51*, 498–506. [CrossRef] [PubMed]
33. Gillies, R.J.; Liu, Z.; Bhujwalla, Z. ^{31}P-MRS measurements of extracellular pH of tumors using 3-aminopropylphosphonate. *Am. J. Physiol.* **1994**, *267*, C195–C203. [CrossRef]
34. McCoy, C.L.; Parkins, C.S.; Chaplin, D.J.; Griffiths, J.R.; Rodrigues, L.M.; Stubbs, M. The effect of blood flow modification on intra- and extracellular pH measured by ^{31}P magnetic resonance spectroscopy in murine tumours. *Br. J. Cancer.* **1995**, *72*, 905–911. [CrossRef] [PubMed]
35. Raghunand, N.; Mahoney, B.; van Sluis, R.; Baggett, B.; Gillies, R.J. Acute metabolic alkalosis enhances response of C3H mouse mammary tumors to the weak base mitoxantrone. *Neoplasia* **2001**, *3*, 227–235. [CrossRef] [PubMed]

36. Lutz, N.W.; Le Fur, Y.; Chiche, J.; Pouyssegur, J.; Cozzone, P.J. Quantitative in vivo characterization of intracellular and extracellular pH profiles in heterogeneous tumors: A novel method enabling multiparametric pH analysis. *Cancer Res.* **2013**, *73*, 4616–4628. [CrossRef] [PubMed]
37. Hensley, C.T.; Faubert, B.; Yuan, Q.; Lev-Cohain, N.; Jin, E.; Kim, J.; Jiang, L.; Ko, B.; Skelton, R.; Loudat, L.; et al. Metabolic Heterogeneity in Human Lung Tumors. *Cell* **2016**, *164*, 681–694. [CrossRef]
38. Davidson, S.M.; Papagiannakopoulos, T.; Olenchock, B.A.; Heyman, J.E.; Keibler, M.A.; Luengo, A.; Bauer, M.R.; Jha, A.K.; O'Brien, J.P.; Pierce, K.A.; et al. Environment Impacts the Metabolic Dependencies of Ras-Driven Non-Small Cell Lung Cancer. *Cell Metab.* **2016**, *23*, 517–528. [CrossRef]
39. Neveu, M.A.; De Preter, G.; Marchand, V.; Bol, A.; Brender, J.R.; Saito, K.; Kishimoto, S.; Porporato, P.E.; Sonveaux, P.; Grégoire, V.; et al. Multimodality Imaging Identifies Distinct Metabolic Profiles In Vitro and In Vivo. *Neoplasia* **2016**, *18*, 742–752. [CrossRef] [PubMed]
40. Gui, D.Y.; Sullivan, L.B.; Luengo, A.; Hosios, A.M.; Bush, L.N.; Gitego, N.; Davidson, S.M.; Freinkman, E.; Thomas, C.J.; Vander Heiden, M.G. Environment Dictates Dependence on Mitochondrial Complex I for NAD+ and Aspartate Production and Determines Cancer Cell Sensitivity to Metformin. *Cell Metab.* **2016**, *24*, 716–727. [CrossRef]
41. Hanahan, D.; Coussens, L.M. Accessories to the crime: Functions of cells recruited to the tumor microenvironment. *Cancer Cell.* **2012**, *21*, 309–322. [CrossRef] [PubMed]
42. Baghban, R.; Roshangar, L.; Jahanban-Esfahlan, R.; Seidi, K.; Ebrahimi-Kalan, A.; Jaymand, M.; Kolahian, S.; Javaheri, T.; Zare, P. Tumor microenvironment complexity and therapeutic implications at a glance. *Cell Commun. Signal.* **2020**, *18*, 59. [CrossRef]
43. Schiliro, C.; Firestein, B.L. Mechanisms of Metabolic Reprogramming in Cancer Cells Supporting Enhanced Growth and Proliferation. *Cells* **2021**, *10*, 1056. [CrossRef] [PubMed]
44. Schoonjans, C.A.; Gallez, B. Metabolic Plasticity of Tumor Cells: How They Do Adapt to Food Deprivation. *Adv. Exp. Med. Biol.* **2020**, *1219*, 109–123. [PubMed]
45. Shuvalov, O.; Daks, A.; Fedorova, O.; Petukhov, A.; Barlev, N. Linking Metabolic Reprogramming, Plasticity and Tumor Progression. *Cancers* **2021**, *13*, 762. [CrossRef]
46. Bergers, G.; Fendt, S.M. The metabolism of cancer cells during metastasis. *Nat. Rev. Cancer* **2021**, *21*, 162–180. [CrossRef]
47. Vacanti, N.M.; Divakaruni, A.S.; Green, C.R.; Parker, S.J.; Henry, R.R.; Ciaraldi, T.P.; Murphy, A.N.; Metallo, C.M. Regulation of substrate utilization by the mitochondrial pyruvate carrier. *Mol. Cell.* **2014**, *56*, 425–435. [CrossRef]
48. Yang, C.; Ko, B.; Hensley, C.T.; Jiang, L.; Wasti, A.T.; Kim, J.; Sudderth, J.; Calvaruso, M.A.; Lumata, L.; Mitsche, M.; et al. Glutamine oxidation maintains the TCA cycle and cell survival during impaired mitochondrial pyruvate transport. *Mol. Cell.* **2014**, *56*, 414–424. [CrossRef]
49. McCommis, K.S.; Chen, Z.; Fu, X.; McDonald, W.G.; Colca, J.R.; Kletzien, R.F.; Burgess, S.C.; Finck, B.N. Loss of mitochondrial pyruvate carrier 2 in the liver leads to defects in gluconeogenesis and compensation via pyruvate-alanine cycling. *Cell Metab.* **2015**, *22*, 682–694. [CrossRef] [PubMed]
50. Menke, H.; Vaupel, P. Effect of injectable or inhalational anesthetics and of neuroleptic, neuroleptanalgesic, and sedative agents on tumor blood flow. *Radiat. Res.* **1988**, *114*, 64–76. [CrossRef]
51. Hou, H.; Grinberg, O.Y.; Taie, S.; Leichtweis, S.; Miyake, M.; Grinberg, S.; Xie, H.; Csete, M.; Swartz, H.M. Electron paramagnetic resonance assessment of brain tissue oxygen tension in anesthetized rats. *Anesth. Analg.* **2003**, *96*, 1467–1472. [CrossRef]
52. Baudelet, C.; Gallez, B. Effect of anesthesia on the signal intensity in tumors using BOLD-MRI: Comparison with flow measurements by Laser Doppler flowmetry and oxygen measurements by luminescence-based probes. *Magn. Reason. Imag.* **2004**, *22*, 905–912. [CrossRef] [PubMed]
53. Coman, D.; Huang, Y.; Rao, J.U.; De Feyter, H.M.; Rothman, D.L.; Juchem, C.; Hyder, F. Imaging the intratumoral-peritumoral extracellular pH gradient of gliomas. *NMR Biomed.* **2016**, *29*, 309–319. [CrossRef] [PubMed]
54. Huang, Y.; Coman, D.; Herman, P.; Rao, J.U.; Maritim, S.; Hyder, F. Towards longitudinal mapping of extracellular pH in gliomas. *NMR Biomed.* **2016**, *29*, 1364–1372. [CrossRef] [PubMed]
55. Rao, J.U.; Coman, D.; Walsh, J.J.; Ali, M.M.; Huang, Y.; Hyder, F. Temozolomide arrests glioma growth and normalizes intratumoral extracellular pH. *Sci. Rep.* **2017**, *7*, 7865. [CrossRef]
56. Coman, D.; Peters, D.C.; Walsh, J.J.; Savic, L.J.; Huber, S.; Sinusas, A.J.; Lin, M.; Chapiro, J.; Constable, R.T.; Rothman, D.L.; et al. Extracellular pH mapping of liver cancer on a clinical 3T MRI scanner. *Magn. Reason. Med.* **2020**, *83*, 1553–1564. [CrossRef]
57. Müller-Lutz, A.; Khalil, N.; Schmitt, B.; Jellus, V.; Pentang, G.; Oeltzschner, G.; Antoch, G.; Lanzman, R.S.; Wittsack, H.J. Pilot study of Iopamidol-based quantitative pH imaging on a clinical 3T MR scanner. *MAGMA* **2014**, *27*, 477–485. [CrossRef]
58. Tang, Y.; Xiao, G.; Shen, Z.; Zhuang, C.; Xie, Y.; Zhang, X.; Yang, Z.; Guan, J.; Shen, Y.; Chen, Y.; et al. Noninvasive Detection of Extracellular pH in Human Benign and Malignant Liver Tumors Using CEST MRI. *Front. Oncol.* **2020**, *10*, 578985. [CrossRef] [PubMed]

2. Evaluation of Syrosingopine, an MCT Inhibitor, as Potential Modulator of Tumor Metabolism and Extracellular Acidification

Published in *Metabolites*, 2022, 12, 557

Buyse, C.; Joudiou, N.; Warscotte, A.; Richiardone, E.; Mignion, L.; Corbet, C.; Gallez, B.

doi: 10.3390/metabo12060557

metabolites

MDPI

Article

Evaluation of Syrosingopine, an MCT Inhibitor, as Potential Modulator of Tumor Metabolism and Extracellular Acidification

Chloe Buyse [1], Nicolas Joudiou [2], Aude Warscotte [1], Elena Richiardone [3], Lionel Mignion [1], Cyril Corbet [3] and Bernard Gallez [1,*]

[1] Louvain Drug Research Institute, Biomedical Magnetic Resonance (REMA), Université Catholique de Louvain (UCLouvain), 1200 Brussels, Belgium; chloe.buyse@uclouvain.be (C.B.); aude.warscotte@student.uclouvain.be (A.W.); lionel.mignion@uclouvain.be (L.M.)
[2] Louvain Drug Research Institute, Nuclear and Electron Spin Technologies (NEST) Platform, Université Catholique de Louvain (UCLouvain), 1200 Brussels, Belgium; nicolas.joudiou@uclouvain.be
[3] Pole of Pharmacology and Therapeutics (FATH), Institut de Recherche Expérimentale et Clinique (IREC), Université Catholique de Louvain (UCLouvain), 1200 Brussels, Belgium; elena.richiardone@uclouvain.be (E.R.); cyril.corbet@uclouvain.be (C.C.)
* Correspondence: bernard.gallez@uclouvain.be

Abstract: Extracellular acidification has been shown to be an important characteristic of invasive tumors, as it promotes invasion and migration but also resistance to treatments. Targeting transporters involved in the regulation of tumor pH constitutes a promising anti-tumor approach, as it would disrupt cellular pH homeostasis and negatively impact tumor growth. In this study, we evaluated the impact of syrosingopine, an inhibitor of MCT1 and MCT4, as a modulator of tumor metabolism and extracellular acidification in human breast cancer (MDA-MB-231) and pharyngeal squamous cell carcinoma (FaDu) cell models. In both models in vitro, we observed that exposure to syrosingopine led to a decrease in the extracellular acidification rate, intracellular pH, glucose consumption, lactate secretion and tumor cell proliferation with an increase in the number of late apoptotic/necrotic cells. However, in vivo experiments using the MDA-MB-231 model treated with a daily injection of syrosingopine did not reveal any significant change in extracellular pH (pHe) (as measured using CEST-MRI) or primary tumor growth. Overall, our study suggests that targeting MCT could lead to profound changes in tumor cell metabolism and proliferation, and it warrants further research to identify candidates without off-target effects.

Keywords: tumor metabolism; pHe; proliferation; MCT; CEST-MRI; syrosingopine

check for updates

Citation: Buyse, C.; Joudiou, N.; Warscotte, A.; Richiardone, E.; Mignion, L.; Corbet, C.; Gallez, B. Evaluation of Syrosingopine, an MCT Inhibitor, as Potential Modulator of Tumor Metabolism and Extracellular Acidification. *Metabolites* **2022**, *12*, 557. https://doi.org/10.3390/metabo12060557

Academic Editors: Oliver Bathe and Rattner Jodi

Received: 30 May 2022
Accepted: 16 June 2022
Published: 17 June 2022

Publisher's Note: MDPI stays neutral with regard to jurisdictional claims in published maps and institutional affiliations.

Copyright: © 2022 by the authors. Licensee MDPI, Basel, Switzerland. This article is an open access article distributed under the terms and conditions of the Creative Commons Attribution (CC BY) license (https://creativecommons.org/licenses/by/4.0/).

1. Introduction

Altered glucose metabolism is considered a hallmark of cancer [1]. Elevated glycolysis and lactate production are often found in tumor cells and persist even under normoxic conditions [2]. This upregulated glucose consumption leads to the production of a large amount of lactate and protons, which can result in extracellular acidosis when wash-out of the latter is impaired due to a dysfunctional tumor vasculature [3]. Extracellular acidification has been shown to be an important characteristic of invasive tumors, as it promotes invasion and migration but also resistance to treatments [4–6]. As variations in intracellular pH (pHi) can influence the ionization and function of diverse proteins, ultimately leading to cell death, cells need to fight against intracellular acidification [7]. Several transporters and proteins are involved in the regulation of tumor pH. Their expression and/or activity are increased by intracellular acidification and the activation of hypoxia-inducible factor-1 (HIF-1) [7]. The most commonly described pH regulators include carbonic anhydrases 2, 9 and 12 (CAII, CAIX and CAXII, respectively); Na^+/H^+ exchanger 1 (NHE1); Na^+/HCO_3^- co-transporters (NBCs); and monocarboxylate transporters MCT1, MCT2, MCT3 and MCT4 [8]. Targeting one or more of these transporters constitutes a promising

anti-tumor approach, as it would disrupt pH homeostasis and possibly negatively impact tumor growth [8]. Preclinical and some clinical studies have shown that targeting acidity can improve therapeutic responses [9]. Proton-pump inhibitors (PPIs), such as omeprazole, are well-tolerated antiacids and have been used to decrease tumor acidity, suppress tumor growth in mouse models and overcome acid-related chemoresistance [7,10,11]. Targeting CAIX has also received consideration because CAIX is usually overexpressed in the majority of solid tumors. Studies have shown that CAIX inhibition might reduce tumor cell proliferation, invasion and migration [12].

Monocarboxylate transporters are lactate/H^+ symporters, playing a major role in H^+ and lactate efflux and pH homeostasis regulation. There are 14 identified MCT isoforms, with two of them, MCT1 and MCT4, being associated with cancer aggressiveness and poor prognosis [13,14]. MCT1 and MCT4 are important actors in the metabolic symbiosis between glycolytic and oxidative tumor cells, where both cell types rely on each other to regulate their energy metabolites [15]. Sonveaux et al. [15] showed that MCT1 inhibition led to a metabolic switch from lactate-fueled respiration to glycolysis, induced cell death in hypoxic/glycolytic tumor cells and increased tumor radiosensitization. The pharmacological or genetic ablation of MCT1 or MCT4 activity led to reduced proliferation in vitro and in vivo [16]. Benjamin et al. [17,18] reported that lactate and H^+ efflux could be inhibited by syrosingopine. Syrosingopine is an antihypertensive reserpine derivative, also known to inhibit MCT1 and MCT4, with a 60-fold higher potency on MCT4. They found that syrosingopine, combined with metformin, an inhibitor of the mitochondrial NADH dehydrogenase, had interesting anti-cancer properties in HL60 (promyelocytic leukemia), OPM2 (multiple myeloma) and HT1080 (fibrosarcoma) cells. They reported that the association between syrosingopine and metformin was able to induce the loss of NAD^+ regeneration capacity in tumor cells, which is required for the ATP-generating steps of glycolysis. This resulted in a glycolysis blockade, leading to ATP depletion and cell death.

In the present study, our goal was to characterize the effects of syrosingopine alone as an MCT1 and MCT4 inhibitor on different metabolic processes in vitro, including extracellular acidification rate (ECAR), glucose metabolism, intra- and extra-cellular pH (pHi and pHe, respectively), cell proliferation and viability. As we could anticipate differential effects depending on the metabolic phenotypes, these effects were evaluated in the MDA-MB-231 glycolytic breast cancer model and in the oxidative FaDu squamous cell carcinoma of the hypopharynx [15,19,20]. As effects were more important in the breast cancer model, the impact of syrosingopine on pHe was also evaluated in vivo in the MDA-MB-231 tumor model, using non-invasive Chemical Exchange Saturation Transfer (CEST)-MRI [3,21,22].

2. Results

2.1. MCT1 and MCT4 Expressions in MDA-MB-231 and FaDu Cells

The basal expressions of MCT1 and MCT4 were evaluated in MDA-MB-231 and FaDu cells. We observed that MCT4 was expressed in both cell lines, while MCT1 was only expressed in FaDu cells (Figure 1). These results are in accordance with a study conducted by Hussien in 2011, where they showed that MCT1 is silenced by gene methylation in human breast cancer cell lines [23].

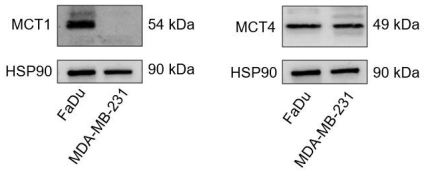


Figure 1. Western blot of MCT1 and MCT4 in FaDu and MDA-MB-231 cells. HSP90 was used as loading control.

2.2. Exposure to Syrosingopine Reduces the Extracellular Acidification Rate and Induces Intracellular Acidification in Cancer Cells

The influence of treatment with syrosingopine on the extracellular acidification rate (ECAR) and intracellular acidification was first assessed.

As a consequence of MCT inhibition, we found that exposure to increasing concentrations of syrosingopine induced a significant reduction in the extracellular acidification rate (ECAR) in MDA-MB-231 cells (Figure 2A). The decrease in ECAR was stable over time when the experiments were repeated with cells treated with 10 µM, with no difference between an exposition of 24 or 72 h (data not shown). For the more oxidative FaDu model, a significant decrease in ECAR was observed after treatment with 25 µM of syrosingopine (Figure 2C). No differences were observed when FaDu cells were treated for 24–48 or 72 h with 10 µM of syrosingopine (data not shown). Intracellular pH values were not impacted significantly after 24 h of treatment (data not shown). Reduced pHi values were observed, starting at 50 µM for MDA-MB-231 cells and 25 µM for FaDu when cells were treated for 72 h (Figure 2B–D).

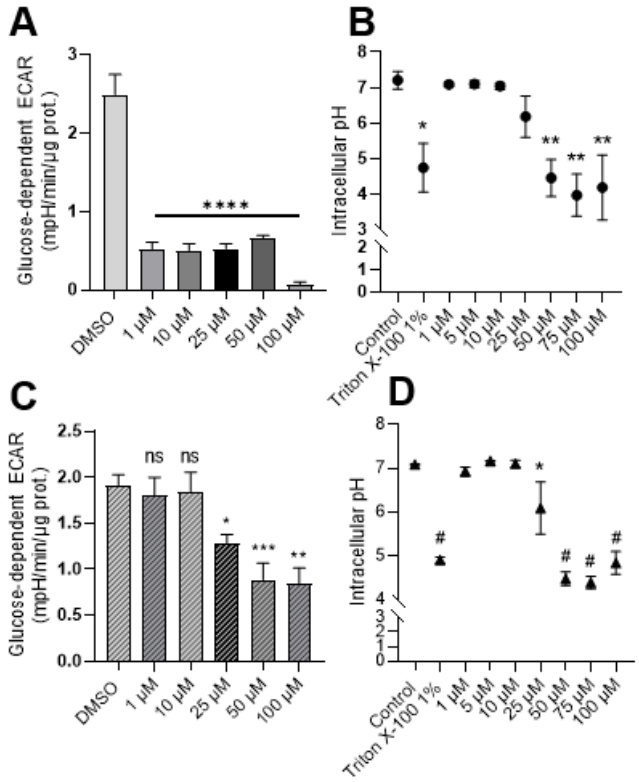


Figure 2. Syrosingopine reduces the extracellular acidification rate (ECAR) and decreases intracellular pH in cancer cells. Glucose-dependent ECAR was determined using the Seahorse XF96 bioenergetic analyzer in MDA-MB-231 (**A**) and FaDu cells (**C**) after 24 h of treatment with increasing concentrations of syrosingopine. Intracellular pH values were measured in MDA-MB-231 (**B**) and FaDu cells (**D**) after 72 h of treatment with increasing concentrations of syrosingopine. Data are represented as mean ± SEM of at least three independent experiments. Significance was determined using one-way or two-way ANOVA: * $p < 0.05$; ** $p < 0.01$; *** $p < 0.001$; # = **** $p < 0.0001$. ns = not significant.

We found that syrosingopine had an impact on ECAR after 24 h, while changes in intracellular pH values were observed only after 72 h.

2.3. Metabolic Shifts after Exposure to Syrosingopine and Consequences on Proliferation and Viability

To evaluate the impact of changes in intra- and extra-cellular pH, we analyzed the effect of syrosingopine on glucose metabolism, cell proliferation, cell viability and apoptosis.

Glucose consumption and lactate secretion were assessed upon direct measurements of metabolite concentrations in the extracellular medium of FaDu and MDA-MB-231 cancer cells treated for 24, 48 and 72 h with 10 µM syrosingopine. Significant reductions in glucose consumption and lactate secretion were observed in MDA-MB-231 (Figure 3A,B) but not in FaDu cells (Figure 3C,D).

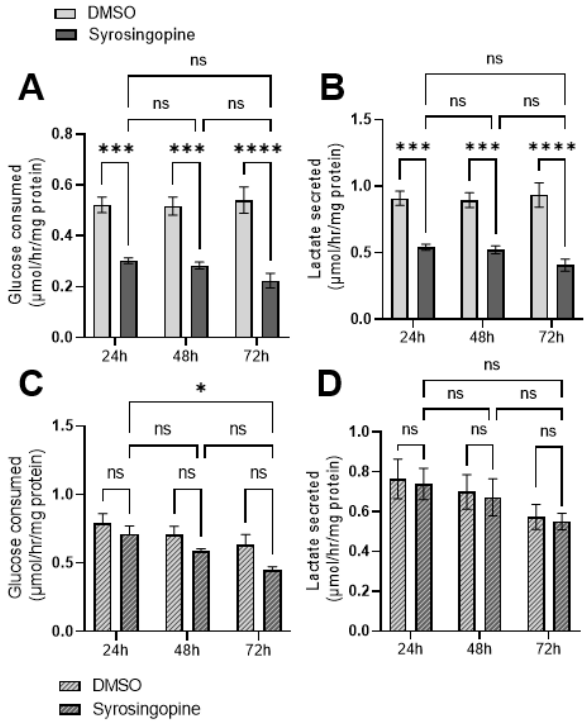


Figure 3. Impact of syrosingopine on glucose consumption and lactate secretion. Glucose consumption and lactate secretion in MDA-MB-231 (**A**,**B**) and FaDu (**C**,**D**) cell lines. Cells were treated for 24, 48 and 72 h with 10 µM of syrosingopine. Data are represented as mean ± SEM of at least three independent experiments. Significance was determined using two-way ANOVA: * $p < 0.05$; *** $p < 0.001$; **** $p < 0.0001$. ns = not significant.

Cell proliferation was assessed using a bromodeoxyuridine (BrdU) proliferation assay. BrdU is a synthetic analogue of thymidine, which can be incorporated into cells during the S phase of the cell cycle. We observed that proliferation was significantly reduced when cells were treated for 72 h with increasing concentrations of syrosingopine, starting at 5 µM for MDA-MB-231 and 25 µM for FaDu cells (Figure 4A–D).

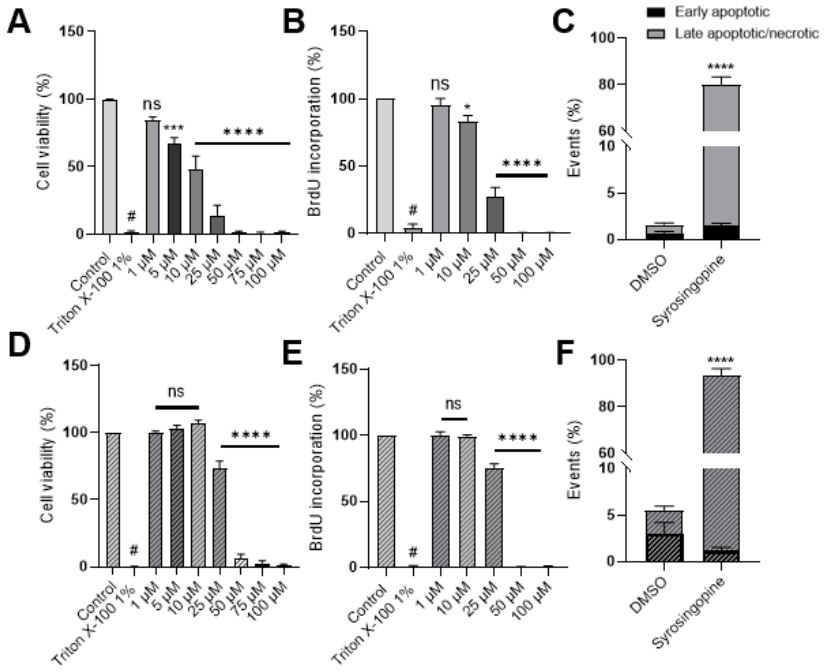


Figure 4. Impact of syrosingopine on tumor cell viability and proliferation. MDA-MB-231 (top, **A**–**C**) and FaDu (bottom, **D**–**F**) cells were treated with syrosingopine for 24, 48 and 72 h. Cell viability (**A**,**D**) and proliferation (**B**,**E**) are represented after 72 h of treatment. Percentages of early apoptotic/necrotic cells were calculated after treatment with 25 µM of syrosingopine for 72 h (**C**,**F**). Data are represented as mean ± SEM of at least three independent experiments. Significance was determined using one-way or two-way ANOVA: * $p < 0.05$; *** $p < 0.001$; # = **** $p < 0.0001$. ns = not significant.

A Presto Blue assay was used to determine the effect on cell viability. This test is based on the reduction of the weakly fluorescent dye resazurin to highly fluorescent resorufin by cell mitochondria. Cell viability can thus be extrapolated from the fluorescence signal. Viability was impacted, starting at a concentration of 5 µM syrosingopine for MDA-MB-231 and 25 µM for FaDu cells (Figure 4B–E).

Fluorescence-Activated Cell Sorting (FACS) using propidium iodine and Annexin V was performed at 10 µM and 25 µM. Treatment with 10 µM for 72 h did not affect cell mortality, as we did not observe any difference between control or treated cells (data not shown). However, when cells were treated with 25 µM, an increase in the percentage of late apoptotic and/or necrotic cells was noticed, after 72 h (Figure 4C–F).

Syrosingopine impacts glucose metabolism, as well as cell viability, cell proliferation and apoptosis.

2.4. In Vivo pHe Measurements with CEST-MRI

As the effects of syrosingopine on tumor cell proliferation were more pronounced on MDA-MB-231 cells than on FaDu cells, in vivo studies were carried out on the MDA-MB-231 tumor model to measure potential changes in pHe and in tumor growth. CEST-MRI was applied using a protocol adapted from our previous work on mitochondrial pyruvate carrier (MPC) inhibition [24]. The administration pattern of syrosingopine was inspired by the work of Benjamin et al. [17,18]. The MR protocols were applied before and after 4 days of treatment with syrosingopine (5 mg/kg body weight, daily administration) or vehicle (DMSO). The distribution of pHe values before and after treatment is presented in Figure 5.

Ten tumors were analyzed in each group. Acquisitions were acquired before and after the injection of iopamidol, used as a pH-sensitive CEST contrast agent.

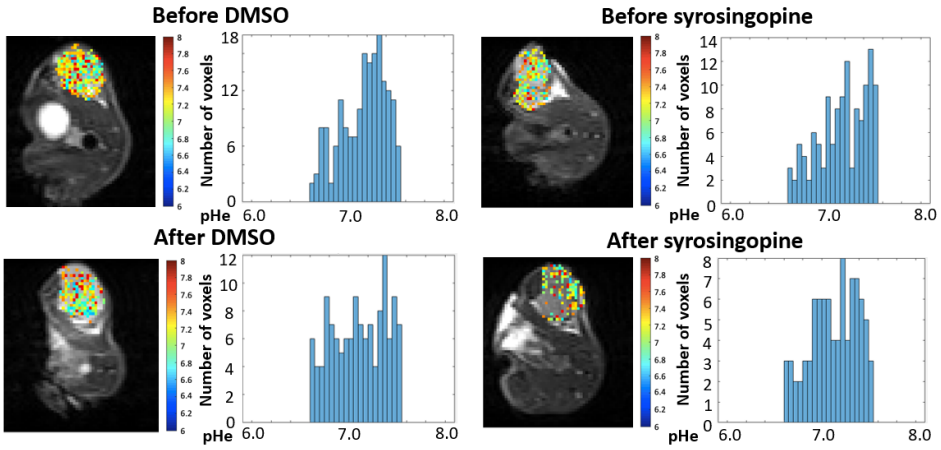


Figure 5. Impact of syrosingopine on tumor pHe. The evolution of pHe was evaluated using CEST-MRI in MDA-MB-231 tumor xenografts. Typical images and histograms of distribution of pHe values recorded before and after vehicle administration (**left**), and before and after syrosingopine administration (**right**) (daily IP injection over 4 days, 5 mg/kg). Images were acquired from the same mice.

We did not observe any significant difference in the mean or median values between the treated and control groups (Figure 6). The histograms of the pHe distribution show that the pHe values are similar before and after treatment in both groups. Besides the MRI analysis, we studied the effects of treatment with syrosingopine on tumor growth. We did not observe different growth patterns between the groups (Figure 7A). There was also no difference in survival between the two groups (Figure 7B).

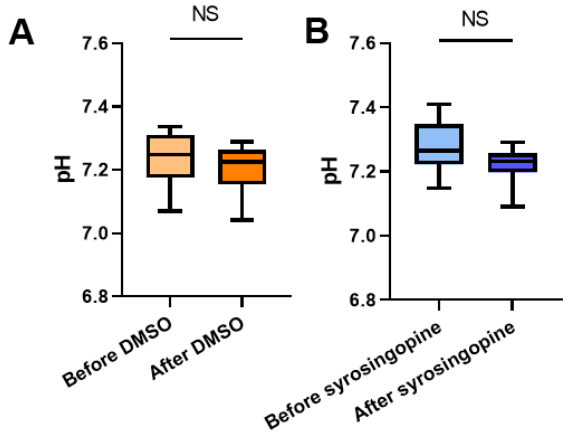


Figure 6. Impact of syrosingopine on tumor pHe. Evolution of pHe (estimated using CEST-MRI) in MDA-MB-231 tumors in mice before and after 4 days of treatment with DMSO (control, (**A**)) or syrosingopine (**B**). Data are represented as mean ± SEM. Significance was determined using Paired *t*-test; $n = 10$ in both groups. NS = not significant.

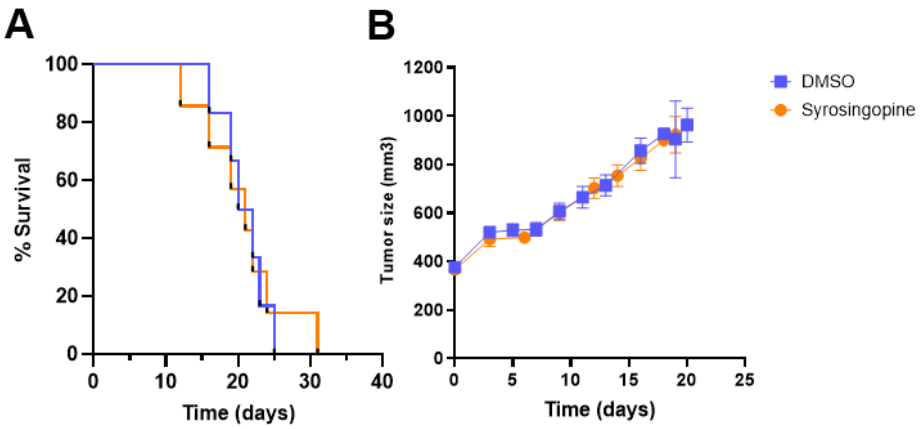


Figure 7. Impact of syrosingopine treatment on tumor growth and survival. (**A**): Evolution of tumor size over time in control (blue) and syrosingopine-treated mice (daily IP injection over 4 days, 5 mg/kg) (orange). (**B**): percentage of survival of mice after treatment with DMSO (control) or syrosingopine for 4 days. Data are represented as mean ± SEM; n = 10 in both groups.

3. Discussion

Targeting proton extrusion in cancer represents a promising therapeutic approach. Being able to monitor the effect of treatments on tumor growth and therapeutic response using noninvasive magnetic resonance methods could be a step forward to personalized medicine. In this work, we focused on an MCT1/4 inhibitor, syrosingopine, and its effects on several metabolic processes and on extracellular acidification, in vitro and in vivo. First, we showed that the inhibition of MCT with syrosingopine in vitro reduced extracellular acidification in two different cell types: breast cancer MDA-MB-231 and pharynx squamous cell carcinoma FaDu cells, after 24 h of treatment. Discrepancies between the cell lines could be due to their different metabolic profiles. MDA-MB-231 cells are well known to have a more glycolytic metabolism, while FaDu cells tend to depend more on oxidative respiration [15,19,20]. We speculate that MDA-MB-231 cells are more sensitive to the inhibition of MCT because they rely more on glucose metabolism.

As MCT1 is not expressed in MDA-MB-231 cells, the effect observed is likely due to MCT4 inhibition. MCT4 is responsible for the excretion of lactate out of cells, with protons. Treatment with syrosingopine should lead to an accumulation of lactate inside cells together with a drop in glucose consumption, intracellular acidification and a reduction in lactate secretion. Our observations are consistent with this scenario in the glycolytic MDA-MB-231 tumor model. We also noted a reduction in cell proliferation and an increase in the number of late apoptotic/necrotic cells when they were treated with 25 µM syrosingopine. The effects on glucose and lactate were less pronounced in FaDu cells, but the effects on intra- and extra-cellular pH values, cell proliferation, viability and apoptosis were still notable. Altogether, these observations support the idea that the co-expression of MCT1 and MCT4 in the same cancer cell (as reported in FaDu cells) may facilitate their metabolic plasticity by adapting their bioenergetics and/or biosynthetic preferences to grow and survive under drug- and/or environment-induced stress. In line with this, a recent study has reported that cancer cells become highly dependent on MCT4 expression/activity when MCT1 expression is epigenetically lost upon exposure with the anti-metabolic drug 3-bromopyruvate [25], thereby highlighting the need to identify the best combination of treatments to overcome tumor metabolic plasticity [26,27].

In light of all these in vitro results, syrosingopine was considered for in vivo studies. Syrosingopine has been reported to induce the sensitization of tumors to metformin, an antidiabetic and mitochondrial inhibitor, in vivo. Benjamin et al. observed a reduction in the number of tumor nodules when mice were treated with either one or a combination of the two molecules [17]. We decided to test the effect of chronic treatment with syrosingopine alone on extracellular pH in MDA-MB-231 tumors. As it is an antihypertensive drug, we selected a lower dose than Benjamin et al. did, as our treatment period was longer, and we wanted to avoid any hemodynamic consequences that could change tumor perfusion. The 4-day treatment did not affect either extracellular pH, tumor growth or mice mortality.

The discrepancies between the in vitro and in vivo results could be explained in several ways. The first hypothesis is that the dose that we used was not sufficient to mimic the actual dose used in vitro. The amount of syrosingopine that actually reached the tumor was not sufficient to recapitulate the concentration used in vitro. Unfortunately, dose escalation over 5 mg/kg was precluded, as syrosingopine presents hypotensive effects. It was indeed previously described that syrosingopine deprived rodents from sympathetic vasomotor tone by the depletion of peripheral neuronal noradrenaline stores at a similar dose (5 mg/kg) to the one used in our study [28]. The absence of effects could also be due to the fact that the period of treatment was not long enough to induce changes in pHe. In our study, mice were treated with syrosingopine or vehicle (DMSO) every day for 4 days in total, whereas Benjamin et al. treated their mice every two days for 16 days. We cannot exclude that a longer period of treatment could affect pHe values, as well as tumor growth. Another possibility is that syrosingopine can only induce little to no effects when used on its own. Syrosingopine is known to inhibit both MCT1 and MCT4, but it is around 60-fold more potent against MCT4 than MCT1 and only at high concentrations. Further studies are needed to evaluate the effect of MCT inhibition in vivo, with more potent inhibitors and with Ki reported in the nM range in order to avoid off-target effects.

4. Materials and Methods

4.1. Cell Culture

MDA-MB-231 cells were cultured at 37 °C in a humidified atmosphere with 5% CO_2 and maintained in DMEM medium (Thermo Fisher Scientific, Merelbeke, Belgium) supplemented with 10% heat-inactivated FBS. FaDu cells were maintained in DMEM GlutaMAX medium supplemented with 10% FBS and 1% non-essential amino acids. Both cell lines were acquired from ATCC, where they are regularly authenticated by short tandem repeat profiling. All cell lines were tested for mycoplasma contamination with the PCR-based MycoplasmaCheck assay (Eurofins, Ebersberg, Germany) before being used.

4.2. Glucose Consumption, Lactate Secretion and Extracellular Acidification Rate (ECAR)

For glucose and lactate dosages, cells (2×10^5 cells/well; 3 wells/condition) were seeded in 12-well plates with 2 mL of their routine culture medium. After 24 h, medium was replaced by 500 µL of DMEM containing 10 mmol/L D-glucose and supplemented with 2 mmol/L L-glutamine and 10% dialyzed FBS (Sigma-Aldrich, Overijse, Belgium), in the presence of 10 µmol/L syrosingopine (Sigma-Aldrich, Overijse, Belgium) or vehicle (DMSO; Sigma- Aldrich, Overijse, Belgium). The initial concentrations of glucose and lactate in the experimental medium were also assessed by including control wells containing only cell culture medium (no cells) on each plate. After incubation for 24 h, extracellular media were collected and deproteinized by centrifugation (15 min, 10,000 rpm, 4 °C) in 10 kDa cut-off filter tubes (VWR, Leuven, Belgium). Glucose and lactate concentrations were measured in the samples (50 µL) using enzymatic assays (CMA Microdialysis AB, Kista, Sweden) and a CMA 600 analyzer (Aurora Borealis, Solna, Sweden). Data analysis was carried out by calculating the difference in metabolite concentrations between the control wells and the experimental wells. Data were then normalized by the protein content in each well and expressed in µmol/h/mg protein.

Extracellular acidification rates (ECARs) were measured using the Seahorse XF96 analyzer (Agilent, Santa Clara, CA, USA). Briefly, cells (1.5×10^4 cells/well; 6 wells/condition) were seeded in Seahorse 96-well cell culture plates in their routine culture medium, in the presence of different concentrations of syrosingopine or vehicle (DMSO). After 24 h, medium was replaced by 175 µL unbuffered serum-free DMEM, pH 7.4, supplemented with 2 mmol/L L-glutamine, still in the presence of the treatment. ECAR values were assessed before and after the injection of 10 mmol/L D-glucose. Glucose-dependent ECAR was calculated by comparing the values before and after addition of the substrate. Data were normalized by the protein content in each well and expressed in mpH/min/µg protein.

4.3. Western Blot

Adherent MDA-MB-231 and FaDu cells were lysed in RIPA buffer (Thermo Scientific, Merelbeke, Belgium) supplemented with 1% protease and phosphatase inhibitors (Thermo Scientific, Merelbeke, Belgium). Protein amount in whole-cell lysates was measured with a Pierce™ BCA Protein Assay Kit (Thermo Scientific, Merelbeke, Belgium). Equal amounts of protein were loaded onto 4–15% Mini-PROTEAN®® TGX™ Precast Gels (Bio-Rad, Temse, Belgium). Following electrophoresis in 1x Tris/glycine/SDS running buffer (Bio-Rad, Temse, Belgium), proteins were transferred to PVDF membranes using the Trans-Blot®® Turbo™ RTA Mini PVDF Transfer Kit (Bio-Rad, Temse, Belgium) according to the manufacturer's instructions. Non-specific binding was blocked by soaking the membranes in 5% milk in tTBS (1x Tris-Buffered Saline, 0.1% Tween 20, Bio-Rad, Temse, Belgium) at room temperature for 1 h. Membranes were incubated with primary anti-HSP90 (4875S, Cell Signaling, Leiden, The Netherland), anti-MCT1 (Ab93048, Abcam, Amsterdam, The Netherland) and anti-MCT4 (AB3316P, Sigma-Aldrich, Hoeilaart, Belgium) antibodies in tTBS/milk 5% at 4 °C overnight, followed by incubation with anti-rabbit or anti-mouse secondary antibodies (Jackson IR, Ely, UK) in tTBS/milk 1% at room temperature for 1 h. Detection was performed using the SuperSignal™ West Pico Plus kit (Thermo Scientific, Merelbeke, Belgium).

4.4. Cell Viability

Cell viability was assessed using the Presto Blue reagent (Thermo Scientific, Merelbeke, Belgium) according to the manufacturer's instructions. MDA-MB-231 (7000 cells/well) or FaDu cells (5000 cells/well) were seeded in 96-well plates. Increasing concentrations of syrosingopine were tested, and cells were incubated for 24, 48 or 72 h. Cell growth was measured by incubating the cells with 10% Presto Blue reagent for 1 h. Fluorescence was measured at 560 nm after excitation at 590 nm with a SpectraMax plate reader (M2 Molecular Devices, Wokingham, UK).

4.5. Cell Proliferation Assay

To assess cell proliferation, a 5-bromo-2′-deoxyuridine (BrdU) assay was performed using a BrdU Cell Proliferation Assay Kit according to the manufacturer's instructions (Sigma Aldrich, Overijse, Belgium). MDA-MB-231 and FaDu cells were seeded at 7000 and 5000 cells/well, respectively, in a 96-well plate and incubated overnight. To assess proliferative activity under different concentrations of syrosingopine, cells were incubated for 24, 48 or 72 h. On the day of the experiment, 20 µL of BrdU was added to each well, and cells were incubated for 2 h. The absorbance at a wavelength of 370 and 492 nm was measured using a SpectraMax (M2 Molecular Devices, Wokingham, UK).

4.6. Intracellular pH Measurements

Intracellular pH was measured using the pH sensor 5-(and-6)-carboxy-seminaphthorhodafluor-acetoxymethylester (C.SNARF1-AM; Invitrogen, Merelbeke, Belgium). Cells were seeded in a 96-well plate. Calibration solutions (pH 6.6, 6.8, 7, 7.2, 7.4 and 8) were prepared in order to calculate pHi values. On the day of the analysis, cells were incubated with pH-sensitive C-SNARF1-AM for 30 min. After washing, fluorescence was

measured at 580 and 642 nm after excitation at 485 nm using a SpectraMax (M2 Molecular Devices, Wokingham, UK).

4.7. Apoptosis/Necrosis

Apoptotic changes in cells were assessed using the eBioscience ™ Annexin V Apoptosis Detection Kit APC (Sigma Aldrich, Overijse, Belgium). A total of 80,000 MDA-MB-231 and 70,000 FaDu cells per condition were plated in a 6-well plate 4 days before the experiment. Cells were treated for 24 h, 48 h or 72 h before the experiment with 10 or 25 μM of syrosingopine or with DMSO into their respective culture media. On the day of the experiment, cells were detached with trypsin (0.05%), harvested into their respective old media, transferred into a FACS tube and centrifuged. The staining protocol briefly included washing the cells with PBS and then adding 80 μL of binding buffer along with 5 μL Annexin V (AnnV) and 5 μL propidium iodide (PI) per tube. Cells were kept in the dark for 15 min until FACS assessment, with an additional 100 μL of binding buffer. Data were acquired using a BD FACSCantoII flow cytometer equipped with Diva Software (BD Biosciences, Erembodegem, Belgium) and processed with FlowJo software (BD Biosciences, Erembodegem, Belgium). At least 10,000 events were analyzed for each condition. Cells' subpopulations were identified according to unstained control cells and distinguished between alive (AnV− PI−), early apoptotic (AnV+ PI−) and late apoptotic/necrotic (AnV+ PI+).

4.8. Tumor Model

All experiments involving animals were performed in accordance with the Belgian law concerning the protection and welfare of animals and were approved by the UCLouvain Ethics Committee (Agreement reference: 2018/UCL/MD/021).

MDA-MB-231 cells (10×10^6 cells in 100 μL of PBS) were injected intramuscularly in the right hind paw of 6-week-old female NMRI nude mice (Janvier). When tumors reached a volume of $\pm$ 350 mm^3, the pHe of tumors was measured using CEST-MRI. Mice were treated with a daily intraperitoneal injection of syrosingopine (5 mg/kg) or vehicle for 4 days. The pHe was measured after treatment. Tumor growth was monitored until tumors reached a size of $\pm$ 1500 mm^3. Tumor size were monitored three times per week using an electronic caliper, and two distances were measured, X and Y (X < Y). Tumor shape was assumed to be ellipsoidal; hence, the volume was considered Pi/6.

4.9. CEST-MRI Experiments

4.9.1. CEST Calibration In Vitro

All experiments were performed on an 11.7T Biospec MRI (Bruker, Ettlingen, Germany). Calibration studies were performed as previously described [24]. CEST acquisitions were acquired with a ^{1}H volume coil with a 40 mm inner diameter. The CEST sequence was a RARE sequence (TR = 4.0 s, TE = 23.0 milliseconds, rare factor = 10, slice thickness = 2 mm, FOV = 30 mm, matrix size = 64 × 64, in-plane special resolution = 468 μm) with an additional continuous 4 μT irradiation for 4 s. The Z spectrum was acquired between 8 and 8 ppm (81 frequencies) for a total acquisition time of 27 min 20 s.

4.9.2. In Vivo Analysis

In vivo studies were performed as described in [24], but a modified version of the CEST protocol was applied. First, acquisitions were acquired before the injection of iopamidol. CEST images were acquired using the same parameters as in the in vitro experiment. Iopamidol was then injected intravenously through the tail vein (3 g Iodine/kg). The second acquisition started 20 min after the injection. All voxels were analyzed using a custom-written script in Matlab (The MathWorks Inc., Natick, MA, USA). The Z-spectra were centered on the bulk water signal to correspond to the zero frequency. Values were measured at the frequency offsets of 4.2 and 5.5 ppm and used in Equation (1):

$$ST = (S_{-\Delta\omega} - S_{+\Delta\omega})/S_0 \quad (1)$$

where S = signal intensity at 4.2 or 5.5 ppm, and S0 = bulk water signal intensity without saturation. Saturation transfer values at 4.2 and 5.5 ppm can be used to calculate their ratio (2):

$$RST = (ST\ 5.5)/(ST\ 4.2) \quad (2)$$

In order to eliminate outliers, different filters were applied to the data. A threshold of 2% was used to discriminate between enhanced and non-enhanced voxels. Negative ST values were excluded, as well as RST values above 0.2 and below 1.55. pH values were calculated based on the RST and the corresponding pH values of the calibration curve. pH maps were obtained by overlaying anatomical images and pH values in each voxel. Only tumors with a pH map that included more than 10 voxels (representing a total volume of 4.4 µL) were kept for the statistical analysis.

4.10. Statistical Analysis

Statistical analysis was performed using GraphPad Prism software (San Diego, CA, USA). Significance was determined using one-way or two-way ANOVA. In vivo pH values before and after treatments were compared using a paired *t*-Student test, with $p \leq 0.05$ considered significant. Results are represented as mean ± SEM. The number of experiments is provided in each figure legend.

5. Conclusions

The inhibition of MCT with syrosingopine led to large effects in vitro on several important metabolic processes in MDA-MB-231 and FaDu tumor cell models. In vivo, no significant changes in pHe values, tumor growth or survival were observed, as we were limited by the potential off-target effects of syrosingopine on hemodynamics. Our study shows that MCT represents an interesting target for anti-cancer therapies but that further studies with more specific MCT inhibitors are needed to determine the effect of its inhibition in vivo.

Author Contributions: Conceptualization, B.G., N.J., C.B. and C.C.; methodology, C.B., N.J., A.W., C.C., L.M., E.R. and B.G.; software, N.J.; validation, C.B., N.J., C.C. and B.G.; formal analysis, C.B. and N.J.; investigation, C.B., A.W., E.R. and N.J.; resources, N.J., C.C., L.M. and B.G.; writing—original draft preparation, C.B., N.J. and B.G.; writing—review and editing, C.B., N.J., A.W., C.C., L.M., E.R. and B.G.; supervision, N.J. and B.G.; project administration, B.G.; funding acquisition, C.C. and B.G. All authors have read and agreed to the published version of the manuscript.

Funding: This research was funded by Fonds National de la Recherche Scientifique (FNRS J008220F and 7463520) (B.G.). C. Buyse is a Televie student. The study used the facilities of the Nuclear and Electron Spin Technologies (NEST) platform of UCLouvain.

Institutional Review Board Statement: All experiments involving animals were performed in accordance with the Belgian law concerning the protection and welfare of animals and were approved by the UCLouvain Ethics Committee (Agreement reference: 2018/UCL/MD/021).

Informed Consent Statement: Not applicable.

Data Availability Statement: Data is contained within the article.

Conflicts of Interest: The authors declare no conflict of interest.

References

1. Hanahan, D.; Weinberg, R.A. Hallmarks of cancer: The next generation. *Cell* **2011**, *144*, 646–674. [CrossRef] [PubMed]
2. Fang, J.S.; Gillies, R.D.; Gatenby, R.A. Adaptation to hypoxia and acidosis in carcinogenesis and tumor progression. *Semin. Cancer Biol.* **2008**, *18*, 330–337. [CrossRef] [PubMed]
3. Anemone, A.; Consolino, L.; Arena, F.; Capozza, M.; Longo, D.L. Imaging tumor acidosis: A survey of the available techniques for mapping in vivo tumor pH. *Cancer Metastasis Rev.* **2019**, *38*, 25–49. [CrossRef] [PubMed]
4. Gatenby, R.A.; Gillies, R.J. Why do cancers have high aerobic glycolysis? *Nat. Rev. Cancer* **2004**, *4*, 891–899. [CrossRef]
5. Wojtkowiak, J.W.; Verduzco, D.; Schramm, K.J.; Gillies, R.J. Drug resistance and cellular adaptation to tumor acidic pH microenvironment. *Mol. Pharm.* **2011**, *8*, 2032–2038. [CrossRef] [PubMed]

6. Linden, C.V.; Corbet, C. Therapeutic Targeting of Cancer Stem Cells: Integrating and Exploiting the Acidic Niche. *Front. Oncol.* **2019**, *9*, 159. [CrossRef]
7. Corbet, C.; Feron, O. Tumour acidosis: From the passenger to the driver's seat. *Nat. Rev. Cancer* **2017**, *17*, 577–593. [CrossRef]
8. Neri, D.; Supuran, C.T. Interfering with pH regulation in tumours as a therapeutic strategy. *Nat. Rev. Drug Discov.* **2011**, *10*, 767–777. [CrossRef]
9. Pillai, S.R.; Damaghi, M.; Marunaka, Y.; Spugnini, E.P.; Fais, S.; Gillies, R.J. Causes, consequences, and therapy of tumors acidosis. *Cancer Metastasis Rev.* **2019**, *38*, 205–222. [CrossRef]
10. De Milito, A.; Iessi, E.; Logozzi, M.; Lozupone, F.; Spada, M.; Marino, M.L.; Federici, C.; Perdicchio, M.; Matarrese, P.; Lugini, L.; et al. Proton pump inhibitors induce apoptosis of human B-cell tumors through a caspase-independent mechanism involving reactive oxygen species. *Cancer Res.* **2007**, *67*, 5408–5417. [CrossRef]
11. Taylor, S.; Spugnini, E.P.; Assaraf, Y.G.; Azzarito, T.; Rauch, C.; Fais, S. Microenvironment acidity as a major determinant of tumor chemoresistance: Proton pump inhibitors (PPIs) as a novel therapeutic approach. *Drug Resist. Updates* **2015**, *23*, 69–78. [CrossRef] [PubMed]
12. Dolatkhah, M.; Omidi, Y. Renewed interests in carbonic anhydrase IX in relevance to breast cancer treatment. *Bioimpacts* **2019**, *9*, 195–197. [CrossRef] [PubMed]
13. Pinheiro, C.; Longatto-Filho, A.; Azevedo-Silva, J.; Casal, M.; Schmitt, F.C.; Baltazar, F. Role of monocarboxylate transporters in human cancers: State of the art. *J. Bioenerg. Biomembr.* **2012**, *44*, 127–139. [CrossRef] [PubMed]
14. Counillon, L.; Bouret, Y.; Marchiq, I.; Pouyssegur, J. Na(+)/H(+) antiporter (NHE1) and lactate/H(+) symporters (MCTs) in pH homeostasis and cancer metabolism. *Biochim. Biophys. Acta* **2016**, *1863*, 2465–2480. [CrossRef]
15. Sonveaux, P.; Vegran, F.; Schroeder, T.; Wergin, M.C.; Verrax, J.; Rabbani, Z.N.; De Saedeleer, C.J.; Kennedy, K.M.; Diepart, C.; Jordan, B.F.; et al. Targeting lactate-fueled respiration selectively kills hypoxic tumor cells in mice. *J. Clin. Investig.* **2008**, *118*, 3930–3942. [CrossRef]
16. Le Floch, R.; Chiche, J.; Marchiq, I.; Naiken, T.; Ilc, K.; Murray, C.M.; Critchlow, S.E.; Roux, D.; Simon, M.P.; Pouysségur, J. CD147 subunit of lactate/H^+ symporters MCT1 and hypoxia-inducible MCT4 is critical for energetics and growth of glycolytic tumors. *Proc. Natl. Acad. Sci. USA* **2011**, *108*, 16663–16668. [CrossRef]
17. Benjamin, D.; Colombi, M.; Hindupur, S.K.; Betz, C.; Lane, H.A.; El-Shemerly, M.Y.; Lu, M.; Quagliata, L.; Terracciano, L.; Moes, S.; et al. Syrosingopine sensitizes cancer cells to killing by metformin. *Sci. Adv.* **2016**, *2*, e1601756. [CrossRef]
18. Benjamin, D.; Robay, D.; Hindupur, S.K.; Pohlmann, J.; Colombi, M.; El-Shemerly, M.Y.; Maira, S.M.; Moroni, C.; Lane, H.A.; Hall, M.N. Dual Inhibition of the Lactate Transporters MCT1 and MCT4 Is Synthetic Lethal with Metformin due to NAD+ Depletion in Cancer Cells. *Cell Rep.* **2018**, *25*, 3047–3058. [CrossRef]
19. De Preter, G.; Danhier, P.; Porporato, P.E.; Payen, V.L.; Jordan, B.F.; Sonveaux, P.; Gallez, B. Direct Evidence of the Link Between Energetic Metabolism and Proliferation Capacity of Cancer Cells In Vitro. *Adv. Exp. Med. Biol.* **2016**, *876*, 209–214.
20. Corbet, C.; Bastien, E.; Draoui, N.; Doix, B.; Mignion, L.; Jordan, B.F.; Marchand, A.; Vanherck, J.C.; Chaltin, P.; Schakman, O.; et al. Interruption of lactate uptake by inhibiting mitochondrial pyruvate transport unravels direct antitumor and radiosensitizing effects. *Nat. Commun.* **2018**, *9*, 1208. [CrossRef]
21. Consolino, L.; Anemone, A.; Capozza, M.; Carella, A.; Irrera, P.; Corrado, A.; Dhakan, C.; Bracesco, M.; Longo, D.L. Non-invasive Investigation of Tumor Metabolism and Acidosis by MRI-CEST Imaging. *Front. Oncol.* **2020**, *10*, 161. [CrossRef] [PubMed]
22. Chen, L.Q.; Pagel, M.D. Evaluating pH in the Extracellular Tumor Microenvironment Using CEST MRI and Other Imaging Methods. *Adv. Radiol.* **2015**, *2015*, 206405. [CrossRef] [PubMed]
23. Hussien, R.; Brooks, G.A. Mitochondrial and plasma membrane lactate transporter and lactate dehydrogenase isoform expression in breast cancer cell lines. *Physiol. Genom.* **2011**, *43*, 255–264. [CrossRef]
24. Buyse, C.; Joudiou, N.; Corbet, C.; Feron, O.; Mignion, L.; Flament, J.; Gallez, B. Impact of Inhibition of the Mitochondrial Pyruvate Carrier on the Tumor Extracellular pH as Measured by CEST-MRI. *Cancers* **2021**, *13*, 4278. [CrossRef] [PubMed]
25. Vander Linden, C.; Corbet, C.; Bastien, E.; Martherus, R.; Guilbaud, C.; Petit, L.; Wauthier, L.; Loriot, A.; De Smet, C.; Feron, O. Therapy-induced DNA methylation inactivates MCT1 and renders tumor cells vulnerable to MCT4 inhibition. *Cell Rep.* **2021**, *35*, 109202. [CrossRef] [PubMed]
26. Oshima, N.; Ishida, R.; Kishimoto, S.; Beebe, K.; Brender, J.R.; Yamamoto, K.; Urban, D.; Rai, G.; Johnson, M.S.; Benavides, G.; et al. Dynamic Imaging of LDH Inhibition in Tumors Reveals Rapid In Vivo Metabolic Rewiring and Vulnerability to Combination Therapy. *Cell Rep.* **2020**, *30*, 1798–1810. [CrossRef]
27. Beloueche-Babari, M.; Wantuch, S.; Galobart, T.C.; Koniordou, M.; Parkes, H.G.; Arunan, V.; Chung, Y.L.; Eykyn, T.R.; Smith, P.D.; Leach, M.O. MCT1 Inhibitor AZD3965 Increases Mitochondrial Metabolism, Facilitating Combination Therapy and Noninvasive Magnetic Resonance Spectroscopy. *Cancer Res.* **2017**, *77*, 5913–5924. [CrossRef]
28. Lefevre-Borg, F.; Cavero, I. Stimulation of peripheral dopamine receptors in rats: A mechanism for novel antihypertensive agents. *Clin. Sci.* **1980**, *59* (Suppl. S6), 291s–294s. [CrossRef]

3. Sensitive simultaneous measurements of oxygenation and extracellular pH by EPR using a stable monophosphonated trityl radical and lithium phthalocyanine

Published in *Free Radical Biology And Medecine*, 2024, 213, 11-18

Buyse C., Mignion L., Joudiou N., Melloul S., Driesschaert B., Gallez B.

doi: 10.1016/j.freeradbiomed.2024.012

Free Radical Biology and Medicine 213 (2024) 11–18

Contents lists available at ScienceDirect

Free Radical Biology and Medicine

journal homepage: www.elsevier.com/locate/freeradbiomed

Sensitive simultaneous measurements of oxygenation and extracellular pH by EPR using a stable monophosphonated trityl radical and lithium phthalocyanine

Chloe Buyse [a], Lionel Mignion [b], Nicolas Joudiou [b], Samia Melloul [a], Benoit Driesschaert [c], Bernard Gallez [a,*]

[a] Biomedical Magnetic Resonance Research Group (REMA), Louvain Drug Research Institute (LDRI), UCLouvain, Brussels, Belgium
[b] Nuclear and Electron Spin Technologies Platform (NEST), Louvain Drug Research Institute (LDRI), UCLouvain, Brussels, Belgium
[c] Department of Pharmaceutical Sciences, School of Pharmacy & In Vivo Multifunctional Magnetic Resonance Center, West Virginia University, Morgantown, WV, USA

ARTICLE INFO

Keywords:
EPR
ESR
In vivo
Oxygenation
pH
Tumor microenvironment
Metabolism
Mitochondria
Hypoxia

ABSTRACT

The monitoring of acidosis and hypoxia is crucial because both factors promote cancer progression and impact the efficacy of anti-cancer treatments. A phosphonated tetrathiatriarylmethyl (pTAM) has been previously described to monitor both parameters simultaneously, but the sensitivity to tackle subtle changes in oxygenation was limited. Here, we describe an innovative approach combining the pTAM radical and lithium phthalocyanine (LiPc) crystals to provide sensitive simultaneous measurements of extracellular pH (pH_e) and pO_2. Both parameters can be measured simultaneously as both EPR spectra do not overlap, with a gain in sensitivity to pO_2 variations by a factor of 10. This procedure was applied to characterize the impact of carbogen breathing in a breast cancer 4T1 model as a proof-of-concept. No significant change in pH_e and pO_2 was observed using pTAM alone, while LiPc detected a significant increase in tumor oxygenation. Interestingly, we observed that pTAM systematically overestimated the pO_2 compared to LiPc. In addition, we analyzed the impact of an inhibitor (UK-5099) of the mitochondrial pyruvate carrier (MPC) on the tumor microenvironment. *In vitro*, the exposure of 4T1 cells to UK-5099 for 24 h induced a decrease in pH_e and oxygen consumption rate (OCR). *In vivo*, a significant decrease in tumor pH_e was observed in UK-5099-treated mice, while there was no change for mice treated with the vehicle. Despite the change observed in OCR, no significant change in tumor oxygenation was observed after the UK-5099 treatment. This approach is promising for assessing *in vivo* the effect of treatments targeting tumor metabolism.

1. Introduction

The reprogramming of energy metabolism of cancer cells is considered a hallmark of cancer [1–3]. The extracellular acidosis associated with the altered energy metabolism may have a profound impact on cancer progression, on immunosurveillance and on the efficacy of treatments [4–6]. In addition, hypoxia is a common feature of solid tumors that contributes to angiogenesis, invasiveness, metastasis, genomic instability and resistance to anticancer therapy (radiotherapy, chemotherapy and immunotherapy) [7,8]. Importantly, it has been demonstrated that both extracellular acidosis and oxygen availability are not necessarily associated in solid tumors [9]. Having the capability to assess both extracellular pH (pH_e) and partial pressure of oxygen (pO_2) in tumors should lead to improvements in patient stratification regarding the selection of treatment and optimization of combined therapies [8,10]. In this context, low-frequency Electron Paramagnetic Resonance (EPR) spectroscopy has gained interest for its capability to measure both tissue acidosis and oxygenation.

The measurement of pH in tissues using EPR can be achieved by measuring variation in hyperfine splitting constants in the EPR spectra of pH-sensitive imidazolidine nitroxides [11–13] or phosphonated trityl radicals [14,15]. EPR has also been investigated for its capability to provide highly sensitive measurements of tissue oxygenation [16–20] thanks to the oxygen-induced changes in electron relaxation properties of paramagnetic oxygen sensors such as soluble stable free radicals (nitroxide or trityl radicals) [21,22] or particulate materials (charcoals,

* Corresponding author.
E-mail address: bernard.gallez@uclouvain.be (B. Gallez).

https://doi.org/10.1016/j.freeradbiomed.2024.01.012
Received 20 November 2023; Received in revised form 9 January 2024; Accepted 10 January 2024
Available online 11 January 2024
0891-5849/© 2024 Elsevier Inc. All rights reserved.

carbon blacks, lithium phthalocyanine (LiPc) and derivatives) [23–27]. Several dual probes allowing the simultaneous characterization of parameters of the tumor microenvironment have been described [28–31]. For example, Ilangovan et al. used LiPc crystals together with a nitroxide to measure tumor oxygenation and redox status during hyperoxygenation treatment [32]. An interesting development has been the synthesis of the monophosphonated tetrathiatriarylmethyl (pTAM or HOPE) radical that is able to provide simultaneous measurement of pH_e and pO_2 [33–35]. This asymmetric monophosphonated trityl radical displays a doublet pattern. The pH can be derived from the respective heights of the EPR lines (that depend on the molar fraction of the acidic form *Pa* versus basic form *Pb*) while the pO_2 can be measured from the linewidths (Fig. 1a) [34].

While the multifunctionality of the probe represents a remarkable achievement, soluble paramagnetic sensors present an intrinsic limited sensitivity to tackle subtle variations in oxygenation that may occur *in vivo*. Because it is known that particulate materials display a much higher sensitivity to variations in partial pressure of oxygen [16], this prompted us to develop a new approach with a combination of pTAM together with lithium phthalocyanine crystals. We selected LiPc because this material presents an extremely narrow EPR signal and a high sensitivity to oxygen variations (Fig. 1b) [25]. In addition, the EPR signal of LiPc does not interfere with the doublet of pTAM (Fig. 1c). To assess the value of our approach, we first compared *in vitro* the sensitivity of pTAM and LiPc to variations in the oxygen environment. We then evaluated the value of pTAM alone and pTAM/LiPc *in vivo* in tumors using treatments that could potentially have an impact on the pO_2 and/or the pH_e. In a first step, we exposed mice to carbogen (95% O_2, 5% CO_2) breathing. This treatment is indeed often used in experimental studies as a positive control for its capability to increase tumor oxygenation [36–40]. In addition, acidification could potentially occur due to the CO_2 component of the inspired gas [41]. In a second step, we evaluated the effect of the inhibition of the mitochondrial pyruvate carrier (MPC). MPC is a heterodimeric complex located in the mitochondrial inner membrane that is responsible for importing pyruvate, the end-product of glycolysis, from the cytosol into the mitochondrial matrix (Fig. 2). It was previously found that 7ACC2, an inhibitor of MPC,

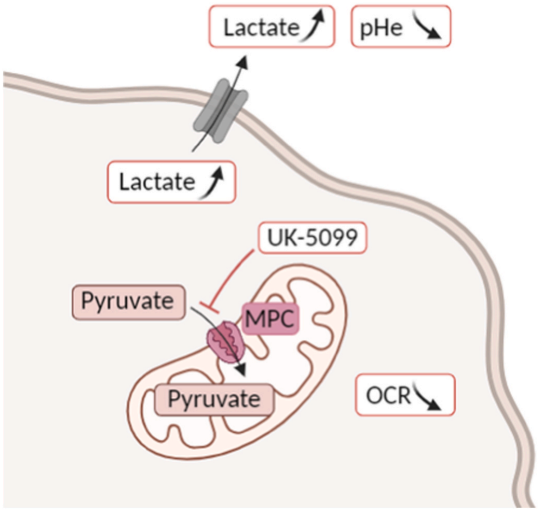


Fig. 2. Role of the mitochondrial pyruvate carrier (MPC).
MPC is responsible for importing pyruvate, the end-product of glycolysis, from the cytosol into the mitochondrial matrix. Its inhibition may potentially lead to extracellular acidification and a decrease in oxygen consumption.

increased the extracellular acidification rate in squamous cervix carcinoma cells (SiHa) and alleviated tumor hypoxia through a decrease in oxygen consumption rate (OCR) in squamous hypopharyngeal carcinoma cells (FaDu) [42]. We also recently demonstrated, using CEST-MRI with iopamidol, that another inhibitor of MPC, UK-5099, induced acidification in a breast cancer model (4T1) [43]. Therefore, this model and this treatment were selected to evaluate the performances of the dual EPR probes. This was achieved *in vitro* by monitoring the effect of cell exposure to UK-5099 on extracellular acidification and oxygen

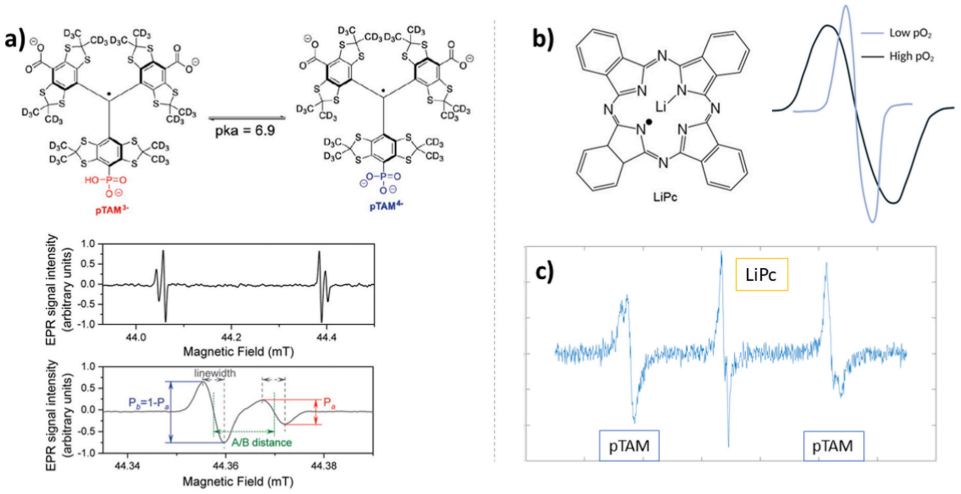


Fig. 1. EPR sensors used in the present study.
a) Structure of monophosphonated triarylmethyl radical (pTAM/HOPE) and its typical EPR spectrum showing both ionic forms (acidic form, Pa and basic form, Pb). The respective height of both forms provides information on the pH of the environment while the linewidth provides information on the oxygen concentration. Adapted from Ref. [33] b) Structure of lithium phthalocyanine (LiPc) and its EPR spectrum. The variation in linewidth can be calibrated as a function of pO_2. c) Typical EPR spectrum of both pTAM and LiPc recorded *in vivo* using a 1 GHz spectrometer. Note that the EPR spectra of pTAM and LiPc do not overlap.

consumption rate. We also monitored *in vivo* the effect of UK-5099 on pH_e and pO_2 in 4T1 tumor-bearing mice.

2. Materials & methods

2.1. Reagents

The mono-phosphonated tetrathiatriarylmethyl radical was synthesized as previously described [34]. ^{15}N-PDT (4-oxo-2,2,6,6-tetramethylpiperidine-d_{16}-^{15}N-1-oxyl) was purchased from CDN Isotopes (Pointe-Claire, Canada). Lithium phthalocyanine crystals were provided by H.M. Swartz (Dartmouth Medical School, Hanover, NH, USA). UK-5099, dextran from *Leuconostoc Mesenteroides* (average MW 60000-76000) and dimethyl sulfoxide (DMSO) were from Sigma-Aldrich (Overijse, Belgium).

2.2. Cell lines and culture

4T1 breast cancer cells were cultured at 37 °C in a humidified atmosphere with 5% CO_2 and maintained in RPMI medium (Thermo Fisher Scientific, Seneffe, Belgium) supplemented with 10% heat-inactivated FBS. The cell line was purchased from ATCC where it was regularly authenticated by short tandem repeat profiling. The 4T1 cell line was tested for mycoplasma contamination with the PCR-based MycoplasmaCheck assay (Eurofins, Ebersberg, Germany) before being used.

2.3. EPR instrumentations

In vitro studies were performed using a Bruker EMX-Plus spectrometer operating in X-band (9.85 GHz) and equipped with a PremiumX ultra-low noise microwave bridge and a SHQ high sensitivity resonator. The EPR cavity was heated to 310 K with continuous air flow during all experiments.

In vivo EPR spectra were recorded using an EPR spectrometer (electromagnet from Magnettech, Berlin, Germany; electronic console from Clin-EPR, Lyme, NH, USA) with a low-frequency microwave bridge operating at 1.1 GHz and an extended loop (surface coil) resonator (Clin-EPR). The sensitive volume under the loop is about 1 cm^3.

2.4. pH_e and pO_2 calibrations

Saline solutions (containing 0, 1, 2, 3, 4 % albumin) containing either pTAM (200 μM) or LiPc were placed in a gas-permeable polytetrafluoroethylene (PTFE) tubing (inner diameter 0.025 in.; outer diameter 0.029 in.; Zeus Industrial Products, Letterkenny, Ireland). The oxygen content was varied between 0 and 21% O_2 using an Aalborg gas mixer. The oxygen content in the mixed gas was measured using a Servomex MiniMP 5200 oxygen analyzer (precision 0.1% oxygen content). pH was adjusted using NaOH or HCl. pH was measured using a pH meter. The experimental acquisition parameters for the pTAM and LiPc calibrations were as follows: microwave power, 2.518 mW; modulation frequency, 10 kHz; modulation amplitude, 0.0012 mT; sweep width, 5 mT.

2.5. Oxygen consumption rate (OCR) and pH_e measurements in vitro

4T1 tumor cells were treated for 24 h with either a vehicle (DMSO) or UK-5099 (10 μM). On the day of the experiment, cells were harvested to obtain 5×10^6 cells/mL. The experimental mixture was prepared with 60 μL of cells, 40 μL of dextran (20%) and pTAM (200 μM. Parallel experiments were also done using ^{15}N-PDT (2 mM) as oxygen sensor instead of pTAM because this nitroxide has been classically used in OCR experiments measured by EPR [44,45]. This mixture was placed in a gas-impermeable hematocrit capillary sealed with gum, inserted into a quartz tube and placed in the heated cavity (310 K). The experimental parameters were the following: microwave power, 2.518 mW; modulation frequency, 10 kHz; modulation amplitude, 0.0012 mT; sweep width, 5 mT. EPR spectra were recorded every other minute during 20 min for linewidth determination. As the linewidth reports on pO_2, oxygen consumption rates were obtained by measuring the pO_2 in the closed tube over time and determining the slope of the resulting linear plot (Fig. S1). Full detailed practical procedure has been published elsewhere [46].

2.6. Tumor models and animal procedures

All experiments involving animals were performed in agreement with the Belgian law concerning the protection and welfare of the animals and were approved by the UCLouvain ethics committee (Agreement reference: 2022/UCL/MD/047). 2 x 10^5 4T1 cells in 100 μL of PBS were injected intramuscularly in the right hind paw of 6-week-old female BALB/cAnNRj mice.

LiPc crystals were implanted inside the tumor tissue of anesthetized animals 24 h before the first measurement when tumors reached a volume of 200 ± 50 mm^3. A small incision was made in the hind paw to insert 3-4 LiPc crystals. The small wound was sutured after insertion of the sensors. 50 μL of pTAM (3 mM in saline) was injected inside the tumor 3 min before positioning the mouse in the center of the 1 GHz spectrometer and launching the first EPR acquisition. Acquisitions parameters were as follows: power, 7.94 mW; modulation frequency, 3.29 kHz; modulation amplitude, 0.04 G; scan range, 3 G; scan time, 30 s; 10 acquisitions).

Animals were anesthetized by inhalation of isoflurane mixed with air (21% oxygen) in a continuous flow (2 l/min) delivered by a nose cone. The induction of anesthesia was performed with 3% isoflurane which was then stabilized at 1.5% for a minimum of 15 min before any measurement. It was previously demonstrated that this anesthesia regimen did not disturb the hemodynamics in mice [47]. A circulating water system was used for body-temperature regulation at 37 °C.

2.7. In vivo manipulation of pO_2 and/or pH_e

Carbogen Breathing: 50 μL of pTAM (3 mM in saline) was injected inside the tumor 3 min before the first EPR acquisition when mice were breathing air. After the first acquisitions, mice were kept in place but the gas was switched to carbogen (95% O_2, 5% CO_2). EPR spectra were acquired after 10 min of carbogen breathing.

MPC inhibition: The treatment administration scheme was based on a previous established to monitor the pH_e changes induced by UK-5099 changes using CEST-MRI in the same tumor model [43]. Mice were treated with daily intraperitoneal injection of UK-5099 (3 mg/kg) or vehicle for 4 days. The basal pH_e and the basal pO_2 were measured on day first before the administration of the first dose of UK-5099. The measurement post-treatment was performed on day 4, 1 h after the last injection of UK-5099. Control experiments were done using the vehicle (DMSO) instead of UK-5099.

The *in vivo* protocols are summarized in Fig. 3.

3. Results

3.1. LiPc is 10 times more sensitive to oxygen changes than pTAM

The *in vitro* calibration curve (Pa fraction as a function of pH) using pTAM is shown in Fig. 4a. We also performed a direct comparison of the changes in linewidth measured for LiPc and pTAM (at different concentrations of albumin) as a function of pO_2 variation (Fig. 4b). The comparison of the slopes showed that the sensitivity of LiPc was 10 times higher than that of pTAM to variations in the oxygen environment. The presence of albumin did not significantly change the response to variations in oxygenation as all calibration curves obtained were superimposable.

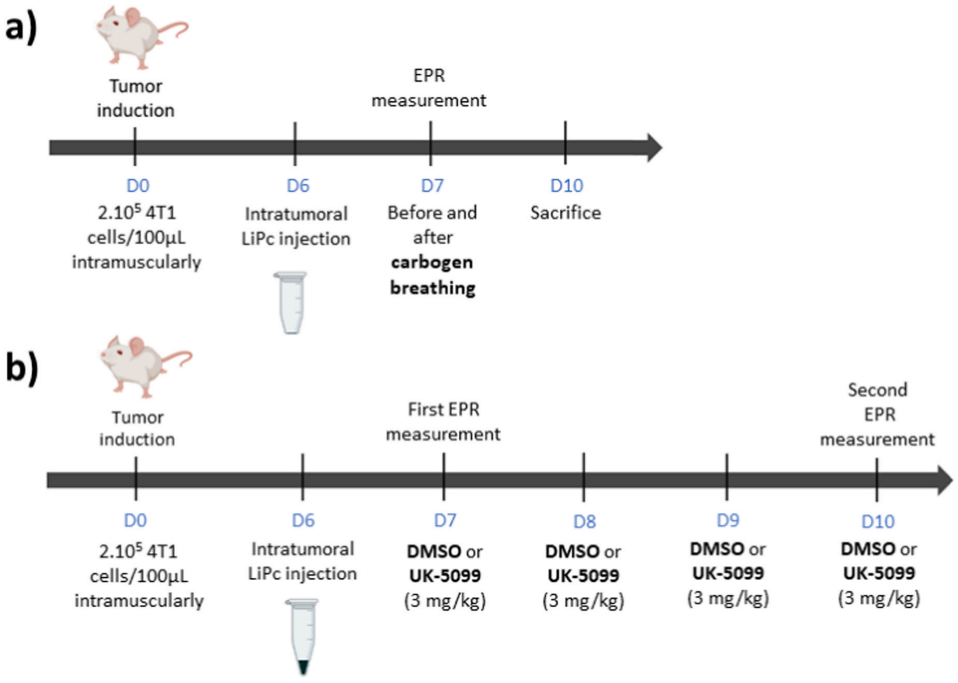


Fig. 3. Experimental protocols applied *in vivo* with simultaneous assessments of pO_2 and pH_e.
a) Protocol of carbogen breathing b) Protocol of MPC inhibition using UK-5099.

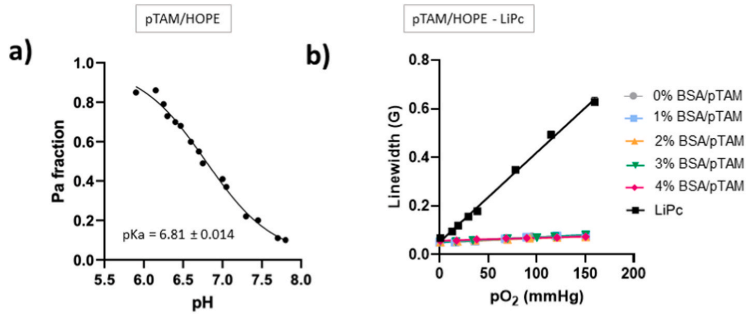


Fig. 4. Calibrations of the EPR sensors.
a) pH_e calibration (ratio Pa/Pb as a function of pH) of pTAM b) pO_2 calibrations (linewidth as a function of pO_2) of LiPc (in saline) and pTAM (in saline and 1-2-3-4 % albumin).

3.2. LiPc, not pTAM, detects significant changes in pO2 after carbogen breathing

As the EPR signal of pTAM decreased rapidly in tumors ($T_{1/2}$ = 13 min), measurements were done rapidly after pTAM administration. The carbogen challenge was used in order to increase the oxygenation and possibly modify the pH in the tumors. We did not observe any significant change in pH_e after carbogen breathing (Fig. 5a). The results obtained for the evolution of tumor oxygenation were different between the pTAM and the LiPc oxygen sensors. While pTAM did not detect a significant change in tumor pO_2 after carbogen breathing (Fig. 5b), LiPc indicated that breathing carbogen led to a significant increase in pO_2 in the same tumors (Fig. 5c). Intriguingly, as shown in Fig. 5d, the pO_2 readings obtained with pTAM were systematically and significantly higher than those measured with LiPc.

3.3. pTAM detected changes in extracellular pH and in OCR in vitro in cells exposed to UK-5099

Oxygen consumption was monitored in 4T1 cells exposed for 24 h to either DMSO (vehicle) or 10 µM of UK-5099. This was achieved using pTAM (Fig. 6a) or ^{15}N-PDT (Fig. 6b), the latter probe being classically used for OCR measurement using EPR [44–46]. Both probes similarly revealed that the exposure to UK-5099 induced a decrease in OCR. The extracellular pH was also monitored *in vitro* using pTAM revealing that the pH_e was significantly decreased after UK-5099 exposure (Fig. 6c).

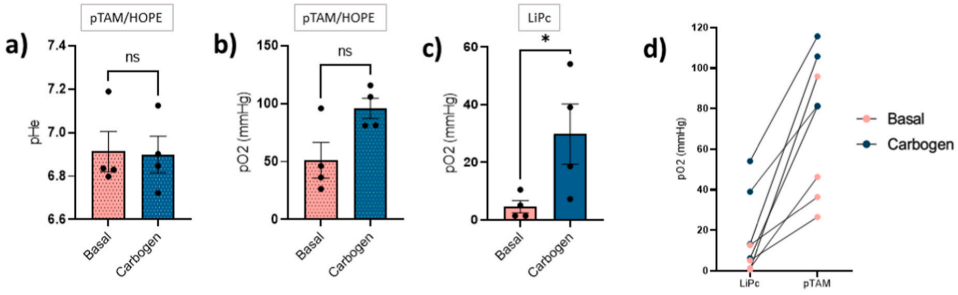


Fig. 5. Effect of carbogen breathing on the tumor pH_e and pO_2 measured simultaneously.
a) pH_e measured before and after 10 min of carbogen breathing (n = 4) b) pO_2 measured before and after 10 min of carbogen breathing using the calibration of pTAM (n = 4) c) pO_2 measured before and after 10 min of carbogen breathing using the calibration of LiPc (n = 4) d) Individual comparison between pO_2 readings obtained from LiPc and pTAM from the same tumors *, $p < 0.05$; **, $p < 0.01$, Student's t-test. Note that pH_e does not seem altered by the treatment with carbogen. Note that pTAM was not able to tackle any significant variation in pO_2 while LiPc suggested a significant increase in pO_2. The pO_2 readings obtained with pTAM were systematically and significantly higher than those measured with LiPc.

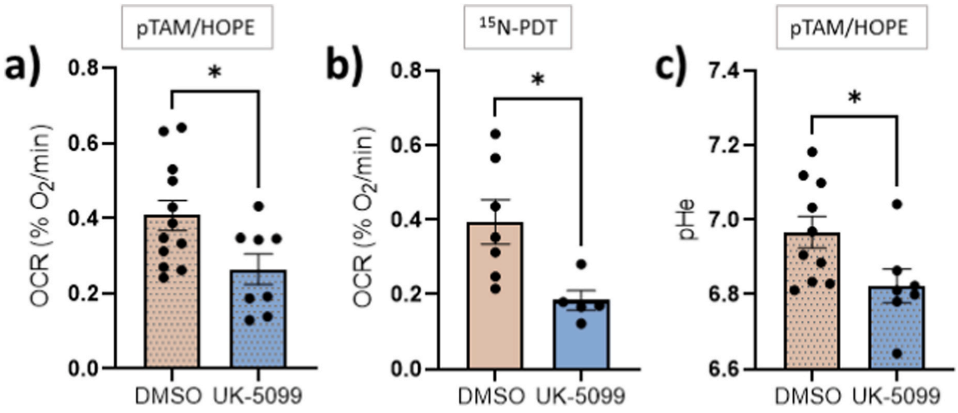


Fig. 6. Effect of UK-5099 exposure for 24 h on oxygen consumption rate and extracellular pH.
a) OCR measured using pTAM b) OCR measured using ^{15}N-PDT c) pH_e measured using pTAM *, $p < 0.05$, Student's t-test.

3.4. UK-5099 treatment induced changes in pH_e but not in pO_2 in vivo in 4T1 tumor models

Mice bearing 4T1 tumors implanted in the leg were treated for 4 days either with DMSO (vehicle) or UK-5099 (3 mg/kg). This administration pattern was inspired by our previous work with UK-5099 which showed a significant effect on pH_e values when measured by CEST-MRI [43]. The results obtained *in vivo* showed a significant decrease in tumor pH_e (by 0.39 pH units) in UK-5099-treated mice while there was no significant change over time for mice treated with the vehicle (Fig. 7a and b). The oxygenation was also monitored using the EPR linewidths of pTAM or LiPc. Both readings indicate no significant change in tumor oxygenation after vehicle administration or UK-5099 treatment for 4 days (Fig. 7c–f). Again, we observed that pO_2 readings obtained with pTAM were much higher than those obtained using LiPc. For example, the pO_2 estimated before UK-5099 treatment was 89.20 ± 13.14 mmHg (mean ± SE) using pTAM while it was 6.231 ± 1.757 mmHg (mean ± SE) using LiPc.

4. Discussion

Acidosis and hypoxia are features often observed in malignant tumors. Both factors are considered as poor prognostic markers because their presence affects the curability of solid tumors [48,49]. In this context, assessing both pO_2 and pH_e is of paramount importance not only to evaluate the aggressiveness of a tumor but also to select treatment options. Indeed, intense research is currently under development to define therapeutic interventions that may modulate the tumor metabolism and tumor microenvironment to optimize anti-cancer strategies [4,50–54]. Innovative EPR sensors have been developed with the capability to monitor simultaneously tissue oxygenation and acidity [28,31,33–35,55–58] with interesting applications for tumor profiling [59]. Unfortunately, the sensitivity of soluble probes to variations in tissue oxygenation is limited. Our results obtained *in vivo* after carbogen breathing illustrate this limited sensitivity of pTAM (Fig. 5). Oxygen-enriched gas breathing (including pure oxygen, carbogen or hyperbaric oxygen) has been used in many experimental studies (including EPR oximetry studies) to manipulate tumor oxygenation and alleviate tumor hypoxia [36–40,60]. In the present study, the soluble probe pTAM did not detect significant changes in pO_2 in sharp contrast to readings done with the particulate probe LiPc. To understand the limited sensitivity of soluble probes, it is worth looking back at the principles of EPR oximetry [16,18,61]. Bimolecular collisions between paramagnetic oxygen and free radicals are at the origin of changes in EPR spectra because they modify the resonance characteristics of the radical and consequently the EPR spectrum. The enhancement of

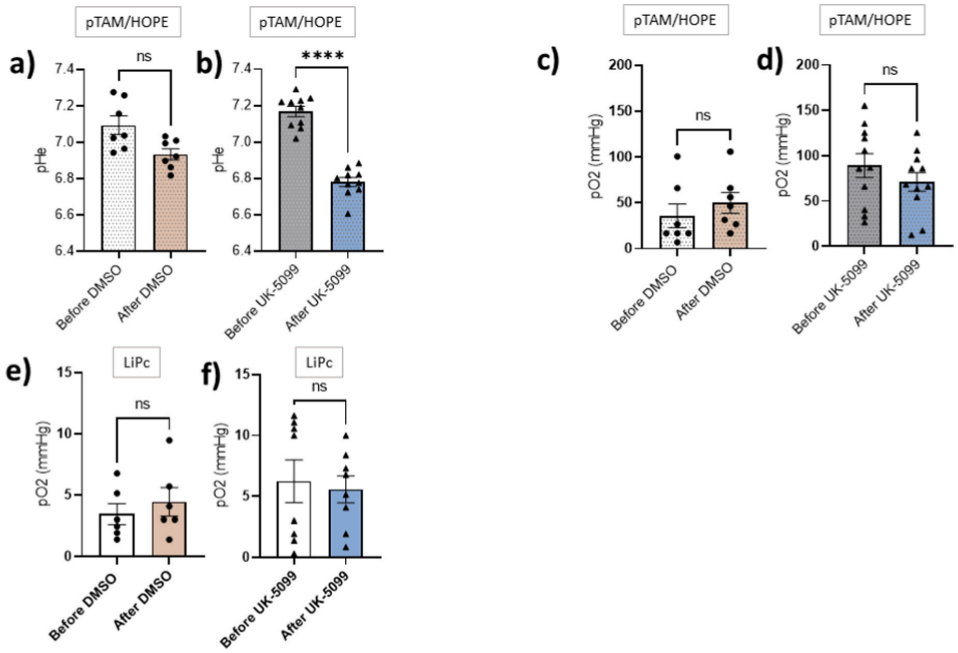


Fig. 7. Effect of UK-5099 treatment on pH_e and pO_2 measured *in vivo* in 4T1 tumor models
a) pH_e measured before and after 4 days of DMSO treatment (n = 7) b) pH_e measured before and after 4 days of UK-5099 treatment (3 mg/kg) (n = 10) c) pO_2 measured before and after 4 days of DMSO treatment as estimated by pTAM (n = 7) d) pO_2 measured before and after 4 days of UK-5099 treatment (3 mg/kg) as estimated by pTAM (n = 11) e) pO_2 measured before and after 4 days of DMSO treatment as estimated by LiPc (n = 6) f) pO_2 measured before and after 4 days of UK-5099 treatment (3 mg/kg) as estimated by LiPc (n = 8) ****, $p < 0.0001$, Student's t-test.

relaxation rates scales linearly with the concentration of oxygen. For soluble probes, there is a direct relationship between the EPR line exchange broadening and the radical-radical collision rate [60] The exchange rate ω is governed by the Smoluchowski equation:

$$\omega = 4\,\pi\,R\,\{\,D(O_2) + D(SP)\,\}\,[O_2]$$

and the variation of the EPR linewidth Δ LW is

$$\Delta\,LW = 4\,\pi\,R\,k\,p\,\{\,D(O_2) + D(SP)\,\}\,(\Delta\,[O_2])$$

where R is the interaction distance, k is a proportionality constant, p is the probability that exchange will occur upon each collision, D(O2) and D(SP) are the diffusion coefficients of oxygen and the spin probe, respectively, and $[O_2]$ is the concentration of oxygen in solution. In practice, it means that, for small nitroxides spin probe in water solution, the variation in Δ LW when shifting from nitrogen (0 % O_2) to air (21 % O_2) will be around 10 μT This value actually depends on the R parameter as bulky radicals present a smaller oxygen sensitivity (8.5 μT for dFT (deuterated Finland trityl), 5.6 μT for OXO63 (Finland trityl substituted with $–CH_2CH_2OH$), 3.0 μT for SOX71 (succinylated derivative of Finland trityl OXO71), as illustrative examples) [62]. Of note, changes in oxygen concentrations in tissues are generally ranging from 0 to 7 % O_2. In contrast, the sensitivity in linewidth variation for particulate material is much larger, with a broadening per unit of pO_2, exceeding that of soluble probes by several orders of magnitude [16]. While the mechanism of the relationship between Δ LW and Δ pO_2 is not fully elucidated for all particulate probes [63], it has been described that, for LiPc, the oxygen sensitivity is critically dependent on the crystal forms. Oxygen has been shown to migrate into the channels presented by the tetragonal x-form where it influences the magnetic properties of the delocalized free electrons present in LiPc [64,65]. The sensitivity measured for LiPc crystals used in the present study was comparable to that described in its first application *in vivo* [25]. As described in Fig. 4b, the sensitivity to oxygen variations was ten times higher for LiPc than for pTAM. This material is particularly interesting because its EPR spectrum does not overlap with that of pTAM. While other particulate materials such as charcoals and carbon blacks present a larger sensitivity to variations in oxygenation, their EPR spectra are too large in oxygenated media for being applied together with pTAM due to the overlapping of the EPR lines.

As pTAM and LiPc were simultaneously present in tissues, it offered the possibility to compare the pO_2 values obtained by both sensors. In both experiments (carbogen challenge or MPC inhibition), we systematically observed that apparent pO_2 values obtained from the linewidth of pTAM were significantly larger than those obtained with LiPc (Figs. 5d and 7d-f). Large pO_2 values using pTAM were also reported recently in a spontaneous breast cancer model [59]. Of note, most readings obtained with LiPc provided pO_2 values lower than 20 mmHg, data consistent with several dozens of studies carried out in tumors using EPR oximetry and Clark electrodes, as reviewed in Gallez and Vaupel et al. [66,67]. While remaining speculative, several factors may contribute to this discrepancy in pO_2 estimates by both probes. Contrarily to LiPc, the EPR linewidth of pTAM is affected by "concentration effects". Indeed, a high local concentration of the probe induces a self-broadening of the EPR linewidth that will lead to an overestimation of the actual pO_2. The concentration used for the injection was 3 mM which was the highest concentration where no self-broadening of the probe was observed *in vitro* (Fig. S2). An increase in the linewidth and a loss in hyperfine resolution was observed at higher concentration (5 and 10 mM) (Fig. S2). Of note, others have used a concentration of 2 mM for injection of pTAM [68]. As the probe is diluted in the biological media

after injection, in principle, we could not expect a self-broadening of the EPR signal. However, we cannot exclude that the probe could concentrate after injection in a specific location leading to a self-broadening. To avoid this concentration effect observed with soluble probes, it has been suggested that measuring the T1 relaxation times should be preferred to T2, a possibility offered by pulsed EPR spectrometers [69]. Another potential factor that could lead to a broadening of the signal is the binding to macromolecules. It has been described that pTAM can bind to albumin [35]. The binding to albumin leads to a significant decrease in the height of the EPR signal (Fig. S3). It is likely that the EPR spectrum is the combination of a narrow signal (due to free pTAM) and a very broad signal due to bound pTAM to albumin. When analyzing the linewidth of pTAM in the absence or in the presence of albumin (up to 4%, the physiological plasma concentration), we did not observe a larger EPR linewidth for pTAM in the presence of albumin (Fig. S3b). Most importantly, the calibration curves obtained using different concentrations of albumin (from 0 to 4%) did not reveal any change in sensitivity to variations in oxygenation (Fig. 4b). It is likely that the very low modulation amplitude and modulation frequency used for pO_2 and pHe measurements in our study makes the contribution of the broad signal negligible in the EPR spectra. Finally, it should be noted that both probes could interrogate different areas of the experimental tumors. LiPc crystals were implanted one day before the EPR spectroscopy experiment. The volume sampled by the LiPc crystals is limited (around 1–2 mm^3). The solution of pTAM was injected just before the acquisition of the EPR spectrum. Being soluble, pTAM may diffuse more largely in the tumor and we can hypothesize that the probe could access to areas better perfused and therefore with higher pO_2 [59].

Using carbogen breathing, we demonstrated the highest value of the association with LiPc to tackle changes in tissue oxygenation. Regarding the pH_e estimation, carbogen breathing did not lead to significant variation in acidity (Fig. 5a). It is likely that the period of gas breathing was too short to lead to a decrease in pH_e due to the dissolution of CO_2 in the blood. Therefore, to illustrate the dual capability of measuring both pO_2 and pH_e simultaneously, we used a treatment that targets MPC. By blocking the import of pyruvate into the mitochondria, we could expect an increase in extracellular acidity (by blocking lactate uptake and favoring lactate export outside the cell) and a decrease in oxygen consumption rate (by blocking the pyruvate-fueled respiration) [42]. *In vitro*, pTAM detected both extracellular acidification (Fig. 6c) and a decrease in OCR (Fig. 6a). Of note, we previously reported a change in extracellular acidification rate in the same model using the Seahorse XF technology [43], and the results obtained with pTAM regarding the change in OCR were consistent with those observed with the ^{15}N-PDT probe used as a standard for this type of measurement [44–46]. Knowing that the model was responsive to UK-5099 treatment *in vitro*, it was rational to translate these experiments *in vivo*. In animals receiving UK-5099 injection (3 mg/kg) during four days, we observed extracellular acidification, a result that is consistent with our previous study using CEST-MRI and iopamidol as contrast agent [43]. Contrary to our expectations, we did not observe any significant change in tumor oxygenation (Fig. 7f). This observation seems counterintuitive as many treatments that decrease tumor cell metabolism and oxygen consumption have been shown to alleviate tumor hypoxia (as reviewed in Ref. [50]). Our hypothesis is that perfusion effects could counteract the effect on oxygen consumption. As the treatment was applied for four days, the tumors continued to grow. As the pO_2 was measured after four days of treatment, we could assume that a decrease in perfusion could have occurred, masking the effect on oxygen metabolism. At this stage, this remains a hypothesis that would require further investigation.

5. Conclusions

We have shown that the combination of a phosphonated tetrathiatriarylmethyl (pTAM) radical with LiPc crystals allows simultaneous quantitative measurement of pO_2 and pH_e. While the use of the single probe pTAM alone allows the measurement of pH_e and pO_2 from the same site in biological media, this probe suffers from limited sensitivity to oxygen variations. The main advantage of this combination over the use of pTAM alone is the gain in sensitivity to oxygen variations (by a factor of 10). This dual-sensor has been successfully applied in animal models. Incidentally, we also observed that pTAM systematically provided higher pO_2 values than those obtained with LiPc. This new method seems promising for studying the effect of treatments targeting tumor metabolism *in vivo*.

Funding

This research was funded by Fonds National de la Recherche Scientifique (FNRS J008220F and 7463520) (B.G.). C. B is a Televie PhD student. The study used the facilities of the Nuclear and Electron Spin Technologies (NEST) platform of UCLouvain. This study was partially funded by the National Institute of Health (NIH, USA) grants numbers: R00EB023990, R21EB028553, R21GM143595, R01EB032321 (BD).

The funding agency had no role in study design; in the collection, analysis and interpretation of data; in the writing of the report; and in the decision to submit the article for publication.

CRediT authorship contribution statement

Chloe Buyse: Writing – review & editing, Writing – original draft, Validation, Methodology, Investigation, Formal analysis, Data curation. **Lionel Mignion:** Writing – review & editing, Validation, Methodology, Investigation, Formal analysis. **Nicolas Joudiou:** Writing – review & editing, Validation, Software, Methodology, Investigation, Formal analysis. **Samia Melloul:** Writing – review & editing, Investigation, Formal analysis. **Benoit Driesschaert:** Writing – review & editing, Validation, Resources, Investigation, Funding acquisition. **Bernard Gallez:** Writing – review & editing, Writing – original draft, Visualization, Validation, Supervision, Resources, Project administration, Methodology, Funding acquisition, Formal analysis, Conceptualization.

Declaration of competing interest

The authors declare no conflict of interest.

Appendix A. Supplementary data

Supplementary data to this article can be found online at https://doi.org/10.1016/j.freeradbiomed.2024.01.012.

References

[1] D. Hanahan, Hallmarks of cancer: new dimensions, Cancer Discov. 12 (1) (2022) 31–46.
[2] R.J. DeBerardinis, N.S. Chandel, Fundamentals of cancer metabolism, Sci. Adv. 2 (5) (2016) e1600200.
[3] M.G. Vander Heiden, L.C. Cantley, C.B. Thompson, Understanding the warburg effect: the metabolic requirements of cell proliferation, Science 324 (5930) (2009) 1029–1033.
[4] C. Corbet, O. Feron, Tumour acidosis: from the passenger to the driver's seat, Nat. Rev. Cancer 17 (10) (2017) 577–593.
[5] S. Taylor, et al., Microenvironment acidity as a major determinant of tumor chemoresistance: proton pump inhibitors (PPIs) as a novel therapeutic approach, Drug Resist. Updates 23 (2015) 69–78.
[6] P. Vaupel, G. Multhoff, Revisiting the Warburg effect: historical dogma versus current understanding, J. Physiol. 599 (6) (2021) 1745–1757.
[7] B.S. Sorensen, M.R. Horsman, Tumor hypoxia: impact on radiation therapy and molecular pathways, Front. Oncol. 10 (2020) 562.
[8] B. Gallez, The role of imaging biomarkers to guide pharmacological interventions targeting tumor hypoxia, Front. Pharmacol. 13 (2022) 853568.
[9] G. Helmlinger, et al., Interstitial pH and pO2 gradients in solid tumors in vivo: high-resolution measurements reveal a lack of correlation, Nat. Med. 3 (2) (1997) 177–182.
[10] L. Consolino, et al., Non-invasive investigation of tumor metabolism and acidosis by MRI-CEST imaging, Front. Oncol. 10 (2020) 161.

Results

[11] B. Gallez, K. Mader, H.M. Swartz, Noninvasive measurement of the pH inside the gut by using pH-sensitive nitroxides. An in vivo EPR study, Magn. Reson. Med. 36 (5) (1996) 694–697.
[12] D.I. Potapenko, et al., Real-time monitoring of drug-induced changes in the stomach acidity of living rats using improved pH-sensitive nitroxides and low-field EPR techniques, J. Magn. Reson. 182 (1) (2006) 1–11.
[13] D.A. Komarov, et al., In vivo extracellular pH mapping of tumors using electron paramagnetic resonance, Anal. Chem. 90 (23) (2018) 13938–13945.
[14] B. Driesschaert, et al., A phosphonated triarylmethyl radical as a probe for measurement of pH by EPR, Chem. Commun. 48 (34) (2012) 4049–4051.
[15] V. Marchand, et al., In vivo EPR extracellular pH-metry in tumors using a triphosphonated trityl radical, Magn. Reson. Med. 77 (6) (2017) 2438–2443.
[16] B. Gallez, C. Baudelet, B.F. Jordan, Assessment of tumor oxygenation by electron paramagnetic resonance: principles and applications, NMR Biomed. 17 (5) (2004) 240–262.
[17] N. Khan, et al., Repetitive tissue pO2 measurements by electron paramagnetic resonance oximetry: current status and future potential for experimental and clinical studies, Antioxidants Redox Signal. 9 (8) (2007) 1169–1182.
[18] R. Ahmad, P. Kuppusamy, Theory, instrumentation, and applications of electron paramagnetic resonance oximetry, Chem. Rev. 110 (5) (2010) 3212–3236.
[19] M.C. Krishna, et al., Electron paramagnetic resonance imaging of tumor pO(2), Radiat. Res. 177 (4) (2012) 376–386.
[20] B. Epel, H.J. Halpern, In vivo pO2 imaging of tumors: oxymetry with very low-frequency electron paramagnetic resonance, Methods Enzymol. 564 (2015) 501–527.
[21] B. Gallez, et al., Use of nitroxides for assessing perfusion, oxygenation, and viability of tissues: in vivo EPR and MRI studies, Magn. Reson. Med. 35 (1) (1996) 97–106.
[22] M. Elas, et al., Electron paramagnetic resonance oxygen images correlate spatially and quantitatively with Oxylite oxygen measurements, Clin. Cancer Res. 12 (14 Pt 1) (2006) 4209–4217.
[23] B.F. Jordan, C. Baudelet, B. Gallez, Carbon-centered radicals as oxygen sensors for in vivo electron paramagnetic resonance: screening for an optimal probe among commercially available charcoals, Magma 7 (2) (1998) 121–129.
[24] M. Lan, et al., Carbon blacks as EPR sensors for localized measurements of tissue oxygenation, Magn. Reson. Med. 51 (6) (2004) 1272–1278.
[25] K.J. Liu, et al., Lithium phthalocyanine: a probe for electron paramagnetic resonance oximetry in viable biological systems, Proc. Natl. Acad. Sci. U. S. A. 90 (12) (1993) 5438–5442.
[26] G. Ilangovan, et al., A naphthalocyanine-based EPR probe for localized measurements of tissue oxygenation, Free Radic. Biol. Med. 32 (2) (2002) 139–147.
[27] R.P. Pandian, et al., Molecular packing and magnetic properties of lithium naphthalocyanine crystals: hollow channels enabling permeability and paramagnetic sensitivity to molecular oxygen, J. Mater. Chem. 19 (24) (2009) 4138–4147.
[28] Y. Liu, F.A. Villamena, J.L. Zweier, Highly stable dendritic trityl radicals as oxygen and pH probe, Chem. Commun. 36 (2008) 4336–4338.
[29] Y. Liu, et al., Synthesis of ^{14}N- and ^{15}N-labeled trityl-nitroxide biradicals with strong spin-spin interaction and improved sensitivity to redox status and oxygen, J. Org. Chem. 75 (22) (2010) 7796–7802.
[30] Y. Liu, et al., Trityl-nitroxide biradicals as unique molecular probes for the simultaneous measurement of redox status and oxygenation, Chem. Commun. 46 (4) (2010) 628–630.
[31] Y. Feng, et al., Trityl quinodimethane derivatives as unimolecular triple-function extracellular EPR probes for redox, pH, and oxygen, Anal. Chem. 95 (2) (2023) 1057–1064.
[32] G. Ilangovan, et al., In vivo measurement of regional oxygenation and imaging of redox status in RIF-1 murine tumor: effect of carbogen-breathing, Magn. Reson. Med. 48 (4) (2002) 723–730.
[33] I. Dhimitruka, et al., Phosphonated trityl probes for concurrent in vivo tissue oxygen and pH monitoring using electron paramagnetic resonance-based techniques, J. Am. Chem. Soc. 135 (15) (2013) 5904–5910.
[34] T.D. Gluth, et al., Large-scale synthesis of a monophosphonated tetrathiatriarylmethyl spin probe for concurrent in vivo measurement of pO2, pH and inorganic phosphate by EPR, RSC Adv. 11 (42) (2021) 25951–25954.
[35] T.D. Gluth, et al., Biocompatible monophosphonated trityl spin probe, HOPE71, for in vivo measurement of pO(2), pH, and [P(i)] by electron paramagnetic resonance spectroscopy, Anal. Chem. 95 (2) (2023) 946–954.
[36] B. Gallez, et al., Pharmacological modifications of the partial pressure of oxygen in murine tumors: evaluation using in vivo EPR oximetry, Magn. Reson. Med. 42 (4) (1999) 627–630.
[37] M. Elas, et al., Quantitative tumor oxymetric images from 4D electron paramagnetic resonance imaging (EPRI): methodology and comparison with blood oxygen level-dependent (BOLD) MRI, Magn. Reson. Med. 49 (4) (2003) 682–691.
[38] T.T. Cao-Pham, et al., Monitoring tumor response to carbogen breathing by oxygen-sensitive magnetic resonance parameters to predict the outcome of radiation therapy: a preclinical study, Int. J. Radiat. Oncol. Biol. Phys. 96 (1) (2016) 149–160.
[39] H.G. Hou, et al., Temporal variation in the response of tumors to hyperoxia with breathing carbogen and oxygen, Med. Gas Res. 6 (3) (2016) 138–146.
[40] K.I. Matsumoto, J.B. Mitchell, M.C. Krishna, Effects of oxygen challenging to tissue redox and pO(2) status, Free Radic. Biol. Med. 130 (2019) 343–347.
[41] B.P.J. van der Sanden, A. H, L. Hoofd, A.W. Simonetti, K. Nicolay, A. van der Toorn, W.N.J.M. Colier, A.J. van der Kogel, Effect of carbogen breathing on the physiological profile of human glioma xenografts, Magn. Reson. Med. (42) (1999) 490–499.
[42] C. Corbet, et al., Interruption of lactate uptake by inhibiting mitochondrial pyruvate transport unravels direct antitumor and radiosensitizing effects, Nat. Commun. 9 (1) (2018) 1208.
[43] C. Buyse, et al., Impact of inhibition of the mitochondrial pyruvate carrier on the tumor extracellular pH as measured by CEST-MRI, Cancers 13 (17) (2021).
[44] C. Diepart, et al., Comparison of methods for measuring oxygen consumption in tumor cells in vitro, Anal. Biochem. 396 (2) (2010) 250–256.
[45] D. d'Hose, et al., A versatile EPR toolbox for the simultaneous measurement of oxygen consumption and superoxide production, Redox Biol. 40 (2021) 101852.
[46] D. d'Hose, B. Gallez, Measurement of mitochondrial (Dys)Function in cellular systems using electron paramagnetic resonance (EPR): oxygen consumption rate and superoxide production, Methods Mol. Biol. 2497 (2022) 83–95.
[47] C. Baudelet, B. Gallez, Effect of anesthesia on the signal intensity in tumors using BOLD-MRI: comparison with flow measurements by Laser Doppler flowmetry and oxygen measurements by luminescence-based probes, Magn. Reson. Imaging 22 (7) (2004) 905–912.
[48] J.C. Walsh, et al., The clinical importance of assessing tumor hypoxia: relationship of tumor hypoxia to prognosis and therapeutic opportunities, Antioxidants Redox Signal. 21 (10) (2014) 1516–1554.
[49] R.J. Gillies, R.A. Gatenby, Metabolism and its sequelae in cancer evolution and therapy, Cancer J. 21 (2) (2015) 88–96.
[50] B. Gallez, et al., Manipulation of tumor oxygenation and radiosensitivity through modification of cell respiration. A critical review of approaches and imaging biomarkers for therapeutic guidance, Biochim. Biophys. Acta Bioenerg. 1858 (8) (2017) 700–711.
[51] S.R. Pillai, et al., Causes, consequences, and therapy of tumors acidosis, Cancer Metastasis Rev. 38 (1–2) (2019) 205–222.
[52] S. Naz, et al., Imaging metabolic processes to predict radiation responses, Semin. Radiat. Oncol. 29 (1) (2019) 81–89.
[53] W. Blaszczak, P. Swietach, What do cellular responses to acidity tell us about cancer? Cancer Metastasis Rev. 40 (4) (2021) 1159–1176.
[54] M. Garcia-Caballero, et al., Metabolic reprogramming in tumor endothelial cells, Int. J. Mol. Sci. 23 (19) (2022).
[55] A.A. Bobko, et al., Trityl radicals as persistent dual function pH and oxygen probes for in vivo electron paramagnetic resonance spectroscopy and imaging: concept and experiment, J. Am. Chem. Soc. 129 (23) (2007) 7240–7241.
[56] I. Dhimitruka, et al., Synthesis and characterization of amino derivatives of persistent trityl radicals as dual function pH and oxygen paramagnetic probes, J. Am. Chem. Soc. 130 (32) (2008) 10780–10787.
[57] A.A. Bobko, et al., Dual-function pH and oxygen phosphonated trityl probe, Anal. Chem. 84 (14) (2012) 6054–6060.
[58] V.V. Khramtsov, In vivo molecular electron paramagnetic resonance-based spectroscopy and imaging of tumor microenvironment and redox using functional paramagnetic probes, Antioxidants Redox Signal. 28 (15) (2018) 1365–1377.
[59] T.D. Eubank, et al., In vivo electron paramagnetic resonance molecular profiling of tumor microenvironment upon tumor progression to malignancy in an animal model of breast cancer, Mol. Imag. Biol. (2023).
[60] P.E. Schaner, et al., First-in-human study in cancer patients establishing the feasibility of oxygen measurements in tumors using electron paramagnetic resonance with the OxyChip, Front. Oncol. 11 (2021) 743256.
[61] H.M. Swartz, J.F. Glockner, in: G.R. Eaton, S.S. Eaton, K. Ohno (Eds.), Measurement of Oxygen by EPRI and EPRS. EPR Imaging and in Vivo EPR, 1991, pp. 261–290.
[62] M.A. Shaw, et al., SOX71, A biocompatible succinyl derivative of the triarylmethyl radical OX071 for in vivo quantitative oxygen mapping using electron paramagnetic resonance, Mol. Imag. Biol. (2023).
[63] V.A. Atsarkin, et al., Mechanism of oxygen response in carbon-based sensors, J. Magn. Reson. 149 (1) (2001) 85–89.
[64] P. Turek, M. Moussavi, J.J. André, Magnetic properties of the lithium phthalocyanine π-radical. Role of dioxygen, Europhys. Lett. 8 (3) (1989) 275–280.
[65] F. Bensebaa, P. Petit, J.J. André, The effect of oxygen on phthalocyanine radicals II. Comparative study of two lithium phthalocyanine powder derivatives by continuous and pulsed ESR, Synth. Met. 52 (1) (1992) 57–69.
[66] B. Gallez, Oxygenation status in normal tissues, pathological tissues and malignant tumors: a pO2 database based on electron paramagnetic resonance (EPR) oximetry measurements, Appl. Magn. Reson. 52 (10) (2021) 1395–1450.
[67] P. Vaupel, A.B. Flood, H.M. Swartz, Oxygenation status of malignant tumors vs. Normal tissues: critical evaluation and updated data source based on direct measurements with pO2 microsensors, Appl. Magn. Reson. 52 (10) (2021) 1451–1479.
[68] A.A. Bobko, et al., In vivo EPR assessment of pH, pO2, redox status, and concentrations of phosphate and glutathione in the tumor microenvironment, J. Vis. Exp. 133 (2018) 56624.
[69] B. Epel, et al., Absolute oxygen R1e imaging in vivo with pulse electron paramagnetic resonance, Magn. Reson. Med. 72 (2) (2014) 362–368.

Sensitive simultaneous measurements of oxygenation and extracellular pH by EPR using a stable monophosphonated trityl radical and lithium phthalocyanine.

Chloe Buyse[1], Lionel Mignion[2], Nicolas Joudiou[2], Samia Melloul[1], Benoit Driesschaert[3], and Bernard Gallez[1]

Supplementary figures

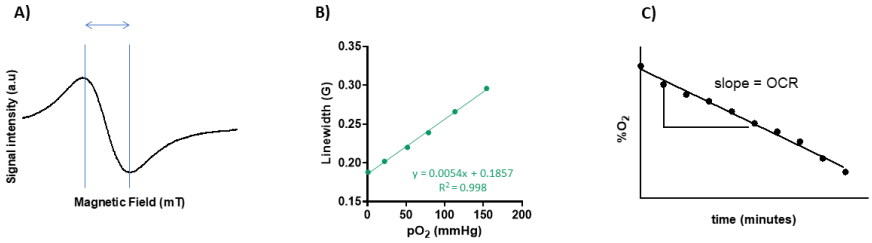


Fig. S1: Principle of OCR measurement. A) Measurement of the EPR linewidth of the low-field signal of ^{15}N-PDT. B) Calibration curve of the EPR linewidth as a function of pO_2. C) Plot of the evolution of the oxygen concentration as function of time in a sealed tube containing the tumor cells in the presence of the oxygen sensor ^{15}N-PDT. The resulting slope represents the OCR.

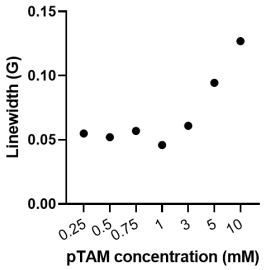


Fig. S2: Effect of pTAM concentration on the EPR linewidth. No self-broadening was observed up to 3 mM. An increase in the linewidth was observed at higher concentration (5 and 10 mM).

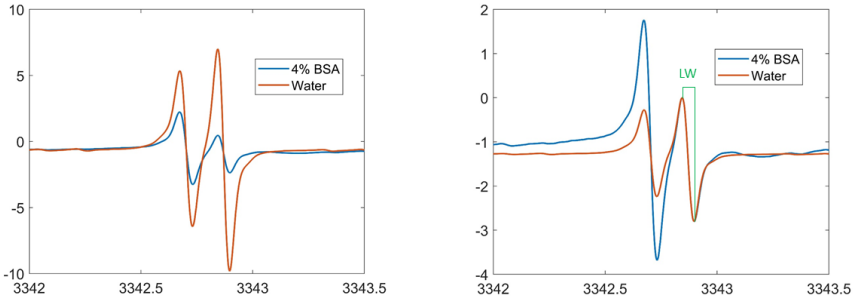


Fig. S2: Effect of the presence of albumin on the EPR spectrum of pTAM. Spectra recorded using pTAM 200 µM in the absence or in the presence of bovine serum albumin (BSA) 4%, the physiological plasma concentration. A) Influence of BSA on the EPR signal of pTAM (recorded in 21% O_2). Note the important decrease in EPR signal height. B) Comparison of EPR linewidth (LW, focused on the high field peak) recorded in the absence of oxygen. The EPR spectra were normalized for signal intensity on the high field peak to allow the visual comparison of linewidth. Note that both EPR spectra (in the presence or in the absence of albumin) overlap indicating no significant influence of BSA on the EPR linewidth.

Discussion and perspectives

1. Main achievements of the thesis

There is a need for biomarkers that can predict which tumor could benefit from treatment targeting metabolism. Our goal was to establish the value of non-invasive Magnetic Resonance biomarkers, measuring pH_e and pO_2, as biomarkers of therapeutic efficacy. The results obtained in this thesis assessed the value of different magnetic resonance techniques: ^{31}P-NMR, CEST-MRI and EPR spectroscopy in the context of therapeutic treatment efficacy.

We were interested in the effects of two different pharmacological treatments targeting tumor metabolism. In this part, we will discuss our results, as well as their limitations.

1.1. pH_e measurements using ^{31}P-NMR and CEST-MRI

^{31}P-NMR has been used for a long time to assess pH_e with 3-APP [92, 139, 268, 269] but also other metabolites, such as ATP, P_i and PCr [270, 271].

Compared to the well-established ^{31}P-NMR, CEST-MRI is more recent. AcidoCEST-MRI has been used to measure pH_e in various studies and has recently been shown to be able to assess the treatment response to various drugs targeting different metabolic pathways by measuring tumor pH changes [152, 153, 163, 166, 167, 272-275].

We first evaluated the effect of an inhibitor of the mitochondrial pyruvate carrier, UK-5099. We found that, while both methods were able to measure pH_e, only CEST-MRI was able to measure a significant acidification of pH_e values in vivo. CEST-MRI offers a high spatial resolution and the possibility to obtain parametric images, which allowed us to assess tumor heterogeneity. CEST-MRI was further used to measure potential modifications of pH_e in vivo after

treatment with a MCT inhibitor, syrosingopine. Once again, we were able to map pH_e values inside tumors before and after treatment with syrosingopine, but no shift in pH_e values was measured.

While we were able to measure pH_e in tumors using ^{31}P-NMR, a change in pH_e was expected after treatment with UK-5099 but was not reported. In addition, only a mean pH_e value inside the tumor can be assessed with ^{31}P-NMR.

1.2. pO_2 measurements

Oxygen is another relevant biomarker that can be assessed with the well-described technique, EPR spectrometry, which has been proven numerous times to be able to measure oxygen with nitroxides, trityl radicals or particulate probes [183, 184, 199, 276].

We investigated the relevance to use a novel probe, the mono-phosphonated trityl radical pTAM, whose spectrum was reported to be sensitive to both parameters of interest, pH_e and pO_2, to follow the changes in those parameters after a treatment targeting metabolism.

We combined this soluble trityl radical with lithium phthalocyanine crystals and were able to measure both pH_e and pO_2 simultaneously in vivo after a treatment with UK-5099. Significant modifications of pH_e values were measured with pTAM on the L-band EPR spectrometer.

2. Limitations, unsolved questions and perspectives

2.1. Methodological/technical issues

2.1.1. Discrepancies between ^{31}P-NMR and CEST-MRI

While both methods were capable of measuring pH_e values, ^{31}P-NMR gave us limited information compared to CEST-MRI in the context of following changes in pH_e values induced by a pharmacological treatment.

For each tumor, we are able to get a ^{31}P spectrum, from which we can calculate a mean pH_e value. The region of interest was selected by placing saturation bands to filter the signal, in order to only get signal from the tumor. No significant effect of the treatment with UK-5099 was measured with ^{31}P-NMR, which could be explained by the presence of residual muscle tissue in the region of interest, as confirmed by the presence of phosphocreatine in some spectra.

On the other hand, CEST-MRI provided high resolution parametric images of pH_e from slices placed in the center of the tumors (0.44 µl/voxel), highlighting the heterogeneity of response within each tumor when exposed to UK-5099 but no significant changes when mice were treated with syrosingopine. However, even if the results showed a significant decrease in pH_e after a treatment with UK-5099 in tumors, a modest 0.22 pH units difference was measured, with only 16% of the voxels showing a shift to pH_e values under 7.0. Nonetheless, this small proportion of shift was sufficient to induce a significant shift towards more acidic values.

It is worth noting that the pH_e values measured with CEST-MRI were slightly higher than the ones measured with ^{31}P-NMR. This could be explained by the

differences in analysis position mentioned in the previous paragraphs. Moreover, it is important to discuss and compare the volumes of analysis between ^{31}P-NMR and CEST-MRI. While it is possible to calculate the volume of analysis in CEST-MRI, it is more complicated for ^{31}P-NMR. Indeed, in CEST-MRI, a single slice is placed in the center of the tumor and several characteristics, such as the field of view, matrix size and slice thickness, are defined and used to measure the volume of analysis. In ^{31}P-NMR, as the volume of analysis is defined by the placement of saturation bands, it is more complicated to have a define value for the volume of analysis, as it varies from mice to mice.

This represents a discrepancy between the two techniques, as the size of analysis for CEST-MRI is ultimately much smaller (size of a voxel = 0.44 µl) compared to the size of analysis in ^{31}P-NMR.

2.1.2. Discrepancies with other studies

In addition, our basal pH_e values were over 7.0 before treatment, for both our techniques, while a different study measured a basal pH_e of 6.96 ± 0.03, in the same 4T1 tumor model, measured by CEST-MRI [277].

We hypothesized that this discrepancy between our experiments and theirs could be due to differences in the forms of anesthesia that were used. Indeed, our experiments were done using isoflurane, whereas they used ketamine/xylazine. However, ketamine/xylazine was shown to induce a rapid drop in tumor perfusion and oxygenation, potentially affecting pH_e values [234, 278, 279].

Another possible explanation is that our CEST measurements were only done on post-contrast images. Recent studies proposed that measuring the difference between the CEST contrast after iopamidol injection, compared to the one before iopamidol injection implies that only the CEST contribution due to

iopamidol is measured, removing the endogenous contribution [164, 277, 280]. We applied this method for our experiments on the evaluation of syrosingopine's effects on pH_e values.

2.1.3. Measurement of pH_e and pO_2 using EPR

While pTAM is theoretically capable of measuring both pH_e and pO_2 simultaneously [184], we noticed that in the context of our work, its sensitivity to measure pO_2 changes was limited. We decided to combine it with LiPc crystals, which has been used in oximetry [281]. However, as explained in the "*Insoluble particulate probes*" section of this work, carbon-based materials have a higher sensitivity at small pO_2 values. While it could have been an advantage for our experiment, carbon-based materials present a broad linewidth, which would have superimposed with the spectrum lines of pTAM, making it impossible to combine both probes.

We, as well as others, have found that pTAM systematically overestimates pO_2 values [282]. Usually, in hypoxic regions in tumors in vivo, pO_2 values are about 10 mmHg, or less [241, 283]. In our study, pTAM reported values ten times higher than that, sometimes going up to 150 mmHg.

The use of a new monophosphonated trityl radical, HOPE71, derived from the trityl probe Ox071 could resolve this. It was showed that while HOPE71 and pTAM have comparable X-band and L-band sensitivities, HOPE71 offers biocompatibility improvements [284]. In addition, it does not bind to albumin and can thus be administered intravenously without any effect on the intensity of its signal. Most importantly, a systemic administration of HOPE71 could possibly offer a more even diffusion throughout the tumor and erase a self-

broadening of the probe due to a high concentration found at the injection site [188].

To overcome the self-broadening due to concentration effects, it has been proposed to measure T_1 relaxation times instead of T_2, by pulsed EPR spectrometers, as T_1 relaxation times are much less sensitive to concentration effect [249]. Some studies have shown that it is possible to measure pO_2 values using trityl by pulsed EPR [249, 285-288].

As CEST MRI provides parametric maps of pH_e, giving us an idea about the heterogeneity inside tumors, it would be interesting to have more than a mean pO_2 value for each tumor. As acidosis and hypoxia could be closely related, it would be interesting to correlate both parameters and follow their evolution after treatment. In this context, it is interesting to note that Helmlinger et al. [289], using microelectrodes, showed in 1997 that there was no correlation between interstitial pH and pO_2 gradients in human colon adenocarcinoma tumors in vivo (Figure 36).

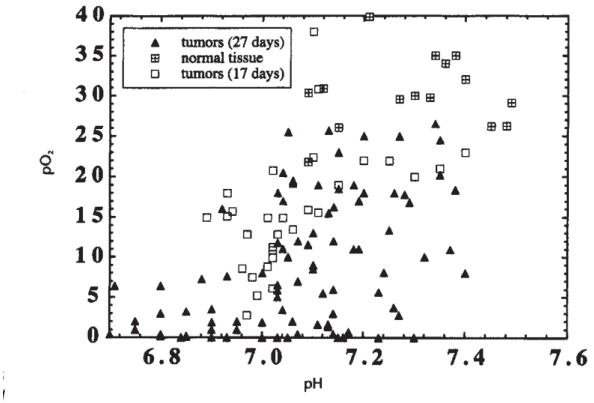


Figure 36 – pO_2 as a function of pH. There is no correlation between pO_2 and pH: for the same pO_2, a large dispersion of pH values is observed as well as for the same pH, many pO_2 are recorded. Original figure from Helmlinger **[289]**.

2.1.4. Accuracy of calibrations

In addition to position and volume of analysis that differ between the techniques, accuracy of calibration could possibly impact the results.

While we only performed our calibration in vitro in solutions, we cannot exclude that calibrations in tumor tissue homogenates could have given slightly different results. For CEST MRI, the group of Longo et al. have compared calibration measured in PBS with measurements in tumor tissue homogenates. Interestingly, they found that the ratiometric values were very similar [164].

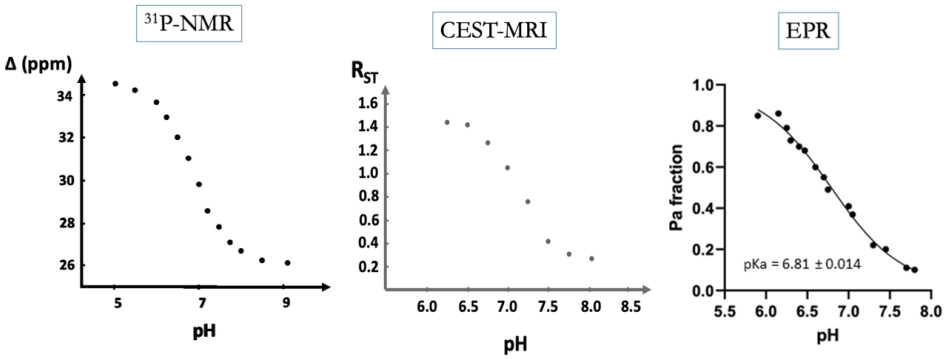


Figure 37 – Comparison of the calibration curves.

In our work, we have not fully evaluated the precision of the pH estimation using the different methods. This would have been interesting to perform.

Of note, in previous works the accuracy of acidoCEST was evaluated for iopromide and iopamidol. Iopamidol was found to present a standard deviation of precision (SDP) of 0.04 pH units and a R^2 value of 0.99 compared to iopromide that presented an SDP of 0.13 pH units and a R^2 of 0.93 [290].

Another study has shown that iopamidol is able to measure tumor pH_e with an accuracy of 0.034 pH units [123].

The accuracy of pH measurements with triarylmethyl radicals is about 0.05 pH units [185].

Lastly, it is important to keep in mind that the three techniques are investigating pH_e values differently. The pH_e measurements with ^{31}P-NMR is dependent on the tumor volume, placed on a surface coil and only gives a mean pH_e value for the whole tumor. CEST MRI is used with a volume coil, the whole tumor being integrated while pH_e values are only measured in one slice placed in the center of this tumor. Finally, L-band EPR is limited to a penetration depth of 1 cm inside the tissue of interest along with also giving only a mean pH_e value for the tumor volume, which could represent an obstacle for accurate measurements in bigger tumors.

2.1.5. Probe distribution

Probe distribution within the tissue of interest, as well as sufficient probe concentration are crucial components of getting good signal. Probe distribution is highly dependent on the vasculature and perfusion of the tissue. As tumor vasculature is often chaotic, this can represent a problem. Keeping that in mind, we performed our experiments after researching the best concentration to use.

Gillies et al. [139] reported that an intraperitoneal injection of 63.8 mg/ml of 3-APP resulted in an extracellular concentration of 15 mM and a clearly separable ^{31}P-NMR signal, while Raghunand et al. used a dose of 128 mg/ml [92]. We chose to work at a dose of 75 mg/ml.

Even though the CEST MRI measurements are not dependent on the concentration (ratiometric measurements), a sufficient local concentration of iopamidol is needed. Some of the work from the research group of Pr. Pagel has shown that while estimating in vivo concentrations of iopamidol is challenging, a minimum of 15-20 mM (this interval changes depending on the T_1 of the tissue) of iopamidol is needed for clinical CEST MRI at 3T [163, 291, 292]. This concentration could be hard to reach in some regions of the tumor, which could explain why we can sometimes observe tumor areas with no calculated pH_e values.

For our L-band EPR experiments, we were conflicted between getting a sufficient local probe concentration and avoiding the self-broadening of the probe, which happens at high concentrations. Several concentrations were tested and the chosen concentration was the one we deemed best matched those two conditions (Figure found in the supplementary data of "Sensitive simultaneous measurements of oxygenation and extracellular pH by EPR using a stable monophosphonated trityl radical and lithium phthalocyanine").

2.1.6. Clinical translation

2.1.6.1. ^{31}P-NMR

^{31}P-NMR has been used in clinical trials to measure ATP, Pi and PCr in the brain of Parkinson's disease patients [271] on a 3T MRI or to measure pH_i [117]. So far, it has not yet been used for the measurement of pH_e with 3-APP. Since our studies have been performed on an 11.7T Biospec MRI, it would be important to reproduce the experiments and obtain the same results in a clinical setting, with a lower magnetic field, usually 1.5 or 3T.

2.1.6.2. CEST-MRI

One major advantage of iopamidol is that it is already FDA-approved and used in the clinical setting as a contrast agent for CT scans. However, high doses of iopamidol need to be injected, which can lead to adverse effects, including renal failures or thyroid disorders. Furthermore, our protocol for CEST-MRI has a relatively long acquisition time (27 minutes), which represents a hindrance for clinical translation. To reduce the time of acquisition, spatial resolution can be decreased.

As described in the "*Clinical applications of CEST-MRI*" section of this work, iopamidol has been administered in the knee cartilage of patients, where pH_e was measured on a 3T clinical MRI scanner [173]. Once again, before thinking of moving on to clinical studies, we need to confirm our experiments on a lower magnetic field.

2.1.6.3. EPR spectroscopy

Clinical EPR spectroscopy is now started to be viewed as a potential standard clinical practice to measure pO_2 [293]. India Ink, safely used in tattoos, has been investigated for its possible use in oximetry in humans [294, 295]. One clinical study has shown that it is possible to implant an oxygen sensor, the "OxyChip", which is composed of embedding lithium octa-butoxynaphthalocyanine (LiNc-BuO) crystals in the oxygen-permeable polymer polydimethylsiloxane (PDMS) to measure pO_2 in humans on a 1.15 GHz EPR scanner [30].

The implantation of particulate probes, although rather invasive, has the advantage of allowing a continuous following of the pO_2 evolution. The use of soluble probe could also allow a following of the evolution in pO_2, but with the

need to be injected before each experiment. Moreover, trityl probes still need to be approved by the European Medicines Agency (EMA) and the Food and Drug Administration (FDA).

2.2. (Patho)physiological issues

2.2.1. Cell models

2.2.1.1. Selected cell models

The effects of two different pharmacological treatments on tumor pH_e and pO_2 have been studied: UK-5099, a mitochondrial pyruvate carrier inhibitor and syrosingopine, an monocarboxylate transporter inhibitor.

We based our work on the study of Corbet et al [216] who had demonstrated that an inhibition of MPC using 7ACC2, an analog of UK-5099, leads to an increased extracellular acidification rate in vitro in SiHa cells. As we first wanted to validate our methods, we needed a treatment which we knew could possibly induce a shift in pH_e. We worked with the murine triple-negative breast cancer model 4T1. As we measured a shift in pH_e after a treatment with UK-5099, we decided to continue with the same cell model for the EPR studies.

We evaluated the effects of syrosingopine first in vitro in two different cell lines: the human triple-negative breast cancer model MDA-MB-231 and the human head and neck squamous cell carcinoma model FaDu, which were chosen for their differences in expression of MCTs. Indeed, MDA-MB-231 cells only express MCT4, whereas FaDu cells express both MCT1 and MCT4. MDA-MB-231 cells are also known for being more glycolytic while FaDu cells depend more on oxidative metabolism. As the results we observed when treating cells with

syrosingopine were more pronounced in the MDA-MB-231 model, we carried out our in vivo experiments using this cell model.

In addition to studying the normal phenotype of our models of interest, it could have been interesting to add to our experiments small interfering RNA (siRNA) or short hairpin RNA (shRNA) targeting MPC or MCT1/4, expressed in a plasmid only transfected in the models of our choice, limiting the effect of the downregulation to our cell models.

2.2.1.2. Other models

Other cell models could also have been chosen. First, we studied the effects of those molecules only on immortal cells. Even if their general characteristics are well-described online, because they are cultured for the time of the experiments, they are subject to potential phenotype changes, that we do not know about. Even though a control condition is always assessed, it can be of added value to study the effects on normal non-immortal cells.

The effects and contribution to pH_e and pO_2 changes of a treatment with UK-5099 and syrosingopine could be investigated in other cells of the TME, as it is known that cancer cells do not represent the majority of cells present in the TME.

- *TECs and CAFs*

It was found that stromal cells of the tumor microenvironment are involved in at least seven of the hallmarks of cancer, including activation of invasion and metastasis, inducing of angiogenesis or resisting cell death [296]. Tumor-derived vascular endothelial cells (TECs) were shown to play a role in tumor progression

and metastasis by releasing "angiocrine factors" such as growth factors or chemokines [297]. It was shown that, in endothelial cells under hypoxia, an accumulation of ROS could lead to the upregulation of HIF-1α, which increases PI3K and PKC signaling, resulting in the increased expression of GLUT1 and HK2 [298].

Cancer-associated fibroblasts (CAFs) have an important implication in cancer progression [296, 299]. Indeed, CAFs can express and secrete signaling proteins, such as TGF-β, associated to an epithelial-to-mesenchymal transition [296]. Cancer cells can secrete ROS and induce oxidative stress in surroundings fibroblasts, leading to aerobic glycolysis and production of lactate, fatty acids and ketone bodies, metabolites representing high energy fuels. Lactate is exported out of the fibroblasts by MCT4, creating a metabolic symbiosis with cancer cells which can uptake this lactate via MCT1 [300].

As MPC [301, 302] and MCT4 [300, 303] are expressed in TECs and CAFs, both of which play such an important role in tumor metabolism, it would be interesting to evaluate the effects of our inhibitors, UK-5099 and syrosingopine, first on TECs and CAFs alone. To further investigate the relationship between cancer cells, endothelial cells and fibroblasts and to have a more representative model, a three-dimensional spheroid coculture could have been an option.

- *Immune cells*

The study of immune cells could have been an interesting addition to this work. Indeed, extracellular acidosis and hypoxia are important factors that contribute to immunotherapy resistance. Immune cells are highly dependent on the glycolytic pathway for their proliferation, survival and activity. This means that

they participate to the extracellular accumulation of lactate and H^+ ions. Hypoxia can modify the function and proliferation of T lymphocytes [304].

Once again, it would have been interesting to study the effect of a treatment with UK-5099 and syrosingopine on immune cells alone, before studying a coculture of immune and tumor cells, in normoxia and in hypoxic conditions. It has been shown that an inhibition of MPC in T cells does not affect their effector function but promotes their differentiation [217]. Extracellular lactate and H^+ ions importantly impact the proliferation and cytokine production of cytotoxic T cells and natural killer cells [39, 305]. Thus, a treatment with an MCT inhibitor such as syrosingopine leading to a decrease in lactate secretion, could have an impact on the metabolism, proliferation and activity of immune cells.

One more perspective is to use pH_e and pO_2, as biomarkers to follow changes when treating mice with modulators of pH_e and pO_2, used as immunotherapy sensitizers. It has been demonstrated that increasing tumor pH_e with $NaHCO_3$ could impair tumor growth of a B16 melanoma murine model and was associated with increased T cell infiltration [306].

- *Other cancer cell models*

To have a better overview of how our inhibitors can affect tumor metabolism, it would be interesting to compare more cancer cell models. For the EPR experiments for example, we only evaluated the impact of UK-5099 in one tumor cell model. It could have been interesting to investigate the impact of UK-5099 on SiHa cells, as it was done in the first experiment, when comparing 4T1 and SiHa cells.

2.2.1.3. Different cell culture conditions

As discussed in the "Hypoxia" part of this work, cells can respond and adapt to hypoxia by activating signaling pathways to maintain their proliferation. This induces changes in the expression of transporters and enzymes involved in glucose metabolism, such as GLUT1, LDHA but also carbonic anhydrase IX, which generates H^+ ions. As hypoxia can affect the metabolism of cancer cells but also of other cells present in the TME, and thus could influence the response to our inhibitors, studying the metabolism of cells under hypoxia is important. Moreover, studying cells under hypoxia allows to be closer to in vivo conditions.

2.2.1.4. Different induction sites

We have worked only with ectopic models, always injecting our cells in the leg muscle of mice. We cannot exclude that we could have obtained different results if we would have injected our models orthotopically, in the mammary fat pad.

When comparing subcutaneous with orthotopic SKOV3 ovarian tumors, Jones et al. [292] have found that there was a difference in the growing rate of tumors, depending on their implantation sites, the orthotopic tumors never reaching the same size as the subcutaneous tumors. Second, the subcutaneous tumors showed a decrease in pH_e, measured with CEST MRI, as the tumor volume increased when no relationship between pH_e and tumor volume was found for the subcutaneous tumors.

Ho et al. [307] have compared the vasculature between MDA-MB-231-H2N tumors injected either orthotopically in the mammary fat pad or subcutaneously. They found that the subcutaneous tumors required longer development times to reach the same size as the orthotopic tumors. They observed differences in

vasculature with orthotopic tumors presenting a greater permeability to macromolecules. This could influence pH_e values.

However, the research group of Pr. Pagel has found that 4T1 tumors implanted orthotopically in the mammary fat pad compared to subcutaneously on the right rear flank showed no difference in pH_e. Contrary to previously cited work, they observed that the subcutaneous model grew faster than the orthotopic model and presented a slightly more acidic pH_e (M. Pagel, personal communication).

In conclusion, implantation sites seem to impact the growing rate of tumors. Faster-growing tumors should be metabolically more active and potentially present a lower pH_e.

2.2.2. Metabolism issues

While the main objective of this thesis was not to study metabolism by itself but the value of imaging biomarkers, some issues regarding the consequences of the treatments applied could be investigated.

Why do cells consume more glucose when their mitochondrial metabolism is altered?

Our experiments were done with medium containing glucose. If the entry of pyruvate inside the mitochondria is altered by a treatment with UK-5099, their oxidative phosphorylation will be hindered. However, glucose-derived pyruvate is not the only nutrient that can fuel the mitochondrial respiration. Indeed, depending on their environment, cells can adapt and rely on different nutrient sources for their biosynthesis requirements. Cells can use glutamine which can follow an oxidative metabolism, converted to α-ketoglutarate by the glutamate dehydrogenase, then oxidized to succinate, that fuels the TCA cycle [40, 45, 308].

This was confirmed by the fact that no differences in OCR were observed, with or without UK-5099 treatment, as our medium contained glutamine.

It is important to note that glutamine is not the only nutrient that can fuel the TCA cycle. The short-chain fatty acid acetate has been shown to be able to be completely oxidized and used as an energy source for the TCA cycle, in glioblastoma and metastases of the central nervous system [309]. However, there was no acetate in our culture medium.

It is also important to note that the modest effect observed after UK-5099 treatment in vivo could also be explained by the fact that glucose-derived pyruvate can be converted into malate or alanine, which can enter mitochondria and fuel the TCA cycle, without the need for MPC, as described in Figure 38. This means that cells do not completely rely on glycolysis when MPC is inhibited, highlighting the high plasticity of cell metabolism in vivo.

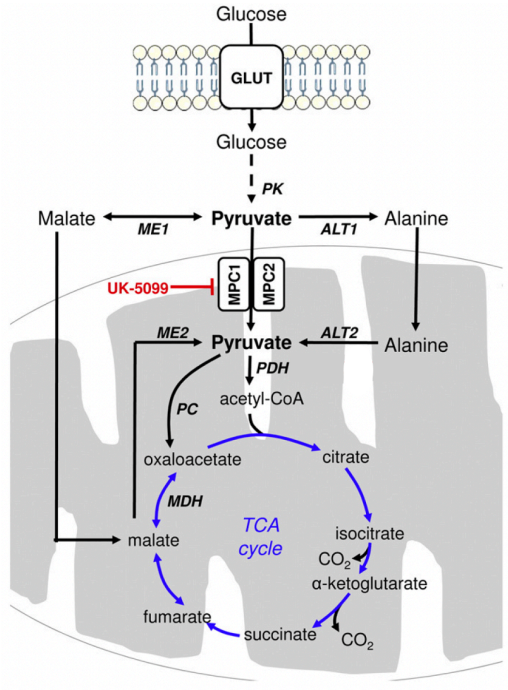


Figure 38 – Pyruvate oxidative metabolism. When the entry of glucose-derived pyruvate inside the mitochondria via MPC is inhibited by UK-5099, it can also be converted into malate or alanine, by malic enzymes (ME1 and ME2) and alanine aminotransferase (ALT1 and ALT2), respectively. Adapted figure from Corbet and Feron [51].

2.2.3. Open questions about metabolic plasticity

Overall, when looking at the in vivo results, from the modest shift of tumor pH_e induced by UK-5099 to no visible effects of syrosingopine, one common explanation is the metabolic plasticity. Indeed, when one specific metabolic pathway is targeted by a pharmacological drug, metabolites upstream of the inhibition will accumulate, or downstream metabolites concentration will decrease, leading the cancer cells to shift their metabolism to another metabolic pathway, to continue filling their biosynthesis needs. Vander Linden et al. [119] have shown that when targeting one metabolic pathway, it creates a metabolic

addition that can be targeted by a transient exposure to another therapeutic agent (Figure 39).

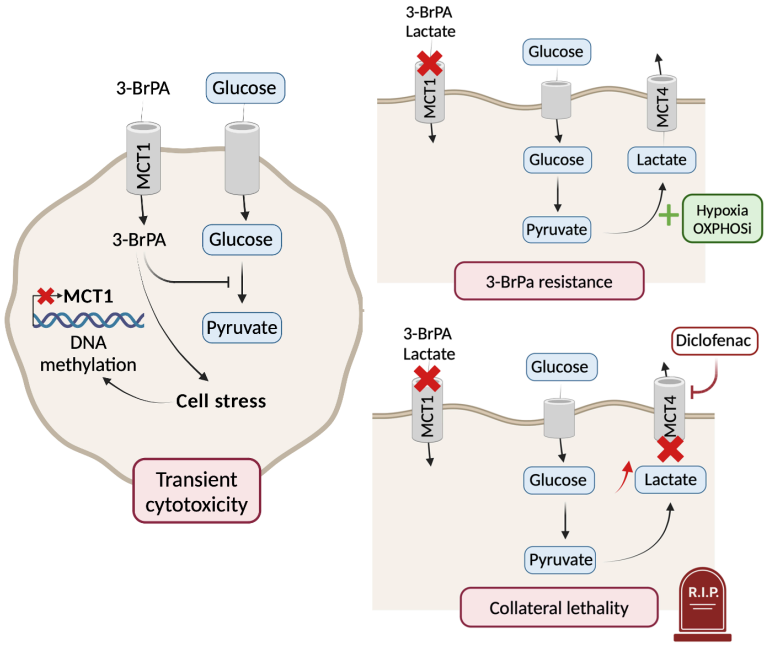


Figure 39 – Drug-induced shift in metabolism, followed by metabolic dependence to a pathway. Treatment with 3-BrPA induces the DNA methylation of MCT1's promotor, silencing its expression. 3-BrPA-resistant cells now rely on glycolysis and lactate export through MCT4. Cells are now vulnerable to MCT4 inhibition with diclofenac. 3-BrPa: 3-bromopyruvate. Adapted figure from Vander Linden et al. [119].

As described in the "MCT inhibitors" section of this work, they have found significant effects after a DNA methylation-dependent silencing of MCT1 with 3-BrPA, followed by an inhibition of MCT4 with diclofenac.

We applied this reasoning to see if we could observe a difference in our parameters of choice, pH_e and pO_2 values, using and comparing our magnetic resonance methods. The ultimate perspectives of this part would have been to observe a shift in pH_e and/or pO_2, values which could have been monitored with our techniques.

Preliminary results show that there is a dose-dependent effect of 3-bromopyruvate on cell proliferation in 4T1 cells, as seen in Figure 40. Effects on cell viability were only observed at high concentrations.

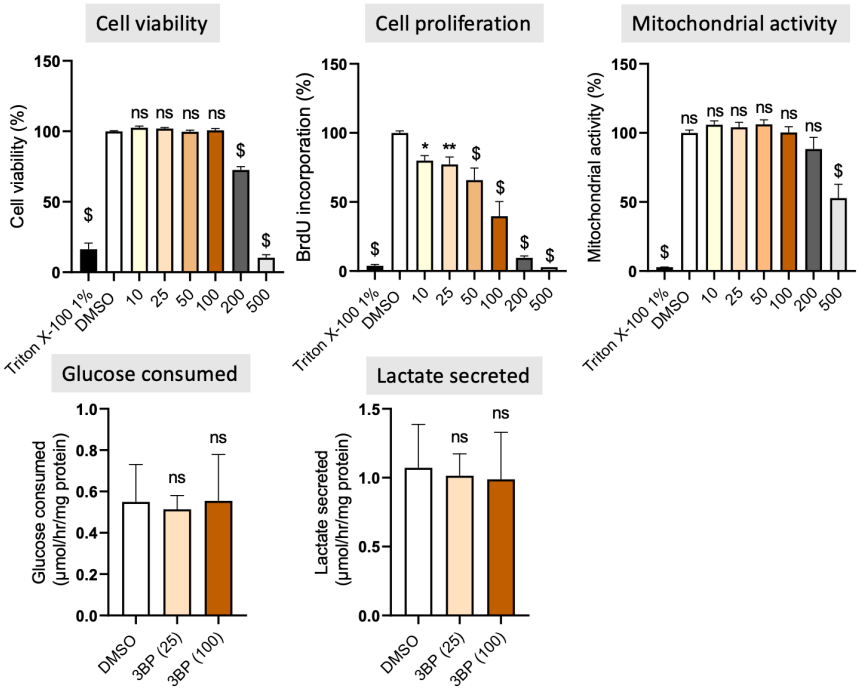


Figure 40 – Effects of a treatment of 3-bromopyruvate on several metabolic processes in 4T1 cells. Different concentration (µM) of 3-BrPA were tested for 24 hours on 4T1 cell viability, proliferation, mitochondrial activity, glucose consumed and lactate secreted. **Top:** N = 3 ; one-way ANOVA ; * $p < 0.05$; ** $p < 0.01$; $ = **** $p < 0.001$. **Bottom:** N = 2 ; two-way ANOVA.

We also measured pH_e and OCR using pTAM on X-band EPR (Figure 41). The next steps would be to continue the investigations of the effects of 3-BrPA on 4T1 and compare them with MDA-MB-231 cells. After the characterization of the effects of 3-BrPA alone, we want to investigate the consequences of a diclofenac treatment, as well as a combination of both molecules.

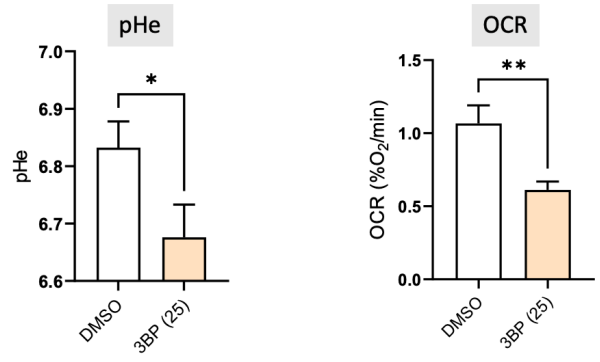


Figure 41 – pH_e and OCR measured using pTAM on the X-band EPR. 4T1 cells were treated for 24 hours with 25 μM of 3-bromopyruvate. pH_e and OCR were measured on a Bruker EMX-Plus spectrometer operating in X-band (9.85 GHz). N = 4 ; unpaired t-test ; * $p < 0.05$; ** $p < 0.01$.

Ultimately, these results are only preliminary but could be exploited in future experiments.

2.2.4. Interest in measuring pH_i

As stated before, measuring pH_i could provide valuable information on the metabolic state of tumors, as it is involved in proliferation, cell survival and invasion, migration and metastasis formation [310].

Intracellular pH can be evaluated using the chemical shift of endogenous inorganic phosphate (Pi) using ^{31}P-NMR. The endogenous Pi signal mainly reflects pH_i, as its concentration in the intracellular compartment is 75-80% higher than in the extracellular compartment (3-4 mM versus ~1 mM) [311, 312]. While it has been shown in cells suspensions that it is possible to separate the signals from intracellular and extracellular P_i (Figure 42, [311]), the assessment of both components in vivo using MRI remains a challenge [313].

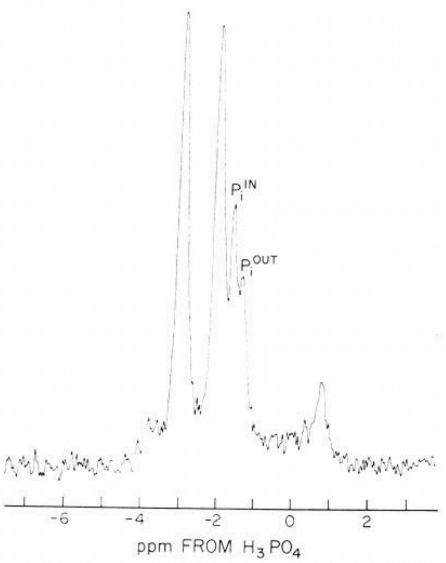


Figure 42 – Separation of the Pi peak into two different ones, coming from the pool of intracellular and extracellular Pi in vitro. Adapted from Moon and Richards [311].

Although it could have been interesting to study the changes in pH_i values along with those in pH_e values during our analysis, the limited precision to measure the small range in pH_i changes (~7.3 - 7.6) of MRS would have made it difficult to get accurate measurements.

3. Integrating biomarkers imaging in the development of treatment targeting cancer metabolism

To conclude, this work could be integrated to other methods studying cancer metabolism: for example, ^{13}C-NMR, hyperpolarized by dissolution-Dynamic Nuclear Polarization (d-DNP). Of note, parahydrogen-induced polarization (PHIP) has been described as easier and more cost-effective than d-DNP with

a fast sample turnover and the ability to provide ≥ 20% hyperpolarization of ^{13}C MR signals in pyruvate, acetate and fumarate, in a few seconds [314]. Both hyperpolarized techniques could be combined with one or several methods presented in this work, to help correlate metabolites and their metabolic becoming with pH_e and pO_2 changes.

Our methods could be also be integrated to ^{18}F-FDG PET protocols, that measures the uptake of glucose, which potentially affects our parameters of interest.

There are still many open questions and perspectives to this work. We focused only on two different targets with two different treatments, but there are plenty of actors participating in the regulation of pH_e and pO_2 or ways to modify them, a few of them were presented in this work. In order to, one day, apply these treatments in the clinic, investigations are still needed to study the relevance of different courses of action, affecting pH_e and pO_2, in terms of tumor growth or survival. Precise measurements of pH_e and pO_2 in vivo could be of clinical value for diagnosis, selection and response to therapy as well as survival prognosis.

Conclusions

The acidosis and hypoxia of the tumor microenvironment may have profound impact on cancer progression and on the efficacy of treatments.

In this thesis, the goal was to evaluate the effects of different pharmacological treatments on tumor pH_e and pO_2 measurements, using ^{31}P-NMR spectroscopy, Chemical Exchange Saturation Transfer-MRI and Electron Paramagnetic Resonance spectroscopy.

The effects of two different pharmacological treatments on tumor pH_e and pO_2 have been studied: UK-5099, a mitochondrial pyruvate carrier inhibitor and syrosingopine, a monocarboxylate transporter inhibitor.

We were able to evaluate those parameters, before and after treatment, and to compare the different non-invasive methods. No change in pH_e was measured using ^{31}P-NMR. CEST MRI provided high resolution parametric images (0.44 µl/voxel) of pH_e highlighting the heterogeneity of response within the tumor when exposed to UK-5099 but no significant changes when mice were treated with syrosingopine. EPR spectroscopy was able to give us information about both pH_e and pO_2, in vitro and in vivo, with a significant decrease in pH_e found in vivo.

Our results show that following the evolution of parameters involved in tumor progression, such as pH_e and pO_2, is possible in vivo, with non-invasive magnetic resonance techniques.

Bibliography

Bibliography

1. Warburg, O., *On respiratory impairment in cancer cells.* Science, 1956a. **124**(3215): p. 269-270.
2. Hanahan, D. and R.A. Weinberg, *Hallmarks of cancer: the next generation.* Cell, 2011. **144**(5): p. 646-74.
3. DeBerardinis, R.J., et al., *The biology of cancer: metabolic reprogramming fuels cell growth and proliferation.* Cell Metab, 2008. **7**(1): p. 11-20.
4. DeBerardinis, R.J. and N.S. Chandel, *Fundamentals of cancer metabolism.* Sci Adv, 2016. **2**(5): p. e1600200.
5. Cairns, R.A., I.S. Harris, and T.W. Mak, *Regulation of cancer cell metabolism.* Nat Rev Cancer, 2011. **11**(2): p. 85-95.
6. Gatenby, R.A. and R.J. Gillies, *Why do cancers have high aerobic glycolysis?* Nat Rev Cancer, 2004. **4**(11): p. 891-9.
7. Shaw, R.J. and L.C. Cantley, *Ras, PI(3)K and mTOR signalling controls tumour cell growth.* Nature, 2006. **441**(7092): p. 424-30.
8. Stine, Z.E., et al., *MYC, Metabolism, and Cancer.* Cancer Discov, 2015. **5**(10): p. 1024-39.
9. Kruiswijk, F., C.F. Labuschagne, and K.H. Vousden, *p53 in survival, death and metabolic health: a lifeguard with a licence to kill.* Nat Rev Mol Cell Biol, 2015. **16**(7): p. 393-405.
10. Hoxhaj, G. and B.D. Manning, *The PI3K-AKT network at the interface of oncogenic signalling and cancer metabolism.* Nat Rev Cancer, 2020. **20**(2): p. 74-88.
11. Vander Heiden, M.G., L.C. Cantley, and C.B. Thompson, *Understanding the Warburg Effect: The Metabolic Requirements of Cell Proliferation.* Science, 2009. **324**(5930): p. 1029-1033.
12. Warburg, O., *On the origin of cancer cells.* Science, 1956b. **123**(3191): p. 309-314.
13. Moreno-Sanchez, R., et al., *Energy metabolism in tumor cells.* FEBS J, 2007. **274**(6): p. 1393-418.
14. Vander Heiden, M.G., L.C. Cantley, and C.B. Thompson, *Understanding the Warburg effect: the metabolic requirements of cell proliferation.* Science, 2009. **324**(5930): p. 1029-33.
15. De Preter, G., et al., *Inhibition of the pentose phosphate pathway by dichloroacetate unravels a missing link between aerobic glycolysis and cancer cell proliferation.* Oncotarget, 2016. **7**(3): p. 2910-20.
16. Yang, M. and K.H. Vousden, *Serine and one-carbon metabolism in cancer.* Nat Rev Cancer, 2016. **16**(10): p. 650-62.
17. Mattaini, K.R., M.R. Sullivan, and M.G. Vander Heiden, *The importance of serine metabolism in cancer.* J Cell Biol, 2016. **214**(3): p. 249-57.

18. Elstrom, R.L., et al., *Akt stimulates aerobic glycolysis in cancer cells.* Cancer Res, 2004. **64**(11): p. 3892-9.
19. Rathmell, J.C., et al., *Akt-directed glucose metabolism can prevent Bax conformation change and promote growth factor-independent survival.* Mol Cell Biol, 2003. **23**(20): p. 7315-28.
20. Adekola, K., S.T. Rosen, and M. Shanmugam, *Glucose transporters in cancer metabolism.* Curr Opin Oncol, 2012. **24**(6): p. 650-4.
21. Foran, P.G., et al., *Protein kinase B stimulates the translocation of GLUT4 but not GLUT1 or transferrin receptors in 3T3-L1 adipocytes by a pathway involving SNAP-23, synaptobrevin-2, and/or cellubrevin.* J Biol Chem, 1999. **274**(40): p. 28087-95.
22. Roberts, D.J., et al., *Akt phosphorylates HK-II at Thr-473 and increases mitochondrial HK-II association to protect cardiomyocytes.* J Biol Chem, 2013. **288**(33): p. 23798-806.
23. Deprez, J., et al., *Phosphorylation and activation of heart 6-phosphofructo-2-kinase by protein kinase B and other protein kinases of the insulin signaling cascades.* J Biol Chem, 1997. **272**(28): p. 17269-75.
24. Hue, L. and M.H. Rider, *Role of fructose 2,6-bisphosphate in the control of glycolysis in mammalian tissues.* Biochem J, 1987. **245**(2): p. 313-24.
25. Chae, Y.C., et al., *Mitochondrial Akt Regulation of Hypoxic Tumor Reprogramming.* Cancer Cell, 2016. **30**(2): p. 257-272.
26. Szwed, A., E. Kim, and E. Jacinto, *Regulation and metabolic functions of mTORC1 and mTORC2.* Physiol Rev, 2021. **101**(3): p. 1371-1426.
27. Hay, N. and N. Sonenberg, *Upstream and downstream of mTOR.* Genes Dev, 2004. **18**(16): p. 1926-45.
28. Semenza, G.L., *Targeting HIF-1 for cancer therapy.* Nat Rev Cancer, 2003. **3**(10): p. 721-32.
29. Svensson, R.U., et al., *Inhibition of acetyl-CoA carboxylase suppresses fatty acid synthesis and tumor growth of non-small-cell lung cancer in preclinical models.* Nat Med, 2016. **22**(10): p. 1108-1119.
30. Schaner, P.E., et al., *First-In-Human Study in Cancer Patients Establishing the Feasibility of Oxygen Measurements in Tumors Using Electron Paramagnetic Resonance With the OxyChip.* Front Oncol, 2021. **11**: p. 743256.
31. Gallez, B., *The Role of Imaging Biomarkers to Guide Pharmacological Interventions Targeting Tumor Hypoxia.* Front Pharmacol, 2022. **13**: p. 853568.
32. d'Hose, D., et al., *A versatile EPR toolbox for the simultaneous measurement of oxygen consumption and superoxide production.* Redox Biol, 2021. **40**: p. 101852.

33. Nakazawa, M.S., B. Keith, and M.C. Simon, *Oxygen availability and metabolic adaptations.* Nat Rev Cancer, 2016. **16**(10): p. 663-73.
34. Fang, J.S., R.D. Gillies, and R.A. Gatenby, *Adaptation to hypoxia and acidosis in carcinogenesis and tumor progression.* Semin Cancer Biol, 2008. **18**(5): p. 330-7.
35. Boroughs, L.K. and R.J. DeBerardinis, *Metabolic pathways promoting cancer cell survival and growth.* Nat Cell Biol, 2015. **17**(4): p. 351-9.
36. Wise, D.R., et al., *Myc regulates a transcriptional program that stimulates mitochondrial glutaminolysis and leads to glutamine addiction.* Proc Natl Acad Sci U S A, 2008. **105**(48): p. 18782-7.
37. Reitzer, L.J., B.M. Wice, and D. Kennell, *Evidence that glutamine, not sugar, is the major energy source for cultured HeLa cells.* J Biol Chem, 1979. **254**(8): p. 2669-76.
38. Coles, N.W. and R.M. Johnstone, *Glutamine metabolism in Ehrlich ascites-carcinoma cells.* Biochem J, 1962. **83**(2): p. 284-91.
39. Corbet, C. and O. Feron, *Tumour acidosis: from the passenger to the driver's seat.* Nat Rev Cancer, 2017. **17**(10): p. 577-593.
40. DeBerardinis, R.J., et al., *Beyond aerobic glycolysis: transformed cells can engage in glutamine metabolism that exceeds the requirement for protein and nucleotide synthesis.* Proc Natl Acad Sci U S A, 2007. **104**(49): p. 19345-50.
41. Altman, B.J., Z.E. Stine, and C.V. Dang, *From Krebs to clinic: glutamine metabolism to cancer therapy.* Nature Reviews Cancer, 2016. **16**(10): p. 619-634.
42. Pérez-Escuredo, J., et al., *Lactate promotes glutamine uptake and metabolism in oxidative cancer cells.* Cell Cycle, 2016. **15**(1): p. 72-83.
43. Yang, L., S. Venneti, and D. Nagrath, *Glutaminolysis: A Hallmark of Cancer Metabolism.* Annu Rev Biomed Eng, 2017. **19**: p. 163-194.
44. Menendez, J.A. and R. Lupu, *Fatty acid synthase and the lipogenic phenotype in cancer pathogenesis.* Nat Rev Cancer, 2007. **7**(10): p. 763-77.
45. Röhrig, F. and A. Schulze, *The multifaceted roles of fatty acid synthesis in cancer.* Nat Rev Cancer, 2016. **16**(11): p. 732-749.
46. Swinnen, J.V., K. Brusselmans, and G. Verhoeven, *Increased lipogenesis in cancer cells: new players, novel targets.* Curr Opin Clin Nutr Metab Care, 2006. **9**(4): p. 358-65.
47. Carracedo, A., L.C. Cantley, and P.P. Pandolfi, *Cancer metabolism: fatty acid oxidation in the limelight.* Nat Rev Cancer, 2013. **13**(4): p. 227-32.
48. Beckers, A., et al., *Chemical inhibition of acetyl-CoA carboxylase induces growth arrest and cytotoxicity selectively in cancer cells.* Cancer Res, 2007. **67**(17): p. 8180-7.

49. Schug, Z.T., et al., *Acetyl-CoA synthetase 2 promotes acetate utilization and maintains cancer cell growth under metabolic stress.* Cancer Cell, 2015. **27**(1): p. 57-71.
50. Horton, J.D., J.L. Goldstein, and M.S. Brown, *SREBPs: activators of the complete program of cholesterol and fatty acid synthesis in the liver.* J Clin Invest, 2002. **109**(9): p. 1125-31.
51. Corbet, C. and O. Feron, *Cancer cell metabolism and mitochondria: Nutrient plasticity for TCA cycle fueling.* Biochim Biophys Acta Rev Cancer, 2017. **1868**(1): p. 7-15.
52. Kalluri, R., *The biology and function of fibroblasts in cancer.* Nat Rev Cancer, 2016. **16**(9): p. 582-98.
53. Anderson, N.M. and M.C. Simon, *The tumor microenvironment.* Curr Biol, 2020. **30**(16): p. R921-r925.
54. Neri, D. and C.T. Supuran, *Interfering with pH regulation in tumours as a therapeutic strategy.* Nat Rev Drug Discov, 2011. **10**(10): p. 767-77.
55. Draoui, N. and O. Feron, *Lactate shuttles at a glance: from physiological paradigms to anti-cancer treatments.* Dis Model Mech, 2011. **4**(6): p. 727-32.
56. Mookerjee, S.A., et al., *The contributions of respiration and glycolysis to extracellular acid production.* Biochim Biophys Acta, 2015. **1847**(2): p. 171-181.
57. Dubois, L., et al., *Specific inhibition of carbonic anhydrase IX activity enhances the in vivo therapeutic effect of tumor irradiation.* Radiotherapy and Oncology, 2011. **99**(3): p. 424-431.
58. Webb, B.A., et al., *Dysregulated pH: a perfect storm for cancer progression.* Nat Rev Cancer, 2011. **11**(9): p. 671-7.
59. Chen, Q., et al., *Increased NHE1 expression is targeted by specific inhibitor cariporide to sensitize resistant breast cancer cells to doxorubicin in vitro and in vivo.* BMC Cancer, 2019. **19**(1): p. 211.
60. Amith, S.R. and L. Fliegel, *Regulation of the Na+/H+ Exchanger (NHE1) in Breast Cancer Metastasis.* Cancer Res, 2013. **73**(4): p. 1259-64.
61. Harguindey, S., et al., *Cariporide and other new and powerful NHE1 inhibitors as potentially selective anticancer drugs--an integral molecular/biochemical/metabolic/clinical approach after one hundred years of cancer research.* J Transl Med, 2013. **11**: p. 282.
62. Parks, S.K., J. Chiche, and J. Pouyssegur, *Disrupting proton dynamics and energy metabolism for cancer therapy.* Nat Rev Cancer, 2013. **13**(9): p. 611-23.
63. Dolatkhah, M. and Y. Omidi, *Renewed interests in carbonic anhydrase IX in relevance to breast cancer treatment.* Bioimpacts, 2019. **9**(4): p. 195-197.
64. Supuran, C.T., *Carbonic anhydrases: novel therapeutic applications for inhibitors and activators.* Nat Rev Drug Discov, 2008. **7**(2): p. 168-81.

65. Lou, Y., et al., *Targeting tumor hypoxia: suppression of breast tumor growth and metastasis by novel carbonic anhydrase IX inhibitors.* Cancer Res, 2011. **71**(9): p. 3364-76.
66. Halestrap, A.P., *The monocarboxylate transporter family--Structure and functional characterization.* IUBMB Life, 2012. **64**(1): p. 1-9.
67. Benjamin, D., et al., *Dual Inhibition of the Lactate Transporters MCT1 and MCT4 Is Synthetic Lethal with Metformin due to NAD+ Depletion in Cancer Cells.* Cell Rep, 2018. **25**(11): p. 3047-3058 e4.
68. Felmlee, M.A., et al., *Monocarboxylate Transporters (SLC16): Function, Regulation, and Role in Health and Disease.* Pharmacol Rev, 2020. **72**(2): p. 466-485.
69. Hong, C.S., et al., *MCT1 Modulates Cancer Cell Pyruvate Export and Growth of Tumors that Co-express MCT1 and MCT4.* Cell Rep, 2016. **14**(7): p. 1590-1601.
70. Sonveaux, P., et al., *Targeting lactate-fueled respiration selectively kills hypoxic tumor cells in mice.* J Clin Invest, 2008. **118**(12): p. 3930-42.
71. Juel, C. and A.P. Halestrap, *Lactate transport in skeletal muscle - role and regulation of the monocarboxylate transporter.* J Physiol, 1999. **517 (Pt 3)**(Pt 3): p. 633-42.
72. Ullah, M.S., A.J. Davies, and A.P. Halestrap, *The plasma membrane lactate transporter MCT4, but not MCT1, is up-regulated by hypoxia through a HIF-1alpha-dependent mechanism.* J Biol Chem, 2006. **281**(14): p. 9030-7.
73. Swietach, P., et al., *The chemistry, physiology and pathology of pH in cancer.* Philos Trans R Soc Lond B Biol Sci, 2014. **369**(1638): p. 20130099.
74. Swietach, P., et al., *New insights into the physiological role of carbonic anhydrase IX in tumour pH regulation.* Oncogene, 2010. **29**(50): p. 6509-21.
75. Hulikova, A., R.D. Vaughan-Jones, and P. Swietach, *Dual role of CO2/HCO3(-) buffer in the regulation of intracellular pH of three-dimensional tumor growths.* J Biol Chem, 2011. **286**(16): p. 13815-26.
76. Hulikova, A., et al., *Stromal uptake and transmission of acid is a pathway for venting cancer cell-generated acid.* Proc Natl Acad Sci U S A, 2016. **113**(36): p. E5344-53.
77. Chen, J.L., et al., *The genomic analysis of lactic acidosis and acidosis response in human cancers.* PLoS Genet, 2008. **4**(12): p. e1000293.
78. Corbet, C., et al., *The SIRT1/HIF2alpha axis drives reductive glutamine metabolism under chronic acidosis and alters tumor response to therapy.* Cancer Res, 2014. **74**(19): p. 5507-19.
79. Morita, T., et al., *Clastogenicity of low pH to various cultured mammalian cells.* Mutat Res, 1992. **268**(2): p. 297-305.

80. Corbet, C., et al., *Acidosis Drives the Reprogramming of Fatty Acid Metabolism in Cancer Cells through Changes in Mitochondrial and Histone Acetylation.* Cell Metab, 2016. **24**(2): p. 311-23.
81. Kondo, A., et al., *Extracellular Acidic pH Activates the Sterol Regulatory Element-Binding Protein 2 to Promote Tumor Progression.* Cell Rep, 2017. **18**(9): p. 2228-2242.
82. Pouyssegur, J., et al., *Cytoplasmic pH, a key determinant of growth factor-induced DNA synthesis in quiescent fibroblasts.* FEBS Lett, 1985. **190**(1): p. 115-9.
83. Trivedi, B. and W.H. Danforth, *Effect of pH on the kinetics of frog muscle phosphofructokinase.* J Biol Chem, 1966. **241**(17): p. 4110-2.
84. Gillies, R.J., et al., *MRI of the tumor microenvironment.* J Magn Reson Imaging, 2002. **16**(4): p. 430-50.
85. Corbet, C., et al., *TGFβ2-induced formation of lipid droplets supports acidosis-driven EMT and the metastatic spreading of cancer cells.* Nat Commun, 2020. **11**(1): p. 454.
86. Raghunand, N. and R.J. Gillies, *pH and drug resistance in tumors.* Drug Resist Updat, 2000. **3**(1): p. 39-47.
87. Gerweck, L.E., S. Vijayappa, and S. Kozin, *Tumor pH controls the in vivo efficacy of weak acid and base chemotherapeutics.* Mol Cancer Ther, 2006. **5**(5): p. 1275-9.
88. Haveman, J., *The influence of pH on the survival after X-irradiation of cultured malignant cells. Effects of carbonylcyanide-3-chlorophenylhydrazone.* Int J Radiat Biol Relat Stud Phys Chem Med, 1980. **37**(2): p. 201-5.
89. Baskar, R., et al., *Cancer and radiation therapy: current advances and future directions.* Int J Med Sci, 2012. **9**(3): p. 193-9.
90. Lee, H.S., et al., *Radiation-induced apoptosis in different pH environments in vitro.* Int J Radiat Oncol Biol Phys, 1997. **38**(5): p. 1079-87.
91. Song, C.W., Griffin, R., Park, H.J. , *Influence of Tumor pH on Therapeutic Response.* Teicher, B.A. (eds) Cancer Drug Resistance., 2006: p. 21-42.
92. Raghunand, N., et al., *Enhancement of chemotherapy by manipulation of tumour pH.* British Journal of Cancer, 1999. **80**(7): p. 1005-1011.
93. Robey, I.F., et al., *Bicarbonate increases tumor pH and inhibits spontaneous metastases.* Cancer Res, 2009. **69**(6): p. 2260-8.
94. Silva, A.S., et al., *The potential role of systemic buffers in reducing intratumoral extracellular pH and acid-mediated invasion.* Cancer Res, 2009. **69**(6): p. 2677-84.
95. Pan, P., et al., *Carbonic anhydrase gene expression in CA II-deficient (Car2-/-) and CA IX-deficient (Car9-/-) mice.* J Physiol, 2006. **571**(Pt 2): p. 319-27.

96. De Milito, A., et al., *Proton pump inhibitors induce apoptosis of human B-cell tumors through a caspase-independent mechanism involving reactive oxygen species.* Cancer Res, 2007. **67**(11): p. 5408-17.
97. Luciani, F., et al., *Effect of proton pump inhibitor pretreatment on resistance of solid tumors to cytotoxic drugs.* J Natl Cancer Inst, 2004. **96**(22): p. 1702-13.
98. Dhakan, C., et al., *Assessing the Therapeutic Efficacy of Proton Transport Inhibitors in a Triple-Negative Breast Cancer Murine Model with Magnetic Resonance Imaging-Chemical Exchange Saturation Transfer Tumor pH Imaging.* Metabolites, 2023. **13**(11).
99. Roberto, M., et al., *Combination Therapy of High-Dose Rabeprazole Plus Metronomic Capecitabine in Advanced Gastro-Intestinal Cancer: A Randomized Phase II Trial.* Cancers (Basel), 2020. **12**(11).
100. Sparks RL, P.T., Smith NK, Cameron IL, *Effects of amiloride on tumor growth and intracellular element content of tumor cells in vivo.* Cancer Res, 1983. **43**: p. 73-7.
101. Frelin, C., et al., *Interaction of guanidinium and guanidinium derivatives with the Na+/H+ exchange system.* Eur J Biochem, 1986. **154**(2): p. 241-5.
102. Aihara, K., et al., *Cardioprotective effect of TY-12533, a novel Na(+)/H(+) exchange inhibitor, on ischemia/reperfusion injury.* Eur J Pharmacol, 2000. **404**(1-2): p. 221-9.
103. Masereel, B., L. Pochet, and D. Laeckmann, *An overview of inhibitors of Na(+)/H(+) exchanger.* Eur J Med Chem, 2003. **38**(6): p. 547-54.
104. Matthews, H., M. Ranson, and M.J. Kelso, *Anti-tumour/metastasis effects of the potassium-sparing diuretic amiloride: an orally active anti-cancer drug waiting for its call-of-duty?* Int J Cancer, 2011. **129**(9): p. 2051-61.
105. Gastelum, G., et al., *Acidification of intracellular pH in MM tumor cells overcomes resistance to hypoxia-mediated apoptosis in vitro and in vivo.* Front Oncol, 2023. **13**: p. 1268421.
106. Wang, Y., et al., *Mice with a null mutation in the NHE1 Na+-H+ exchanger are resistant to cardiac ischemia-reperfusion injury.* Circ Res, 2003. **93**(8): p. 776-82.
107. Supuran, C.T., et al., *Inhibition of carbonic anhydrase IX targets primary tumors, metastases, and cancer stem cells: Three for the price of one.* Med Res Rev, 2018. **38**(6): p. 1799-1836.
108. Puech, C., et al., *Umbelliferone Decreases Intracellular pH and Sensitizes Melanoma Cell Line A375 to Dacarbazin. Comparison with Acetazolamide.* Curr Mol Pharmacol, 2018. **11**(2): p. 133-139.
109. Tennant, D.A., R.V. Durán, and E. Gottlieb, *Targeting metabolic transformation for cancer therapy.* Nat Rev Cancer, 2010. **10**(4): p. 267-77.

110. Pillai, S.R., et al., *Causes, consequences, and therapy of tumors acidosis.* Cancer Metastasis Rev, 2019. **38**(1-2): p. 205-222.
111. Dewick, P.M., *The Shikimate Pathway: Aromatic Amino Acids and Phenylpropanoids*, in *Medicinal Natural Products*. 2001. p. 121-166.
112. Ovens, M.J., et al., *AR-C155858 is a potent inhibitor of monocarboxylate transporters MCT1 and MCT2 that binds to an intracellular site involving transmembrane helices 7-10.* Biochem J, 2010. **425**(3): p. 523-30.
113. Le Floch, R., et al., *CD147 subunit of lactate/H+ symporters MCT1 and hypoxia-inducible MCT4 is critical for energetics and growth of glycolytic tumors.* Proc Natl Acad Sci U S A, 2011. **108**(40): p. 16663-8.
114. Counillon, L., et al., *Na(+)/H(+) antiporter (NHE1) and lactate/H(+) symporters (MCTs) in pH homeostasis and cancer metabolism.* Biochim Biophys Acta, 2016. **1863**(10): p. 2465-80.
115. Beloueche-Babari, M., et al., *MCT1 Inhibitor AZD3965 Increases Mitochondrial Metabolism, Facilitating Combination Therapy and Noninvasive Magnetic Resonance Spectroscopy.* Cancer Res, 2017. **77**(21): p. 5913-5924.
116. Pernicova, I. and M. Korbonits, *Metformin--mode of action and clinical implications for diabetes and cancer.* Nat Rev Endocrinol, 2014. **10**(3): p. 143-56.
117. Halford, S., et al., *A Phase I Dose-escalation Study of AZD3965, an Oral Monocarboxylate Transporter 1 Inhibitor, in Patients with Advanced Cancer.* Clin Cancer Res, 2023. **29**(8): p. 1429-1439.
118. Benjamin, D., et al., *Syrosingopine sensitizes cancer cells to killing by metformin.* Sci Adv, 2016. **2**(12): p. e1601756.
119. Vander Linden, C., et al., *Therapy-induced DNA methylation inactivates MCT1 and renders tumor cells vulnerable to MCT4 inhibition.* Cell Rep, 2021. **35**(9): p. 109202.
120. Raghunand, N., *Tissue pH measurement by magnetic resonance spectroscopy and imaging.* Methods Mol Med, 2006. **124**: p. 347-64.
121. Wu, Y., et al., *A generalized ratiometric chemical exchange saturation transfer (CEST) MRI approach for mapping renal pH using iopamidol.* Magn Reson Med, 2018. **79**(3): p. 1553-1558.
122. Wike-Hooley, J.L., J. Haveman, and H.S. Reinhold, *The relevance of tumour pH to the treatment of malignant disease.* Radiother Oncol, 1984. **2**(4): p. 343-66.
123. Chen, L.Q., et al., *Evaluations of Tumor Acidosis Within In Vivo Tumor Models Using Parametric Maps Generated with Acido CEST MRI.* Mol Imaging Biol, 2015. **17**(4): p. 488-96.

124. Andreev, O.A., et al., *Mechanism and uses of a membrane peptide that targets tumors and other acidic tissues in vivo.* Proc Natl Acad Sci U S A, 2007. **104**(19): p. 7893-8.
125. Anemone, A., et al., *Imaging tumor acidosis: a survey of the available techniques for mapping in vivo tumor pH.* Cancer Metastasis Rev, 2019. **38**(1-2): p. 25-49.
126. Chen, L.Q. and M.D. Pagel, *Evaluating pH in the Extracellular Tumor Microenvironment Using CEST MRI and Other Imaging Methods.* Adv Radiol, 2015. **2015**.
127. Wyatt, L.C., et al., *Applications of pHLIP Technology for Cancer Imaging and Therapy.* Trends Biotechnol, 2017. **35**(7): p. 653-664.
128. Schild, P.D.H.H., *MRI made easy*. 1990: Schering.
129. Ali, H., *An automated system for the classification and segmentation of brain tumours in MRI images based on the modified grey level co-occurence matrix*. 2017, University of Salford, Salford, UK.
130. Tognarelli, J.M., et al., *Magnetic Resonance Spectroscopy: Principles and Techniques: Lessons for Clinicians.* J Clin Exp Hepatol, 2015. **5**(4): p. 320-8.
131. Krafft, M.P., *Alleviating tumor hypoxia with perfluorocarbon-based oxygen carriers.* Curr Opin Pharmacol, 2020. **53**: p. 117-125.
132. Pooley, R.A., *AAPM/RSNA physics tutorial for residents: fundamental physics of MR imaging.* Radiographics, 2005. **25**(4): p. 1087-99.
133. H., S.H., *MRI made easy*. 1990: Schering.
134. Gallez, B., *Biophysique appliquée aux médicaments*. UCLouvain.
135. Acciardo, S., et al., *Metabolic imaging using hyperpolarized (13) C-pyruvate to assess sensitivity to the B-Raf inhibitor vemurafenib in melanoma cells and xenografts.* J Cell Mol Med, 2020. **24**(2): p. 1934-1944.
136. Schoonjans, C.A., et al., *Acidosis-induced metabolic reprogramming in tumor cells enhances the anti-proliferative activity of the PDK inhibitor dichloroacetate.* Cancer Lett, 2020. **470**: p. 18-28.
137. Aime, S., et al., *Paramagnetic complexes as novel NMR pH indicators.* Chemical Communications, 1996(11).
138. Ojugo, A.S.E., et al., *Measurement of the extracellular pH of solid tumours in mice by magnetic resonance spectroscopy: a comparison of exogenous19F and31P probes.* NMR in Biomedicine, 1999. **12**(8): p. 495-504.
139. Gillies, R.J., Z. Liu, and Z. Bhujwalla, *31P-MRS measurements of extracellular pH of tumors using 3-aminopropylphosphonate.* Am J Physiol, 1994. **267**(1 Pt 1): p. C195-203.
140. Bhujwalla, Z.M., et al., *Estimations of intra- and extracellular volume and pH by 31P magnetic resonance spectroscopy: effect of therapy on RIF-1 tumours.* Br J Cancer, 1998. **78**(5): p. 606-11.

141. Aoki, Y., et al., *Measurement of intratumor pH by pH indicator used in 19F-magnetic resonance spectroscopy. Measurement of extracellular pH decrease caused by hyperthermia combined with hydralazine.* Invest Radiol, 1996. **31**(11): p. 680-9.
142. Gibby, W.A., *Basic principles of magnetic resonance imaging.* Neurosurg Clin N Am, 2005. **16**(1): p. 1-64.
143. IMAIOS. *e-MRI : MRI step-by-step, interactive course on magnetic resonance imaging.* Available from: https://www.imaios.com/fr/e-mri.
144. Info-radiologie.ch. *Imagerie par résonance magnétique (IRM).* Available from: https://www.info-radiologie.ch/resonance_magnetique.php.
145. Wu, B., et al., *An overview of CEST MRI for non-MR physicists.* EJNMMI Phys, 2016. **3**(1): p. 19.
146. Vinogradov, E., A.D. Sherry, and R.E. Lenkinski, *CEST: from basic principles to applications, challenges and opportunities.* J Magn Reson, 2013. **229**: p. 155-72.
147. Liepinsh, E. and G. Otting, *Proton exchange rates from amino acid side chains--implications for image contrast.* Magn Reson Med, 1996. **35**(1): p. 30-42.
148. Mori, S., et al., *NMR Study of Rapidly Exchanging Backbone Amide Protons in Staphylococcal Nuclease and the Correlation with Structural and Dynamic Properties.* Journal of the American Chemical Society, 1997. **119**(29): p. 6844-6852.
149. Wang, M., et al., *Simultaneous detection and separation of hyperacute intracerebral hemorrhage and cerebral ischemia using amide proton transfer MRI.* Magn Reson Med, 2015. **74**(1): p. 42-50.
150. Zhou, J., et al., *Using the amide proton signals of intracellular proteins and peptides to detect pH effects in MRI.* Nat Med, 2003. **9**(8): p. 1085-90.
151. Kenya, M., *Basics of Chemical Exchange Saturation Transfer (CEST) Magnetic Resonance Imaging.* High-Resolution Neuroimaging - Basic Physical Principles and Clinical Applications, 2018.
152. Longo, D.L., et al., *Iopamidol as a responsive MRI-chemical exchange saturation transfer contrast agent for pH mapping of kidneys: In vivo studies in mice at 7 T.* Magn Reson Med, 2011. **65**(1): p. 202-11.
153. Aime, S., et al., *Iopamidol: Exploring the potential use of a well-established x-ray contrast agent for MRI.* Magn Reson Med, 2005. **53**(4): p. 830-4.
154. Terreno, E., et al., *Ln(III)-DOTAMGly complexes: a versatile series to assess the determinants of the efficacy of paramagnetic chemical exchange saturation transfer agents for magnetic resonance imaging applications.* Invest Radiol, 2004. **39**(4): p. 235-43.

155. McVicar, N., et al., *Quantitative tissue pH measurement during cerebral ischemia using amine and amide concentration-independent detection (AACID) with MRI.* J Cereb Blood Flow Metab, 2014. **34**(4): p. 690-8.
156. Zhang, L., et al., *Imaging Extracellular Lactate In Vitro and In Vivo Using CEST MRI and a Paramagnetic Shift Reagent.* Chemistry, 2017. **23**(8): p. 1752-1756.
157. Aime, S., et al., *Paramagnetic lanthanide(III) complexes as pH-sensitive chemical exchange saturation transfer (CEST) contrast agents for MRI applications.* Magn Reson Med, 2002. **47**(4): p. 639-48.
158. Stancu, I.C., et al., *Tauopathy contributes to synaptic and cognitive deficits in a murine model for Alzheimer's disease.* FASEB J, 2014. **28**(6): p. 2620-31.
159. van Zijl, P.C. and N.N. Yadav, *Chemical exchange saturation transfer (CEST): what is in a name and what isn't?* Magn Reson Med, 2011. **65**(4): p. 927-48.
160. Lal, A., et al., *Transcriptional response to hypoxia in human tumors.* J Natl Cancer Inst, 2001. **93**(17): p. 1337-43.
161. Muller-Lutz, A., et al., *Pilot study of Iopamidol-based quantitative pH imaging on a clinical 3T MR scanner.* MAGMA, 2014. **27**(6): p. 477-85.
162. Longo, D.L., et al., *Noninvasive evaluation of renal pH homeostasis after ischemia reperfusion injury by CEST-MRI.* NMR Biomed, 2017. **30**(7).
163. Chen, L.Q., et al., *Evaluations of extracellular pH within in vivo tumors using acidoCEST MRI.* Magn Reson Med, 2014. **72**(5): p. 1408-17.
164. Longo, D.L., et al., *In Vivo Imaging of Tumor Metabolism and Acidosis by Combining PET and MRI-CEST pH Imaging.* Cancer Res, 2016. **76**(22): p. 6463-6470.
165. Consolino, L., et al., *Non-invasive Investigation of Tumor Metabolism and Acidosis by MRI-CEST Imaging.* Front Oncol, 2020. **10**: p. 161.
166. Jardim-Perassi, B.V., et al., *Intraperitoneal Delivery of Iopamidol to Assess Extracellular pH of Orthotopic Pancreatic Tumor Model by CEST-MRI.* Contrast Media Mol Imaging, 2023. **2023**: p. 1944970.
167. Lombardi, A.F., et al., *AcidoCEST MRI Evaluates the Bone Microenvironment in Multiple Myeloma.* Mol Imaging Biol, 2021. **23**(6): p. 865-873.
168. Lindeman, L.R., et al., *Differentiating lung cancer and infection based on measurements of extracellular pH with acidoCEST MRI.* Sci Rep, 2019. **9**(1): p. 13002.
169. Krikken, E., et al., *Contradiction between amide-CEST signal and pH in breast cancer explained with metabolic MRI.* NMR Biomed, 2019. **32**(8): p. e4110.
170. Zhou, J., et al., *APT-weighted and NOE-weighted image contrasts in glioma with different RF saturation powers based on magnetization transfer ratio asymmetry analyses.* Magn Reson Med, 2013. **70**(2): p. 320-7.

171. Paech, D., et al., *Nuclear overhauser enhancement mediated chemical exchange saturation transfer imaging at 7 Tesla in glioblastoma patients.* PLoS One, 2014. **9**(8): p. e104181.
172. Heo, H.Y., et al., *Whole-brain amide proton transfer (APT) and nuclear overhauser enhancement (NOE) imaging in glioma patients using low-power steady-state pulsed chemical exchange saturation transfer (CEST) imaging at 7T.* J Magn Reson Imaging, 2016. **44**(1): p. 41-50.
173. High, R.A., et al., *In vivo assessment of extracellular pH of joint tissues using acidoCEST-UTE MRI.* Quant Imaging Med Surg, 2019. **9**(10): p. 1664-1673.
174. Schmitz-Abecassis, B., et al., *Investigation of metabolite correlates of CEST in the human brain at 7 T.* NMR Biomed, 2024. **37**(5): p. e5104.
175. B., G., *Principes et applications biophysique des méthodes de spectroscopie de résonance magnétique nucléaire et électronique*. UCLouvain.
176. Vanea, E., et al., *Molecular electron paramagnetic resonance imaging of melanin in melanomas: a proof-of-concept.* NMR Biomed, 2008. **21**(3): p. 296-300.
177. Desmet, C.M., et al., *Towards in vivo melanin radicals detection in melanomas by electron paramagnetic resonance (EPR) spectroscopy: a proof-of-concept study.* Free Radic Res, 2019. **53**(4): p. 405-410.
178. Davies, M.J., *Detection and characterisation of radicals using electron paramagnetic resonance (EPR) spin trapping and related methods.* Methods, 2016. **109**: p. 21-30.
179. Gallez, B., K. Mader, and H.M. Swartz, *Noninvasive measurement of the pH inside the gut by using pH-sensitive nitroxides. An in vivo EPR study.* Magn Reson Med, 1996. **36**(5): p. 694-7.
180. Bobko, A.A., et al., *In vivo monitoring of pH, redox status, and glutathione using L-band EPR for assessment of therapeutic effectiveness in solid tumors.* Magn Reson Med, 2012. **67**(6): p. 1827-36.
181. Dhimitruka, I., et al., *Synthesis and characterization of amino derivatives of persistent trityl radicals as dual function pH and oxygen paramagnetic probes.* J Am Chem Soc, 2008. **130**(32): p. 10780-7.
182. Dhimitruka, I., et al., *Phosphonated trityl probes for concurrent in vivo tissue oxygen and pH monitoring using electron paramagnetic resonance-based techniques.* J Am Chem Soc, 2013. **135**(15): p. 5904-10.
183. Bobko, A.A., et al., *Interstitial Inorganic Phosphate as a Tumor Microenvironment Marker for Tumor Progression.* Sci Rep, 2017. **7**: p. 41233.
184. Gluth, T.D., et al., *Large-scale synthesis of a monophosphonated tetrathiatriarylmethyl spin probe for concurrent in vivo measurement of pO2, pH and inorganic phosphate by EPR.* RSC Adv, 2021. **11**(42): p. 25951-25954.

185. Bobko, A.A., et al., *Dual-function pH and oxygen phosphonated trityl probe.* Anal Chem, 2012. **84**(14): p. 6054-60.
186. Taguchi, A., et al., *In vitro simultaneous mapping of the partial pressure of oxygen, pH and inorganic phosphate using electron paramagnetic resonance.* Analyst, 2020. **145**(9): p. 3236-3244.
187. Buyse, C., et al., *Sensitive simultaneous measurements of oxygenation and extracellular pH by EPR using a stable monophosphonated trityl radical and lithium phthalocyanine.* Free Radic Biol Med, 2024. **213**: p. 11-18.
188. Gluth, T.D., et al., *Biocompatible Monophosphonated Trityl Spin Probe, HOPE71, for In Vivo Measurement of pO(2), pH, and [P(i)] by Electron Paramagnetic Resonance Spectroscopy.* Anal Chem, 2023. **95**(2): p. 946-954.
189. Bertout, J.A., S.A. Patel, and M.C. Simon, *The impact of O2 availability on human cancer.* Nat Rev Cancer, 2008. **8**(12): p. 967-75.
190. Vaupel, P., M. Hockel, and A. Mayer, *Detection and characterization of tumor hypoxia using pO2 histography.* Antioxid Redox Signal, 2007. **9**(8): p. 1221-35.
191. Vaupel, P. and A. Mayer, *Hypoxia in tumors: pathogenesis-related classification, characterization of hypoxia subtypes, and associated biological and clinical implications.* Adv Exp Med Biol, 2014. **812**: p. 19-24.
192. Gallez, B., C. Baudelet, and B.F. Jordan, *Assessment of tumor oxygenation by electron paramagnetic resonance: principles and applications.* NMR Biomed, 2004. **17**(5): p. 240-62.
193. Vaupel, P. and A. Mayer, *Tumor Hypoxia: Causative Mechanisms, Microregional Heterogeneities, and the Role of Tissue-Based Hypoxia Markers.* Adv Exp Med Biol, 2016. **923**: p. 77-86.
194. Horsman, M.R. and P. Vaupel, *Pathophysiological Basis for the Formation of the Tumor Microenvironment.* Front Oncol, 2016. **6**: p. 66.
195. Metallo, C.M., et al., *Reductive glutamine metabolism by IDH1 mediates lipogenesis under hypoxia.* Nature, 2011. **481**(7381): p. 380-4.
196. Bensaad, K., et al., *Fatty acid uptake and lipid storage induced by HIF-1a contribute to cell growth and survival after hypoxia-reoxygenation.* Cell Rep, 2014. **9**(1): p. 349-365.
197. Horsman, M., Wouters, B., Joiner, M., and Overgaard, J., *The Oxygen Effect and Fractionated Radiotherapy.* Basic Clinical Radiobiology, 2009: p. 207-216.
198. Noman, M.Z., et al., *Hypoxia: a key player in antitumor immune response. A Review in the Theme: Cellular Responses to Hypoxia.* Am J Physiol Cell Physiol, 2015. **309**(9): p. C569-79.

199. Gallez, B., et al., *Pharmacological modifications of the partial pressure of oxygen in murine tumors: Evaluation using in vivo EPR oximetry.* Magnetic Resonance in Medicine, 1999. **42**(4): p. 627-630.
200. Bergers, G. and L.E. Benjamin, *Tumorigenesis and the angiogenic switch.* Nat Rev Cancer, 2003. **3**(6): p. 401-10.
201. Sonveaux, P., *Provascular strategy: targeting functional adaptations of mature blood vessels in tumors to selectively influence the tumor vascular reactivity and improve cancer treatment.* Radiother Oncol, 2008. **86**(3): p. 300-13.
202. Jain, R.K., *Normalizing tumor vasculature with anti-angiogenic therapy: a new paradigm for combination therapy.* Nat Med, 2001. **7**(9): p. 987-9.
203. Mpekris, F., et al., *Combining microenvironment normalization strategies to improve cancer immunotherapy.* Proceedings of the National Academy of Sciences, 2020. **117**(7): p. 3728-3737.
204. Segers, J., et al., *Potentiation of cyclophosphamide chemotherapy using the anti-angiogenic drug thalidomide: importance of optimal scheduling to exploit the 'normalization' window of the tumor vasculature.* Cancer Lett, 2006. **244**(1): p. 129-35.
205. Teicher, B.A., et al., *Allosteric effectors of hemoglobin as modulators of chemotherapy and radiation therapy in vitro and in vivo.* Cancer Chemother Pharmacol, 1998. **42**(1): p. 24-30.
206. Hou, H., et al., *Effect of RSR13, an allosteric hemoglobin modifier, on oxygenation in murine tumors: an in vivo electron paramagnetic resonance oximetry and bold MRI study.* Int J Radiat Oncol Biol Phys, 2004. **59**(3): p. 834-43.
207. Siemann, D.W., R.P. Hill, and R.S. Bush, *The importance of the pre-irradiation breathing times of oxygen and carbogen (5% CO2: 95% O2) on the in vivo radiation response of a murine sarcoma.* International Journal of Radiation Oncology*Biology*Physics, 1977. **2**(9-10): p. 903-911.
208. Powell, M.E., et al., *Human tumor blood flow is enhanced by nicotinamide and carbogen breathing.* Cancer Res, 1997. **57**(23): p. 5261-4.
209. Horsman, M.R., et al., *Mechanism of action of the selective tumor radiosensitizer nicotinamide.* Int J Radiat Oncol Biol Phys, 1988. **15**(3): p. 685-90.
210. Secomb, T.W., et al., *Analysis of the effects of oxygen supply and demand on hypoxic fraction in tumors.* Acta Oncol, 1995. **34**(3): p. 313-6.
211. Durand, R.E. and J.E. Biaglow, *Radiosensitization of Hypoxic Cells of an in Vitro Tumor Model by Respiratory Inhibitors.* Radiation Research, 1977. **69**(2).
212. Crokart, N., et al., *Tumor radiosensitization by antiinflammatory drugs: evidence for a new mechanism involving the oxygen effect.* Cancer Res, 2005. **65**(17): p. 7911-6.

213. Crokart, N., et al., *Glucocorticoids modulate tumor radiation response through a decrease in tumor oxygen consumption.* Clin Cancer Res, 2007. **13**(2 Pt 1): p. 630-5.
214. Ashton, T.M., et al., *The anti-malarial atovaquone increases radiosensitivity by alleviating tumour hypoxia.* Nat Commun, 2016. **7**: p. 12308.
215. Gallez, B., et al., *Manipulation of tumor oxygenation and radiosensitivity through modification of cell respiration. A critical review of approaches and imaging biomarkers for therapeutic guidance.* Biochim Biophys Acta Bioenerg, 2017. **1858**(8): p. 700-711.
216. Corbet, C., et al., *Interruption of lactate uptake by inhibiting mitochondrial pyruvate transport unravels direct antitumor and radiosensitizing effects.* Nat Commun, 2018. **9**(1): p. 1208.
217. Wenes, M., et al., *The mitochondrial pyruvate carrier regulates memory T cell differentiation and antitumor function.* Cell Metab, 2022. **34**(5): p. 731-746.e9.
218. Danhier, F., et al., *Electron paramagnetic resonance highlights that the oxygen effect contributes to the radiosensitizing effect of paclitaxel.* PLoS One, 2012. **7**(7): p. e40772.
219. Bénédicte F. Jordan, V.G., Roger J. Demeure, Pierre Sonveaux, Olivier Feron, Julia O'Hara, Valérie P. Vanhulle, Nathalie Delzenne, and Bernard Gallez, *Insulin Increases the Sensitivity of Tumors to Irradiation: Involvement of an Increase in Tumor Oxygenation Mediated by a Nitric Oxide-dependent*

Decrease of the Tumor Cells Oxygen Consumption. Cancer Research, 2002. **62**: p. 3555–3561.
220. Jordan, B.F., et al., *Nitric oxide as a radiosensitizer: evidence for an intrinsic role in addition to its effect on oxygen delivery and consumption.* Int J Cancer, 2004. **109**(5): p. 768-73.
221. Sonveaux, P., et al., *Nitric oxide delivery to cancer: why and how?* Eur J Cancer, 2009. **45**(8): p. 1352-69.
222. Jiang, H., et al., *Activated macrophages as a novel determinant of tumor cell radioresponse: the role of nitric oxide-mediated inhibition of cellular respiration and oxygen sparing.* Int J Radiat Oncol Biol Phys, 2010. **76**(5): p. 1520-7.
223. Li, Y., L. Zhao, and X.F. Li, *Targeting Hypoxia: Hypoxia-Activated Prodrugs in Cancer Therapy.* Front Oncol, 2021. **11**: p. 700407.
224. Vilaplana-Lopera, N., M. Besh, and E.J. Moon, *Targeting Hypoxia: Revival of Old Remedies.* Biomolecules, 2021. **11**(11).
225. Dische, S.C., D.; Hope-Stone, H.F.; Dawes, P.J.D.K.; Roberts, J.T.; Yosef, H.; Bey, P.; Horiot, J.C.; Jacobson, A.; and B. Frankendal, *A trial of Ro 03-8799 (pimonidazole) in carcinoma of the uterine cervix: an interim report*

from the Medical Research Council Working Party on advanced carcinoma of the cervix. Radiother Oncol, 1993. **26**(2): p. 93-103.
226. Rischin, D., et al., *Tirapazamine, Cisplatin, and Radiation versus Fluorouracil, Cisplatin, and Radiation in patients with locally advanced head and neck cancer: a randomized phase II trial of the Trans-Tasman Radiation Oncology Group (TROG 98.02).* J Clin Oncol, 2005. **23**(1): p. 79-87.
227. Rischin, D., et al., *Tirapazamine, cisplatin, and radiation versus cisplatin and radiation for advanced squamous cell carcinoma of the head and neck (TROG 02.02, HeadSTART): a phase III trial of the Trans-Tasman Radiation Oncology Group.* J Clin Oncol, 2010. **28**(18): p. 2989-95.
228. Yu, T., B. Tang, and X. Sun, *Development of Inhibitors Targeting Hypoxia-Inducible Factor 1 and 2 for Cancer Therapy.* Yonsei Med J, 2017. **58**(3): p. 489-496.
229. Semenza, G.L., *Development of novel therapeutic strategies that target HIF-1.* Expert Opin Ther Targets, 2006. **10**(2): p. 267-80.
230. Jeong, W., et al., *Pilot trial of EZN-2968, an antisense oligonucleotide inhibitor of hypoxia-inducible factor-1 alpha (HIF-1a), in patients with refractory solid tumors.* Cancer Chemother Pharmacol, 2014. **73**(2): p. 343-8.
231. Evans, S.M. and C.J. Koch, *Prognostic significance of tumor oxygenation in humans.* Cancer Lett, 2003. **195**(1): p. 1-16.
232. Griffiths, J.R. and S.P. Robinson, *The OxyLite: a fibre-optic oxygen sensor.* Br J Radiol, 1999. **72**(859): p. 627-30.
233. Jordan, B.F., G.O. Cron, and B. Gallez, *Rapid monitoring of oxygenation by 19F magnetic resonance imaging: Simultaneous comparison with fluorescence quenching.* Magn Reson Med, 2009. **61**(3): p. 634-8.
234. Baudelet, C. and B. Gallez, *Effect of anesthesia on the signal intensity in tumors using BOLD-MRI: comparison with flow measurements by Laser Doppler flowmetry and oxygen measurements by luminescence-based probes.* Magn Reson Imaging, 2004. **22**(7): p. 905-12.
235. Frank, J., et al., *Injectable LiNc-BuO loaded microspheres as in vivo EPR oxygen sensors after co-implantation with tumor cells.* Free Radic Biol Med, 2015. **89**: p. 741-9.
236. Vikram, D.S., et al., *A comparative evaluation of EPR and OxyLite oximetry using a random sampling of pO(2) in a murine tumor.* Radiat Res, 2007. **168**(3): p. 308-15.
237. Tatum, J.L., et al., *Hypoxia: importance in tumor biology, noninvasive measurement by imaging, and value of its measurement in the management of cancer therapy.* Int J Radiat Biol, 2006. **82**(10): p. 699-757.

238. Mason, R.P., R.L. Nunnally, and P.P. Antich, *Tissue oxygenation: a novel determination using 19F surface coil NMR spectroscopy of sequestered perfluorocarbon emulsion.* Magn Reson Med, 1991. **18**(1): p. 71-9.
239. Magat, J., et al., *Noninvasive mapping of spontaneous fluctuations in tumor oxygenation using 19F MRI.* Med Phys, 2010. **37**(10): p. 5434-41.
240. Diepart, C., et al., *Arsenic trioxide treatment decreases the oxygen consumption rate of tumor cells and radiosensitizes solid tumors.* Cancer Res, 2012. **72**(2): p. 482-90.
241. Gallez, B., *Oxygenation Status in Normal Tissues, Pathological Tissues and Malignant Tumors: A pO2 Database Based on Electron Paramagnetic Resonance (EPR) Oximetry Measurements.* Applied Magnetic Resonance, 2021. **52**(10): p. 1395-1450.
242. Taylor, S., et al., *Microenvironment acidity as a major determinant of tumor chemoresistance: Proton pump inhibitors (PPIs) as a novel therapeutic approach.* Drug Resist Updat, 2015. **23**: p. 69-78.
243. Hyde, J.S., Subczynski, W.K. , *In Spin Labeling: Theory and Applications.* Biological Magnetic Resonance, 1989. **8**: p. 399-425.
244. d'Hose, D., *Dual EPR measurement of oxygen consumption and superoxide production : principle and applications.* 2021, UCLouvain.
245. Danhier, P., et al., *Influence of cell detachment on the respiration rate of tumor and endothelial cells.* PLoS One, 2013. **8**(1): p. e53324.
246. Gallez B., J.B.F., Baudelet C., Misson P-D., *Pharmacological modifications of the partial pressure of oxygen in murine tumors: Evaluation using in vivo EPR oximetry.* Magnetic Resonance in Medicine, 1999.
247. Shi, Y., et al., *Triarylmethyl Radical: EPR Signal to Noise at Frequencies between 250 MHz and 1.5 GHz and Dependence of Relaxation on Radical and Salt Concentration and on Frequency.* Z Phys Chem (N F), 2017. **231**(4): p. 923-937.
248. Kishimoto, S., et al., *Pulsed Electron Paramagnetic Resonance Imaging: Applications in the Studies of Tumor Physiology.* Antioxid Redox Signal, 2018. **28**(15): p. 1378-1393.
249. Epel, B., et al., *Absolute oxygen R1e imaging in vivo with pulse electron paramagnetic resonance.* Magn Reson Med, 2014. **72**(2): p. 362-8.
250. Gertsenshteyn, I., et al., *Absolute oxygen-guided radiation therapy improves tumor control in three preclinical tumor models.* Front Med (Lausanne), 2023. **10**: p. 1269689.
251. Jordan, B.F., C. Baudelet, and B. Gallez, *Carbon-centered radicals as oxygen sensors for in vivo electron paramagnetic resonance: screening for an optimal probe among commercially available charcoals.* MAGMA, 1998. **7**(2): p. 121-9.

252. Matsumoto, K., et al., *MR assessment of changes of tumor in response to hyperbaric oxygen treatment.* Magn Reson Med, 2006. **56**(2): p. 240-6.
253. O'Connor, J.P.B., S.P. Robinson, and J.C. Waterton, *Imaging tumour hypoxia with oxygen-enhanced MRI and BOLD MRI.* Br J Radiol, 2019. **92**(1095): p. 20180642.
254. O'Connor, J.P., et al., *Organ-specific effects of oxygen and carbogen gas inhalation on tissue longitudinal relaxation times.* Magn Reson Med, 2007. **58**(3): p. 490-6.
255. Baudelet, C. and B. Gallez, *How does blood oxygen level-dependent (BOLD) contrast correlate with oxygen partial pressure (pO2) inside tumors?* Magn Reson Med, 2002. **48**(6): p. 980-6.
256. Baudelet, C. and B. Gallez, *Current Issues in the Utility of Blood Oxygen Level Dependent MRI for the Assessment of Modulations in Tumor Oxygenation.* Current Medical Imaging Reviews, 2005. **1**(3): p. 229-243.
257. Hou, W., et al., *Evaluation of Tumor Hypoxia in C6 Glioma Rat Model With Dynamic Contrast-Enhanced Magnetic Resonance Imaging.* Acad Radiol, 2019. **26**(8): p. e224-e232.
258. Nunn, A., K. Linder, and H.W. Strauss, *Nitroimidazoles and imaging hypoxia.* Eur J Nucl Med, 1995. **22**(3): p. 265-80.
259. Hirata, K., et al., *The Roles of Hypoxia Imaging Using (18)F-Fluoromisonidazole Positron Emission Tomography in Glioma Treatment.* J Clin Med, 2019. **8**(8).
260. Sorger, D., et al., *[18F]Fluoroazomycinarabinofuranoside (18FAZA) and [18F]Fluoromisonidazole (18FMISO): a comparative study of their selective uptake in hypoxic cells and PET imaging in experimental rat tumors.* Nucl Med Biol, 2003. **30**(3): p. 317-26.
261. Busk, M., et al., *Cellular uptake of PET tracers of glucose metabolism and hypoxia and their linkage.* Eur J Nucl Med Mol Imaging, 2008. **35**(12): p. 2294-303.
262. Piert, M., et al., *Hypoxia-specific tumor imaging with 18F-fluoroazomycin arabinoside.* J Nucl Med, 2005. **46**(1): p. 106-13.
263. Busk, M., et al., *Imaging hypoxia in xenografted and murine tumors with 18F-fluoroazomycin arabinoside: a comparative study involving microPET, autoradiography, PO2-polarography, and fluorescence microscopy.* Int J Radiat Oncol Biol Phys, 2008. **70**(4): p. 1202-12.
264. Tran, L.B., et al., *Hypoxia imaging with the nitroimidazole 18F-FAZA PET tracer: a comparison with OxyLite, EPR oximetry and 19F-MRI relaxometry.* Radiother Oncol, 2012. **105**(1): p. 29-35.
265. Bussink, J., J.H. Kaanders, and A.J. van der Kogel, *Tumor hypoxia at the micro-regional level: clinical relevance and predictive value of exogenous and endogenous hypoxic cell markers.* Radiother Oncol, 2003. **67**(1): p. 3-15.

266. Wykoff, C.C., et al., *Hypoxia-inducible expression of tumor-associated carbonic anhydrases.* Cancer Res, 2000. **60**(24): p. 7075-83.
267. Thiruthaneeswaran, N., et al., *Lost in application: Measuring hypoxia for radiotherapy optimisation.* Eur J Cancer, 2021. **148**: p. 260-276.
268. Robinson, S.P., et al., *Response of hepatoma 9618a and normal liver to host carbogen and carbon monoxide breathing.* Neoplasia, 1999. **1**(6): p. 537-43.
269. Raghunand, N., et al., *Acute metabolic alkalosis enhances response of C3H mouse mammary tumors to the weak base mitoxantrone.* Neoplasia, 2001. **3**(3): p. 227-35.
270. Iles, R.A., et al., *Phosphorylation status of liver by 31P-n.m.r. spectroscopy, and its implications for metabolic control. A comparison of 31P-n.m.r. spectroscopy (in vivo and in vitro) with chemical and enzymic determinations of ATP, ADP and Pi.* Biochem J, 1985. **229**(1): p. 141-51.
271. Payne, T., et al., *Multimodal assessment of mitochondrial function in Parkinson's disease.* Brain, 2024. **147**(1): p. 267-280.
272. Chen, M., et al., *Extracellular pH is a biomarker enabling detection of breast cancer and liver cancer using CEST MRI.* Oncotarget, 2017. **8**(28): p. 45759-45767.
273. Anemone, A., et al., *In vivo evaluation of tumour acidosis for assessing the early metabolic response and onset of resistance to dichloroacetate by using magnetic resonance pH imaging.* Int J Oncol, 2017. **51**(2): p. 498-506.
274. Irrera, P., et al., *Effect of Esomeprazole Treatment on Extracellular Tumor pH in a Preclinical Model of Prostate Cancer by MRI-CEST Tumor pH Imaging.* Metabolites, 2022. **13**(1).
275. Albatany, M., et al., *Brain tumor acidification using drugs simultaneously targeting multiple pH regulatory mechanisms.* J Neurooncol, 2019. **144**(3): p. 453-462.
276. Halpern, H.J., et al., *Oxymetry deep in tissues with low-frequency electron paramagnetic resonance.* Proc Natl Acad Sci U S A, 1994. **91**(26): p. 13047-51.
277. Anemone, A., et al., *Tumour acidosis evaluated in vivo by MRI-CEST pH imaging reveals breast cancer metastatic potential.* Br J Cancer, 2021. **124**(1): p. 207-216.
278. Menke, H. and P. Vaupel, *Effect of injectable or inhalational anesthetics and of neuroleptic, neuroleptanalgesic, and sedative agents on tumor blood flow.* Radiat Res, 1988. **114**(1): p. 64-76.
279. Hou, H., et al., *Electron paramagnetic resonance assessment of brain tissue oxygen tension in anesthetized rats.* Anesth Analg, 2003. **96**(5): p. 1467-1472.
280. Jones, K.M., et al., *Clinical Translation of Tumor Acidosis Measurements with AcidoCEST MRI.* Mol Imaging Biol, 2017. **19**(4): p. 617-625.

281. Liu, K.J., et al., *Lithium phthalocyanine: a probe for electron paramagnetic resonance oximetry in viable biological systems.* Proc Natl Acad Sci U S A, 1993. **90**(12): p. 5438-42.
282. Eubank, T.D., et al., *In Vivo Electron Paramagnetic Resonance Molecular Profiling of Tumor Microenvironment upon Tumor Progression to Malignancy in an Animal Model of Breast Cancer.* Mol Imaging Biol, 2023.
283. Vaupel, P., A.B. Flood, and H.M. Swartz, *Oxygenation Status of Malignant Tumors vs. Normal Tissues: Critical Evaluation and Updated Data Source Based on Direct Measurements with pO2 Microsensors.* Applied Magnetic Resonance, 2021. **52**(10): p. 1451-1479.
284. Kishimoto, S., et al., *Evaluation of a deuterated triarylmethyl spin probe for in vivo R(2) ∗-based EPR oximetric imaging with enhanced dynamic range.* Magn Reson Med, 2024. **91**(1): p. 413-423.
285. Epel, B., et al., *Electron paramagnetic resonance oxygen imaging of a rabbit tumor using localized spin probe delivery.* Med Phys, 2010. **37**(6): p. 2553-9.
286. Kotecha, M., et al., *In vitro oxygen imaging of acellular and cell-loaded beta cell replacement devices.* Sci Rep, 2023. **13**(1): p. 15641.
287. Shaw, M.A., et al., *SOX71, A Biocompatible Succinyl Derivative of the Triarylmethyl Radical OX071 for In Vivo Quantitative Oxygen Mapping Using Electron Paramagnetic Resonance.* Mol Imaging Biol, 2023.
288. Epel, B., et al., *Assessment of blood-brain barrier leakage and brain oxygenation in Connexin-32 knockout mice with systemic neuroinflammation using pulse electron paramagnetic resonance imaging techniques.* Magn Reson Med, 2024. **91**(6): p. 2519-2531.
289. Helmlinger, G., et al., *Interstitial pH and pO2 gradients in solid tumors in vivo: high-resolution measurements reveal a lack of correlation.* Nat Med, 1997. **3**(2): p. 177-82.
290. Moon, B.F., et al., *A comparison of iopromide and iopamidol, two acidoCEST MRI contrast media that measure tumor extracellular pH.* Contrast Media Mol Imaging, 2015. **10**(6): p. 446-55.
291. Randtke, E.A., et al., *Multislice CEST MRI improves the spatial assessment of tumor pH.* Magn Reson Med, 2017. **78**(1): p. 97-106.
292. Jones, K.M., et al., *Respiration gating and Bloch fitting improve pH measurements with acidoCEST MRI in an ovarian orthotopic tumor model.* Proc SPIE Int Soc Opt Eng, 2016. **9788**.
293. Swartz, H.M., *Using Stable Free Radicals to Obtain Unique and Clinically Useful Data In Vivo in Human Subjects.* Radiat Prot Dosimetry, 2016. **172**(1-3): p. 3-15.
294. Swartz, H.M., et al., *India ink: a potential clinically applicable EPR oximetry probe.* Magn Reson Med, 1994. **31**(2): p. 229-32.

295. Flood, A.B., V.A. Wood, and H.M. Swartz, *Using India Ink as a Sensor for Oximetry: Evidence of its Safety as a Medical Device.* Adv Exp Med Biol, 2017. **977**: p. 297-312.
296. Hanahan, D. and L.M. Coussens, *Accessories to the crime: functions of cells recruited to the tumor microenvironment.* Cancer Cell, 2012. **21**(3): p. 309-22.
297. Butler, J.M., H. Kobayashi, and S. Rafii, *Instructive role of the vascular niche in promoting tumour growth and tissue repair by angiocrine factors.* Nat Rev Cancer, 2010. **10**(2): p. 138-46.
298. Paik, J.Y., et al., *Reactive oxygen species-driven HIF1a triggers accelerated glycolysis in endothelial cells exposed to low oxygen tension.* Nucl Med Biol, 2017. **45**: p. 8-14.
299. Gentric, G. and F. Mechta-Grigoriou, *Tumor Cells and Cancer-Associated Fibroblasts: An Updated Metabolic Perspective.* Cancers (Basel), 2021. **13**(3).
300. Fu, Y., et al., *The reverse Warburg effect is likely to be an Achilles' heel of cancer that can be exploited for cancer therapy.* Oncotarget, 2017. **8**(34): p. 57813-57825.
301. Bricker, D.K., et al., *A mitochondrial pyruvate carrier required for pyruvate uptake in yeast, Drosophila, and humans.* Science, 2012. **337**(6090): p. 96-100.
302. Leung, S.W.S. and Y. Shi, *The glycolytic process in endothelial cells and its implications.* Acta Pharmacol Sin, 2022. **43**(2): p. 251-259.
303. Du, W., et al., *Endothelial Cell Glucose Metabolism and Angiogenesis.* Biomedicines, 2021. **9**(2).
304. Damgaci, S., et al., *Hypoxia and acidosis: immune suppressors and therapeutic targets.* Immunology, 2018. **154**(3): p. 354-362.
305. Kalyanaraman, B., G. Cheng, and M. Hardy, *Therapeutic Targeting of Tumor Cells and Tumor Immune Microenvironment Vulnerabilities.* Front Oncol, 2022. **12**: p. 816504.
306. Pilon-Thomas, S., et al., *Neutralization of Tumor Acidity Improves Antitumor Responses to Immunotherapy.* Cancer Research, 2016. **76**(6): p. 1381-1390.
307. Ho, K.S., et al., *Blood vessel hyperpermeability and pathophysiology in human tumour xenograft models of breast cancer: a comparison of ectopic and orthotopic tumours.* BMC Cancer, 2012. **12**: p. 579.
308. Fendt, S.M., et al., *Reductive glutamine metabolism is a function of the a-ketoglutarate to citrate ratio in cells.* Nat Commun, 2013. **4**: p. 2236.
309. Mashimo, T., et al., *Acetate is a bioenergetic substrate for human glioblastoma and brain metastases.* Cell, 2014. **159**(7): p. 1603-14.
310. White, K.A., B.K. Grillo-Hill, and D.L. Barber, *Cancer cell behaviors mediated by dysregulated pH dynamics at a glance.* J Cell Sci, 2017. **130**(4): p. 663-669.

311. Moon, R.B. and J.H. Richards, *Determination of intracellular pH by 31P magnetic resonance.* J Biol Chem, 1973. **248**(20): p. 7276-8.
312. Kim, H., L.C. Krishnamurthy, and P.Z. Sun, *Brain pH Imaging and its Applications.* Neuroscience, 2021. **474**: p. 51-62.
313. Tiret, B., E. Brouillet, and J. Valette, *Evidence for a "metabolically inactive" inorganic phosphate pool in adenosine triphosphate synthase reaction using localized 31P saturation transfer magnetic resonance spectroscopy in the rat brain at 11.7 T.* J Cereb Blood Flow Metab, 2016. **36**(9): p. 1513-8.
314. Cavallari, E., et al., *Studies to enhance the hyperpolarization level in PHIP-SAH-produced C13-pyruvate.* J Magn Reson, 2018. **289**: p. 12-17.